UNIVERSIDAD COMPLUTENSE DE MADRID

FACULTAD DE CIENCIAS FÍSICAS

DEPARTAMENTO DE FÍSICA DE MATERIALES

INTERACTIONS, EXTERNAL FIELDS AND DISORDER IN LOW-DIMENSIONAL SYSTEMS

INTERACCIONES, CAMPOS EXTERNOS Y DESORDEN EN SISTEMAS DE BAJA DIMENSIONALIDAD

TESIS DOCTORAL DE:

CLARA GONZÁLEZ-SANTANDER DE LA CRUZ

DIRIGIDA POR:

FRANCISCO DOMÍNGUEZ-ADAME ACOSTA

Madrid, 2014

Interactions, external fields and disorder in low-dimensional systems

Interacciones, campos externos y desorden en sistemas de baja dimensionalidad

Clara González-Santander de la Cruz

Departamento de Física de Materiales

Universidad Complutense de Madrid

Under the supervision of

Francisco Domínguez-Adame Acosta

A thesis submitted for the degree of

PhilosophiæDoctor (PhD)

2013

To Aitor

Contents

Chapter 1

Introduction and motivation of the Thesis

1.1 General scope of the Thesis

Condensed matter physics could be distinguished as one of the most prolific fields of contemporary physics research. It is devoted to studying the physical properties of condensed phases of matter, both at the microscopic and the macroscopic levels. Physicists pursue to understand the diverse and unexpected phenomena that arise when matter is formed from its fundamental constituents. Discoveries of novel phases of matter and many technological inventions present in our everyday life have been developed as a result of the research in this branch of physics. Due to the diversity of topics with which is related, this active field is deeply connected to other scientific disciplines such as biology, chemistry, material science, nanotechnology and mathematics. A detailed revision of the scope of condensed matter physics and the fertile and multitudinous phenomena found under this name is given in the general and very complete book *Introduction to Condensed Matter Physics* by F. Duan and J. Guojun [1]. For a short inspect, in the webpage of the Institute of Physics (United Kingdom) a booklet that addresses the main challenges of this area of research and examples of some recent scientific advances can be found [2].

Traditionally, this field is divided in soft and hard condensed matter physics, differentiating between them as a function of the energy and length scale where the interactions between constituents happen. Hard condensed matter, usually known as solid state physics, deals with materials with structural rigidity such as crystalline solids. Their physical properties are fundamentally governed by atomic forces and quantum mechanics. However, soft condensed matter is centred on the study of liquids, membranes, polymers and biological materials. The energy scale at which their physical behaviours occur is comparable to room temperature multiplied by the Boltzmann constant. Therefore,

quantum effects generally do not play any role, and their properties are mainly described by classical mechanics [1]. However, the boundary separating the two branches is becoming diffuse, and they are framed in the new paradigm of condensed matter physics, which emphasises many-body effects and broken symmetry [1]. This Thesis is embodied itself in the study of structures that operate in the quantum regime. The main purpose of this work is to explore different problems that have been faced in the past and in the present in the framework of theoretical hard condensed matter.

The building blocks of this research are settled on the foundations of quantum mechanics, which in the early 20th century revolutionised the way we understand matter. Quantum physics was the seed from which many other theories and models emerged and provided insights on the interaction between particles and the effects of external potentials on microscopic systems [3]. On the other hand, during the second half of the 20th century another important step in understanding the physical properties of matter was gained by the advances in nanotechnology [4]. In artificial nanostructures electrons are confined in one, two or three dimensions. When the size of the confinement is large enough to modify the optical, transport and magnetic properties of the system compared to the ones observed in the bulk material, the nanosize structure is subjected to quantum effects. This opens the door to explore scales where the interaction among matter constituents becomes significant. Therefore, the better the understanding of the physical laws present at that scale, the better the tailoring of the physical properties and the subsequent designing of electronic devices. Theoretical studies, although having a smaller impact on commercial applications, constitute a fundamental step for understanding observed phenomena and predicting new ones.

Inspired by the recent developments and experiments in the nanoscale regime, in this Thesis previous theoretical models are revised and new models are proposed to calculate, explain and augur physical properties in diverse quantum systems. The low-dimensional systems under study include two-dimensional (2D) systems such as graphene and quantum rings (QRs), one-dimensional (1D) structures like quantum wires (QWs) and zero-dimensional (0D) geometries such as artificial atoms or quantum dots (QDs). Specifically, this work is divided in three distinct areas of research related to fundamental mechanisms that govern the behaviour of particles in the quantum regime. We study different approaches for modelling the interaction with other particles, the effects of external fields on detectable properties of the system and finally, the way that imperfections could modify the particles' wave function behaviour. Each of these themes is introduced below. The reader will see that the connection of the chapters with the main topics of this Thesis does not follow a chronological scheme because they appear simultaneously along all the work. However, the chapters are self-contained and a full description of their theoretical framework is given at their beginning in order to make them more understandable.

1.2 Modelling of interaction between particles

One of the pillars of condensed matter physics is the energy band theory. And hence, it is one of the most fundamental lessons in the solid state physics undergraduate courses [1]. But it is one of the conceptually more complex models. This is not only due its crude approximations or complicated mathematical calculations, but also to all the physical properties that could be explained from it. Most of the electronic, optical and thermal properties of solids could be understood by this theory. Beyond the nearly-free electron or the tight-binding models, more complex methods, such as the pseudopotential method, the $\boldsymbol{k} \cdot \boldsymbol{p}$ method or the local density approximation have been demonstrated effective and efficient for realistic band calculations. The main challenge behind the different approaches is how to model the real crystalline potential and the interaction among electrons in order to find the most reliable band structure of the solid. Nevertheless, it should not be forgotten that there are other physical phenomena that cannot be explained by band theory. It is the case of electronic systems with correlated electrons. In this area, models such as the Hubbard model [5] and the Anderson impurity model [6] have been proved as convenient theories for understanding the physics of Mott insulators [7] and the Kondo effect [8], respectively. In this Thesis we are not going to take into account many-body effects.

In the context of band theory, the Non Local Separable Potential (NLSP) was one of the proposals for band structure calculations in valence crystals [9]. It was successfully used to determine the energy bands of perfect crystals [9] and crystals with impurities [10]. In Chapter 2 we extend the use of this method to the world of low-dimensional systems, but with the aim of obtaining information about electronic and scattering states. The main advantage of the NLSP is that it allows replacing a local potential by a separable non local potential. Then, the mathematical complexity and time of computing are reduced. In summary, we take the opportunity to apply the NLSP theory, which works for energy band calculations, to systems with reduced dimensionality where external fields are present.

As a first working example, we use the NLSP for modelling the Coulomb interaction between an electron and a hole forming an exciton in a QW based on a semiconductor material. The excitonic problem in a three-dimensional (3D) crystal is solved in most solid state textbooks and leads to discrete levels below the energy gap quantized in terms of an effective Rydberg energy. However, when the system is confined to lower dimensions, the exciton states are usually obtained by means of variational or perturbative methods [11–14]. Two competitive effects should be taken into account simultaneously, the confinement and the Coulomb interaction. Some studies have shown that the formation of excitons could improve the figures of merit of lasers based in QWs [15, 16]. The reduction of the length over which charge carriers are allowed to move leads to an enhancement of the excitonic effects. We have studied what happens as well in a 2D system. In Chapter 4 the binding energy

of excitons in QRs is calculated. Moreover, we include the effect of a magnetic field and analyse the combined effect of the Coulomb attraction and the magnetic potential. In this case, we do not explicitly use the NLSP but a short-range potential. The theoretical framework behind this problem is explained with more detail in the next section.

In the field of low-dimensional systems, other area with a growing interest is the confinement of ultracold atomic gases. Different techniques have been developed for trapping cold atoms in optical lattices [17]. Scattering processes govern the interaction in atomic gases [18], and a detailed description of the interaction potential becomes necessary as the confinement length is decreased. It is usually approximated by a zero-range potential [19]. But the validity of this approach is under debate when the confinement is enhanced and the characteristic length of the interaction becomes comparable to the trap size. Due to the simple analytical treatment of the two-body interaction that the NLSP provides, in the second part of Chapter 2 we use this method for describing two-body collisions under strong confinement conditions. We obtain the main parameters of the scattering properties and the energy levels of the system as the scattering length is varied.

1.3 Effects of external fields

The knowledge and tailoring of the quantum states and transport properties in low-dimensional systems is crucial to envision new optoelectronic devices [20]. One of the most effective ways to obtain an effective and precise control of the charge transport is the application of an external electromagnetic field, which could be time-varying. The scientific advances accomplished for building, measuring and theoretical modelling quantum systems where new effects could be observed had a huge boost over the past decades due to the simultaneous improvements in the experimental techniques and in the computing resources. The presence of an external field can lead to a wide range of phenomena. Without attempting to do a complete review of all the effects that have been observed in the context of condensed matter physics in recent years, below are some examples that allow the reader to get an idea of the amplitude and complexity of this study. A demonstrated effect of an electrostatic gate is to drive a current through a semiconductor, which is the fundamental ingredient for the operation of a transistor [21]. However, in quantum systems other surprising effects have been observed when a constant force is applied, such as Bloch oscillations in superlattices [22] and in ultracold atoms in optical lattices [23]. On the other hand, a static magnetic field splits the electronic states in Landau levels, which is reflected in the longitudinal conductivity as oscillations, known as the Shubnikov-de Haas effect [1]. Finally, we should mention the integer quantum Hall effect, which is the clearest and most studied consequence of a strong magnetic field applied on a 2D electron gas at low temperatures. It is a prominent signature of the quantum mechanical behaviour of carriers, and is now used as a fundamental standard for determining $e^2/\hbar$ [24].

Several theoretical approaches have been suggested for including and analysing the effects of external fields on the physical properties of low-dimensional systems. In this Thesis we focus our attention on three different phenomena related to the application of an external potential on quantum systems. In the first place, it is widely known that the interaction between light and matter modifies the physical properties of solids. For example it leads to energy shifts of the electronic states. This is the case of the optical Stark effect when a semiconductor is irradiated with a very intense laser pulse [25]. This inspired us to develop a detailed description of the laser interaction in low-dimensional systems and, in particular, the way it affects the energy states when impurities or excited states are also present. For a proper description of the interaction, a many-body treatment is needed, but different simplified models have been suggested to account for the laser effect. In general, they are based on the renormalization of the energy gap and effective masses [26, 27] or on a dressing of the interaction potentials [28, 29]. In Chapter 3 the latter model is used for obtaining the binding energy of impurity states in a QD and the optical absorption for excitonic states in a QW.

Secondly, external fields could be used to tune interference effects, which are one of the main ingredients for engineering actual electronic devices. The quantum interference effect par excellence when a magnetic field is present in a mesoscopic loop geometry is the Aharonov-Bohm (AB) effect [30]. It provides a beautiful evidence of the importance of the magnetic vector potential in the physical properties of the electronic system. The most striking consequence is that electrons could be affected by a vector potential even though they never feel the magnetic field itself. The wave function phase factor in each arm of the circular structure is modulated by the vector potential, and the interference pattern result depends on the magnetic flux enclosed by the ring. Therefore, at the quantum level, the vector potential is not a simple mathematical construct but also a real entity. In the low-dimensional world the best candidate for observing the AB effect is a QR. However, in this system, due to the confinement to which the electronic carriers are constrained, excitonic effects are promoted. This means that the competitive effects of the electron-hole interaction and the magnetic field should be studied with more detail. This gave birth to the excitonic AB (XAB) effect [31, 32] that is modelled and analysed for a 2D QR in Chapter 4.

Finally, another well suited mechanism for controlling quantum transport in low-dimensional systems is the application of time-dependent fields. They may lead to new ways of electronic transport that, in combination with the reduced dimensionality, gives rise to unexpected phenomena. That is the case, for example, of the dynamical localisation and absolute negative conductance observed in semiconductor superlattices [33], super Bloch oscillations detected in Bose-Einstein condensates [34] and the possible quantum pumping in graphene-based devices [35]. The methods employed for studying these diverse systems include a wide variety of theoretical tools, such as the nonequilibrium Green's function technique, the Floquet formalism or the scattering approach (in [36] a complete description

of these methods is presented). The transmission coefficient, and correspondingly the conductance at low temperature, is one of the most used magnitudes that allow researchers to analyse the effects of time-dependent potentials in quantum systems. Moreover, the transmission profile provides a clue for detecting bound or resonant states of the system. Considering this, in Chapter 5 we explore the existence of bound states in the continuum (BIC) in a QR when an AC side-gate voltage is applied. BIC refers to a state that is embedded in the continuum part of the spectrum but is normalisable [37].

On the other hand, due to the recent interest in tailoring the properties of graphene, some studies have focused their attention on how time-dependent potential barriers modify the Klein tunnelling (KT) present in this material. KT is a property of the relativistic Dirac equation [38], with which the graphene states at low energy could be described [39]. This effect explains why relativistic particles impinging normally into a step barrier are always transmitted [40]. Aiming to give some light on this subject, we also provide, in the second part of Chapter 5, a detailed description of the transmission coefficients for masless Dirac particles in 1D scattered by a time-dependent potential barrier.

1.4 Presence of imperfections

Low-dimensional systems are built and characterised nowadays by a wide range of technological methods, which are contained under the general name of nanotechnology due to the dimensions where it operates. Some of the fabrication techniques employed are chemical vapour deposition, molecular beam epitaxy and nanolitography [4]. Although the methods are now well known and technical improvements are continuous, none of them can ensure that the structures will be clean and perfectly crystalline after the full procedure of manufacturing. Geometrical imperfections and embedded impurities can appear in the system, and their effect in the physical properties needs to be studied. In particular, optical and transport properties of low-dimensional structures could be modified by the presence of localised electronic states formed from the interaction of electrons with defects.

Imperfections could be divided into two main groups [1]. On the one hand, dilute impurities, which are addressed as an isolated impurity in the solid. In this case, the main task for evaluating the impurity influence on the electronic states is to find a proper interaction potential for modelling its effects. In this framework, the band theory is slightly modified and almost all states are extended, but some localised modes could emerge. On the other hand, when defects are randomly distributed in the whole crystal states may become localised. Under these circumstances, the structures are referred to as disordered systems. Scattering processes are responsible for the localisation, which is classified in weak and strong localisation depending on the relative values of the wavelength of the electronic eigenstate and the elastic mean free path, characteristic of the disorder. In a 3D system, in the weak regime there are still a great number of extended states. However, in strongly disordered systems

electron waves are localised if the randomness of the disorder potential is strong enough. The seminal theory for studying the diffusion of electrons in random potentials is the Anderson model [41]. In this Thesis we have studied the effects of diluted impurities and disorder in low-dimensional systems.

Firstly, in Chapter 3 we deal with a single impurity in a QD. It may be caused by a substitutional donor in the crystal lattice. Several methods have been developed for studying the scattering effects that this impurity could produce on the Bloch states. The simplest way is to approach the problem from the viewpoint of a static impurity embedded in a metal described as a free electron gas. This leads to oscillations of the electron density in the neighbourhood of a localised charged impurity. They are known as Friedel oscillations and are related to the quantum behaviour of particles and screening effects of the sea of electrons [1]. However, assuming that the impurity is in a semiconductor, the problem could be addressed from the effective-mass approximation. In that case the extra electron introduced by the impurity feels a Coulomb potential screened by the dielectric constant of the host material. It is commonly called hydrogenic impurity. Besides this Coulomb attraction is much weaker than the Coulomb potential in the hydrogen atom. The presence of these defects has been widely studied in the past years, both theoretically and experimentally [42–50]. They produce discrete bound states that, in the case of nanostructure systems, are strongly affected by the reduction of dimensionality. As mentioned before, in Chapter 2 we present an analytical method for dealing with the Coulomb interaction, so we extend its use in combination with an external field to calculate the energy states of hydrogenic impurities in QDs.

Secondly, in Chapter 6 we examine the Anderson localisation in graphene flakes. Graphene is a truly 2D structure made of carbon atoms arranged in a hexagonal lattice. Its band structure was originally obtained in the first half of the 20th century showing an extraordinary behaviour close the Fermi energy [51]. In that region, the dispersion relation is linear, leading to zero effective mass for electrons and holes. Then, they are described as massless relativistic particles governed by the Dirac equation. It remained as an astonishing theoretical predicted material until the early years of the 21st century when it was successfully synthesised [52]. For this discovery, Geim and Novoselov were awarded by the Nobel Prize in 2010 [53]. The physical properties of graphene are even more striking than originally assumed. This carbon material has a high carrier mobility, large mean free path and long spin-coherence lengths, making it one of the best candidates for future technological devices [54]. But also it has attracted much interest from the theoretical point of view because it provides a perfect framework for examining quantum effects at the 2D scale. That is why the study of localisation effects is so interesting in this material. Anderson model predicts a disorder-induced localised-deslocalised states transition in 3D [41]. Beyond this model, the one parameter scaling theory revealed that in 2D and 1D all states are localised despite the strength of the disorder, so the transition is only possible in 3D systems [55]. However, several theoretical works suggested that

graphene could undergo an Anderson transition in spite of its 2D structure. In this Thesis we develop a method for analysing the localisation properties of the wave functions in graphene. We clarify under which conditions this material shows Anderson-type localisation and which are the possible reasons of the controversy about this problem.

1.5 Objectives and outline of the Thesis

As mentioned before, the work of this Thesis is divided into three main areas. Although they are presented simultaneously in the manuscript, the chapters are self-contained being organised in the following way. The different approaches used for modelling the interaction between particles are contained in **Chapter 2** to **Chapter 4**. In them, the theoretical study of electronic states in QWs, QDs, QRs and harmonic traps are shown. The effects of external fields on the optical and transport properties of low-dimensional systems are presented in **Chapter 3** to **Chapter 5**. The study is focused on the effects of an intense laser field in some nanostructures, a solenoid magnetic field in a QR and time-dependent potentials on two different quantum systems. Finally, the influence of imperfections on the electronic structure of low-dimensional systems is described in **Chapter 3** and **Chapter 6**. In these chapters the presence of hydrogenic impurities in a QD and Anderson-type disorder in graphene flakes is studied, respectively.

In order to show at first glance the most important results that have been obtained in each of the projects that make up this Thesis, the reader will find below a summary of the accomplished objectives in each of them. A detailed description of the theoretical framework will be explained at the beginning of each Chapter.

In **Chapter 2** we study the energy states of two interacting particles confined in harmonic potentials. On the one hand, we obtain the binding energy of excitons as a function of the lateral size of a parabolic QW. On the other hand, we analyse the energy levels of two atoms in a harmonic trap depending on the scattering length. Chapter 2 begins with a complete description of the theoretical model employed, the NLSP method. We show that the mathematical and computational efforts are reduced when using this approach instead of the common perturbative or variational methods. Moreover, the strong confinement limitations observed with other theories could be overcome.

In **Chapter 3** we examine the effects of an intense laser radiation on the electronic states and optical properties of low-dimensional systems. Our attention is centred on how to modify the binding energy of hydrogenic impurities in a QD and excitons in a QW. We show that the laser field could be modelled by dressing the interaction potentials. This introduces an extra controlling parameter of the physical properties. Thanks to it, firstly, we find an increase in the binding energy of the hydrogenic impurity as it is moved towards the edge of the QD and secondly, how the absorption coefficient may be used to characterise exciton transitions in QWs.

In **Chapter 4** we consider the XAB effect in a 2D QR. We study the effects that a transition from a 1D QR to a 2D QR, which is a more realistic geometry, has on the amplitude of the AB oscillations. We present a simple theoretical approach for modelling the excitonic problem when the electron-hole interaction is short ranged. The method developed allows us to obtain the exciton binding energy as a function of the magnetic flux enclosed in the ring geometry. We find that the XAB effect persists in a 2D QR, in agreement with the recent experimental results.

In **Chapter 5** we extend the study of BICs to time-dependent driven quantum systems. We show that applying an AC side-gate voltage in a QR the formation of BICs could be detected in the conductance. It displays Fano shape lines that could be interpreted as the signature of a BIC. Moreover, their energies could be controlled by varying the driving frequency. In Chapter 5 we also study the scattering of masless Dirac particles by oscillating barriers. We find that the transmission coefficient is unity, which is another manifestation of the KT in time-harmonic potentials. This problem is connected with recent studies on graphene. In order to include the time-varying potentials, the Floquet approach is used.

In **Chapter 6** we study the localisation and finite-size effects in graphene. Our calculation is based in the Anderson model adapted to the 2D structure of graphene. The problem is solved by means of the transfer-matrix method (TMM), which we modify for allowing the treatment of flakes of finite size. We clarify that, in order to observe Anderson localisation at weak disorder, the sizes of graphene flakes should be in the order of cents of nm. For smaller samples a regime of apparently extended states is identified.

Finally, the main results and conclusions will be summarised in **Chapter 7**. New research lines motivated by and derived from the present work will be commented as well. Following the rules for obtaining the PhD degree with *Mención Doctorado Europeo* at the Universidad Complutense de Madrid, at the end of this manuscript a brief summary in English and Spanish with the main objectives and the fundamental contributions of this Thesis will be given.

A list of abbreviations used within this Thesis and the list of publications published during this work are provided at the end.

Chapter 2

Modelling of two interacting particles confined in harmonic potentials

2.1 Introduction

The study of atomic and electronic interactions in 3D crystals has been one of the fundamental problems in condensed matter physics. In the framework of adiabatic and mean-field approximations the main obstacle for determining the energy levels of the crystal is the lack of knowledge of the averaged potential seen by electrons. Usually this is calculated by means of numerical methods based on first principles or by empirical approaches based on fittings to experimental results. In most of solid state textbooks this is the starting point for calculating the band structure of crystals. In the last years, the fast development of new experimental techniques led to the reduction of the crystal dimensionality and the appearance of confinement of electronic carriers. So, the study of atomic and electronic interactions in such low-dimensional systems has attracted much attention. Not only new methods have been suggested for studying the confining potentials but also for analysing the effects of interactions in these systems.

In this Chapter we revise and propose the use of the NLSP method to deal with the interaction of two particles when they are confined in harmonic potentials such as those present in nanostructures like QDs and QWs or in traps used in Bose-Einstein condensates. In order to understand the importance of the NLSP method we will start with a summary of the key ideas behind nonlocal and local interactions. In general, an interacting potential includes local and nonlocal characteristics, and acting over a wave function has the integral representation

$$V(\boldsymbol{r})\psi(\boldsymbol{r}) \rightarrow \int d^3\boldsymbol{r}'\, V(\boldsymbol{r},\boldsymbol{r}')\psi(\boldsymbol{r}') \ . \tag{2.1}$$

A local potential is represented by the form $V(\boldsymbol{r},\boldsymbol{r}') = V(\boldsymbol{r})\delta(\boldsymbol{r}-\boldsymbol{r}')$. Thus, the action of the interaction at the point $\boldsymbol{r}$ only depends on the values of $\psi(\boldsymbol{r})$ at that point [56]. The Coulomb potential is a clear example of this kind of interaction. But the Coulomb two-body problem cannot be solved in a closed form in confined systems. On the other side, for example, the nucleon-nucleon interaction is characterised by a non-local dependence and the inclusion of the general expression for the interacting potential, eq. (2.1), leads to an integral-differential equation that should be solved by numerical methods. To facilitate the numerical calculations some *separable* nonlocal potentials haven been suggested in nuclear physics [57, 58]. However a complete model that allows us to study accurately both local and nonlocal interactions is needed. The NLSP proposed by Knight and Sievert in 1963 [9] presents an alternative way to solve the Schrödinger equation for periodic potentials when exact solutions are not available. They developed a lattice model where the atomic potential at each site is replaced by a NLSP operator of the form

$$V(\boldsymbol{r})\psi(\boldsymbol{r}) \rightarrow -\gamma\, v(\boldsymbol{r}) \int d^3\boldsymbol{r}'\, v(\boldsymbol{r}')\psi(\boldsymbol{r}') \tag{2.2}$$

where $\gamma = \pm 1$ in general and the strength of the potential is embodied in $v(\boldsymbol{r})$. Mathematically, the potential of eq. (2.2) is a projective operator, in the sense that it maps all function space $\psi(\boldsymbol{r})$ into the space given by the $v(\boldsymbol{r})$. It is the simplest possible Hermitian operator, in contrast to a local potential, whose vector-space properties are more involved. Therefore, the model not only captures the essence of the separable potentials used in nuclear physics [57, 58] but also is suitable for replacing local potentials arising in condensed matter physics [9].

This NLSP is the natural extension of the 1D Kroning-Penney model to the 3D case and leads to an exactly solvable Schrödinger equation from which the electron energy can be easily obtained without tedious calculations and little computational effort. It is important to note that the Schrödinger equation after the replacement of the potential by a NLSP has precisely the same bound state solutions as the starting equation. A clear and detailed explanation of this exact replacement was presented in 1976 by Glasser [59]. We reproduce here his explanation in order to gain a better understanding of the NLSP method.

Assuming that the local potential $V(\boldsymbol{r})$ has the bound states: $\phi_1(\boldsymbol{r}), E_1; \ldots \phi_n(\boldsymbol{r}), E_n$, the following Hermitian matrix is defined

$$\alpha_{ij} = \int d^3\boldsymbol{r}'\phi_i^\dagger(\boldsymbol{r}')V(\boldsymbol{r}')\phi_j(\boldsymbol{r}')\ , \tag{2.3}$$

with its inverse $\beta = \alpha^{-1}$. Then, we define $v_i(\boldsymbol{r}) = V(\boldsymbol{r})\phi_i(\boldsymbol{r})$ and form the nonlocal potential

$$V'(\boldsymbol{r})\psi(\boldsymbol{r}) = \sum_{i,j}\beta_{ij}v_i(\boldsymbol{r}) \int d^3\boldsymbol{r}'v_j^\dagger(\boldsymbol{r}')\psi(\boldsymbol{r}')\ . \tag{2.4}$$

Then, the Schrödinger equation with the nonlocal potential, eq. (2.4), has precisely the same bound states solutions as $V(\boldsymbol{r})$. Hence, it is always possible to find a NLSP (or a sum of them) of the form

$$V(\boldsymbol{r})\psi(\boldsymbol{r}) = v(\boldsymbol{r}) \int d^3\boldsymbol{r}' v^\dagger(\boldsymbol{r}')\psi(\boldsymbol{r}') \ , \tag{2.5}$$

that supports the same bound states as the original local potential. This equation obtained by Glasser [59] is exactly the same introduced by Knight and Sievert [9], given by eq. (2.2), for the NLSP method with $\lambda = -1$ and assuming that $v(\boldsymbol{r}')$ is real. Consequently, there is no theoretical limitation to the numerical precision with which physical results may be obtained. Nevertheless, the key problem of the NLSP procedure is to set up an appropriate potential that reproduces the observed energy values of the physical situation being considering. As defined before, $v(\boldsymbol{r})$ is nothing but the local potential times the wave functions of its bound sates, which are unknown. Therefore, the main drawback of the NLSP method is that the potential function $v(\boldsymbol{r})$ is expressed in terms of the solutions of the original Schrödinger equation with the local interaction, which obviously is not known.

The way to overcome this problem is to choose a NLSP containing several free parameters which can be adjusted to give the correct eigenvalues. For example, it has been shown that placing a Gaussian potential with two free adjustable parameters at each site of a fcc lattice reproduces the band structure of germanium with remarkable precision in a short time of computation [9]. The two adjustable parameters of the potential, its range and strength, are chosen in order to match a bound-state energy and the atomic radius of a specific atom. The presence of impurities in the crystal can be also modelled by this two parameter Gaussian NLSP. Energy levels for a point impurity and energy bands for a linear chain and a plane of impurities were obtained by Fock in 1971 [10].

Not only studies of band structures have been performed by means of the NLSP. It has been successfully used to determine in a closed form the binding energy of an electron in the H_2^+ ion within the Born-Oppenheimer approximation [60]. In that case a Yamaguchi potential [61] was suggested because it has been tested as the most suitable for describing Coulomb bound states. The Yamaguchi potential is nothing but a Coulomb potential times the electron ground state wave function for this potential, so satisfies the assumptions of the exact replacement demonstrated by Glasser [59]. However for other kind of systems different potentials were proposed with satisfactory results. Surface δ-function potentials, which are a force field vanishing everywhere except on a spherical shell of a certain radius, are very well suited to simulate multicentre 3D interactions on quasi-1D polymers [60, 62, 63]. The NLSP has been also applied to the study of relativistic electrons in 1D polyatomic crystals [64].

Hence, the NLSP method is proved as an effective technique for studying a wide range of interacting problems in condensed matter physics. Our next step is to apply this method in low-dimensional systems where some kind of confinement potential is present and to develop a systematic

way for obtaining the ground state energy for the electrons or atoms confined. The external confining potential is not known a priori in real systems and it is usually obtained by means of self-consistent solutions of the Schrödinger equation, pseudopotentials or ab-initio calculations. In this sense, we will assume harmonic confinement potentials. Both theoretical [65] and experimental [66] studies have shown that parabolic potentials describe reasonably well actual potentials in QDs [67, 68] and QWs [69–71] and the deepest part of the confining potential of optical lattices [72]. We will study these three kinds of systems in this Chapter and in the next one. Moreover, the main advantage of a harmonic potential is that the one particle Hamiltonian is exactly solvable, which is a great benefit if we use the NLSP. Additionally, in the case of a two particle system, the centre of mass degree of freedom can be separated and solved exactly.

2.2 Nonlocal separable potential method

In this Thesis we will demonstrate that this method is well suited for studying two-body interactions in a variety of systems. For the sake of concreteness, we present a more detailed description of the NLSP method that has been applied to the low-dimensional systems studied in this Thesis. Consider a Hamiltonian written as $\mathcal{H} = \mathcal{H}_0 + V(r)$, where $\mathcal{H}_0$ is a Hamiltonian including the kinetic energy and the confinement potential where the two particles are embedded and $V(r)$ is the interparticle interaction potential, assumed to be spherically symmetric. Here $r = |\boldsymbol{r}_1 - \boldsymbol{r}_2|$. Therefore, this technique is in principle suitable to any kind of confinement potential. However as we have already explained, we restrict ourselves to harmonic potentials because their eigenenergies and eigenfunctions are well known. Likewise, the interacting potential can be originated by a variety of sources. For instance, we will deal with Coulomb interaction between an electron and a hydrogenic impurity, or with electron-hole interaction leading to an exciton. We will also apply this method to two atoms trapped in a narrow harmonic trap.

Before continuing with the theoretical description, a comment about the treatment of semiconductor materials is in order. In the case of low-dimensional systems based on these materials, we assume the effective-mass approximation. It means that we will solve an effective Hamiltonian where the periodic potential of the crystal lattice is explicitly omitted from the equation, but embedded in the kinetic energy through an effective mass of charge carriers. Therefore, the Bloch functions vanishes of the full wave function of the system and we just solve the effective Schrödinger equation for an envelope function. This function is nothing but a slowly varying function in real space that modulates the Bloch function. In summary, with this approach, the Scrödinger equation resembles the one for free electrons except for their effective masses [20].

As suggested by Knight and Sievert [9] the local potential is replaced by a NLSP in order to obtain the envelope function of the new Hamiltonian:

$$(\mathcal{H}_0 + V_{\mathrm{NLSP}}) \mid \chi \rangle = E \mid \chi \rangle \ , \tag{2.6a}$$

where for simplicity the NLSP potential is defined by

$$V_{\mathrm{NLSP}} \equiv -\frac{\lambda\hbar^2}{2m} \mid v \rangle\langle v \mid \ . \tag{2.6b}$$

We introduce two explicit adjustable parameters that model the strength and range of the interaction: λ is the **coupling constant** and v will be referred to as **shape function** hereafter. Their exact expressions depend on the considering system and are introduced later on. It is important to stress again that this replacement is exact, in the sense that it is always possible to find an NLSP (or sum of them) able to reproduce any set of given electronic states, and, consequently, there is no theoretical limitation to the numerical accuracy with which physical results are obtained. To solve eq. (2.6a) we consider the resolvent of the Hamiltonian $\mathcal{H}_0$ as follows

$$\mid \chi \rangle = -\left(\mathcal{H}_0 - E\right)^{-1} V_{\mathrm{NLSP}} \mid \chi \rangle = \frac{\lambda\hbar^2}{2m} \sum_{\nu} \frac{\mid \phi_\nu \rangle\langle \phi_\nu \mid}{E_\nu - E} \mid v \rangle\langle v \mid \chi \rangle \ , \tag{2.7}$$

where $\mid \phi_\nu \rangle$ labels the eigenstates of $\mathcal{H}_0$, E_ν being the corresponding eigenvalues. ν is a well-defined quantum number, which characterises each state. This approach is nothing but obtaining the Green's function of $\mathcal{H}_0$. For simplicity we assumed that the energy spectrum of $\mathcal{H}_0$ is discrete, although the case of a continuous spectrum can be also easily handled. Finally, projecting onto the ket $\mid v \rangle$ and assuming that $\langle v \mid \chi \rangle \neq 0$ we arrive at

$$\frac{\lambda\hbar^2}{2m} \sum_{\nu} \frac{|\langle \phi_\nu \mid v \rangle|^2}{E_\nu - E} = 1 \ . \tag{2.8}$$

This transcendental equation provides a closed expression for the energy E of the electronic state in the system under study. This equation is valid for any *arbitrary* shape function v and coupling constant λ. In the case of low-dimensional systems, usually naive shape functions provide accurate results. For example, a Yamaguchi and a δ-shell shape function were used for studying excitons confined in a QD [73], giving similar results to the exact diagonalisation of the Hamiltonian. In other study, electrons bounded to hydrogenic impurities in a QD where modelled by means of a Gaussian shape function, leading to very accurate result for the ground state energy [74].

The coupling constant λ introduced in eq. (2.6b) is not an adjustable parameter of the model and we will determine it for each system. This can be understood from the fact that when the confining potential is switched off, we might obtain the energy level of a free particle under the local interaction we are replacing. It should be noted that the dimensionality of the system plays an

important role because it determines the number of degrees of freedom and then the ground state energy without confinement.

The calculation in eq. (2.8) reduces to obtain the overlap integral between the shape function v and the eigenfunctions ϕ_ν. For a proper shape function this overlap will be a decreasing function of E_ν since the number of nodes of ϕ_ν increases with energy. This implies that the numerator of eq. (2.8) decreases with ν. Therefore the sum over eigenstates can be safely truncated after some terms if a closed expression is not known. This is usually the case, and the numerical procedure is implemented by means of an iterative bisection approach. We start with a certain interval of guessing values for the energy E and we look for a root. Then a new interval is defined in the vicinity of the crude estimated root, and the process is repeated until we find the root with the desired accuracy.

In general, the NLSP method proceed in the following steps:

1. Find the eigenvalues and eigenfunctions of the Hamiltonian $\mathcal{H}_0$.
2. Choose a shape function v.
3. Obtain the coupling constant λ from the ground state energy without confinement.
4. Solve the transcendental equation (2.8).
5. Compare the results with the expected values:
   (a) If the results are accurate, the problem is solved.
   (b) If the results are not within the desired accuracy, start again the problem from step 2.

2.3 Excitons in parabolic quantum wires

As a first example, we consider a single exciton in a parabolic QW. Due to the high crystal quality, interface roughness is often negligible and electrons and holes are free to move along the wire direction. Therefore, these systems are seen as quasi-1D nanostructures and thus exhibit properties related to this dimensionality. One of the most common fingerprints of the confinement achieved in the system is the enhancement of the excitons binding energy as the size of the QW is reduced. The Coulomb interaction plays a crucial role for an electron and a hole to stay close to each other to form a Wannier exciton assuming that the QW is made of semiconductors materials [12, 71, 75, 76]. The interplay of Coulomb interaction and the lateral confinement has attracted much attention due to remarkable properties of the exciton transitions in QWs. The most striking result is that in principle the binding energy in a purely 1D system should diverge, so the excitonic binding energy can be dramatically increased if the size of the QW is decreased enough. However, real QWs have a finite lateral size and some studies have demonstrated that the binding energy is finite but can be scaled

with the strength of the confinement in the perpendicular direction to the free wire direction [76, 77]. Moreover, it has been found an enhancement of the optical gain and low threshold current in QW lasers having exciton transitions as compared to those having free-carrier transitions [15, 16].

There are several theoretical works on the calculation of the binding energy of electrons and holes due to Coulomb interaction in QWs assuming a wide variety of confinement profiles. For example a simple rectangular well was originally proposed [78] and, later, the band offset of the materials that build the QWs were the responsible of the confinement [13, 15, 16, 75]. Detailed studies of the real geometrical shape of the confinement were also performed. Some were deduced from real microscopy images of V-shaped and T-shaped QWs [76, 77, 79] and others from the influence of strain effects on the confinement for V-shaped and self-assembly QWs [80]. Harmonic potentials have been also suggested as good candidates to describe reasonably well the QW confinement [71, 81, 82]. The binding energy is usually computed within the framework of the envelope function approximation [83–85]. This approach holds when the diameter of the QW is much larger than the spacing of the crystal lattice, which is not a serious restriction in QWs available nowadays. Neglecting the coupling to far bands and many body effects, the exciton envelope function in wide gap semiconductors obeys a Schrödinger-like equation. Since no analytical solutions are available in many geometries of interest, the exciton envelope function and the binding energy are often obtained by means of variational or numerical techniques.

Nevertheless, our proposal is to replace the Coulomb potential between the electron and the hole by a suitable NLSP. We assume that there is no interaction with other particles. The problem has some resemblances to the above mentioned confined excitons in QDs [73]. However, the solution to the problem of an exciton in a QW is more complex because the mixing of perpendicular and parallel degrees of freedom and the resulting potential for the relative motion of the electron and the hole cannot be separated. The same shortcoming appears after replacing the Coulomb potential by the Yamaguchi's NLSP [61]. These difficulties can be overcome by introducing a Gaussian NLSP [74], as shown below.

2.3.1 Model Hamiltonian

Consider an electron bound to a hole within the effective-mass approximation. The exciton is embedded in a parabolic QW which, for simplicity, will be considered of infinite length along the Z axis and relative dielectric constant ϵ made of a wide-gap semiconductor. Within these approximations, the two-particle Hamiltonian can be written as

$$\mathcal{H} = \sum_{i=e,h} \left[\frac{p_i^2}{2m_i} + V_i(x_i, y_i) \right] - \frac{e^2}{\epsilon |\boldsymbol{r}_e - \boldsymbol{r}_h|} \ , \tag{2.9}$$

where the sum index i refers to the electron (e) and the hole (h) with effective masses m_e and m_h, respectively. The lateral confinement potential is written as $V_i(x_i, y_i) = (1/2)\, m_i\omega^2(x_i^2 + y_i^2)$, where ω determines the lateral size of the QW.

For the parabolic potential it is convenient to separate the problem into centre of mass and relative coordinates as $\boldsymbol{r} = \boldsymbol{r}_e - \boldsymbol{r}_h$ and $\boldsymbol{R} = (m_e\boldsymbol{r}_e + m_h\boldsymbol{r}_h)/M$, where the total and reduced masses are $M = m_e + m_h$ and $m = m_e m_h/M$, respectively. The total Hamiltonian eq. (2.9) can be expressed as $\mathcal{H} = \mathcal{H}_{CM} + \mathcal{H}_r$ with

$$\mathcal{H}_{CM} = \frac{P^2}{2M} + \frac{1}{2}\, M\omega^2(X^2 + Y^2)\ , \tag{2.10a}$$

$$\mathcal{H}_r = \frac{p^2}{2m} + \frac{1}{2}\, m\omega^2\rho^2 - \frac{e^2}{\epsilon r} \equiv \mathcal{H}_0 - \frac{e^2}{\epsilon r}\ , \tag{2.10b}$$

where $\boldsymbol{\rho} = (x, y)$, and $\boldsymbol{P}$ and $\boldsymbol{p}$ are the conjugate momenta of the coordinates $\boldsymbol{R}$ and $\boldsymbol{r}$. The centre of mass problem, eq. (2.10a), is exactly solvable since $\mathcal{H}_{CM}$ corresponds to a 2D harmonic oscillator plus the kinetic energy of the free motion along the QW. A similar statement holds for $\mathcal{H}_0$ in eq. (2.10b). However, the Coulomb term in eq. (2.10b) mixes the parallel and perpendicular degrees of freedom, and the resulting Schrödinger equation cannot be exactly solved. Our study is devoted to find an accurate solution of the Schrödinger equation obtained from eq. (2.10b).

It has been previously shown that Coulomb forces in QDs [73] and molecular systems [60] can be accurately replaced by a NLSP. Consequently, the Schröndinger equation to obtain the envelope function $|\,\chi\,\rangle$ from eq. (2.10b) is replaced as explained in section 2.2.

2.3.2 Free excitons

The coupling constant λ is not an adjustable parameter of the model. This can be understood from the fact that we might obtain the energy level $E_0 = -\mathrm{Ry}^*$ of the free exciton from eq. (2.8) when the confining potential is switched off ($\omega \to 0$). Here Ry^* is the exciton effective Rydberg in 3D [1]. The calculation of the coupling constant λ is easily achieved in momentum space when $\omega = 0$. The Hamiltonian of the relative particle reads in this case $\mathcal{H}_r = \boldsymbol{k}^2\hbar^2/2m + V_{\mathrm{NL}}$ and therefore $\mathcal{H}_0 = \boldsymbol{k}^2\hbar^2/2m$. The eigenstates of $\mathcal{H}_0$ are plane waves $\langle\, \boldsymbol{r} \mid \boldsymbol{k}\,\rangle = (2\pi)^{-3/2}\exp(i\,\boldsymbol{k}\cdot\boldsymbol{r})$ with energy $E_{\boldsymbol{k}} = \hbar^2k^2/2m$. Thus, the energy spectrum is continuous and the summation appearing in eq. (2.8) is replaced by an integration in momentum space. Defining $k_0^2 = 2m|E_0|/\hbar^2$, we get

$$\frac{1}{\lambda} = \int d^3\boldsymbol{k}\, \frac{|\langle\, \boldsymbol{k} \mid v\,\rangle|^2}{k^2 + k_0^2}\ . \tag{2.11}$$

It becomes apparent that the coupling constant can be calculated from the Fourier transform of the shape function $\langle\, \boldsymbol{k} \mid v\,\rangle$. Hereafter, we will consider the following Gaussian shape function

[1] Note that we should recover the ground state energy of a 3D exciton because once that the confinement is recovered we have a 2D electronic gas on the transversal direction of the QW and free movement along the Z axis

$v(r) = (1/\sqrt{\pi}\,a)^3 \exp\left(-r^2/a^2\right)$, which also ensures a simple way to get the overlap integral with the eigenstates of $\mathcal{H}_0$. Taking into account that $\langle\, \boldsymbol{k} \mid v \,\rangle = \exp(-k^2a^2/4)$ and performing the integration in eq. (2.11) we arrive at

$$\lambda = 2\pi^2 a \left[\sqrt{\frac{\pi}{2}} - \frac{\pi}{2}\sqrt{\delta}\, e^{\delta/2}\,\mathrm{erfc}(\sqrt{\delta/2})\right]^{-1} , \tag{2.12}$$

where $\mathrm{erfc}(z)$ is the complementary error function [86]. For brevity we have defined $\delta = (a/a_{3\mathrm{D}})^2$, where $a_{3\mathrm{D}}$ is the effective Bohr radius of the exciton in 3D. This parameter should be as small as possible in the numerical calculation so that the Gaussian function approaches the δ-function limit. This limitation is related to the definition of the NLSP, as explained in section 2.1. The shape function is actually the local potential times the wave function of its ground state. Therefore, in order to reproduce accurately this condition, so the use of this method is well justified, the Gaussian function should be as much similar as we can to a δ-function, which is a more realistic form of the shape function.

2.3.3 Excitons in a quantum wire

After having discussed the main features of the NLSP, we now turn to its application to excitons in QWs ($\omega \neq 0$). In this case the normalised eigenfunctions of $\mathcal{H}_0$ in eq. (2.10) can be factorised in cylindrical coordinates as follows

$$\varphi_{n\ell k_z}(\boldsymbol{r}) = R_{n\ell}(\rho)\,\frac{e^{i\ell\theta}}{\sqrt{2\pi}}\,\frac{e^{ik_z z}}{\sqrt{2\pi}} , \tag{2.13}$$

with quantum numbers $\ell = 0, \pm1, \pm2\ldots$, $n = 0, 1, 2, \ldots$ and k_z. The axial function corresponding to a 2D harmonic oscillator is given by (see e.g. Ref. [87])

$$R_{n\ell}(\rho) = \sqrt{\frac{2\,n!}{(n+|\ell|)!}}\,\frac{\rho^{|\ell|}}{\mathcal{L}^{|\ell|+1}}\,e^{-\rho^2/2\mathcal{L}^2}\,L_n^{|\ell|}\left(\rho^2/\mathcal{L}^2\right) , \tag{2.14}$$

where $\mathcal{L} = \sqrt{\hbar/m\omega}$ is the QW radius for the exciton and $L_n^{|\ell|}$ denotes the generalised Laguerre polynomial [86]. The corresponding eigenenergies of the 2D oscillator are $E_{n\ell} = \hbar\omega(2n + |\ell| + 1)$. Consequently, the total energy of the eigenstate, eq. (2.13), is $E_{n\ell k_z} = E_{n\ell} + k_z^2\hbar^2/2m$.

To proceed we calculate $\langle\, \varphi_{n\ell k_z} \mid v \,\rangle$ and use eq. (2.8), where the sum runs over the three quantum numbers n, ℓ and k_z. Due to axial symmetry of the shape function, $\langle\, \varphi_{n\ell k_z} \mid v \,\rangle$ is nonvanishing only if $\ell = 0$. From eq. (2.13) we get

$$\langle\, \varphi_{n\ell k_z} \mid v \,\rangle = \frac{2\mathcal{L}\beta\delta}{\sqrt{2}\pi a^2(1+\beta\delta)}\left(\frac{1-\beta\delta}{1+\beta\delta}\right)^n \exp\left(-\frac{k_z^2a^2}{4}\right)\delta_{\ell 0} , \tag{2.15}$$

where $\beta \equiv a_{3\mathrm{D}}^2/2\mathcal{L}^2$ defines the strength of the confinement.

After some lengthy but straightforward algebra, inserting eq. (2.15) in eq. (2.8) gives the following transcendental equation for the exciton energy

$$1 = \frac{\lambda\sqrt{\beta\delta}}{2\pi a(1+\beta\delta)^2} \sum_{n=0}^{\infty} \frac{1}{\xi_n} \left(\frac{1-\beta\delta}{1+\beta\delta}\right)^{2n} \operatorname{erfc}(\sqrt{2\beta\delta}\xi_n)\, \exp\left(2\beta\delta\xi_n^2\right) \ , \tag{2.16}$$

where the coupling constant λ is given by eq. (2.12). For brevity we have defined $\xi_n \equiv \sqrt{2n+1-E/\hbar\omega}$.

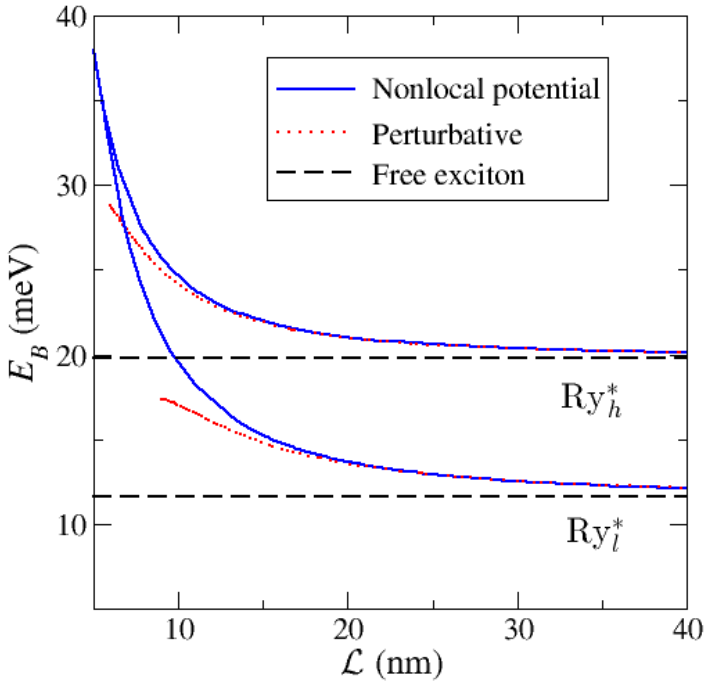

Figure 2.1: Binding energy as a function of the QW width for light- and heavy-hole excitons (upper and lower solid lines, respectively). The binding energy of free excitons ($E_B = \mathrm{Ry}^*$) is indicated by dashed lines. Perturbative results are plotted as dotted lines for comparison.

As an illustrative example of the NLSP approach, we consider light- and heavy-hole excitons in a QW of width $\mathcal{L}$ based on $In_{0.06}Ga_{0.94}N$. The effective masses of electrons, light-holes and heavy-holes are $0.19m_0$, $0.17m_0$ and $0.78m_0$, respectively, in units of the free electron mass m_0. The relative dielectric constant is $\epsilon = 10.24$. Consequently, the effective Bohr radii for light- and heavy-hole excitons are $a_{3D}^l = 6.04\,\mathrm{nm}$ and $a_{3D}^h = 3.54\,\mathrm{nm}$. The effective Rydberg is $\mathrm{Ry}_l^* = 11.6\,\mathrm{meV}$ and $\mathrm{Ry}_h^* = 19.8\,\mathrm{meV}$ for light- and heavy-hole excitons, respectively. We then obtain the energy level E of the exciton inside the QW by solving eq. (2.16) as a function of the QW width $\mathcal{L}$. In the absence of Coulomb interaction, the energy of the ground state of the electron and the hole is that

of two independent harmonic oscillators in 2D, namely $2\hbar\omega$. When the Coulomb interaction is taken into account, the energy of the ground state is $\hbar\omega + E$, the first term arising from the centre of mass motion [see eq. (2.10)]. The binding energy E_B is defined as the energy difference between the ground state energy of these two situations and therefore $E_B = \hbar\omega - E$. Figure 2.1 shows the binding energy as a function of the QW width. We have taken the adjustable parameter $\delta = 0.01$ in eq. (2.12) to perform the calculation, although we have checked that the results remain almost unchanged when $\delta = 0.005$. The binding energy approaches the effective Rydberg ($E_B \to \mathrm{Ry}^*$) in wide QWs ($\mathcal{L} \gg a_{3\mathrm{D}}$), as expected. By decreasing the QW radius the binding energy increases due to confinement effects. This behaviour can be understood as follows. Both $\hbar\omega$ and E, obtained after solving eq. (2.16), increases upon reducing the QW radius because the wave function is pushed toward the centre of the QW. However, the shift of the energy E of the relative particle is smaller since the corresponding wave function is already more localised around the centre of the QW due to the presence of the Coulomb term in eq. (2.10). As a consequence, the difference $\hbar\omega - E = E_B$ increases, as observed in fig. 2.1.

For comparison, we have also performed a first order perturbative calculation, assuming that the confining potential is weaker than the Coulomb interaction. This approach holds when $a_{3\mathrm{D}} \ll \mathcal{L}$, namely in the weak confinement regime. The unperturbed envelope function is written as $\chi^0(r) = (1/\sqrt{\pi a_{3\mathrm{D}}^3})\,\exp(-r/a_{3\mathrm{D}}^3)$ and the energy shift due to the parabolic confining potential is $\Delta E \equiv \langle \chi^0 \mid (1/2)m\omega^2\rho^2 \mid \chi^0 \rangle = m\omega^2 a_{3\mathrm{D}}^2$. Perturbative results are compared to those obtained by the NLSP approach in fig. 2.1. Remarkably, the perturbative calculation provides a reasonable value of the binding energy in the range $\mathcal{L} \gtrsim 3a_{3\mathrm{D}}$.

2.4 The two-body problem of ultra-cold atoms in a harmonic trap

The rapid development of experimental techniques in the field of laser cooling of atoms has led to a renewed interest in the two-body problem. Moreover, the ability to trap cold atoms in optical lattices opened a new perspective in the collision properties of atoms. In the first experiments performed in this area of research, trap sizes were very large compared with the scale length of the interaction between atoms. So, in general one can ignore that collisions take place in a trap. However, recent experiments show that when atoms are tightly confined in optical lattices the effect of the confinement has to be taken into account in order to understand new phenomena observed. For example, Greiner *et al*. have detected a quantum phase transition from a superfluid to a Mott insulator in a 3D optical lattice as the depth of the lattice is increased [88]. And more recently, Stöferle *et al*. show the creation of molecules from fermionic atoms using a magnetically induced Feshbach resonance [72]. A Feshbach resonance is the essential tool for controlling the interaction between atoms. A complete review of Feshbach resonances in ultracold gases could be found in [89].

In the both mentioned studies the 3D confining potential, when the tunnelling between individual potential wells of the lattice is suppressed, can be regarded as a 3D harmonic potential.

Scattering processes mediate the interactions in atomic gases. By means of Feshbach resonances, the scattering properties of an atomic collision between two atoms can be tuned to arbitrary repulsive or attractive values, allowing the access to a wide range of positive or negative values of the scattering length. Therefore, strongly interacting quantum gases can be created [90]. Furthermore, if atoms are subjected to a strong confinement the collision properties can be modified and a new description of the interaction has to be considered. For trapped atoms interactions manifest themselves as a shift in the quantised energy levels of the two atom system [91]. However, in some experiments the particles are confined to a length scale comparable to the scattering length that characterises low-energy atomic collisions. This happens near the Feshbach resonance [72]. Consequently, it is needed an accurate description of the interactions that accounts the possible effects of the reduction of atom trap to the order of the scattering length.

The first step is to determine the real atom-atom interaction, which is presumed rather complicated. From recent studies, the Hamiltonian structure for two colliding atoms in the absence of a trapping potential is well known. Commonly, alkali-metal or alkaline-earth-metal atoms are used in optical lattices, and their interaction is described by adiabatic Born-Oppenheimer potentials, which are often available from ab-initio or semiempirical sources [89, 91, 92]. The scattering properties are determined by the long-range interaction among the atoms. In the case under study, the leading term in the long-range part of the Born-Oppenheimer potentials has the same dependence as the Van der Waals potential $1/r^6$. Therefore, the scale associated by the Van der Waals interaction will govern the collision properties.

In order to avoid these difficulties, at low-energy regime the actual atom-atom interaction potential is replaced by a zero-range potential [93], known as regularised Fermi pseudopotential. In the context of cold atom physics, it was earlier considered theoretically in Ref. [19]. This replacement is well justified because it is not necessary to account for the finer details of the interaction potential because the de Broglie wavelength of the ultracold atoms is large enough [19]. However, as the size of the harmonic trap decreases, it is apparent that the details of the interaction potential between atoms become more important. Therefore, atomic collisions in narrow harmonic traps are not expected to be accurately described by a zero-range potential. The lack of accuracy will appear when the range of the atom-atom interaction potential is comparable to the size of the harmonic trap.

The aim of our work is to develop a suitable approximation of the interaction potential to describe two-body collisions under strong confinement conditions. This study has two main goals. In the first place, we look for a replacement of the actual interaction potential by a NLSP, while keeping the computational effort to a minimum. In other terms, we introduce a solvable model of the two-body

problem that allows us to obtain the main parameters of the scattering properties, the scattering length and the effective range, when the two particles are subjected to a finite-range interaction. Later, we add a 3D harmonic trap in order to model a strong confinement and the energy levels are obtained in a closed form. In the second place, the results obtained with the regularised Fermi pseudopotential should be recovered when the size of the harmonic trap is much larger than the range of the two-body potential.

2.4.1 The trapping potential

In the last 20 years an enormous advance in the control of ultracold atoms and molecular quantum gases has been achieved. Ultracold gases are usually cooled by laser cooling with a subsequent evaporative cooling performed in a magneto or optical trap. When the atomic de Broglie wavelength exceeds the mean spacing between particles quantum degenerate states of matter are produced, namely Bose-Einstein condensates. These studies have been awarded with two Nobel Prizes. In 1997 the developments of the techniques for cooling and trapping atoms were recognised and so happened also with the achievement of Bose-Einstein condensates in dilute gases of alkali atoms and the early fundamental studies of their properties in 2001 [94, 95].

Optical dipole traps allow the generation of stronger confinements than those produce by magnetic fields [96]. In an optical trap atoms interact with the oscillating electric field of a laser generating an oscillating dipole moment in the atom, which finally results in a trapping potential. A periodic potential can be formed by simply overlapping different laser beams. The interference between them produces an optical standing wave that traps the atoms [95]. The deepest part of the wells can be approximated by a harmonic trapping potential [72] described by

$$V_{\rm trap}(r_i) = \frac{1}{2}\, M\omega^2 r_i^2 \ , \tag{2.17}$$

where ω is the trapping frequency, M the atomic mass and r_i the position of the atom. Typical experimental trap frequencies range from $50\,$kHz to $1\,$MHz [91]. For an isotropic harmonic trap, the Hamiltonian for two particles is separable in the centre-of-mass and relative coordinates. Therefore, we can restrict ourselves to the Hamiltonian for the relative motion

$$\mathcal{H}_{\rm rel} = -\,\frac{\hbar^2}{2\mu}\,\nabla^2 + \frac{1}{2}\,\mu\omega^2 r^2 + V(r) \equiv \mathcal{H}_0 + V(r) \ , \tag{2.18}$$

where $\mu = M/2$ is the reduced mass, $\boldsymbol{r} = \boldsymbol{r}_1 - \boldsymbol{r}_2$ is the relative coordinate and $V(r)$ is the interaction potential, assumed to be spherically symmetric hereafter. The size of the harmonic trap is defined by $L = \sqrt{\hbar/\mu\omega}$. For the experimental achievable trapping frequencies it ranges from $10\,$nm to $150\,$nm [91].

2.4.2 The regularised Fermi pseudopotential

The simplest model for dealing with the interaction potential replaces the actual interaction potential by a regularised Fermi pseudopotential of the form [19, 90, 91, 93]

$$V(r)\psi(\boldsymbol{r}) \longrightarrow \frac{\hbar^2}{2\mu}\, 4\pi a_s \delta(\boldsymbol{r}) \frac{\partial}{\partial r}\Big[r\psi(\boldsymbol{r})\Big] \;, \tag{2.19}$$

where a_s is the s-wave scattering length and $\delta(\boldsymbol{r})$ is the 3D δ-function. As the atoms are ultracold and their exact potentials are independent of relative mechanical angular momentum ℓ, it is sufficient to assume s-wave ($\ell = 0$) scattering between the atoms.

This pseudopotential has a single bound state with $E < 0$ for positive scattering lengths. The interaction energy E of the two particles can be calculated. In [19] the Schrödinger equation is solved by an expansion of the wave function into the complete set of the wave functions of the harmonic oscillator. However, here we obtain the energy by the Green's function for the 3D harmonic oscillator

$$(\mathcal{H}_0 - E)\, G(\boldsymbol{r}, \boldsymbol{r}'; E) = \delta(\boldsymbol{r} - \boldsymbol{r}') \;, \tag{2.20}$$

from which the corresponding eigenfunction is obtained as follows

$$\psi(\boldsymbol{r}) = -4\pi a_s \frac{\hbar^2}{2\mu}\, G(\boldsymbol{r}, 0; E)\, \frac{\partial}{\partial r'}\left[r'\psi(\boldsymbol{r}')\right]_{\boldsymbol{r}'=0} \;. \tag{2.21}$$

The consistency of eq. (2.21) leads to an implicit equation for the interaction energy

$$1 = -4\pi a_s \frac{\hbar^2}{2\mu} \frac{\partial}{\partial r}\Big[rG(\boldsymbol{r}, 0; E)\Big]_{\boldsymbol{r}=0} \;. \tag{2.22}$$

The Green's function associated to the 3D harmonic oscillator is well known [97]

$$\begin{aligned} G(\boldsymbol{r}, \boldsymbol{r}'; E) = &-\frac{1}{\hbar\omega}\left(\frac{\mu\omega}{\pi\hbar}\right)^{3/2} \exp\left(-\frac{r^2 + r'^2}{2L^2}\right) \int_0^1 z^{1/2-\epsilon}\left(1 - z^2\right)^{-3/2} \\ &\times \exp\left(\frac{2\boldsymbol{r}\cdot\boldsymbol{r}' z - (r^2 + r'^2)z^2}{L^2(1 - z^2)}\right) dz \;, \end{aligned} \tag{2.23}$$

where $\epsilon = E/\hbar\omega$. Inserting eq. (2.23) in eq. (2.22) and after a lengthy but straightforward algebra one gets

$$\frac{L}{a_s} = 2\,\frac{\Gamma(3/4 - \epsilon/2)}{\Gamma(1/4 - \epsilon/2)} \;, \tag{2.24}$$

$\Gamma(z)$ being the Gamma function. This result is in agreement with the obtained earlier in Ref. [19]. Note that our definition of L is different from the one used in that previous work, and therefore equations differs by a $\sqrt{2}$ factor. Figure 2.2 shows the energies, obtained from eq. (2.24), as a function of the scattering length. For positive scattering length the energy levels are shifted upward compared to the harmonic oscillator spectrum of energies. Note that the s-states energies of the unperturbed harmonic oscillator are $E = 3/2, 7/2, 11/2, \ldots$ in units of $\hbar\omega$. At large positive (negative) values

of a_s, the energy levels are shifted upward (downward) by an amount $\hbar\omega$ with respect to the levels of the non-interacting case. In conclusion, the effect of the trapping potential is translated in a shifting on the energy levels, and for instance the single bound sate of the isolated regularised Fermi pseudopotential is shifted upward.

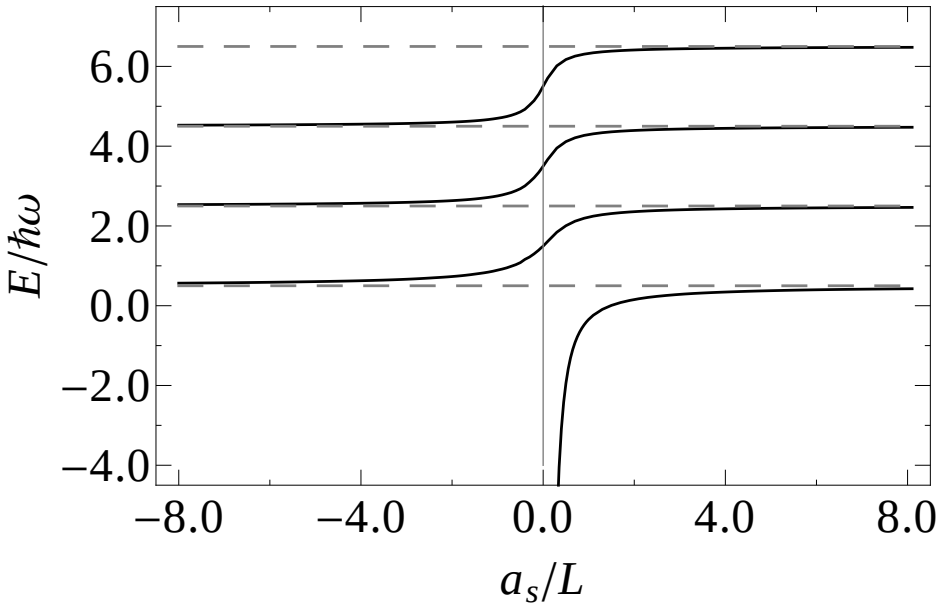

Figure 2.2: Energy levels of the two particles in a 3D harmonic trap, in units of $\hbar\omega$, as a function of the scattering length, expressed in units of L, given by eq. (2.24). The asymptotic energies at $a_s \to \pm\infty$ are indicated by dashed lines.

As explained before, in the long-range regime atoms interact via a van-der-Waals potential which is not at all a δ-function like, but has a tail which drops off as $1/r^6$ for large distances. Consequently, the validity of the regularised Fermi pseudopotential is questionable when the trapping confinement is increased. It has been established that the regularised Fermi pseudopotential treatment is valid as long as the characteristic range of the van-der-Waals interaction is small compared with L [91]. This assures that the interatomic potentials are not modified by the confinement and the atomic physics is not altered. Moreover, the scattering length can have a magnitude larger than the trap width L, and the pseudopotential approach fails. This is observed if the scattering length is modified by means of a Feshbach resonance for some species of atoms [89]. For a proper description of the experimental data two *energy-dependent* pseudopotentials were proposed if the scattering length is larger than L [98] or approaches the characteristic length of the real two-body potential [92]. These two self-consistent methods led to accurate interaction energy respect to exact two-body interaction potential for some alkali atoms. However, both claimed that the model can be expected to break down if the trap becomes too tight and the trap size is comparable to the Van der Waals scale length.

2.4.3 Finite-range interactions

The aim of our work is to propose a novel solvable model for interacting atoms in a 3D harmonic trap when the interaction is not point-like. The experience achieved in the study of interactions in two-body systems by means of the NLSP is the starting point of our study. We rewrite the definition of the NLSP presented at the beginning of this Chapter and given by eq. (2.2) in order to write explicitly the dependence on the effective mass of the two-body system. It replaces $V(r)$ in eq. (2.18) by a projective operator of the form

$$V(r)\psi(\boldsymbol{r}) \to -\frac{\gamma\hbar^2}{2\mu}\, u(\boldsymbol{r}) \int d^3\boldsymbol{r}'\, u(\boldsymbol{r}')\psi(\boldsymbol{r}') \tag{2.25}$$

where we set $\gamma = \pm 1$ hereafter without loss of generality. In contrast to the explicit form of the NLSP introduced in section 2.2 we will keep the strength of the potential embodied in the shape function $u(\boldsymbol{r})$.

As we have shown the NLSP method allows all magnitudes of interest to be expressed in a closed form. In particular, the s-wave scattering phase shift $\delta_0(\boldsymbol{k})$ satisfies the equation [99]

$$k\cot\delta_0(\boldsymbol{k}) = \frac{1}{4\pi\gamma|\widetilde{u}(\boldsymbol{k})|^2}\left[1 + \frac{2\gamma}{\pi}\,\mathcal{P}\int d^3\boldsymbol{q}\,\frac{|\widetilde{u}(\boldsymbol{q})|^2}{k^2-q^2}\right]\,, \tag{2.26}$$

where $\mathcal{P}$ denotes the principal value and

$$\widetilde{u}(\boldsymbol{k}) = \frac{1}{4\pi}\int d^3\boldsymbol{r}\, e^{i\boldsymbol{k}\cdot\boldsymbol{r}} u(\boldsymbol{r}) \tag{2.27}$$

is the Fourier transform of the shape function. From the effective range expansion at low energy, the phase shift is related to the scattering length a_s and the effective range r_0 by

$$k\cot\delta_0(k) \simeq -\frac{1}{a_s} + \frac{1}{2}r_0k^2\,. \tag{2.28}$$

We proposed two NLSP that could model the atom-atom interaction. Firstly, we determine the scattering properties in the absence of a confining potential in order to see whether they support a bounded state. Secondly, a 3D harmonic potential is included for modelling the trap of the optical lattice, and the interacting energy of the two-atoms is obtained. Finally, we compare our results with the regularised Fermi pseudopotential and analyse the range of validity of our model.

Yamaguchi NLSP

The Yamaguchi NLSP, $u(r) = (g/r)\exp(-r/a)$, which was introduced to describe nucleon-nucleon interaction in nuclear physics [61] and later it was also applied to describe Wannier excitons in QDs [73] is our first choice. The scattering length and the effective range of the potential depends

on the parameter a, which gives us information about the finite-size range of the interacting potential. From eq. (2.26) we get

$$k \cot \delta_0(k) = -\frac{1}{2a} + \frac{(1+k^2a^2)^2}{\xi a} \ , \tag{2.29}$$

where $\xi = 4\pi\gamma g^2 a^3$. Taking into account eq. (2.28) one gets

$$a_s = a\left(\frac{1}{2} - \frac{1}{\xi}\right)^{-1} \ , \quad r_0 = \frac{4a}{\xi} \ . \tag{2.30}$$

When γ is positive the NLSP supports a bound state if $\xi > 2$, i.e. $a_s > 0$. The unnormalized eigenfunction is

$$\psi_0(\boldsymbol{r}) = \begin{cases} \dfrac{1}{r}\left(e^{-k_0 r} - e^{-r/a}\right) \ , & k_0 \neq a^{-1} \ , \\ e^{-r/a} \ , & k_0 = a^{-1} \ , \end{cases} \tag{2.31}$$

and the corresponding energy is $E_0 = -\hbar^2 k_0^2/2\mu$, where k_0 is given by

$$k_0 = \frac{1}{a}\left[\sqrt{\xi/2} - 1\right]^{1/2} \ . \tag{2.32}$$

δ-shell NLSP

As a second working example of NLSP we consider the δ-shell, $u(r) = g\delta(r-a)$ [73]. In this case, from eq. (2.26) we obtain

$$k \cot \delta_0(\boldsymbol{k}) = -k \cot ka + \frac{k^2 a}{\xi \sin^2 ka} \ , \tag{2.33}$$

whose limit at low energy leads to

$$a_s = a\left(1 - \frac{1}{\xi}\right)^{-1} \ , \quad r_0 = \frac{2}{3}\, a\left(1 + \frac{1}{\xi}\right) \ . \tag{2.34}$$

The δ-shell NLSP supports a bound state when γ is positive and $\xi > 1$ ($a_s > 0$). In this case the unnormalized eigenfunction is

$$\psi_0(\boldsymbol{r}) = \frac{1}{r}\left[e^{-k_0|r-a|} - e^{-k_0(r+a)}\right] \ , \tag{2.35}$$

where k_0 is the root of the transcendental equation

$$1 = \frac{1 - e^{-2k_0 a}}{2k_0 a}\,\xi \ , \tag{2.36}$$

and the energy of the bound state is $E_0 = -\hbar^2 k_0^2/2\mu$.

Both NLSPs have a bound state for positive scattering length, when γ is positive. The next step is to study how this bound state is modified by the presence of a trapping potential.

2.4.4 Two particles in a harmonic trap

The collision properties of the two particles whose interaction is described by a NLSP are strongly modified when they are placed in a harmonic trap. In this case, instead of considering the eigenfunctions of $\mathcal{H}_0$, we express solution of the Schrödinger equation for the relative motion by means of the Green's function as

$$\psi(\boldsymbol{r}) = -\frac{\hbar^2\gamma}{2\mu}\int d^3\boldsymbol{r}' G(\boldsymbol{r},\boldsymbol{r}';E)u(r')\,\mathcal{I}\ , \tag{2.37}$$

with

$$\mathcal{I} = \int d^3\boldsymbol{r}\, u(r)\psi(\boldsymbol{r})\ , \tag{2.38}$$

where the Green's function is given by eq. (2.23). After inserting eq. (2.37) into eq. (2.38) and performing the angular integration we obtain the following equation for the energy of the relative motion

$$\frac{\mu}{2\pi\gamma\hbar^2} = -\iint dr\, dr'(rr')^2\mathcal{G}_0(r,r';E)u(r)u(r')\ , \tag{2.39}$$

where the radial Green's function (for $\ell = 0$) is given by [100]

$$\begin{aligned}\mathcal{G}_0(r,r';E) &= \frac{\Gamma(3/4-\epsilon/2)}{\Gamma(3/2)L^3\hbar\omega}\,\exp\left(-\frac{r^2+r'^2}{2L^2}\right)\\ &\times\ M(3/4-\epsilon/2,3/2,r_<^2/L^2)U(3/4-\epsilon/2,3/2,r_>^2/L^2)\ ,\end{aligned} \tag{2.40}$$

M and U being the confluent hypergeometric functions [86]. Here $r_>$ and $r_<$ denotes the largest and the smallest value of the pair (r,r'), respectively.

Yamaguchi NLSP

When $u(r)$ is the Yamaguchi potential, the integration in eq. (2.39) cannot be expressed in a closed form. However, it can be obtained easily by numerical methods since both the Green's function and the Yamaguchi potential fall off rapidly with the distance. In addition, using the asymptotic limits [86]

$$M(\alpha,3/2,z)\simeq 1\ ,\quad U(\alpha,3/2,z)\simeq\frac{\sqrt{\pi/z}}{\Gamma(\alpha)}-\frac{2\sqrt{\pi}}{\Gamma(\alpha-1/2)}\ , \tag{2.41}$$

when $z\to 0^+$ we recover the result obtained with the regularised Fermi pseudopotential, eq. (2.24), for $a = 0$. Thus, we come to the conclusion that the low-energy scattering properties of the regularised Fermi pseudopotential, eq. (2.24), and those of the Yamaguchi NLSP when $a\to 0$ are the same.

Figure 2.3 (a) depicts the dependence of the lowest energy level on the positive scattering length $a_s > 0$ for different values of the parameter a, in the case of the Yamaguchi NSLP. Energy is measured in units of $\hbar\omega$ and length is expressed in units of L. We observe that the curves shift to the high scattering length side of the plot on increasing the value of a/L. A more detailed inspection

of the numerical solution of eq. (2.39) reveals that the lowest energy level increases smoothly as a function of the parameter a when $a_s \to \infty$ (weakly interacting particles) and approaches the limiting value $E = (3/2)\hbar\omega$. This is shown in fig. 2.3 (b), where we have taken $a_s/L = 60$ to solve eq. (2.39) numerically, but we have checked that the results remain unchanged within the numerical uncertainty when $a_s/L = 70$.

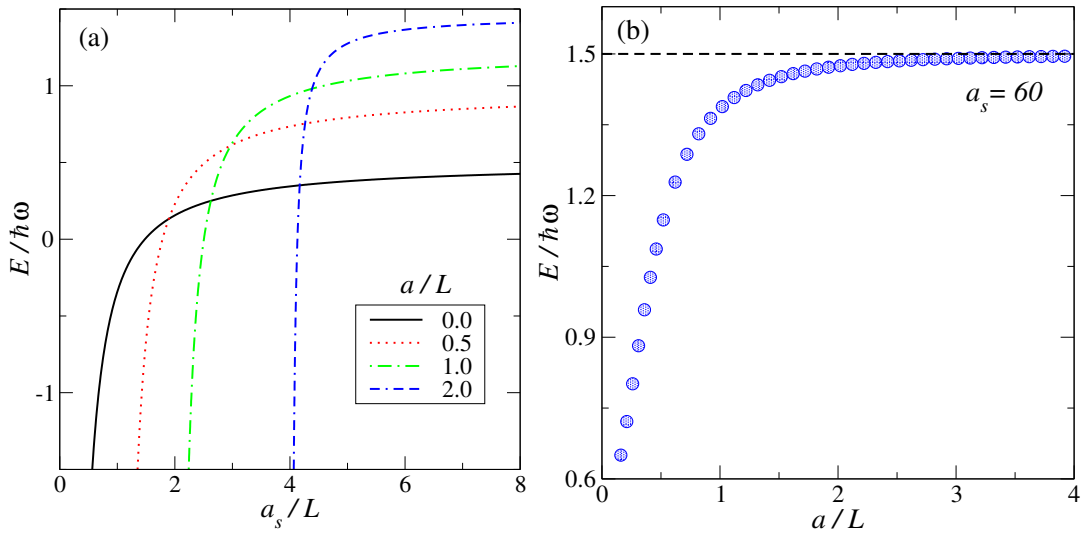

Figure 2.3: (a) Lowest energy level in the case of the Yamaguchi NLSP, in units of $\hbar\omega$, as a function of the scattering length, expressed in units of L, for different values of the parameter a. (b) Lowest energy level as a function of a/L for $a_s/L = 60$.

δ-shell NLSP

In the case of the δ-shell, we arrive at the following equation for the interaction energy from eq. (2.39) using the definitions given by in eq. (2.34)

$$\frac{L}{a_s} = \frac{L}{a} - \frac{\Gamma(3/4-\epsilon/2)}{\sqrt{\pi}} \exp\left(-\frac{a^2}{L^2}\right) \times M(3/4-\epsilon/2, 3/2, a^2/L^2) U(3/4-\epsilon/2, 3/2, a^2/L^2) \ . \tag{2.42}$$

Using the asymptotic limits given by eq. (2.41) we recover again the result obtained with the regularised Fermi pseudopotential, eq. (2.24).

Figure 2.4 (a) shows the lowest energy level as a function of the positive scattering length for different values of the parameter a, in the case of the δ-shell NSLP. The results resemble qualitatively those obtained with the Yamaguchi NLSP, shown in figure 2.3 (a), including the energy decrease without bound as the scattering length vanishes (strongly interacting particles). In the opposite limit, when $a_s \to \infty$, the lowest energy level increases smoothly when the parameter a increases, and approaches the limiting value $E = (3/2)\hbar\omega$. This behaviour is shown in figure 2.4 (b). Furthermore,

using the asymptotic limits of the confluent hypergeometric functions [86], one can obtain the following expression for the lowest energy state when $a/L \gg 1$ and $a_s \to \infty$

$$\frac{E}{\hbar\omega} \approx \frac{3}{2} - \frac{2a}{\sqrt{\pi}L} \exp\left(-\frac{a^2}{L^2}\right) . \tag{2.43}$$

The solid line in the inset of figure 2.4 (b) represents the energy obtained from eq. (2.43), which is fully consistent with the numerical results for $a/L > 3$.

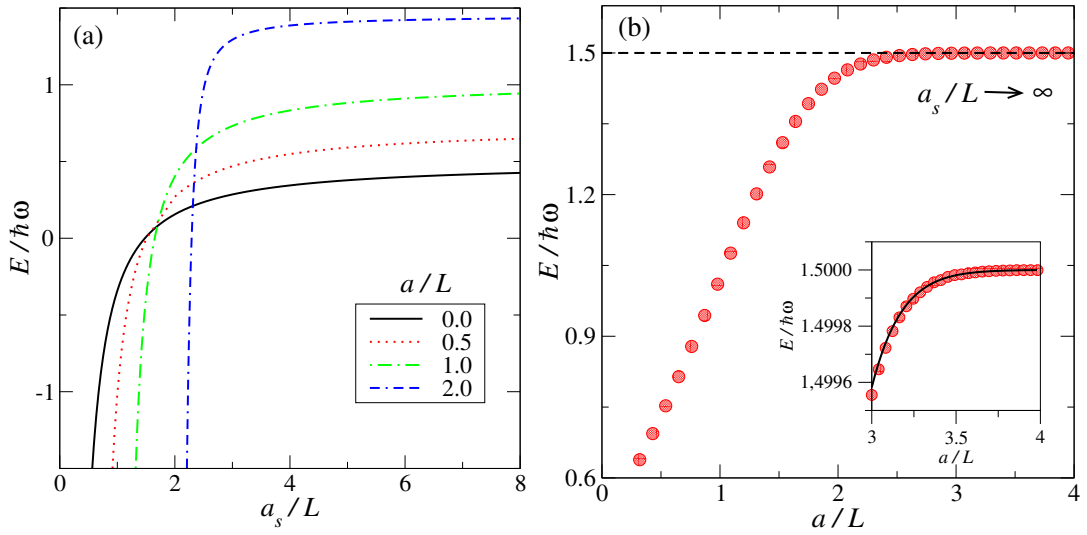

Figure 2.4: (a) Lowest energy level in the case of the δ-shell NLSP, in units of $\hbar\omega$, as a function of the scattering length, expressed in units of L, for different values of the parameter a. (b) Lowest energy level as a function of a/L when $a_s \to \infty$. The solid line in the inset corresponds to the energy obtained from eq. (2.43).

Finally, fig. 2.5 compares the first few levels of a harmonic trap perturbed by a regularised Fermi pseudopotential and NLSPs (Yamaguchi and δ-shell), for positive and negative scattering length. It is important to stress that the results for the regularised Fermi pseudopotential (solid line of fig. 2.5) can be recovered from the NLSP approach by taking $a \ll L$. We also observe that as in the case of the regularised Fermi pseudopotential (section 2.4.2) the trap led to a shifting of the energy levels. And even more, if the parameter a is of the order of the size of the harmonic trap, the NLSP predicts a remarkable increase of the energy levels (dashed and dash-dotted lines of fig. 2.5) as compared to the regularised Fermi pseudopotential result, when the magnitude of the s-wave scattering length a_s is large (irrespective of its sign). Also notice that the interaction energy obtained with the NLSPs reaches an asymptotic limit when a_s is negative or $a_s > 2L$.

The main difference with the previous studies with a contact interaction [19, 90, 91, 93] is found in the saturation values obtained for the energy levels. For positive values of a_s the energy levels are shifted in $2\hbar\omega$ while for negatives values of a_s there is no apparent shifting respect to the unperturbed

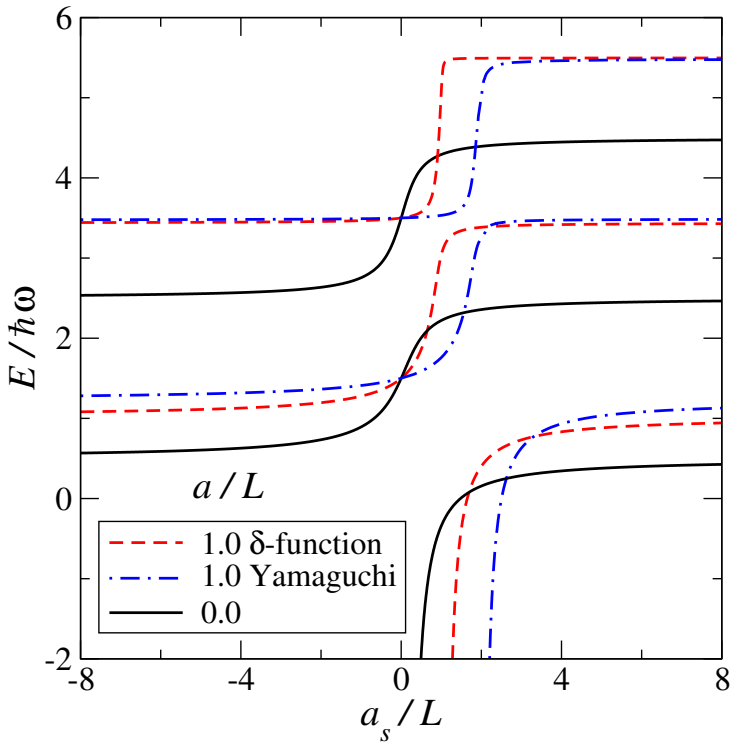

Figure 2.5: Energy levels of the relative motion of the two particles in a harmonic trap, in units of $\hbar\omega$, as a function of the scattering length, expressed in units of L, for different values of the parameter a. Results correspond to the regularised Fermi pseudopotential and the NLSPs (Yamaguchi and δ-shell), as indicated in the legends.

eigenstates of a harmonic oscillator. For both NLSPs the ground state diverges toward $-\infty$ as $a_s \to 0$ as does the corresponding bound state without trapping. The divergence starts at even larger values of a_s when a is increased. However as $a_s \to \infty$ and $a > 2L$ the asymptotic value corresponds to the ground state level of the non-interacting harmonic oscillator. When the scattering length is large the interaction is weaker and the effects of the harmonic trap become more significant. However, when using the regularised Fermi pseudopotential, the interaction dominates over the trapping and the asymptotic states are given by the zeros of eq. (2.24). The inclusion of the parameter a allows us to study different regimes of interaction and compare it with the trap size. When a becomes comparable to L is the harmonic potential the one that dominates the energy states. Therefore, we observe that the system rapidly converges to the eigenstates of the harmonic oscillator. This effect is even greater for negative values of a_s and higher energies as seen in fig. 2.5, in which case the energy does not change with respect to the harmonic oscillator states.

2.5 Summary and conclusions

In this Chapter we introduced a solvable model to calculate the energy levels of two particles trapped in a harmonic trap. Our procedure is based on the NLSP approach, in which the actual interacting potential is replaced by a projective operator. It is important to realise that this technique can be made exact, and so there are no theoretical limitations on this approach. In addition, closed solutions can be found for any arbitrary NLSP, as we actually demonstrated [see eq. (2.8)].

In order to prove the versatility of our approach we have studied two models that represents fundamental problems of condensed matter theory. On the one hand, we have considered exciton states in parabolic QWs made of wide gap semiconductor within the framework of the effective-mass approximation. In this case we have used a Gaussian NLSP, which leads to a closed solution for the energy of the excitonic states. We have compared our predictions to the results obtained by a perturbative approach, and found that the latter gives a reasonable value of the binding energy in the range $\mathcal{L} \gtrsim 3a_{3\mathrm{D}}$. As a major result we observed that when the size of the QW is reduced the binding energy for both heavy and light-excitons increases.

On the other hand, we calculated the energy levels of two atoms trapped in a harmonic trap. As a working example, we considered the Yamaguchi and the δ-shell NLSPs, and compared the predicted energy levels to those obtained by a regularised regularised Fermi pseudopotential. In both cases, the low-energy scattering properties of the NLSPs approach those shown by the regularised regularised Fermi pseudopotential when the parameter a, which model the interaction range, vanishes. Moreover, we have been able to see how the energy states are modified when the trap size becomes comparable to the characteristic length of the interaction.

Finally, we want to stress that the NLSP is a general procedure that can be employed in any kind of confinement, but we restrict ourselves to harmonic potentials because the eigenstates are well known. This is the major requirement in order to apply this method, as explained in section 2.2, with little computational effort. Therefore, it could be used in other low-dimensional systems by a suitable choice NLSP and if the electronic states without confinement potential are known.

Chapter 3

Effects of intense laser radiation on the electronic structure of low dimensional systems

3.1 Introduction

The existence of bound states of two interacting particles has a significant influence on the optical properties of semiconductor nanostructures, like QDs and QWs. In the past several years, much experimental and theoretical work has been done on the binding energy of hydrogenic impurities located in 0D semiconductor nanostructures, like QDs and QRs [42–50, 74, 101]. At the same time, as we discussed earlier (section 2.3), excitonic states in 1D nanostructures, such as QWs, have attracted much attention from the theoretical point of view [12, 13, 71, 75, 76, 82]. The spatial confinement of carriers leads to a strong enhancement of the binding energy and an increase of the oscillator strength in these nanostructures, as compared to bulk semiconductors or even quantum wells [83, 84]. Quantum confinement effects arise when the size of the nanostructure is of the order of the effective Bohr radius in the bulk semiconductor. As a consequence, optical absorption lines in semiconductor nanostructures are blue-shifted and carry information about the confinement of carriers. For example, it has been proved that spectroscopy tools are very useful to characterise electron states bound to hydrogenic impurities and exciton recombination in 0D and 1D nanostructures [102]. Most important, changes in the electronic and optical properties of nanostructures may be properly controlled by an appropriate selection of the sample geometry and material parameters, opening new potential applications in optoelectronics.

In order to understand their dependence on material and geometry parameters, exciton states and electron states bounded to hydrogenic impurities and their corresponding binding energy have

been calculated in a large number of different semiconductor nanostructures. Moreover, the use of optical techniques prompts the question on the influence of a laser field in the binding energy of carriers bound to hydrogenic impurities in QDs [27, 29, 103], QWs [27, 28] and quantum wells [26, 27]. Simultaneously, given the growing interest on the optical properties associated with excitons in 1D systems, some studies have suggested that an intense laser field can be used to tune and enhance the linear optical absorption and the excitonic binding energy [104, 105]. Usually, the effective-mass approximation is taken as starting point to construct the Hamiltonian for the interacting electron-hole pair. In the case of a high-frequency laser irradiation, its contribution to the system dynamics is introduce by a renormalization of the energy gap and effective masses [26, 27] or by a *dressing* effect on both the Coulomb and confinement potential [106–110]. Nevertheless, since no analytical solutions are available in many geometries of interest within this framework, the electronic states and the binding energy are often obtained by means of variational or numerical techniques.

We present an alternative approach based on the NLSP method, in which the actual Coulomb potential is replaced by a projective operator [9, 59]. The NLSP method has already been successfully used to determine in a closed form the binding energy of confined excitons [73] and hydrogenic impurities [74] in parabolic QDs. In the previous Chapter we have shown that it is an appropriate theory for studying excitons in QWs. This method yields an exactly solvable envelope function equation from which the electron states can be readily obtained with the desired accuracy. Our aim in this Chapter is to generalise this method to the case of an applied laser field on the low-dimensional system and give two working examples that are under current interest in the scientific community, namely hydrogenic impurities in QDs and excitons in QWs. For this purpose we will firstly present the theoretical bases that allow us to study theoretically these examples and we will continue with a detailed description of the physical quantities that can be obtained and how they depend on the nanostructure shape and size and laser intensity.

3.1.1 Intense high-frequency laser field

Assume that the system is subjected to the action of an intense high-frequency laser field, represented by a linearly polarised plane wave of frequency Ω. Under the dipole approximation the corresponding vector potential is $\boldsymbol{A}(t) = A_0 \widehat{\boldsymbol{u}} \cos \Omega t$, where A_0 is the amplitude of the incident beam and $\widehat{\boldsymbol{u}}$ is a unit vector that indicates the polarisation. In order to obtain the electron-laser interaction potential, we follow the nonperturbative theory previously developed to describe the atomic states under intense high-frequency laser fields [106–110]. We summarise the main ideas of the method that allows us to obtain a time-independent Schrödinger equation that embeds the effect of the laser field in the interaction potentials present in the system.

The first step is to apply a time-dependent translation transformation $\boldsymbol{r} \rightarrow \boldsymbol{r} + \boldsymbol{\alpha}(t)$ in the potential $V(\boldsymbol{r})$ [106, 107]. Thus the Schrödinger equation is written as

$$i\hbar\frac{\partial\psi(\boldsymbol{r},t)}{\partial t} = \left[-\frac{\hbar^2}{2m}\nabla^2 + V\Big(\boldsymbol{r}+\boldsymbol{\alpha}(t)\Big)\right]\psi(\boldsymbol{r},t)\ , \tag{3.1}$$

where m is the electron effective mass and

$$\boldsymbol{\alpha}(t) = -\frac{e}{mc}\int_0^t \boldsymbol{A}(t)dt = \boldsymbol{\alpha_0}\sin\Omega t\ , \tag{3.2}$$

with $\boldsymbol{\alpha_0} = -eA_0/mc\widehat{\boldsymbol{u}}$ and represents the quiver motion of a classical electron in the field. In Gaussian units, $\alpha_0 \equiv |\boldsymbol{\alpha}_0|$ is related to the time-averaged irradiance, referred for simplicity as intensity, of the laser beam as follows [111]

$$\alpha_0 = \sqrt{\frac{8\pi I}{c}}\,\frac{e}{m\Omega^2}\ . \tag{3.3}$$

The Schrödinger equation eq. (3.1) can be cast in a set of coupled time-dependent differential equations for the Floquet components of the wave function. It could be solved by an iteration scheme but to the lowest order of the iteration, namely in the high-frequency limit, the system reduces to the time-independent Schrödinger equation [108, 109]

$$\left[\frac{\boldsymbol{p}^2}{2m} + V_0(\boldsymbol{r},\boldsymbol{\alpha}_0)\right]\psi_0(\boldsymbol{r}) = E\psi_0(\boldsymbol{r})\ , \tag{3.4}$$

where ψ_0 is the zeroth Floquet component of the wave function and E is the energy. $V_0(\boldsymbol{r},\boldsymbol{\alpha}_0)$ is defined as *dressed potential* which depends on Ω and I only through $\boldsymbol{\alpha}_0$. This approach holds as long as $\hbar\Omega \gg |E_0(\boldsymbol{\alpha}_0)|$ where $E_0(\boldsymbol{\alpha}_0)$ is the ground state energy of eq. (3.4). Then, it means that in the high-frequency regime the electron only feels the static distorted potential $V_0(\boldsymbol{r},\boldsymbol{\alpha}_0)$, the dressed potential associated with the original interaction potential $V(\boldsymbol{r})$. Actually this dressed potential is the time averaged over a period of the oscillating potential $V\Big(\boldsymbol{r},\boldsymbol{\alpha}(t)\Big)$, which is given by the integral [108]

$$V_0(\boldsymbol{r},\boldsymbol{\alpha}_0) = \frac{1}{\pi}\int_{-1}^{1} V(\boldsymbol{r}+\boldsymbol{\alpha_0}u)(1-u^2)^{-1/2}du\ . \tag{3.5}$$

It could be interpreted as a potential created by a linear charge distribution of density $(1-u^2)^{-1/2}/\pi$ extending from $-\boldsymbol{\alpha}_0\,(u=1)$ to $\boldsymbol{\alpha}_0, (u=-1)$, being $V(\boldsymbol{r})$ the original potential created by a unit charge [108]. In our study, electronic carriers are confined in harmonic potentials and interacts trough a Coulomb potential. Therefore, following the procedure introduced above, both potentials have to be dressed by the parameter α_0 which carries the information about the laser irradiation. It has been shown [110] that the Coulomb potential screened by the dielectric constant of the nanostructure, $V(\boldsymbol{r}) = -e^2/\epsilon|\boldsymbol{r}|$, can be reasonably well described by approximating eq. (3.5) to

$$V_{\mathrm{C}}(\boldsymbol{r},\boldsymbol{\alpha}_0) = -\frac{e^2}{2\epsilon}\left[\frac{1}{|\boldsymbol{r}-\boldsymbol{\alpha}_0|} + \frac{1}{|\boldsymbol{r}+\boldsymbol{\alpha}_0|}\right]\ , \tag{3.6}$$

and in the same way for a harmonic potential with frequency ω

$$V_{\mathrm{HP}}(\boldsymbol{r},\alpha_0)=\frac{1}{4}\,m\omega^2\Big[(\boldsymbol{r}+\boldsymbol{\alpha_0})^2+(\boldsymbol{r}-\boldsymbol{\alpha_0})^2\Big]\ . \tag{3.7}$$

These dressed potentials have been used as well in other studies of hydrogen impurities in QWs [28] and QDs [29]. Finally, the Hamiltonian for a single particle confined in a parabolic low-dimensional system interacting by means of a Coulomb field and under a high-frequency laser beam becomes

$$\mathcal{H}=\frac{\boldsymbol{p}^2}{2m}+\frac{1}{2}\,m\omega^2\boldsymbol{r}^2+\frac{1}{2}\,m\omega^2\boldsymbol{\alpha}_0^2-\frac{e^2}{2\epsilon}\left[\frac{1}{|\boldsymbol{r}-\boldsymbol{\alpha}_0|}+\frac{1}{|\boldsymbol{r}+\boldsymbol{\alpha}_0|}\right]\ . \tag{3.8}$$

Some considerations about the range of intensity values within which this approach is valid are in order. The first assumption of the present approach is that the laser field can be properly described under the dipole approximation. Therefore, the dressing parameter α_0 should remain much smaller than the laser wavelength in order to satisfy this condition. This imposes an upper limit on the intensity values applicable to this study. In general, it is greater than the ones used in experimental setups, so it is not a real limit to our calculations. Nevertheless, the real condition for the intensity values comes from comparing α_0 with the size of the bound system in the absence of the laser field, namely the effective Bohr radius. We impose as limiting values for the intensity those that make $\alpha_0 \sim a_{2\mathrm{D}}$, which is the effective Bohr radius in 2D. Therefore, from eq. (3.3) one obtains that the maximum intensity scales as $I_{\max} \sim a_{2\mathrm{D}}^2\Omega^4$ [28, 112]. As an example, for a typical semiconductor such as GaAs and a laser of practical interest, such as CO_2 ($\Omega = 2\times10^{14}\,\mathrm{s}^{-1}$), the model is applicable when the intensity I is in the range $10^7-10^{12}\,\mathrm{W/cm^2}$, which is available in practice.

3.1.2 Nonlocal separable potential for a two-centre field

The solutions of the previous Hamiltonian eq. (3.8) cannot be expressed in terms of elementary functions. From eq. (3.6) it becomes apparent that under the laser field the system is equivalent to a single electron in a two-centre Coulomb field. This analogy allows us to replace the effective Coulomb potentials in eq. (3.6) by a pair of NLSPs to obtain the envelope function $|\,\chi\,\rangle$ from the effective-mass equation

$$\mathcal{H}\,|\,\chi\,\rangle \longrightarrow \Big(\mathcal{H}_0+V_{\mathrm{NL}}\Big)\,|\,\chi\,\rangle = E\,|\,\chi\,\rangle\ , \tag{3.9}$$

with $\mathcal{H}_0=\boldsymbol{p}^2/2m+V_{\mathrm{HP}}(\boldsymbol{r},\alpha_0)$. Comparing with the standard procedure introduced in section 2.2 we should consider two different shape functions because now we are dealing with a two-centre Coulomb field. Therefore, the NLSP is projective operator defined as

$$V_{\mathrm{NL}}\equiv-\frac{\lambda\hbar^2}{4m}\,\Big[\,|\,v_+\,\rangle\langle\,v_+\,|+|\,v_-\,\rangle\langle\,v_-\,|\,\Big]\ . \tag{3.10}$$

Equation (3.9) can be solved exactly for any arbitrary NLSP, provided the eigenstates of the $\mathcal{H}_0$ are known. To compute the envelope function $|\,\chi\,\rangle$, we consider the resolvent of the Hamiltonian $\mathcal{H}_0$ as follows

$$|\,\chi\,\rangle = -\Big(\mathcal{H}_0 - E\Big)^{-1} V_{\rm NL}\,|\,\chi\,\rangle = \frac{\lambda\hbar^2}{4m}\sum_{\nu}\sum_{s=\pm}\frac{|\,\varphi_\nu\,\rangle\langle\,\varphi_\nu\,|}{E_\nu - E}\;|\,v_s\,\rangle\langle\,v_s\,|\,\chi\,\rangle\;, \tag{3.11}$$

where $|\,\varphi_\nu\,\rangle$ denotes the eigenstates of $\mathcal{H}_0$ with eigenvalue E_ν. Projecting onto the kets $|\,v_\pm\,\rangle$ and setting the determinant of the resulting matrix to vanish we arrive at

$$\Big[S_+(E) - 1\Big]\Big[S_-(E) - 1\Big] = |C(E)|^2\;, \tag{3.12}$$

where for brevity we have introduced the following definitions

$$\begin{aligned} S_\pm(E) &= \frac{\lambda\hbar^2}{4m}\sum_{\nu}\frac{1}{E_\nu - E}\;|\langle\,v_\pm\,|\,\varphi_\nu\,\rangle|^2\;, \\ C(E) &= \frac{\lambda\hbar^2}{4m}\sum_{\nu}\frac{1}{E_\nu - E}\,\langle\,v_+\,|\,\varphi_\nu\rangle\,\langle\,\varphi_\nu\,|\,v_-\,\rangle\;. \end{aligned} \tag{3.13}$$

The transcendental equation (3.12) provides the electron energy E in the nanostructure in the presence of the laser field, for any *arbitrary* shape functions $v_\pm$ and coupling constant λ. The problem reduces to evaluate the sums $S_\pm(E)$ and $C(E)$, which should be truncated if there is no analytical expression for them. In the following sections we will apply this method to two different low-dimensional systems and sources of Coulomb interaction: a hydrogenic impurity in a QD and an exciton in a QW.

3.2 Hydrogenic impurities in quantum dots under intense laser radiation

As mentioned above, the use of optical techniques generated an increasing interest in the effects of the laser field in the binding energy of carriers bound to hydrogenic impurities. In this regard, Fanyao *et al.* calculated the binding energy of an on-centre donor hydrogenic impurity in a quantum well [28] and in a spherical QD [29] placed in an intense high-frequency laser. The confinement of carriers in the QD was modelled by a spherical quantum well with finite or infinite barrier. The authors followed the same theory presented in section 3.1.1, and considered that the laser field dresses the Coulomb potential. A variational approach was then used to calculate the binding energy of the on-centre donor hydrogenic impurity. They predicted a fast decrease of the binding energy with increasing field intensity. Recently, Yesilgul *et al.* obtained similar behaviour for impurities in QD when the confining potential is also dressed by the laser radiation [103]. They analysed the effect of shifting the impurity from the centre to the middle of the QD, keeping the laser polarisation parallel to the

growth direction. Furthermore, in these works only the weak confinement regime was considered because the sizes of the QDs were larger than the effective Bohr radius. Therefore, a detailed study of the strong confinement regime and the effects of varying the laser polarisation is needed.

We present a new approach where the NLSP method is applied to this system. On the one hand, previous results have shown that a closed expression can be obtained for the binding energy of hydrogenic impurities in QDs [74]. And on the other hand, as explained before, the NLSP method can be generalised to describe a dressed Coulomb potential when a low-dimensional system is subjected to an intense high-frequency laser field. In this section we will show that closed expressions for the binding energy of hydrogenic impurities can be obtained even if the system is subjected to an intense laser field. To this end we consider the laser effects on both Coulomb potential (replaced by a NLSP) and QD confinement potential. In addition, our approach is more general than the one presented by Fanyao *et al.* [29] and Yesilgul *et al.* [103] since it is valid for both on-centre and off-centre impurities and different laser polarisations.

3.2.1 Theoretical model

We consider a 2D noninteracting electron gas confined in a 0D nanostructure. In the framework of the effective-mass approximation, the single-electron Hamiltonian in the presence of a donor hydrogenic impurity can be written as $\mathcal{H} = \boldsymbol{p}^2/2m + V_{\rm QD}(\boldsymbol{r}) + V_{\rm d}(\boldsymbol{r})$. The pair $\mathbf{p}$ and $\mathbf{r}$ are the usual momentum and coordinate in the plane of the 2D electron gas, respectively. The effective mass of the electron is denoted by m. Here $V_{\rm QD}(\boldsymbol{r})$ is the QD potential assumed to be harmonic. The Coulomb potential due to a hydrogenic impurity located at position $\boldsymbol{r}_{\rm d}$ from the origin and screened by the background dielectric constant ϵ is $V_{\rm d}(\boldsymbol{r}) = -e^2/\epsilon|\boldsymbol{r}-\boldsymbol{r}_{\rm d}|$. The effect of the intense laser field is introduced in the Hamiltonian of the system through a *dressing* parameter α_0 related with the intensity and frequency of the incident laser field. Actually this means that the Coulomb and the confining potential are shifted by $\pm\boldsymbol{\alpha}_0$. Using the equations (3.6) and (3.7) the single-electron Hamiltonian in the presence of an hydrogenic donor is written as

$$\mathcal{H} = \frac{\boldsymbol{p}^2}{2m} + \frac{1}{2}\,m\omega^2\boldsymbol{r}^2 + \frac{1}{2}\,m\omega^2\boldsymbol{\alpha}_0^2 - \frac{e^2}{2\epsilon}\left[\frac{1}{|\boldsymbol{r}-\boldsymbol{r}_d-\boldsymbol{\alpha}_0|} + \frac{1}{|\boldsymbol{r}-\boldsymbol{r}_d+\boldsymbol{\alpha}_0|}\right]\,. \tag{3.14}$$

The Hamiltonian without Coulomb interaction is then $\mathcal{H}_0 = \boldsymbol{p}^2/2m + m\omega^2\boldsymbol{r}^2/2 + m\omega^2\boldsymbol{\alpha}_0^2/2$ and following the procedure of section 3.1.2 we arrive to the transcendental equation (3.12). We should stress again that the coupling constant λ is not an adjustable parameter of the model. This can be understood from the fact that we might obtain the energy level of an electron bound to the donor impurity in an infinite 2D semiconductor $E_{2D} = -4{\rm Ry}^*$ when the confining potential is switched off ($\omega \to 0$) and no laser radiation is applied to the nanostructure ($\alpha_0 \to 0$). Note that because we are dealing with a 2D system, the ground state energy is four times the one in a 3D semiconductor, which

is the effective Rydberg Ry^*. Therefore, the resulting value of the coupling constant depends on the shape function chosen and the dimensionality of the system under study. We focus on Gaussian shape functions which were formerly used for studying hydrogenic impurities located at position $\boldsymbol{r}_\mathrm{d}$ in QD [74, 101]. The dressing effect of the laser radiation on the Coulomb potential is included in the shape functions through a displacement $\pm\boldsymbol{\alpha_0}$ as follows

$$v_\pm(\boldsymbol{r}) = \frac{1}{\pi\, a^2} \exp\left(-\frac{(\boldsymbol{r} - \boldsymbol{r}_\mathrm{d} \pm \boldsymbol{\alpha}_0)^2}{a^2}\right) \,, \tag{3.15}$$

where a is a free parameter that must be set properly to account for the ground state of the hydrogenic impurity in a 2D semiconductor.

The calculation of the coupling constant λ is easily achieved in momentum space when $\omega = 0$ and $\alpha_0 = 0$. Due to the translational invariance of $\mathcal{H}_0$ in this case, we can set $\boldsymbol{r}_\mathrm{d} = 0$ without loss of generality. The Hamiltonian reduces to $\mathcal{H}_0 = \boldsymbol{p}^2/2m$ and its eigenstates are plane waves with energy $E_{\boldsymbol{p}} = \boldsymbol{p}^2/2m$. Thus, the energy spectrum is continuous and the summations appearing in eq. (3.12) are replaced by an integration in momentum space. The shape function eq. (3.15) is simplified to the one proposed in [74] and finally eq. (3.12) reduces to a much simpler transcendental equation. The coupling constant can be calculated easily from the Fourier transform of the shape function. Performing the same derivation as in [74], the coupling constant is found to be

$$\lambda = 4\pi \frac{e^{-\delta/2}}{\Gamma(0, \delta/2)} \,, \tag{3.16}$$

where $\Gamma(b, z)$ is the incomplete Gamma function [86] and $\delta = (a/a_{2\mathrm{D}})^2$ is and adjustable parameter. As in the previous Chapter, this parameter should be as small as possible in the numerical calculation so that the Gaussian function approaches the δ-function limit.

3.2.2 Donor bound electron in a parabolic quantum dot

After having obtained the coupling constant, we now turn to the normalized eigenfunctions of $\mathcal{H}_0$, which are required to obtain the energy from eq. (3.12) when the laser field is switched on and the impurity is located at an arbitrary position $\boldsymbol{r}_\mathrm{d}$. From eq. (3.14) we notice that the eigenfunctions of $\mathcal{H}_0$ are the ones of an electron in a parabolic potential with an offset energy $m\omega^2\alpha_0^2/2$

$$\varphi_{n\ell}(r, \theta) = R_{n\ell}(r)\, \frac{e^{i\ell\theta}}{\sqrt{2\pi}} \,, \tag{3.17}$$

with quantum numbers $\ell = 0, \pm1, \pm2 \ldots$ and $n = 0, 1, 2, \ldots$. The radial function is given by [87]

$$R_{n\ell}(r) = \sqrt{\frac{2\, n!}{(n + |\ell|)!}}\, \frac{r^{|\ell|}}{\mathcal{L}^{|\ell|+1}}\, e^{-r^2/2\mathcal{L}^2}\, L_n^{|\ell|}\left(r^2/\mathcal{L}^2\right) \,, \tag{3.18}$$

where $\mathcal{L} = \sqrt{\hbar/m\omega}$ is the QD size and $L_n^{|\ell|}$ denotes the generalized Laguerre polynomial [86]. The eigenenergies are $E_{n\ell} = \hbar\omega(2n + |\ell| + 1) + m\omega^2\alpha_0^2/2$.

We set the X axis along the direction $\boldsymbol{r}_{\rm d}$ without loss of generality. The overlap between $v_\pm$ defined by eq. (3.15) and $\varphi_{n\ell}$ is given by

$$\begin{aligned} \langle\, v_\pm \mid \varphi_{n\ell}\,\rangle &= \frac{\sqrt{2\pi}}{\pi a^2}\,\exp\left[\,\mp i\ell\lambda_\pm - \frac{1}{a^2}\left(r_{\rm d}^2 + \alpha_0^2 \mp 2r_{\rm d}\alpha_0\cos\phi\right)\right] \\ &\times \int_0^\infty dr r e^{r^2/a^2} R_{n\ell}(r) I_{|\ell|}\left[\sqrt{1+\eta_\pm^2}\left(\frac{2rr_{\rm d} \mp 2r\alpha_0\cos\phi}{a^2}\right)\right]\,, \end{aligned} \tag{3.19}$$

where ϕ is the angle between $\boldsymbol{\alpha}_0$ and the X axis, namely the polarisation angle of the laser field. The following parameters are defined in order to simplify the notation $\eta_\pm = \alpha_0\sin\phi/(r_{\rm d} \mp \alpha_0\cos\phi)$ and $\lambda_\pm = \arctan\eta_\pm$. $I_{|\ell|}$ is the modified Bessel function [86]. After some algebra we obtain

$$\begin{aligned} \langle\, v_\pm \mid \varphi_{n\ell}\,\rangle &= \frac{\sqrt{2\pi}}{\pi a^2}\kappa_{n\ell}\,\exp\left(\mp i\ell\lambda_\pm - \frac{z_{\rm d}^2}{2\mu\beta} - \frac{\gamma^2}{\mu} \pm \frac{2z_{\rm d}\gamma\cos\phi}{\mu\sqrt{2\beta}}\right) \\ &\times \exp\left(\frac{\mu\beta\rho_\pm^2(1+\delta_\pm^2)}{2(1+\mu\beta)}\right) L_n^{|\ell|}\left(\frac{\mu^2\beta^2\rho_\pm^2(1+\eta_\pm^2)}{1-\mu^2\beta^2}\right)\,, \end{aligned} \tag{3.20}$$

with

$$\begin{aligned} \rho_\pm &= \frac{z_{\rm d}}{\mu\beta} \mp \frac{2\gamma\cos\phi}{\mu\sqrt{2\beta}}\,, \\ \kappa_{n\ell} &= \sqrt{\frac{n!}{(n+|\ell|)!}}\left(\frac{1-\mu\beta}{1+\mu\beta}\right)^n \left(1+\frac{1}{\mu\beta}\right)^{-|\ell|-1} \rho_\pm^{|\ell|}(1+\eta_\pm^2)^{|\ell|/2}\,. \end{aligned} \tag{3.21}$$

For brevity we introduce the confining parameter $\beta \equiv a_{\rm 2D}^2/2\mathcal{L}^2$. This parameter determines the magnitude of the donor-bound electron confinement in the QD since the larger β, the higher the confinement. The parameter $\gamma \equiv \alpha_0/a_{\rm 2D}$ gives the ratio between the laser and the Coulomb interactions parameterized by α_0 and $a_{\rm 2D}$, respectively. In this study we will restrict ourselves to the range $0 \leq \gamma \leq 1$. The position of the impurity will be measured in units of the size of the QD, $z_{\rm d} = r_{\rm d}/\mathcal{L}$.

Inserting eq. (3.18) in eq. (3.12) we obtain a transcendental equation that it is solved numerically with little computational effort for any chosen set of parameters. In order to compare the results for different confinement strength, impurity position and laser intensity, we focus on the binding energy of the ground state $E_B = m\omega^2\alpha_0^2/2 + \hbar\omega - E$.

3.2.3 Binding energy of hydrogenic impurities in quantum dots

We present our results for different values of the confining parameter $\beta = a_{\rm 2D}^2/2\mathcal{L}^2$ and the parameter $\gamma = \alpha_0/a_{\rm 2D}$. Energy will be measured in units of the 2D effective Rydberg $4{\rm Ry}^*$. In Ref. [74] it has

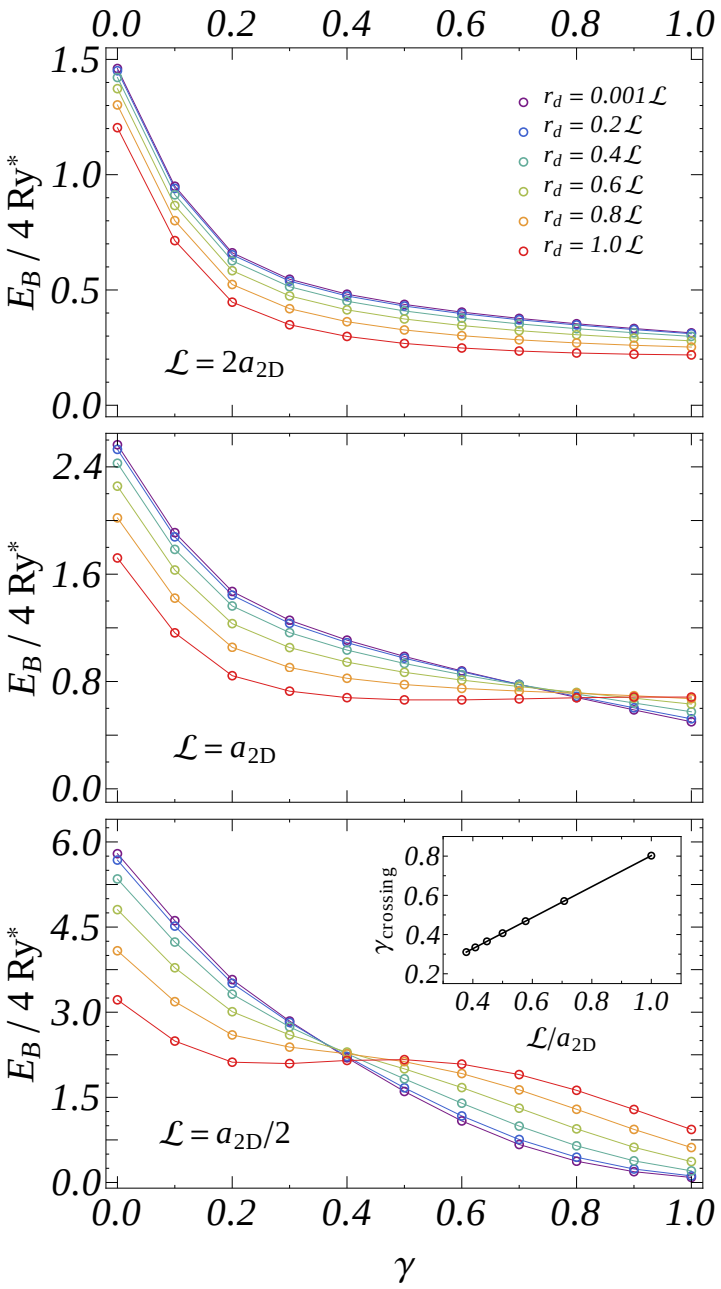

Figure 3.1: Binding energy in units of the 2D effective Rydberg as a function of the parameter $\gamma = \alpha_0/a_{2D}$ for three values of the QD size, indicated on each plot, and different impurity positions r_d. The polarisation angle is $\phi = 0$. The inset shows the linear dependence of the value of γ at the crossing on the QD size.

been shown that good accuracy is achieved with $\delta = 0.01$ in the coupling constant, eq. (3.16), and hereafter we take this value.

Figure 3.1 shows the binding energy of the ground state as a function of the parameter $\gamma = \alpha_0/a_{2D}$ for polarisation angle $\phi = 0$ and for three sizes $\mathcal{L}$. From top to bottom $\mathcal{L} = 2a_{2D}$, $\mathcal{L} = a_{2D}$

and $\mathcal{L} = a_{2\mathrm{D}}/2$, which allows us to study the full range from weak ($\mathcal{L} > a_{2\mathrm{D}}$) to strong ($\mathcal{L} < a_{2\mathrm{D}}$) confinement regimes. The curves correspond to different values of the impurity position, which is continuously shifted from the centre to the edge of the QD. Different trends in the dependence of the binding energy on the laser intensity and the QD size are observed and discussed below.

Binding energy when the laser is switched off

We introduce a much simpler 1D approach to explain qualitatively the decrease of the binding energy when the impurity is slightly shifted from the origin and $\gamma = 0$, observed in fig. 3.1. It should be mentioned that a similar behaviour was reported previously in Refs. [29, 103] for different confinement potentials and theoretical approaches. The simplified model considers an electron moving in one dimension and replaces the Coulomb potential by a δ-function. The Hamiltonian reads $\mathcal{H} = \mathcal{H}_0 - (e^2/\epsilon)\delta(x - x_d)$, where $\mathcal{H}_0 = p^2/2m + (1/2)m\omega^2 x^2$ is the Hamiltonian of a harmonic oscillator. Introducing the Green's function of the harmonic oscillator, it is a matter of simple algebra to arrive at the following equation for the energy levels $G_0(x_d, x_d; E) = \epsilon/e^2$, namely

$$G_0(x_d, x_d; E) = \sum_{n=0}^{\infty} \frac{|\psi_n(x_d)|^2}{E_n - E} = \frac{\epsilon}{e^2} \ , \qquad E < E_n \ , \tag{3.22}$$

where the sum runs over the eigenstates of the harmonic oscillator. The largest contribution to the sum in eq. (3.22) comes from the ground state of the unperturbed oscillator $n = 0$. Taking into account that $E_0 - E = E_B$, equation eq. (3.22) can be approximated as $|\psi_0(x_d)|^2/E_B = \epsilon/e^2$. When the impurity is slightly shifted from the origin the probability density $|\psi_0(x_d)|^2$ decreases and consequently E_B must decrease too, as observed in fig. 3.1.

Binding energy when the laser is switched on

Figure 3.1 shows that E_B decreases when γ is not large (namely $\alpha_0 < \mathcal{L}$), no matter the impurity position. However, when the confinement is enhanced and the size of the QD is of the order of the Bohr radius or even smaller, the curves show a well defined crossing in the range $0 \leq \gamma \leq 1$. As the impurity approaches the edge of the QD, the binding energy around the crossing point even increases with increasing γ. The crossing of the curves appears when the magnitude of the laser intensity is such that α_0 is of the order of the QD size $\mathcal{L}$. Using the condition $\alpha_0 = \mathcal{L}$ we can obtain an estimation of the value of the parameter γ at the crossing $\gamma_{\mathrm{crossing}} = 1/\sqrt{2\beta} = \mathcal{L}/a_{2\mathrm{D}}$. The inset of fig. 3.1 shows this magnitude calculated from the crossing point of the curves for $r_d = 0.001\mathcal{L}$ and $r_d = 1.0\mathcal{L}$ for different $\mathcal{L}/a_{2\mathrm{D}}$. As expected, a linear dependence of the crossing on the QD size is observed.

In order to explain this result we can proceed in the same line as before. Now the 1D Hamiltonian reads $\mathcal{H} = \mathcal{H}_0 - (e^2/2\epsilon)\left[\delta(x - x_d - \alpha_0) + \delta(x - x_d + \alpha_0)\right]$ with $\mathcal{H}_0 = p^2/2m + (1/2)m\omega^2\left(x^2 + \alpha_0^2\right)$. The resulting eigenvalue equation is

$$\left(G_{++}(x_d, x_d; E) - \frac{2\epsilon}{e^2}\right)\left(G_{--}(x_d, x_d; E) - \frac{2\epsilon}{e^2}\right) = G_{+-}(x_d, x_d; E)G_{-+}(x_d, x_d; E) \ , \tag{3.23}$$

where

$$G_{\pm\pm}(x_d, x_d; E) = \sum_{n=0}^{\infty} \frac{\psi_n(x_d \pm \alpha_0)\psi_n^*(x_d \pm \alpha_0)}{E_n - E} \ , \qquad E < E_n \ . \tag{3.24}$$

Considering only the contribution of the ground state to the sum, eq. (3.24), the binding energy is found to be $E_B = E_0 - E \sim |\psi_0(x_d + \alpha_0)|^2 + |\psi_0(x_d - \alpha_0)|^2$, namely

$$E_B \sim \exp\left(-\frac{(x_d + \alpha_0)^2}{\mathcal{L}^2}\right) + \exp\left(-\frac{(x_d - \alpha_0)^2}{\mathcal{L}^2}\right) . \tag{3.25}$$

As explained before, from this simplified 1D model a decrease in the binding energy when the laser is switched off ($\alpha_0 = 0$) is predicted. It can be also observed that when the impurity is located at the origin ($x_d = 0$) a decrease of E_B is also expected, in agreement to what is observed in fig. 3.1. Nevertheless, when the laser intensity and the impurity position are modified simultaneously, two clear regimes are observed. At low laser irradiation $\alpha_0 < \mathcal{L}$, equation eq. (3.25) predicts that the binding energy decreases after shifting the impurity from the origin or increasing the laser irradiation. This prediction is in perfect agreement to the results shown in fig. 3.1 (see the curves of the lower panel at the left of the crossing point). On the other side, when $\alpha_0 > \mathcal{L}$, an increase of the binding energy after increasing x_d is deduced from eq. (3.25), in agreement to the results shown in fig. 3.1 (see the curves of the lower panel at the right of the crossing point). Then, we are led to the conclusion that the 1D model renders the behaviour observed in fig. 3.1 even in the presence of the laser irradiation.

The binding energy also depends on the angle between the polarisation direction and the impurity position $\boldsymbol{r}_{\rm d}$. Figure 3.2 shows the binding energy as a function of the parameter γ in the strong confinement regime ($\mathcal{L} = a_{\rm 2D}/2$) and two different angles, $\phi = \pi/4$ and $\phi = \pi/2$. Results should be compared to those shown in the bottom panel of fig. 3.1, corresponding to $\phi = 0$. When the impurity is close to the centre of the QD ($r_{\rm d} \ll \mathcal{L}$), the binding energy is almost independent of the polarisation angle, as expected. However, the binding energy is strongly influenced by the polarisation angle when the impurity is located close to the edge of the QD ($r_{\rm d} \simeq \mathcal{L}$). As a result, the crossing appears at higher values of the parameter γ. This shift can be easily understood by noting that the projection of the vector $\boldsymbol{\alpha}_0$ on the X axis is $\alpha_0 \cos\phi$. Therefore, the laser intensity must be increased by a factor $1/\cos\phi$ to compensate it. In other words, the crossing scales as $\gamma_{\rm crossing}(\phi) \sim 1/\cos\phi$, as seen in the inset of fig. 3.2.

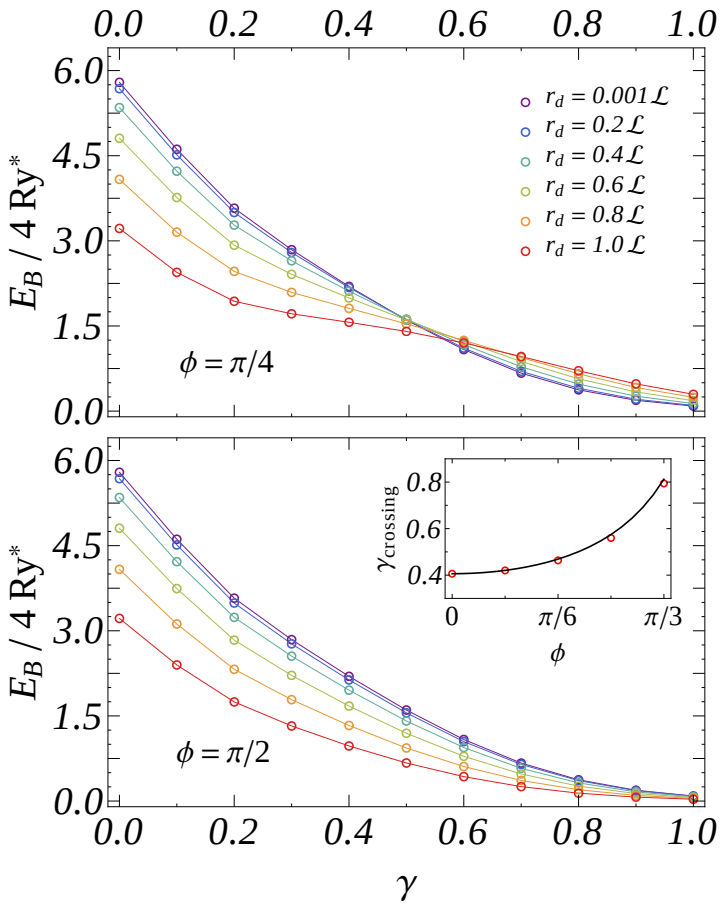

Figure 3.2: Binding energy in units of the 2D effective Rydberg as a function of the parameter $\gamma = \alpha_0/a_{2D}$ for two values of the polarisation angle, indicated on each plot, and different impurity positions r_d. The QD size is $\mathcal{L} = a_{2D}/2$. The inset compares the value of γ at the crossing (open circles) with the theoretical prediction $\gamma_{\rm crossing}(\phi) = \gamma_{\rm crossing}(0)/\cos\phi$ (solid line).

3.3 Effects of an intense laser field on excitons in quantum wires

Since the operation of optoelectronic devices relies on the interaction of carriers with electromagnetic radiation, and following the previous results we presented in section 2.3, we also take into account the effects of an intense laser field on the exciton states. Other studies have suggested that the laser field amplitude provides an important effect on the electronic and optical properties in QWs [104]. In this work the authors employ the same procedure we have explained at the beginning of this Chapter, dressing the interaction potentials due to the laser irradiation, but they solved the problem by means of variational techniques.

We address the study by introducing a solvable model in which the Coulomb potential between the electron and the hole is replaced by a NLSP [9, 59]. Our aim in this section is to show that analytical solutions can be obtained even if the QW is subjected to an intense laser field. With this

goal in mind we consider the laser effects on both Coulomb potential (replaced by a NLSP) and QW confinement potential. Also we evaluate the linear absorption coefficient for searching a signal of the exciton and high-frequency laser irradiation effects.

3.3.1 Theoretical model

We consider an electron-hole pair in a QW, oriented along the Z axis, subjected to a laser field of frequency Ω, whose vector potential is given by $\boldsymbol{A}(t) = A_0\widehat{\boldsymbol{u}}_x \cos\Omega t$. Here $\widehat{\boldsymbol{u}}_x$ is the unit vector along the X axis. Following the method explained in section 3.1.1, in the high frequency limit, the Hamiltonian of the interacting electron-hole pair is given by

$$\mathcal{H} = \sum_{i=e,h}\left[\frac{\boldsymbol{p}_i^2}{2m_i} + V_{\rm QW}^i(\boldsymbol{r}_i, \boldsymbol{\alpha}_0)\right] + V_{\rm C}(\boldsymbol{r}_e - \boldsymbol{r}_h, \boldsymbol{\alpha}_0)\ , \tag{3.26}$$

with $\boldsymbol{\alpha}_0 = \alpha_0\widehat{\boldsymbol{u}}_x$. We assume a lateral parabolic confinement along the X-Y plane, so $V_{\rm QW}^i = m_i\omega_i(x_i+y_i)^2/2$ for electrons and holes. m_i denotes the effective mass for $i = e$ electrons and $i = h$ holes. For instance, we suppose that the confinement frequencies are the same, namely $\omega_e = \omega_h = \omega$. The *dressed* parabolic confinement potential is given by eq. (3.7) for both electron and hole. The Coulomb potential is

$$V_{\rm C}(\boldsymbol{r}_e - \boldsymbol{r}_h, \boldsymbol{\alpha}_0) = -\frac{e^2}{2\epsilon}\left[\frac{1}{|\boldsymbol{r}_e - \boldsymbol{r}_h - \boldsymbol{\alpha}_0|} + \frac{1}{|\boldsymbol{r}_e - \boldsymbol{r}_h + \boldsymbol{\alpha}_0|}\right]\ . \tag{3.27}$$

As in section 2.3, it is convenient to separate the problem into centre of mass and relative coordinates, $\boldsymbol{r} = \boldsymbol{r}_e - \boldsymbol{r}_h$ and $\boldsymbol{R} = (m_e\boldsymbol{r}_e + m_h\boldsymbol{r}_h)/M$, with the total and reduced masses $M = m_e + m_h$ and $m = m_e m_h/M$, respectively. The total Hamiltonian, eq. (3.26), can be expressed as $\mathcal{H} = \mathcal{H}_{CM} + \mathcal{H}_r$ with

$$\mathcal{H}_{CM} = \frac{P^2}{2M} + \frac{1}{2}M\omega^2(X^2 + Y^2 + \alpha_0^2)\ , \tag{3.28a}$$

$$\mathcal{H}_r = \frac{p^2}{2m} + \frac{1}{2}m\omega^2\rho^2 - \frac{e^2}{2\epsilon}\left[\frac{1}{|\boldsymbol{r} + \boldsymbol{\alpha}_0|} + \frac{1}{|\boldsymbol{r} - \boldsymbol{\alpha}_0|}\right]\ . \tag{3.28b}$$

where $\boldsymbol{\rho} = (x, y)$, and $\boldsymbol{P}$ and $\boldsymbol{p}$ are the conjugate momenta of the coordinates $\boldsymbol{R}$ and $\boldsymbol{r}$. Equations (3.28a) and (3.28b) are, respectively, the counterparts of eqs. (2.10a) and (2.10b) when the high-intensity laser is taken into account. From eq. (3.28b) it becomes apparent that the relative dynamics is equivalent to a single particle in a two-centre Coulomb field. The separation between the two centres is $2\alpha_0$, being proportional to $\sqrt{I}$.

Notice that the centre-of-mass problem is exactly solvable since $\mathcal{H}_{CM}$ corresponds to a 2D oscillator Hamiltonian. Thus, we will focus on the relative Hamiltonian $\mathcal{H}_r$ in what follows. The corresponding eigenfunctions of $\mathcal{H}_r$ cannot be expressed in terms of elementary functions. Aiming

to introduce a solvable model, we replace the Coulomb potentials in eq. (3.28b) by a sum of NLPs, as explained in section 3.1.2.

As in the case of the QD, before we proceed further we show how the value of the coupling constant can be determined. To calculate λ we consider the free-exciton case, when there is no confinement due to the QW ($\omega \to 0$) and the laser field is switched off ($\Omega \to 0$ and $\alpha_0 \to 0$). In this limiting case the exciton energy E becomes $-\mathrm{Ry}^*$. The resulting value of the coupling constant depends on the shape function chosen. As we have demonstrated previously, Gaussian NLSPs give accurate results for QW. We use and adapt this shape function to the presence of the dressing parameter α_0

$$v_{\pm}(\boldsymbol{r}) = \left(\frac{1}{\sqrt{\pi}a}\right)^3 \exp\left(-\frac{(\boldsymbol{r} \pm \boldsymbol{\alpha}_0)^2}{a^2}\right) . \tag{3.29}$$

Following the procedure discussed in section 2.3 and taking into account that we set $\alpha_0 = 0$ for obtaining the coupling constant, λ is found to be exactly the same for the case of just an exciton in a QW [eq. (2.12)]. Note that in that definition the parameter $\delta = (a/a_{3\mathrm{D}})^2$, being $a_{3\mathrm{D}}$ the Bohr radius in 3D should be as small as possible in order to reproduce the δ-shape of the Coulomb interaction.

3.3.2 Excitons in a quantum wire under laser irradiation

After having obtained the coupling constant, the normalised eigenfunctions of $\mathcal{H}_0$ are required to obtain the exciton energy in the QW when the laser field is switched on. The required wave functions have been obtained previously in section 2.3.3 and the reader is referred to eq. (2.13) for all the details.

The next step is to search for a closed expression for the energy of the exciton, E, under the action of the laser field. From the definitions of the shape functions, eq. (3.29), and the eigenfunctions of the non-interacting Hamiltonian, eq. (2.13), one finds that $S_+(E) = S_-(E) \equiv S(E)$ and $C(E)$ becomes real. Using eq. (3.12) the ground state energy of the exciton is obtained by solving the equation $S(E) + C(E) = 1$, which leads to

$$\begin{aligned}\frac{2\pi}{\lambda} =& \frac{1}{(1+\eta)^2\mathcal{L}} \exp\left(-\frac{2\gamma^2\beta}{1+\eta}\right) \sum_{n\ell} \frac{2n!\left[1+(-1)^{|\ell|}\right]}{(n+|\ell|)!} \left(\frac{\gamma\sqrt{2\beta}}{1+\eta}\right)^{2|\ell|} \\ & \times \left(\frac{1-\mu}{1+\eta}\right)^{2n} \frac{\exp\left(\eta\varepsilon_{n\ell}\right)}{\sqrt{\varepsilon_{n\ell}}} \operatorname{erfc}(\sqrt{\eta\varepsilon_{n\ell}}) \left[L_n^{|\ell|}\left(\frac{2\gamma^2\beta}{1-\eta^2}\right)\right]^2 ,\end{aligned} \tag{3.30}$$

where λ is given by eq. (2.12). For brevity we have introduced the notation $\eta = a^2/2\mathcal{L}^2$, $\gamma = \alpha_0/a_{3\mathrm{D}}$, $\beta = a_{3\mathrm{D}}^2/2\mathcal{L}^2$ and $\varepsilon_{n\ell} = 2(2n + |\ell| + 1 - E/\hbar\omega)$.

Figure 3.3 shows the exciton energy, in units of the effective Rydberg, as a function of the parameter γ, for several values of the QW radius, parameterised by β. We have taken the adjustable parameter $\delta = 0.01$ [see eq. (2.12)] but we have checked that the results remain almost unchanged when $\delta = 0.005$, as in the results of section 2.3.3. The inset shows that the exciton energy approaches

the value in a bulk semiconductor ($E \to -\mathrm{Ry}^*$) in wide QWs ($\mathcal{L} \gg a_{3\mathrm{D}}$), as expected when the laser field is absent. Note that we are plotting the energy of the ground state, and not the binding energy as it is done in fig. 2.1. The inset also shows that the energy increases when the radius of the QW decreases, indicating strong confinements effects. The effects of the intense laser field are similar, in the sense that the increase of the intensity is accompanied by a remarkable increase of the exciton energy. This effect is more pronounced for smaller QWs. Nevertheless, the exciton energy seems to reach a saturation value beyond a threshold laser intensity. The threshold intensity increases on decreasing the QW radius, as seen from fig. 3.3.

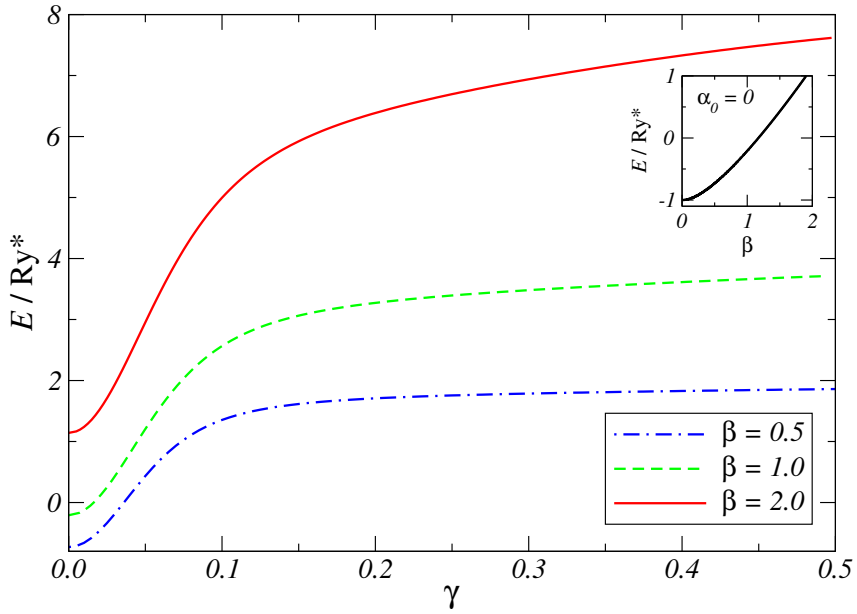

Figure 3.3: Exciton energy as a function of the parameter $\gamma = \alpha_0/a_{3\mathrm{D}}$. Several values of the QW radius are considered, the radius being parameterised by $\beta = a_{3\mathrm{D}}^2/2\mathcal{L}^2$. The inset shows the exciton energy when the laser field is switched off.

3.3.3 Optical absorption

The most clear signature of excitonic effects is the appearance of sharp peaks in the interband absorption spectra. When in the nanostructure an electron is optically promoted from the full valence band to the empty conduction band of the semiconductor, and no interaction is considered between electron and hole, the absorption edge will occur at exactly the energy difference between the states on the conduction and valence band. However, the formation of excitons is revealed by narrow peaks at energies below the electronic bandgap. This effect has been widely studied in different QWs shapes [15, 75, 113]. Therefore, once the exciton energy has been calculated from eq. (3.30), we focus on estimating the linear absorption coefficient due to excitonic transitions to analyse the

effect of the intense laser irradiation on the optical properties. Note that the exciton energies plotted in fig. 2.1 are exactly the localised energies for the exciton states within the gap of the semiconductor.

Commonly the excitonic transition $\mathrm{HH}_1 \to \mathrm{E}_1$ is studied. This nomenclature means that originally we have N electrons occupying the HH_1 valence subband and an empty E_1 conduction subband. In the presence of an electromagnetic wave and within the one-particle effective-mass and dipole approximation, the probability that any transition occurs between two eigenstates ϕ_i and ϕ_f of eq. (3.28b), with eigenergies E_i and E_f respectively, is obtained from the Fermi Golden rule as [114, 115]

$$P_{if} = \frac{2\pi}{\hbar}|\langle\phi_i|V|\phi_f\rangle|^2\delta(E_f - E_i - \hbar\omega_P) \ , \tag{3.31}$$

where we have assumed that the optical excitation is governed by an electromagnetic wave characterised by an angular frequency ω_P, linear polarisation defined by $\boldsymbol{\epsilon}$ polarisation vector and an amplitude F. Then, V is written as

$$V = \frac{ieF}{2m\omega_P}\,\boldsymbol{\epsilon}\cdot\boldsymbol{p} \ , \tag{3.32}$$

$\boldsymbol{p}$ being the electron momentum. The absorption coefficient is proportional to the transition probability given by eq. (3.31). One of the assumptions of this rule is that the initial and final states for the optical transition are completely uncorrelated. However, in the presence of Coulomb interaction, an excited state of the system could be created. It consists in a wave packet of electron-hole pairs, which is the exciton. Then, in eq. (3.31) the exciton states should be taking into account. It means that the final state in eq. (3.31) is nothing but the excitonic state we have obtained previously. It has been demonstrated that the selection rules are the same as the standard interband transitions without electron-hole interaction, which can be found elsewhere [114]. Among them, one is quite important because restricts the excitons that could be created. It should be satisfied that the total momentum in the plane of confinement for the electron-hole pair must be a good quantum number and equal to the momentum of the absorbed photon, which is very small.

Coming back to the transition probability, it can be rewritten as [114]

$$P_{if} = \frac{2\pi}{\hbar}|\langle\Psi_V^h|V|\Psi_C^e\rangle|^2|\Phi_\eta(\mathbf{0})|^2\delta(E_\eta - \hbar\omega_P) \ , \tag{3.33}$$

where Ψ_V^h and Ψ_C^e are the wave functions of the hole and the electron in the valence and conduction band, respectively. They are constructed from the product of the envelope and Bloch functions. In absence of electron-hole interaction, their overlap with V determines the optical absorption. The exciton contribution comes from the new term Φ_η, which is its wave function and E_η its eigenergy [114, 115]. The term $|\Phi_\eta(\mathbf{0})|^2$ is known as the Sommerfeld factor [115] and represents the probability of finding the electron and the hole in the ηth excitonic state at zero distance from each other. Only excitons with non-zero amplitude at $\boldsymbol{r} = \mathbf{0}$ can absorb light. It happens only for s-states. Thus, only excitons with orbital quantum number $L = 0$ can be optically created. Therefore, the

Coulomb interaction has a double effect. Not only it modifies the energy spectrum of the system but also renormalises the transition probability. Consequently, the optical absorption is modified.

Our interest is focused on the effects of the laser irradiation on the excitonic absorption spectra. From eq. (3.33) is clear that the difference between an excitonic and a purely electronic transition is introduced via Φ_η. Therefore, we study the linear absorption coefficient that can be cast in the form

$$A(\hbar\omega_P) \propto \sum_\eta |\Phi_\eta(\mathbf{0})|^2 \delta(E_\eta - \hbar\omega_P) \ . \tag{3.34}$$

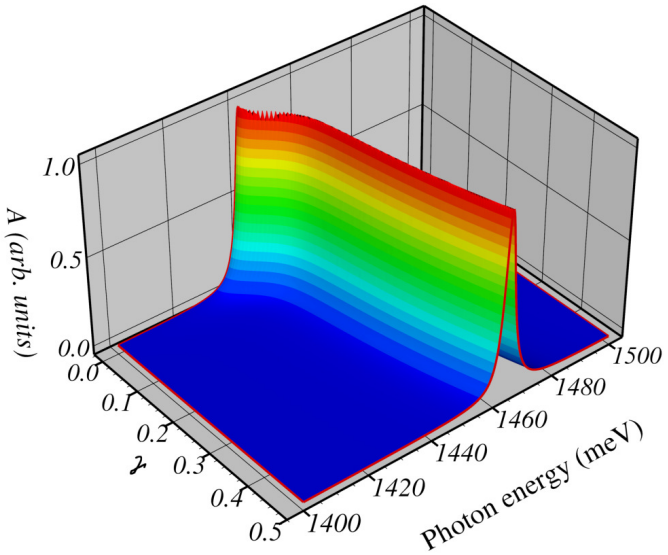

Figure 3.4: Normalized absorption coefficient in GaAs QWs (with $\mathcal{L} = a_{3\mathrm{D}}$) as a function of the photon energy and $\gamma = \alpha_0/a_{3\mathrm{D}}$.

We have to obtain the wave function for the exciton from the NLSP method, which is defined in eq. (3.11). Taking into account that $\langle\, \varphi_\nu \mid v_+ \,\rangle = (-1)^\ell \langle\, \varphi_\nu \mid v_- \,\rangle$ and $S(E) + C(E) = 1$, after a lengthy but straightforward calculation the unnormalised ground state exciton wave function is given by

$$\langle \boldsymbol{r} \mid \chi \,\rangle = \frac{\lambda\hbar^2}{2m} \sum_\nu \frac{\langle \boldsymbol{r} \mid \varphi_\nu \,\rangle \langle \varphi_\nu \mid v_- \rangle}{E_\nu - E} \ , \tag{3.35}$$

where the sum runs over the quantum numbers n, l being even numbers and k_z a continuous variable, E is the solution of eq. (3.30). Keeping only the lowest exciton state and replacing the δ-function by a Lorentzian of width Γ to account any possible broadening effect we obtain

$$A(\hbar\omega_P) \propto \frac{1}{(E_g + 2\hbar\omega + M\omega^2\alpha_0^2/2 + E - \hbar\omega_P)^2 + \Gamma^2} \ , \tag{3.36}$$

where we have used that $E_\eta = E_h^e + E$, with $E_h^e = E_g + 2\hbar\omega + M\omega^2\alpha_0^2/2$ being the effective gap in the QW due to the *dressed* parabolic confinement potential. Figure 3.4 shows the normalised absorption

coefficient in GaAs QWs with $\mathcal{L} = a_{3\mathrm{D}}$, as a function of the photon energy and $\gamma = \alpha_0/a_{3\mathrm{D}}$. The values of the physical parameters used in our calculations are $E_g = 1.424$ eV, $\Gamma = 2$ meV, $m_e = 0.067m_0$, $m_h = 0.45m_0$, where m_0 is the free electron mass. At low laser intensity (i.e. small γ) the absorption peak is strongly blue-shifted. Nevertheless, this shift is less pronounced at large γ, in agreement with the saturation effects discussed above (see Fig. 3.3).

3.4 Summary and conclusions

In summary, we have introduced an exactly solvable model from which the binding energy of on-centre and off-centre hydrogenic impurities in a QD and excitons in a QW under high-frequency laser irradiation can be obtained. In the framework of the effective-mass approximation, the confining potential arising from the QD and the QW are assumed to be parabolic with confining frequency ω. This model is based on the NLSP approach, in which the dressed Coulomb interaction between the electron and the hole is replaced by a projective operator. We have taken Gaussian NLSP, which was found to be suitable for describing off-centre hydrogenic impurities in QDs [74, 101] and excitons in the absence of laser field on QW (section 2.3).

Regarding hydrogenic impurities in QD we have shown that the binding energy is found to decrease as the impurity moves apart from the centre under low irradiation conditions. However, the opposite trend is observed under strong irradiation. The threshold between these two regimes occurs when the laser-dressing parameter equals the size of the QD. Finally, we have introduced a simplified 1D model that captures the relevant regimes observed in our calculations.

On the other hand, when the laser field irradiates the QW, we found an increase of the exciton energy on increasing the laser intensity. The exciton energy reaches a saturation regime at very high laser intensity, the saturation value being larger for small QW radius. We also proved that this effect can be really detected in the linear optical spectrum of the QW.

Chapter 4

Excitonic Aharonov-Bohm effect in a two-dimensional quantum ring

4.1 Introduction

One of the phenomena that arises from the quantum mechanical revolution and the fabrication of low-dimensional materials is the AB effect [30]. Moreover, it has no classical counterpart. It can be explained in a simple but also deep sentence: charged particles are affected by an electromagnetic field even though the particles never felt the field directly. In classical electromagnetism, all physical effects were described by means of electric and magnetic fields. Electric charges, magnets and currents are the sources of the fields and their force field acts locally on other entities. Therefore, their influence can be only produced by direct contact with the fields. Additionally, the electromagnetic potential was seen as a mathematical construct that lacks physical meaning. Nevertheless, in quantum mechanics the electromagnetic potential modifies the description of charged particles by shifting their phase. Although a single phase does not lead to any change in the measurable properties, a phase difference may provide very relevant information. This is the underlying idea in the AB effect. In an astonishing fashion for the scientific community, the AB effect [30] established a link between the electromagnetic potential and a measurable physical result, revolutionising the way we understand the significance of potentials in quantum theory. For a brief introduction to this topic, readers would find in [116] a complete and easy-reading article about the foundations of the AB effect. However, in the next paragraphs, the theoretical basis of the effect and its experimental observation are explained in more detail, in a similar way as in [117].

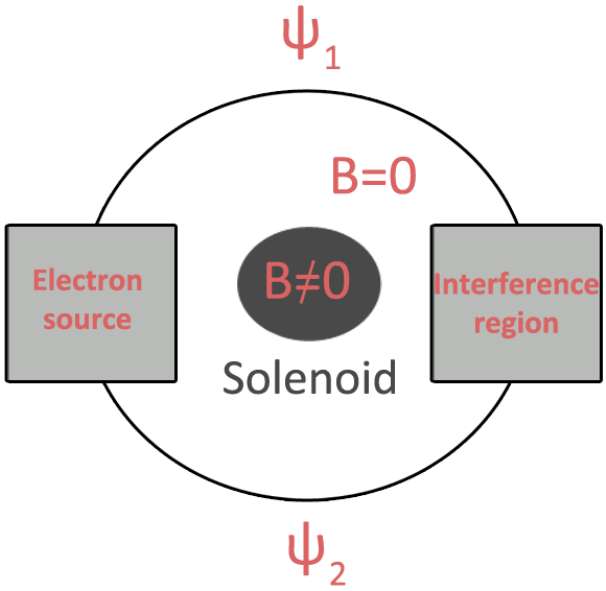

Figure 4.1: Schematic view of the experiment suggested by Aharanov and Bohm [30]. Electrons move in a free field region since the magnetic field is confined in a solenoid.

This effect was firstly predicted by Ehrenberg and Siday in 1949 [118] but remained unnoticed until 1959 when Aharonov and Bohm [30] properly described the physics behind the effect that bears their name. The experiment they proposed consists of a single coherent electron beam split into two parts, in such a way that electrons travel on opposite paths of a region which contains a magnetic field, but avoiding it, at shown in fig. 4.1. The fundamental ingredient of the experiment is that the magnetic field is confined in a certain region (dark region in fig. 4.1) while electrons move in others where the magnetic field is negligible. This could be achieved by using a current flowing through a very closely wound cylindrical solenoid placed at the centre of the experiment setup. Therefore, the two electron paths are in a free field region. However the electromagnetic potential cannot be zero everywhere because the flux should be constant in any path enclosing the solenoid. The beams are brought together to interfere after passing the solenoid.

The magnetic field $\boldsymbol{B}$ is only non zero inside the solenoid, and hence electrons experienced a zero Lorentz force. Therefore, from the classical point of view their physical properties would not be affected. But in contrast, they are subjected to a finite vector potential, $\boldsymbol{A}$, which satisfies the condition $\nabla \times \boldsymbol{A} = \boldsymbol{B}$ inside the solenoid. The magnetic flux satisfies

$$\oint d\boldsymbol{r} \cdot \boldsymbol{A} = \int d\boldsymbol{s} \cdot \boldsymbol{B} = \Phi \ , \tag{4.1}$$

where Φ is the total magnetic flux. Therefore, in the presence of a solenoid, the Hamiltonian for an electron is

$$\mathcal{H} = \frac{(\boldsymbol{P} - (q_e/c)\boldsymbol{A})^2}{2m_e} \ , \tag{4.2}$$

where $q_e = -e$ is the charge of the electron and m_e its mass. The solution of eq. (4.2) in one of the paths, where $\nabla \times \boldsymbol{A} = \boldsymbol{B} = 0$, could be obtained by taking $\psi = \psi_0 e^{i\varphi}$, where ψ_0 is the solution in the absence of the solenoid with an energy E, and $\nabla\varphi = (-e/\hbar c)\boldsymbol{A}$. It can be shown that $\mathcal{H}\psi = E\psi$. Then, the presence of the solenoid implies that the wave function acquires a phase shift φ. In order to see this effect on the whole system shown in fig. 4.1, we focus our attention on the interfering beams at the left lead. Assuming that ψ_1 is the wave function for the electron beam on one side of the solenoid and ψ_2 for the opposite, the intensity of the total beam is related to $\psi_1 + \psi_2$. Each of the wave functions in these beams has a phase that depends on the taken path. The phase difference is, thus, given by

$$\Delta\varphi = \frac{e}{\hbar c}\oint d\boldsymbol{r}\cdot\boldsymbol{A} = \frac{e}{\hbar c}\Phi = 2\pi\frac{\Phi}{\Phi_0}\ , \tag{4.3}$$

where $\Phi_0 = hc/e$ is the universal flux quantum. Therefore, the intensity of the recombined beam would depend on the flux Φ even though there are not magnetic forces acting on the electrons. Then, any physical measurement of the interference pattern will highlight the fundamental role of the potentials in quantum mechanics. This genuine result led Aharonov and Bohm to conclude that the potentials must be considered as physically effective, even where there are no fields acting on the charged particles [30]. They expanded this idea in another paper [119].

Since the publication of this result [30] several theoretical papers tried to show that the calculations were either wrong or that the physical connection of the electromagnetic potential with a realisable measurement was incorrect. Nevertheless, some experimental papers aimed to prove the AB effect [120, 121]. The main criticism of those experiments was that the magnetic field was not strictly zero at the region were electrons move. Finally, Tonomura *et al.* [122–124] confirmed the AB effect in an experiment in which the magnetic field was completely shielded by a superconductor surrounding a toroidal magnet. Then, the electron beam travel in a truly free field region. The interference pattern showed the predicted relative shift in terms of the magnetic flux Φ.

The AB effect has been detected in various experiments that used a wide range of techniques for confining the magnetic field and different materials. There exists a voluminous body of theoretical and experimental work in non-simply connected geometries, such as metal rings and superconducting cylinders, where a magnetic flux pierced its centre. The manifestation of the AB effect is presented in the periodic dependence of the equilibrium properties with the magnetic flux Φ [125–127]. In particular, oscillations in the conductance [128], magnetoresistance [129] and persistent current [130] of metal rings with period Φ_0 have been observed. On the other hand, in superconductor rings the threading flux is quantised in units of $\Phi_0/2$ [131], where the factor 2 is due to the formation of Cooper pairs of electrons. Oscillations with period $\Phi_0/2$ in the critical temperature of superconducting cylinders have been seen [132, 133].

The experimental realisation of nanostructures such as QRs opened a new scenario for the study of the AB effect at the nanoscale, where the confinement potential plays a crucial role in the electronic properties of charged particles. One of the first experiments showed that self-assembled nanoscopic QRs display a magnetic-field-induced transition from ground state angular momentum $\ell = 0$ to $\ell = 1$ that can be explained by means of the periodic AB oscillation of the ground state energy as a function of the magnetic flux [134, 135]. In these studies, experimental results were compared to those obtained assuming that the QR confinement potential is a displaced parabola [136]. Since then, there have been numerous studies on the effects of the confinement potential, the presence of impurities, interactions and external fields on the AB effect in a QR threaded by a magnetic flux.

In order to present a brief but comprehensive overview of the variety of theoretical studies, below is a summary of the most relevant papers in this area. Free electron states in a toroidal QR subjected to an axial magnetic field oscillates with period Φ_0 contributing to an oscillatory magnetisation and subsequent oscillatory persistent current [137]. Additionally, it has been shown that the chosen confinement geometry has a significant importance on the electronic spectrum as a function of Φ, and then optical experimental measurements could be used for determining the geometrical shape of QRs [138]. An improved theoretical model that explains the experimental results of [134, 135] was suggested in Ref. [139]. They proposed a confinement potential with a repulsive central barrier. As its height is varied, the ring properties are modified and better adjusted to the experimental results. Moreover, the $\boldsymbol{k} \cdot \boldsymbol{p}$ method with rectangular band offset potentials in 3D is proposed for describing the experimental results [140, 141]. Finally, more realistic 3D confinement potentials agree with the experimental results [142].

The effect of an electric field on the AB oscillations in QRs threaded by a magnetic field was also studied. One study suggested that the oscillations of the ground state energy as a function of the magnetic field can be suppressed by an in-plane electric field. However, the excited states still oscillates and their energy can be tuned by the electric field strength [143]. The case of a noncircular ring was studied also when an electric field is as well applied to the ring. The results show that the AB oscillations may be suppressed at low energy [144]. Two interacting electrons were also studied in a QR with a perpendicular magnetic field. The interaction changes the energy levels and also influences the absorption spectra, opening up a wider range of electronic structures [136, 145, 146].

4.1.1 Excitonic Aharonov-Bohm effect

Recent advances in nanofabrication of QRs and QDs by self-assembling, [134, 135, 147–151] lithographic [152, 153] or etching techniques [154] have shown that electrons and holes can propagate coherently all throughout the nanostructure. The coupling of electrons and holes with the vector potential has the opposite sign due to its different charge. Moreover, in such systems electrons and

holes are confined in a small region and consequently the Coulomb interaction is enhanced. This raises the question whether an exciton, a bound state of an electron and hole and thus a neutral entity, is sensitive to the vector potential. The possibility of observing a coherent interference pattern such as AB effect for interacting electrons and holes in a circular geometry under a magnetic field opened a new and fascinating area of research both theoretical and experimental.

As a first approach to the problem, one may think that since the exciton charge is zero, the effect would not be observable due to the necessary coupling to the vector potential through the charge. However, two theoretical papers demonstrated that a XAB effect is actually possible in a QR due to the finite size of the exciton inside the QR [31, 32]. In experiments, this sensitivity would show as an oscillatory dependence of both the optical transition energy as well as the oscillator strength upon the magnetic flux [148–151, 153, 154].

Since the publication of the first studies that predicted the XAB effect [31, 32] numerous papers have been devoted to analyse the influence of the QR geometry and the interacting potential on the effect. Initially, a short-range interaction between the electron and the hole was proposed for 1D rings [31, 32, 155–157], where later the effect of an external electric field was included [158]. The model is analytically solvable and AB oscillations were found in the excitonic ground state and in the corresponding oscillator strength. Römer and Raikh explained that the XAB effect is originated from the finite probability for the optically created electron and hole to tunnel in the opposite directions and meet each other on the opposite side of the ring [32, 155]. They also suggested that the AB oscillations would be suppressed if the width of the ring is much bigger than the radius of the exciton. Therefore, most of the research in this area has focused on the proposal of new models for QRs in 2D that reproduce the real confinement in order to analyse the effect of the finite ring width.

Intermediate models assume 2D rings with narrow width under harmonic confinement and Coulomb-like interaction potentials between the electron and the hole. Under these circumstances, the XAB effect is not observed for the ground excitonic state due to the destruction of the non-simply-connected geometry as the width is increased [159, 160]. However, in a 2D attractive annular Hubbard model [161], AB oscillations for the ground state survive for finite ring widths. The XAB effect in strictly 2D QRs has been studied in models with harmonic [162] and geometric [163–165] confining potential. In all cases, the XAB effect has been argued to be suppressed in 2D as the width of the ring is increased. Nevertheless, their results suggest different approaches for experimentally detecting the AB oscillations. For example, on the one hand, smaller and narrower rings are better candidates for experiments because they lead to one-dimensional-like excitons [162]. On the other hand, an alternative is the choice of appropriate materials [164] or noncircular geometries, which enhance the observation of the effect [165].

Other proposals suggest that by radially polarising the excitons the amplitude of the AB oscillations would be greater and then experimentally observable. This can be achieved by either applying a lateral [166] or strong perpendicular electric field [167] to separate at different radii the trajectories of the electron and the hole, or due to a radial asymmetry in the confinement originated from the valence and conduction band alignments, leading to different effective ring radii for electron and hole and thus a distinct magnetic flux for each [168–171]. This happens naturally in certain semiconductor materials such as self-assembled InAs nanorings on a substrate of GaAs [135].

Not only the effects of the confinement geometry have been studied but also the influence of impurities [169, 170, 172] and disorder [173] on the AB oscillations. The scattering potential introduced by an isolated impurity breaks the rotational symmetry and thus, excitonic states with different angular momentum are coupled. This could produce anticrossings in the energy levels, which generate a modulation on the absorption coefficient due to the new optically active states [169, 170]. The presence of disorder on the onsite potentials of the ring may lead also to shifts on the linear optical absorption coefficient. It has been demonstrated that when an ensemble of disorder configurations is averaged over, the magnetic field effect may survive the inhomogenegous broadening due to the impurities. However, for certain disorder configurations the XAB effect would be suppressed because the disorder is strong enough to localise the exciton in a certain portion of the ring [173].

From the experimental point of view, the XAB effect has been observed for neutral and charge excitons in QRs and type-II QDs. In photoluminiscence experiments of QRs made from lithographic techniques, the emission energy of negatively charged excitons oscillates with increasing magnetic field [153]. Later, magnetophotoluminiscence studies of self-assembled type-II QDs reveal AB oscillations for neutral excitons. In this structure, one of the carriers is confined inside the QD and the other carrier in the barrier, creating a ring-like structure [149, 150]. The spatial charge separation produces a polarisation of the exciton and hence, the AB oscillations are actually observed for the single particle that moves in the ring around the QD. However, recently two independent experimental researches report on oscillations in the binding energy of neutral excitons in truly 2D QRs which may be accounted for by the XAB effect [151, 154]. In Ref. [151] self-assembled InAs/GaAs QRs where optically characterised, showing that the photoluminiscence energy peak oscillates as a function of the magnetic field. In Ref. [154] a molecular-beam epitaxy grown nanoring made by $AsBr_3$ etching displays AB oscillations on both photolomuniscence energy and intensity.

As could be seen there are a wide range of theoretical and experimental studies on the XAB effect. But the controversy still remains as to whether the effect would be observable for rings with finite width, as shown by recent experimental results [151, 154]. The aim of this Chapter is to see how the AB signatures change when we pass from a 1D to 2D QR. To this end we consider the XAB effect in a confining potential that can be continuously tuned from strictly 1D to truly 2D with

finite radius-to-width ratio while preserving the central structure of a ring, namely, its non-simply connectedness due to an infinitely strong repulsion at the origin [174]. We present a simple analytic approach to the excitonic problem when the electron-hole attraction is short-ranged [31, 32]. We then study how the amplitude of the AB oscillations in the oscillator strength changes upon increasing the width of the ring. We find that the AB oscillations of the exciton ground state energy decrease with increasing the width of the QR, but nevertheless the effect remains noticeable down to regimes with radius-to-width ratios smaller than unity. This shows the robustness of the XAB effect in 2D.

4.2 Theoretical model

4.2.1 Single particle states in the quantum ring

In the absence of Coulomb interaction, the Hamiltonian of a single particle (electron or hole) subjected to a magnetic flux in a 2D QR is given by (we set $c = 1$)

$$\mathcal{H}_i = \frac{1}{2m_i}\left(\boldsymbol{p}_i - q_i\boldsymbol{A}\right)^2 + V(r_i)\ , \tag{4.4}$$

where m_i, $\boldsymbol{p}_i$ and $\boldsymbol{A}$ are the effective mass, the momentum in the plane and magnetic vector potential, respectively. Here the subscript $i = e, h$ refers to the electron and the hole, respectively. Electric charges are $q_e = -e$ and $q_h = e$. The QR is modelled by an anharmonic, axially symmetric potential with a centrifugal core [174, 175]

$$V(r_i) = \frac{V_0}{2}\left[\frac{R^2}{r_i^2} + \frac{r_i^2}{R^2}\right] - V_0\ . \tag{4.5}$$

The confining potential has the minimum at $|\boldsymbol{r}_i| = R$ (see fig. 4.2) and, for this reason, R will be used as a convenient measure of the effective ring radius. Close to the minimum the potential reduces to the well-known displaced parabola, $V(r_i) = 2V_0(r_i/R - 1)^2 \equiv (1/2)m_i\omega^2(r_i - R)^2$, used in other theoretical studies of electrons and excitons in 2D QRs [135, 136, 162, 176]. As $r_i \to 0$, we see from eq. (4.5) that the centrifugal core assures the survival of the essential feature of a ring: its repulsive barrier in the centre. The effective width W of the QR can be estimated from the single-particle ground state in the harmonic potential, namely $W = (E_0/2V_0)^{1/4}R$, where $E_0 = \hbar^2/2mR^2$ is the ring-size quantisation energy [174]. Notice that we assume that W is the same for electrons and holes, namely $m_e = m_h \equiv m$. For the purpose of this work, all energies will be measured in units of E_0 and we parametrise the strength of the confining potential by the radius-to-width ratio $\gamma \equiv R/W = (2V_0/E_0)^{1/4}$. When $\gamma \to \infty$, we approach the limit of a 1D ring, whereas $\gamma \to 0$ corresponds to an anti-dot geometry [174]. Figure 4.2 shows the radial confining potential for different values of γ.

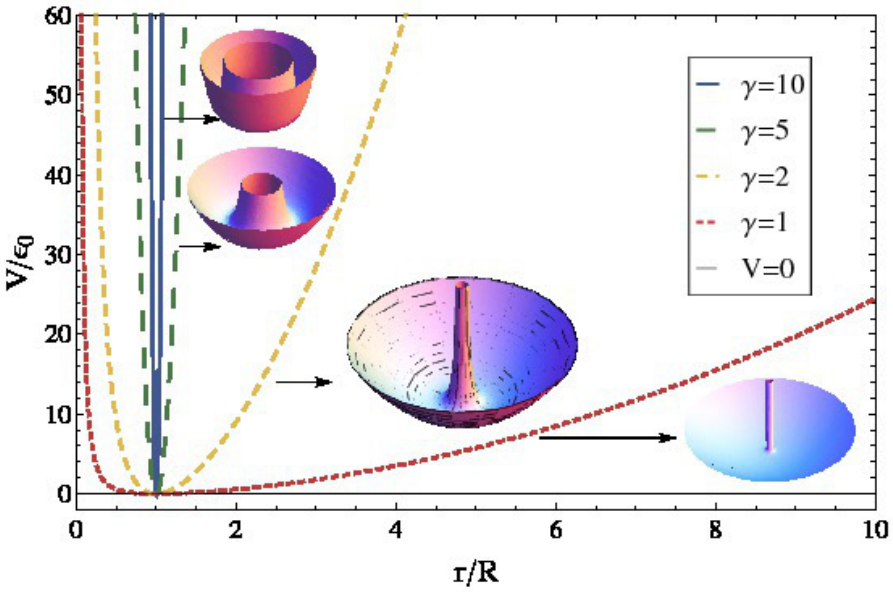

Figure 4.2: Plot of the radial dependence of the confining potential for $\gamma = 1$ (short-dashed), 2 (dashed), 5 (long-dashed) and 10 (solid). The strongly repulsive core at the origin remains very prominent even if γ is small.

This potential is commonly known as *volcano* potential due to the centrifugal core at the origin. Some studies have shown the differences on the single particle electronic spectra between the potential of eq. (4.5) and the displaced parabola, claiming that the latter provides a more suitable theoretical description of self-assembled QRs [177]. Nevertheless, experimental images and data of QRs [178] show that the ring profile is quite similar to that of fig. 4.2. And other theoretical studies claim that the repulsive core is a fundamental ingredient for increasing the oscillator strength for a radiative excitonic ground state transition [179]. In this Thesis we show that the potential of eq. (4.5) provides an accurate model for describing excitons in QRs and are in good agreement with the experimental results [151].

In order to study the XAB effect in the QR, we choose $\boldsymbol{A} \equiv (A_r, A_\theta) = (0, \Phi\, h/e2\pi r)$, corresponding to an infinitely thin magnetic flux piercing the plane of the ring perpendicularly. Here Φ is the dimensionless flux through the ring and h/e the universal flux quantum. The vector potential is defined as usual such that $\oint \boldsymbol{A} d\boldsymbol{r} = \Phi h/e$. We note that due to the axial symmetry around the ring axis, all our results for energies have to be periodic in Φ with period 1 and we hence restrict ourselves to the sector $\Phi \in [0, 1]$. Then the effective-mass equation for the electron in polar coordinates $\boldsymbol{r}_e = (r_e, \theta_e)$ is written in dimensionless form

$$\begin{aligned} \mathcal{H}_e \psi_{M_e}(\boldsymbol{r}_e) &= \lambda_{M_e} \psi_{M_e}(\boldsymbol{r}_e) \\ &= \left[-\frac{\partial^2}{\partial \rho_e^2} - \frac{1}{\rho_e}\frac{\partial}{\partial \rho_e}\frac{1}{\rho_e^2}\frac{\partial^2}{\partial \theta_e^2} + -\frac{2i\Phi}{\rho_e^2}\frac{\partial}{\partial \theta_e} + \frac{\Phi^2}{\rho_e^2} + \frac{V_e}{E_0} \right] \psi_{M_e}(\boldsymbol{r}_e) \ , \end{aligned} \tag{4.6}$$

where $M_e = (n_e, \ell_e)$ represents the set of quantum numbers for the electron, which are $n_e = 0, 1, 2, \ldots$ and $\ell_e = 0, \pm 1 \pm 2, \ldots$ For brevity we define the dimensionless energy $\lambda_{M_e} = E_{M_e}/E_0$ and radial coordinate $\rho_e = r_e/R$. The effective-mass equation for the hole is the same aside from a change in sign in the linear term on Φ, and with a set of quantum numbers $M_h = (n_h, \ell_h)$.

The normalised eigenfunctions of eq. (4.6) are given by [174]

$$\psi_{M_e}(\boldsymbol{r}_e) = \frac{e^{-i\ell_e\theta_e}}{\sqrt{2\pi}}\mathcal{R}_{M_e}(r_e)\ , \tag{4.7a}$$

$$\mathcal{R}_{M_e}(r_e) = \frac{1}{R}\left[\frac{\Gamma(n_e+1)}{2^{k_e}\Gamma(n_e+k_e+1)}\right]^{1/2}(\rho_e\gamma)^{k_e}e^{-\rho_e^2\gamma^2/4}L_{n_e}^{k_e}\left(\frac{\rho_e^2\gamma^2}{2}\right)\ , \tag{4.7b}$$

where $k_e = \sqrt{f_e^2 + \gamma^4/4}$ with $f_e = \ell_e - \Phi$ defining an effective angular quantum number due to the confinement and the magnetic flux. L_n^k stands for the generalised Laguerre polynomials. The corresponding dimensionless energies are $\lambda_{M_e} = \gamma^2(2n_e + 1 + k_e) - \gamma^4/2$. The eigenfunctions and energies for the hole are the same as for the electron, with an effective angular quantum number $f_h = \ell_h + \Phi$. The dimensionless zero point energy ($n_e = \ell_e = \Phi = 0$) for the electron is $\lambda_e^0 = \gamma^2$.

Figure 4.3 shows the electron energy as a function of the parameter γ. We note that levels at higher values of the quantum number n_e become increasingly uncoupled for $\gamma > 5$ and hence we expect to see nearly 1D behaviour for γ values beyond this regime [32]. From the inset is clearly observed that in this 2D confinement regime, in the absence of interaction, the ground state energy for the electron (once subtracted the zero point energy) describes an oscillation with the magnetic flux. For $\gamma > 5$, the 2D oscillation is indistinguishable from the 1D case.

4.2.2 Solution of the excitonic case

Within the effective-mass approximation, the Hamiltonian of the interacting electron-hole pair is given by $\mathcal{H} = \mathcal{H}_e + \mathcal{H}_h + \mathcal{H}_{e-h}$, where $\mathcal{H}_{e-h}$ is the interaction term. We model the excitonic interaction between the electron and the hole as a short-range potential of the form

$$\frac{1}{E_0}\mathcal{H}_{e-h}(\boldsymbol{r}_e, \boldsymbol{r}_h) = (2\pi)^{3/2}v_0 RW\delta(\boldsymbol{r}_e - \boldsymbol{r}_h)\ , \tag{4.8}$$

where $v_0 < 0$ parameterizes the attractive interaction strength in units of E_0. This contact interaction is the same used in Refs. [32, 155, 158] extended to a 2D case, where the area of the ring is $2\pi RW$. In this definition we have carefully chosen the prefactors such that in the 1D limit, $\gamma \to \infty$, the values of v_0 become identical to the corresponding 1D parameter and facilitate comparison with the results of Refs. [32, 155, 158]. Thus, we express v_0 as $-\alpha/\pi^2$ where α denotes the ratio of the ring circumference to the 1D excitonic Bohr radius [32, 155]. As explained in Refs. [32, 155], this factor α is related to the amplitude for a bound electron and hole to tunnel in opposite directions, respect

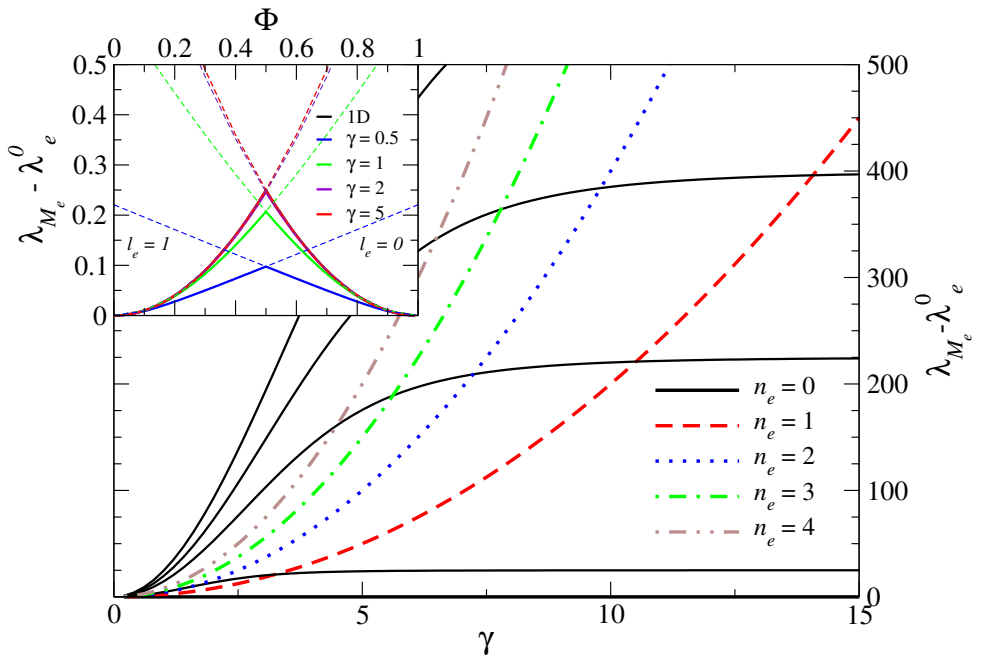

Figure 4.3: Dimensionless electron energy λ_{M_e} as function of the radius-to-width ratio γ. Solid, dashed, dotted, dotted-dashed and double-dotted-dashed lines corresponds to $n_e = 0, 1, 2, 3, 4$ and $l_e = 0$. For $n_e = 0$ we also show $l_e = 5, 10, 15, 20$. The flux is $\Phi = 0$ in all cases. The inset shows the flux dependence of the energy of the ground state for different γ. The black lines corresponds to 1D results.

to where it was created, and meet each other on the opposite side of the ring. Then, the phase acquired of the exciton is given by eq. (4.3) and the XAB effect is observable.

Before continuing with the detailed study of the model, let us discuss some of the assumptions made and the limitations which we will encounter. Let us first emphasise that the restriction to equal electron and hole masses is simply a presentational convenience; all calculations shown here can easily be generalised to the case of unequal masses [158] but with a certain loss of clarity in the mathematical expressions. Nevertheless, we shall present some results for unequal masses later. The assumption of an infinitely thin current-carrying solenoid generating the magnetic flux Φ is a theoretical construct. The experiments cited in the introduction all use a magnetic field B to generate the required Φ. This results in an additional, diamagnetic term proportional to B^2, which we ignore here similarly to the experimental papers [148, 149, 153, 154, 163, 180]. Certainly the most drastic assumption seems to be the δ-function potential for the two-particle interaction. Its use is of course motivated by our resulting ability to reduce the computational difficulties as we will show below. Nevertheless, we wish to emphasise that there are also certain conceptual advantages associated with it: (i) in 1D, the δ-function interacting many-particle problem has been solved exactly and hence the expression for the exciton binding energy on a line is known in terms of v_0 [181]. (ii) In Ref. [32], it was shown how the Bohr radius of the exciton similarly depends on v_0. Both these

parameters will of course vary when another form of interaction is considered. However, as also shown in Ref. [32], it is the ratio α introduced above which governs the strength of the AB oscillations. The effect of other two-particle interaction potentials along the ring, when expressed in terms of α, will lead to similar AB oscillations and we expect at least qualitative agreement. Even for a long-range potential such as the Coulomb interaction, we expect this to hold as long as the overlap of wave packets on opposite sides of the ring, i.e. across the origin at $\boldsymbol{r} = 0$, can be neglected. For the confining potential considered here, with its strong centrifugal core, this should be a rather good approximation.

We construct the exciton eigenfunction as a linear combination of the electron and hole single-particle eigenfunctions

$$\Psi(\boldsymbol{r}_e, \boldsymbol{r}_h) = \sum_{M_e M_h} A_{M_e M_h} \psi_{M_e}(\boldsymbol{r}_e) \psi_{M_h}(\boldsymbol{r}_h) \ . \tag{4.9}$$

The effective-mass equation for the electron-hole pair may now be cast in equivalent form

$$\begin{aligned} \sum_{M_e M_h} & A_{M_e M_h} (\lambda_{M_e} + \lambda_{M_h} - \Delta) \psi_{M_e}(\boldsymbol{r}_e) \psi_{M_h}(\boldsymbol{r}_h) \\ & + (2\pi)^{3/2} v_0 R W \delta(\boldsymbol{r}_e - \boldsymbol{r}_h) \Psi(\boldsymbol{r}_e, \boldsymbol{r}_h) = 0 \ , \end{aligned} \tag{4.10}$$

where Δ is the excitonic energy in units of E_0. Following an analogous procedure as in Ref. [158] the coefficients $A_{M_e M_h}$ are obtained multiplying eq. (4.10) by $\psi^\dagger_{M_e}(\boldsymbol{r}_e) \psi^\dagger_{M_h}(\boldsymbol{r}_h)$ and integrating over the coordinates

$$A_{M_e M_h} = -\frac{(2\pi)^{3/2} v_0 R W}{\lambda_{M_e} + \lambda_{M_h} - \Delta} \, G_{M_e M_h} \ , \tag{4.11}$$

where we have defined

$$G_{M_e M_h} = \int d^2\boldsymbol{r} \Psi(\boldsymbol{r}, \boldsymbol{r}) \, \psi^\dagger_{M_e}(\boldsymbol{r}) \psi^\dagger_{M_h}(\boldsymbol{r}) \ . \tag{4.12}$$

Setting $\boldsymbol{r}_e = \boldsymbol{r}_h = \boldsymbol{r}$ in the expansion of eq. (4.9), multiplying by $\psi^\dagger_{M'_e}(\boldsymbol{r}) \psi^\dagger_{M'_h}(\boldsymbol{r})$ and integrating over the coordinates we finally obtain

$$G_{M'_e M'_h} = \sum_{M_e M_h} G_{M_e M_h} P_{M_e M_h M'_e M'_h}(\Delta) \ , \tag{4.13}$$

with

$$P_{M_e M_h M'_e M'_h} = -\frac{(2\pi)^{3/2} v_0 R W}{\lambda_{M_e} + \lambda_{M_h} - \Delta} \times \int d^2\boldsymbol{r} \, \psi_{M_e}(\boldsymbol{r}) \psi_{M_h}(\boldsymbol{r}) \psi^\dagger_{M'_e}(\boldsymbol{r}) \, \psi^\dagger_{M'_h}(\boldsymbol{r}) \ . \tag{4.14}$$

To proceed we define the total angular momentum of the electron-hole pair in units of $\hbar$ as $L = \ell_e + \ell_h$. Because the system is axially symmetric, only states with $L = L'$ can contribute to the excitonic system. This condition is even more restrictive under the dipole approximation, i.e. only

excitons with total angular momentum $L = 0$ can absorb light polarised perpendicular to the ring. Therefore eq. (4.14) reduces to

$$P_{M_e M_h M'_e M'_h} = -\frac{\sqrt{2\pi} v_0 RW}{\lambda_{M_e} + \lambda_{M_h} - \Delta} \times \int_0^\infty dr\, r\, \mathcal{R}_{M_e}(r)\mathcal{R}_{M_h}(r)\mathcal{R}_{M'_e}(r)\mathcal{R}_{M'_h}(r) \ . \tag{4.15}$$

We note that in the limit $\gamma \to \infty$, the integrals in eq. (4.15) reduce to $1/\sqrt{2\pi}RW$ for $n_e = n_h = n'_e = n'_h = 0$ and $l_e + l_h = l'_e + l'_h$. For other combinations of n_e, n_h, n'_e, and n'_h, the corresponding $P_{M_e M_h M'_e M'_h}$ are less important due to the energy denominator in eq. (4.15).

Similarly as for 1D QRs, [32, 155, 158] there is no analytical solution of eq. (4.13) for finite values of v_0. In order to find approximate solutions, we hence need to cut off the sums at some maximally allowed values for M_e and M_h. Figure 4.3 shows that for smaller values of γ, i.e. increasing ring width W, the level separation between the quantum states of the single particles is decreased. Therefore we use different $\ell_{\max}$ and $n_{\max}$ values depending on our choice of γ. We have tested that our results do not change appreciably for the range of Φ and v_0 considered here. As in Ref. [158], eq. (4.13) is reformulated as a standard left-eigenvalue equation

$$G_{K'} = \sum_K G_K P_{KK'}(\Delta) \ , \tag{4.16}$$

after mapping the quantum numbers $M_e, M_h \to K$ and $M'_e, M'_h \to K'$ according to $K = (\ell + \ell_{\max})(n_{\max}+1)^2 + n_e(n_{\max}+1) + n_h + 1$ such that $K, K' = 1, 2, \ldots, (1+2\ell_{\max})(1+n_{\max})^2$. The excitonic energies are obtained numerically by determining the values of Δ which result in the matrix $P^T_{KK'}$ having an eigenvalue equal to 1. Note that it is the transpose of $P_{KK'}$ the one that have to be diagonalised because eq. (4.16) is an eigenequation from the left. For a given Δ, all eigenstates can be found using eq. (4.13), eq. (4.11) and eq. (4.9). An advantage of our approach is that it allows us to target the ground state directly by choosing a suitable starting value for Δ. From previous studies the excitonic energies are known for a 1D ring [32], which would be the starting point for us. The numerical procedure is similar to the one described in [117]. We set a range of values of Δ and we solve eq. (4.16) until we find a certain value for which the eigenvalue of $P^T_{KK'}$ is less than 1 and other for which is greater than 1. Then, by linearly interpolating between these values, we find a crude approximation for the excitonic ground energy. The process is repeated again but with decreasing the separation step between two subsequent values of Δ and closer to the approximated value. We numerically find a function that interpolates the pair of values which are below and above 1. Finally, we obtain the excitonic ground state energy by setting the function equal to 1 and solving for the corresponding Δ.

4.3 Numerical results

In fig. 4.4 we plot the ground state energy Δ defined by eq. (4.13) with $\ell_{\max} = 40$ for $\gamma > 0.5$ and $n_{\max} = 5$ ($K_{\max} = 2916$) for $\gamma < 5$ or $n_{\max} = 2$ ($K_{\max} = 729$) for $\gamma > 5$ and as a function of v_0 for different values of γ. For $\gamma = 0.5$ we have used $\ell_{\max} = 30$ and $n_{\max} = 6$ ($K_{\max} = 2989$). Here and in all following figures, when plotting the excitonic energies Δ, we have subtracted the zero-point energy $2\gamma^2$ of the non-interacting electron-hole system.

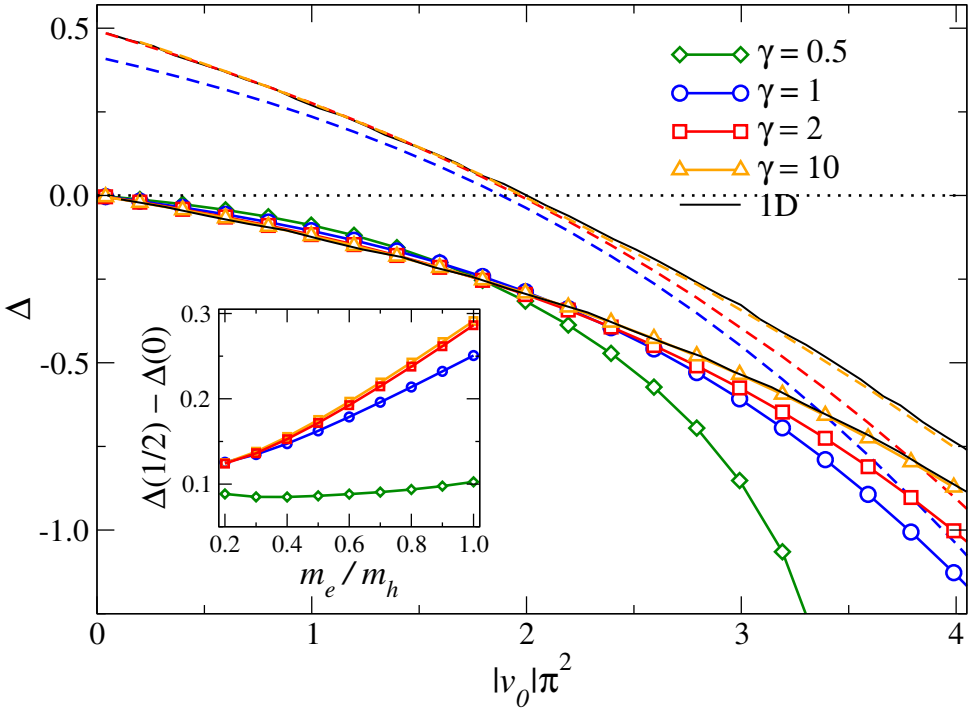

Figure 4.4: Exciton energy Δ at magnetic flux $\Phi = 0$ (solid lines) and $1/2$ (dashed lines) plotted as a function of the interaction strength v_0. For clarity, symbols are shown for $\Phi = 0$ only and the results for $\gamma = 0.5$ at $\Phi = 1/2$ have been suppressed. The thin dotted horizontal line denotes the onset of the single-particle continuum at $\Phi = 0$. The two thin black lines denote the 1D limit for $\Phi = 0, 1/2$. The inset shows the amplitude of the AB oscillations as a function of the ratio m_e/m_h at interaction strength $v_0 = -2/\pi^2$.

We see that for all γ and Φ values, the increase of the interaction strength v_0 leads to the formation of a state with decreasing energy values below the onset of the free-particle continuum. We also compare in fig. 4.4 the 2D exciton results with the 1D ring studied in Refs. [32, 158]. When the radius of the ring is 10 times its width ($\gamma = 10$) the 2D excitonic behaviour is essentially indistinguishable from the 1D results in the range of v_0 values studied. In particular, the differences between energies at different flux values at large γ decrease. Nevertheless, for small $\gamma \lesssim 3$ different magnetic flux values lead to quite distinct Δ values — even in a 2D QR the exciton is sensitive to the magnetic flux. It is also interesting to note that for large γ, the bound state energies are more

negative for larger values of v_0 [32] whereas for $\gamma \lesssim 1$ we find evidence that smaller γ values lead to smaller differences between different values of Φ.

The above results have been obtained assuming the same effective mass for the electron and the hole. To address the question of the robustness of the XAB effect in a more realistic situation with different effective electron and hole masses, we have calculated the exciton energy as a function of the ratio m_e/m_h. Let us define the amplitude of the excitonic AB oscillations as the difference of the exciton energy at $\Phi = 1/2$ and $\Phi = 0$, namely $\Delta(1/2) - \Delta(0)$. The inset of fig. 4.4 shows this amplitude as a function of the ratio m_e/m_h for different values of γ at interaction strength $v_0 = -2/\pi^2$. In 2D rings ($\gamma = 0.5$) the energy difference is almost constant and the assumption of equal masses is well justified. Upon approaching the 1D limit, i.e. increasing γ, the amplitude of AB oscillations increases less for small m_e/m_h ratios but the effect is still revealed. As an example, in common III-V compound semiconductors the ratio of the electron and light hole masses typically ranges from 0.6 to 0.9, and it can be seen in the inset of fig. 4.4 that the reduction of the amplitude is small.

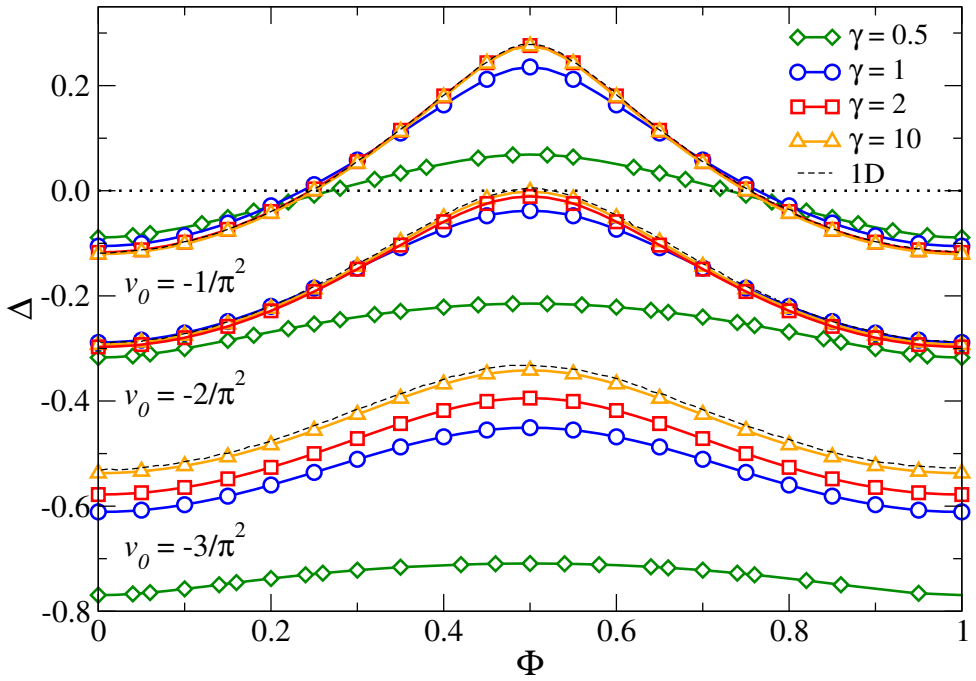

Figure 4.5: Exciton energy Δ as function of the magnetic flux Φ for different values of interaction strength v_0 and radius-to-width ratio γ. The thin dotted horizontal line denotes the onset of the single-particle continuum at $\Phi = 0$. Only every second data point is shown for clarity in each curve.

Figure 4.5 shows the AB oscillations of the exciton energy as a function of the magnetic flux Φ within one flux period at different values of γ and v_0. In agreement with fig. 4.4, we find that the AB oscillations are retained for radius-to-width ratios ranging from $\gamma = 0.5$ to 10. This shows

that the XAB effect remains robust even in a ring of finite width. Upon increasing the γ values for different Φ values, we find mostly a moderate increase of the exciton energy, except in the vicinity of $\Phi = 0.5$ where even the reverse tendency can be observed.

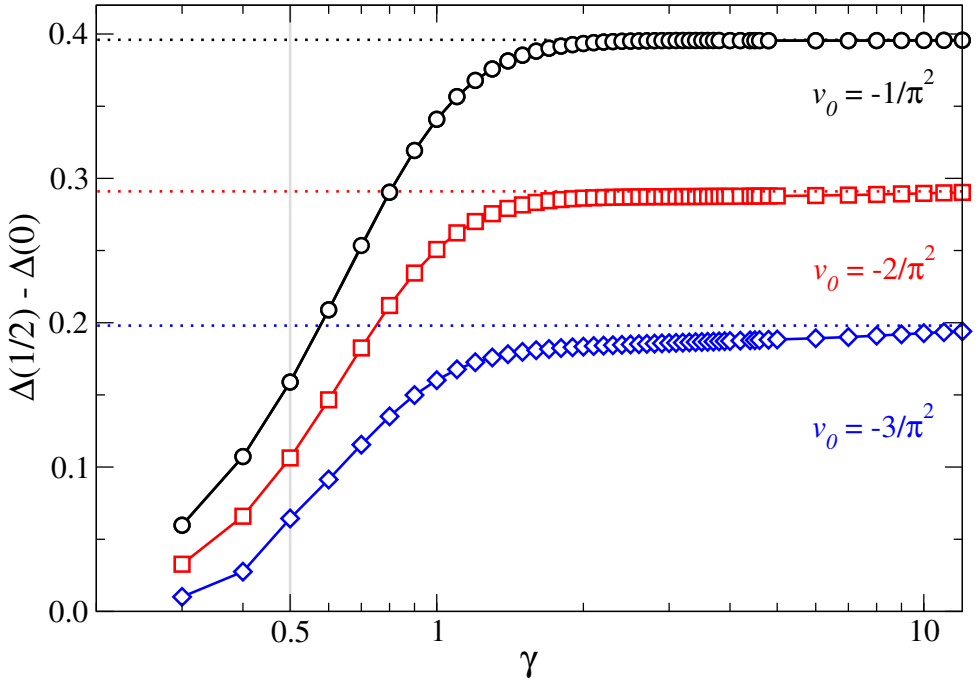

Figure 4.6: Amplitude of the AB oscillations $\Delta(1/2) - \Delta(0)$ as a function of radius-to-width ratio γ for different interaction strength v_0. The dashed horizontal lines correspond to the 1D limit [32], the vertical line denotes the $\gamma = 0.5$ values.

In fig. 4.6 we plot the amplitude of the excitonic AB oscillations for different interaction strength $v_0 = -1/\pi^2, -2/\pi^2, -3/\pi^2$ as γ is varied. We see that upon decreasing γ from the nearly 1D behaviour at $\gamma = 10$ towards $\gamma \approx 1.5$, there is only a slight decrease in the amplitude of the AB oscillations. Upon further decreasing γ, the oscillations weaken more rapidly, but even at $\gamma = 0.5$, they retain about 30–40% of their original value. Results for other values of v_0 are similar. This again shows that even for rather wide rings, the excitonic AB oscillations persist in this 2D case.

In fig. 4.7 we show the exciton probability density $|\Psi(\boldsymbol{r}_e, \boldsymbol{r}_h)|^2$ for different values of γ. We integrate $|\Psi|^2$ over the radial coordinates ρ_e, ρ_h and hence retain the angular dependence in figs. 4.7(a) and 4.7(c), whereas in figs. 4.7(b) and 4.7(d) we integrate out the angular degrees of freedom and retain the ρ_e, ρ_h dependence. From these figures we conclude that the exciton fills the available width of the ring. Figures 4.7(a) and 4.7(c) show that the exciton is indeed bound, i.e. the majority of the weight of $|\Psi|^2$ resides along the diagonal $\theta_e = \theta_h$. Analogous results are obtained for different Φ and v_0. This is similar to the 1D behaviour described in Refs. [32, 158].

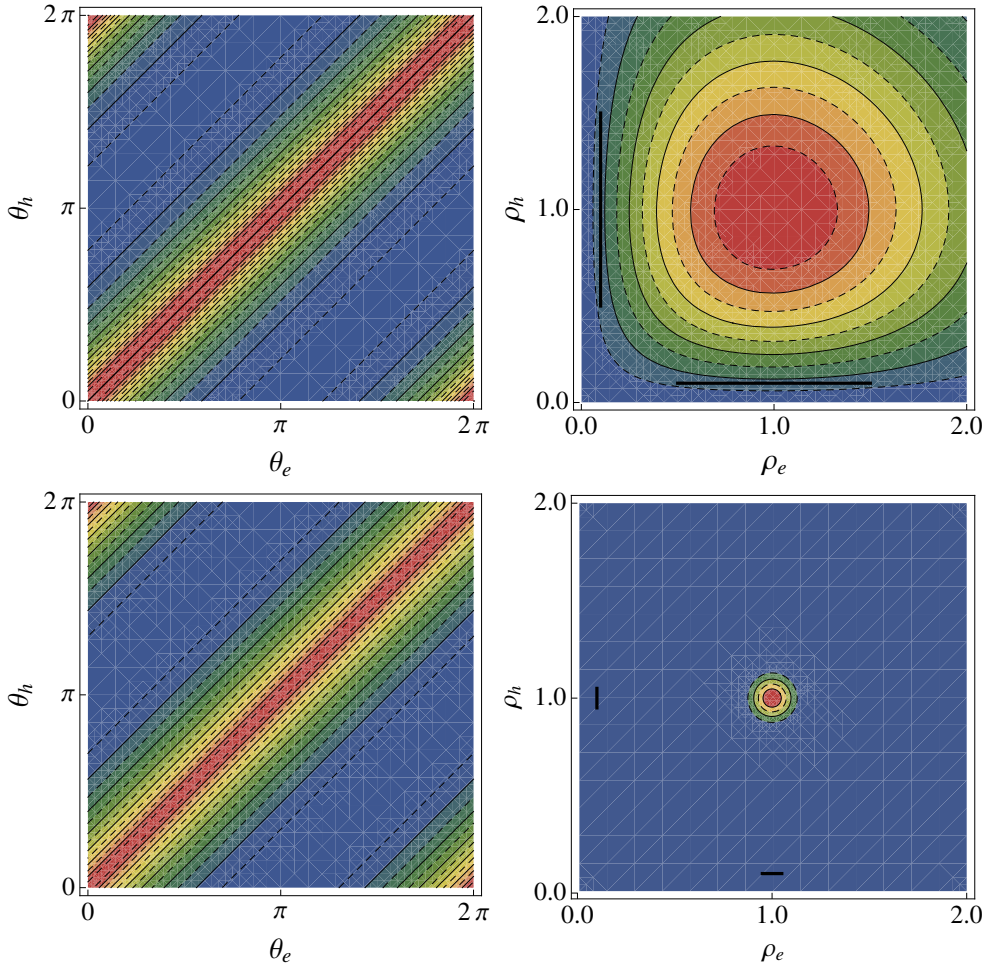

Figure 4.7: Dependence of the *local* wave function probability $|\Psi|^2$ on (a,c) angular coordinates θ_e, θ_h and (b,d) radial coordinates $\rho_e = r_e/R$, $\rho_h = r_h/R$ for $\gamma = 1$ (a,b), and 10 (c,d) for $v_0 = -2/\pi^2$ and $\Phi = 0$. The values of $|\Psi(\theta_e, \theta_h)|^2$ and $|\Psi(\rho_e, \rho_h)|^2$ have been normalised to lie in $[0, 1]$. The colours go from $|\Psi|^2 \in [0.9, 1]$ (red) to $|\Psi|^2 \in [0, 0.1]$ (blue) in steps of 0.05 for (a,c), 0.2 for (b) and 0.1 for (d). The thick black lines indicate in (b) and (d) the width W of the ring in each case.

The oscillator strength, defined as

$$F = \frac{\left| \int d^2\boldsymbol{r} \Psi(\boldsymbol{r}, \boldsymbol{r}) \right|^2}{\int d^2\boldsymbol{r}_e \int d^2\boldsymbol{r}_h |\Psi(\boldsymbol{r}_e, \boldsymbol{r}_h)|^2} , \tag{4.17}$$

is plotted in fig. 4.8. Large values of F corresponds to a large transition matrix element from the exciton ground state into the vacuum via photoemission. We find from fig. 4.8 that the results for large γ are in good agreement with the 1D results [32]. And when decreasing the radius-to-width ratio γ, the value of F does not suddenly drop to zero, again emphasising the robustness of the XAB effect in ring of finite width.

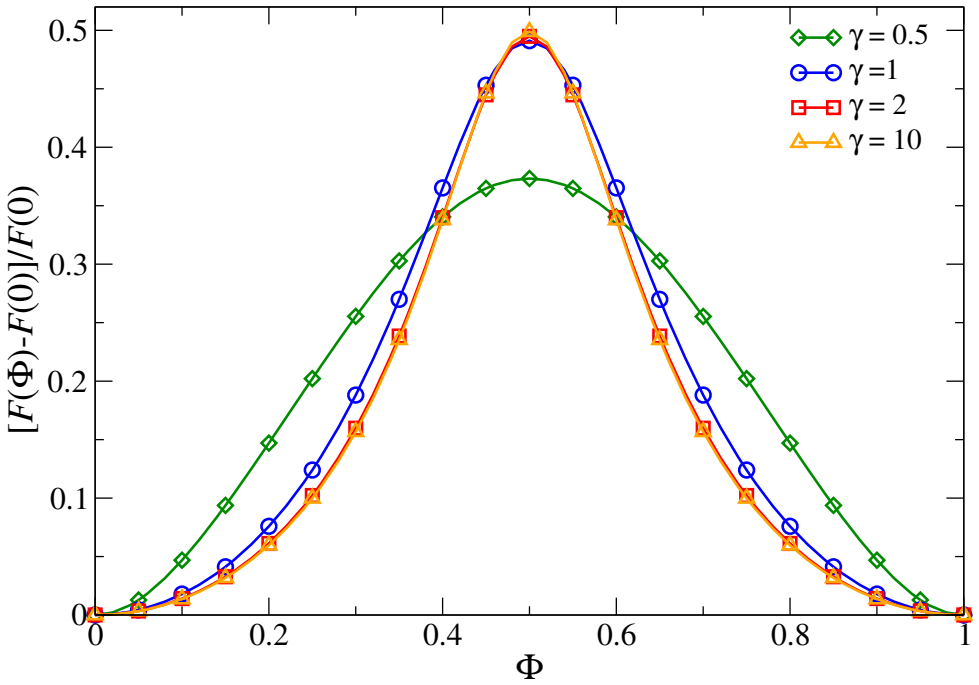

Figure 4.8: Normalised oscillator strength $[F(\Phi) - F(0)]/F(0)$ as a function of magnetic flux Φ for $\gamma = 0.5, 1, 2, 5$ and 10 at interaction strength $v_0 = -2/\pi^2$. Only every second data point is shown for clarity.

4.4 Summary and conclusions

We have shown a solvable model for studying the XAB effect in a truly 2D QR. Our results suggest that this effect originally predicted for a 1D model [31, 32, 155] remains essentially unchanged when allowing for rings of finite widths as given by eq. (4.5). We find that when we enlarge the ring width by one order of magnitude from $1/\gamma = 1/10$ to 1, the magnitude of the AB oscillations drops by about 15% only. In addition, we show that the qualitative behaviour of the oscillations both for the spectral position as well as the oscillator strengths of the exciton luminescence lines are again governed by the relative strength of attractive Coulomb interaction to ring radius. Our results are in good agreement with recent experimental observations where the magnitude of the excitonic AB oscillations was observed to be about 0.5 meV at binding energies of 4.35 meV for rings of about 11–22 nm radius and $\gamma \approx 1$ [151].

We also note that our confining potential [eq. (4.5)] has been chosen to retain its *non-simply connectedness* due to the infinitely repulsive centrifugal core at the centre. Hence even for very wide rings, there is an essential difference with respect to the previously considered 2D confining potentials [159, 160, 162–164, 182]. This demonstrates that it is not so much the width or the exact shape of the confining potential, but rather the avoidance of the ring centre which is the important ingredient needed for the experimental observation of the XAB effect. Moreover, after the publication

of the results presented in this Chapter [183], an experimental and theoretical paper [178] shows that the profile of the confinement potential we use agrees quite well with the real profile of InAs QRs due to the InAs/GaAs gap energy values associated to In-content changes in the ring sample. Therefore, we are confident that XAB effect can actually be observed in experimentally achievable 2D QRs as we demonstrated in this Thesis. In addition, our result show that it is not strictly necessary to polarise the exciton in order to observe AB oscillations. This opens the possibility of seeing the XAB effect in semiconductor materials for which the band alignment does not naturally confine the electron and hole at different effective radii.

Last, regarding external factors in the XAB effect, we expect that the effects of electric fields [158, 166, 167] and the formation of charged excitons remain similarly robust in 2D, whereas impurity [169, 170, 172] and disorder effects [173] should be less important than in the 1D case.

Chapter 5

Quantum systems driven by time-dependent fields

5.1 Introduction

The fundamental properties of low-dimensional systems are highly influenced by the application of time-dependent fields. For this reason, time-oscillating potentials, such as those produced by an AC field, have been studied for several years in connection with photon-assisted tunnelling [36, 184, 185], electronic transmission [186–189], electron pumping and quantum ratches [190, 191], and finally with the formation and detection of quasi-bound states [186, 188]. From the experimental point of view, photon-assisted tunnelling has been observed in coupled QDs, resonant tunnelling diodes and superlattices [36]. The idea underlying this phenomenon is that the oscillating potential can lead to inelastic tunnelling, with finite probability, of an incident particle with energy E to sidebands states of energy $E \pm n\hbar\omega$ by absorbing or emitting n photons while traversing the space where the field is applied. Therefore, from a fundamental point of view, it is important to study the effect of time-dependent external fields on the transmission properties. A simple model was proposed by Tien and Gordon [184] and more complete models are based on the Floquet theorem [192] and non-equilibrium Green's functions [193]. The latter is more suitable for systems under strong driven fields and for describing time-dependent response. One of the most used forms for studying the scattering properties of driven systems assumes that the time-modulated potential could be replaced by an oscillating single barrier [187, 188].

On the other hand, the time-dependent potential can induce the formation of quasi-bound states that could be observed in the transmission profile. Transmission resonances arise when a particle

impinges with an energy near the energy of the quasi-bound states. This could be interpreted as the oscillating potential acts as dynamical trap for electrons with energies below the continuum. The binding energy and lifetime of these states can be derived from the poles of the transmission amplitude [186]. Time-periodic potentials could be used as well as a perturbing mechanism of the bound states and help to reveal them as resonances in the transmission spectrum. This phenomenon is based in the dynamical interaction that appears between states of different energy that could couple bound states with the continuum, leading to sharp peaks in the transmission profile. From it one can obtain their binding energies [194].

Given the different physical phenomena that can be observed from the application of a time-dependent potential, in this Chapter we study how two fundamental quantum mechanical effects are affected by harmonic potentials. In the first place, we report on the formation of bound states in the continuum driven by AC fields. The considered system consists of a QR connected to two leads. An AC side-gate voltage controls the interference of electrons passing through the system. We obtain the transmission probability and the local density of states (LDOS) at the ring sites and show that transmission probability displays a Fano profile when the energy of the incoming electron approaches the driving frequency. Correspondingly, the LDOS presents a narrow peak that approaches a δ-function in the weak coupling limit. We attribute these features to the presence of bound states in the continuum. In the second place, we study the scattering of massless Dirac particles by oscillating barriers in one dimension. Using the Floquet theory, we find the exact scattering amplitudes for time-harmonic barriers of arbitrary shape. In all cases the scattering amplitudes are found to be independent of the energy of the incoming particle and the transmission coefficient is unity. This is a manifestation of the Klein tunnelling in time-harmonic potentials.

5.2 Bound states in the continuum driven by AC fields

At the dawn of quantum mechanics, in 1929, von Neumann and Wigner constructed a spatially oscillating attractive potential with amplitude decreasing with distance that supported a bound state above the potential barrier [37]. This truly localised (square integrable) solution of the time-independent Schrödinger equation is referred to as a BIC. Diffractive interference was suggested as the reason such states could exist. As explained in Ref. [195] the single-particle wave function amplitude is modulated in such a way that the destructive interference with the reflected waves can cause the amplitude to vanish at large distances. Thereby the state is normalisable. The local potential that supports these states is constructed once the wave function and its positive energy are known. However, this method cannot provide the complete spectrum of energies and their wave functions for states other than the BIC [37, 196]. Because of these limitations and the unusual oscillating central potentials needed for producing BICs, those have seen as a mathematical curiosity

more than a feasible physical state. Figure 5.1 shows an example of the BIC wave function and von Neumman and Wigner potential derived in Ref. [195].

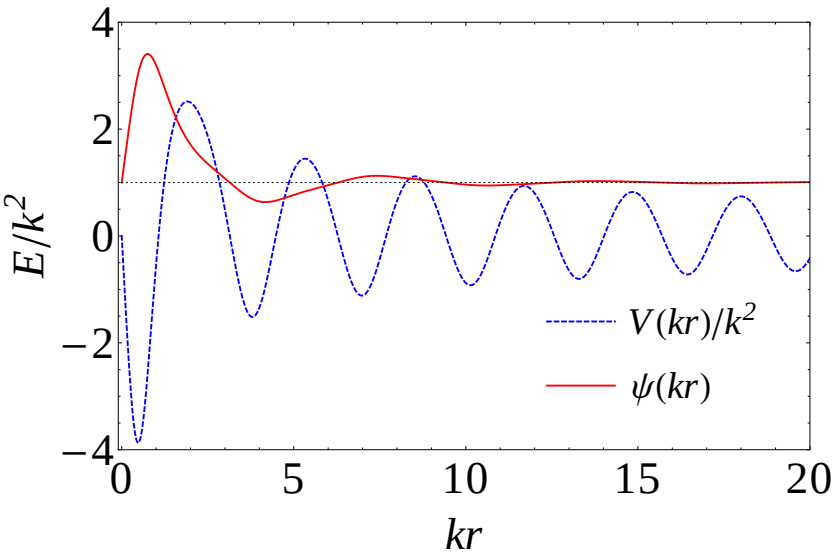

Figure 5.1: von Neumann-Wigner potential $V(r)$ and von Neumann-Wigner bound wave function state, $\psi(r)$. The energy of the BIC is k^2 (dotted line). Result adapted from [195].

Almost fifty years later, Stillinger and Herrick reexamined and extended these ideas [196]. They presented few examples of spherical symmetric attractive potentials which support BICs and they analysed how to produce them in case of higher angular momentum, variable dimensionality and Coulomb interactions. Finally, they studied a double excited atom model, where BICs were formed and had infinite lifetime despite the interaction between electrons. Their method could be extended to the case of separable nonlocal potentials if needed [197]. They arrived at the conclusion that BICs may be a physically realisable phenomenon in real atomic and molecular systems. In this context, Friedrich and Wintgen discussed a system of coupled Coluombic channels and, in particular, a hydrogen atom in a uniform magnetic field [198]. These authors interpreted the formation of BICs as the result of the interference between resonances of different channels and demonstrated their assumptions by means of Feshbach's theory of resonances [199].

The advent of nanotechnology has made possible to devise and fabricate quantum devices whose electronic properties are similar to those of atoms and molecules. The similarity to atomic systems paved the way to experimentally validate the existence of BICs in artificial nanostructures. In 1977 Herrick [200] and Stillinger [201] proposed that GaAs/Al_xGaAs_{1-x} superlattices could be used to build potentials supporting one or more BICs. However, it was in 1994 when the first evidence of an electric bound state above the barrier height was observed experimentally. Capasso *et al.* measured the absorption spectrum at low temperature of a GaInAs quantum well with Bragg reflector barriers

produced by a AlInAs/GaInAs superlattice [202]. A well defined line at $360\,\text{meV}$ in the spectrum was attributed to electron excitations from the ground state of the quantum well to a localised level well above the AlInAs band edge. This narrow absorption peak has been widely recognised as the first manifestation of BIC occurrence in physical systems. Nevertheless, this state cannot be regarded as a true BIC but a bound state above the barrier since it is a defect mode residing in the minigap of the superlattice, as pointed out by Plotnik *et al.* [203]. More recently, Albo *et al.* used intersubband photocurrent spectroscopy to demonstrate that a BIC exists above (Ga,In)(As,N)/(Al,Ga)As quantum wells [204]. These BICs arise from the hybridisation of nitrogen-related defect states and the extended states of the conduction band.

Furthermore, it is worth mentioning that the analogy between photonic systems in the paraxial regime and electronic systems has facilitated the theoretical study of BICs in photonics [205–210] and subsequent experimental observation of BICs in optical waveguides [203]. In this last experiment authors demonstrate that the presence of an optical BIC is mediated solely by breaking the symmetry of the system and not by interfering resonances states with infinite lifetimes as suggested in other studies [205–208, 210].

The influence of impurities or adatoms in the BIC formation has been widely analysed in different physical systems. A single-level Fano-Anderson model coupled to the continuum through a colored interaction that admits BICs was suggested as a proper description of the charge dynamics of adatoms in semi-infinite 1D lattice [211]. Quasibound states (resonant states with very long lifetimes) in the continuum of a QW with an adatom were proposed as a better and more realistic implementation for experiments that look for BICs due to their wider range of reachable parameters [212]. Moreover, the observation of a BIC induced by the interaction between a two-particle Hubbard model in close proximity to an impurity has been recently reported by Zhang *et al.* [213].

The presence of BICs has been also studied in 2D systems. Robnik [214] shows the occurrence of BICs for a point particle in a plane region ($V = 0$) between two infinite parallel hard walls ($V = \infty$) and with a rectangular finite potential well ($V = -V_0$). These states disappear with any small perturbation that breaks the separability of the original Hamiltonian. Sadreev *et al.* [215] demonstrate that BICs in 2D quantum billiards coupled to single-channel leads may be observed varying the shape or energy of the billiard. Other studies have connected BICs with surface states. On the one hand, Sprung *et al.* [216] show that BICs in superlattices, as the ones used in the experiment of Capasso *et al.* [202], are related to surface states because both arise as a result of perturbing an infinite periodic system. On the other hand, very recently, it was demonstrated that surface bound states in the continuum of a semi-infinite discrete lattice could exist and their energy can be tuned by weak nonlinearity [217].

Electronic transport in mesoscopic and nanoscopic systems can be also influenced by the presence of BICs. Nöckel investigated theoretically the ballistic transport across a QD in a weak magnetic field [218]. Resonances in the transmission were found to grow narrower with decreasing the magnetic field, and eventually they become BICs as the magnetic field vanishes. Fabry-Pérot interference of quasibound states of two open QDs connected by a long wire cause the occurrence of BICs [219]. The resulting state is nonlocal, in the sense that the electron is trapped in both QDs at the same time. Interestingly, controlling the size of one of the QD makes the electron to flow or get trapped inside the dots. Moreover, it has been proved that the presence of Coulomb interaction in open QDs does not affect the single-electron BICs [220] and that they are robust if the number of dots is increased [221]. BICs were also observed in parallel double QD systems [222] and they were found to be sturdy even if electron-electron interaction is taken into account [223]. Other suggested mechanism for observing BICs in QDs is based on controlling the gate voltage between the QD and the electron waveguide [224]. Recently, González *et al.* have demonstrated that not only QDs based on semiconductor materials but also on graphene can support BICs [225]. Furthermore, Dutta and Roy have shown that BICs may arise in heterogeneous nanostructures by engineering the spatial dependence of the effective mass of carriers [226]. All these features stimulate the interest of BICs to develop new applications in nanoelectronics.

In this Thesis we extend the notion of BIC to the domain of time-dependent potentials. Our aim is twofold. First, we explore the possibility of the occurrence of BICs when the electronic system is driven by a time-harmonic potential. Second, we introduce a physical realisable system which opens a novel possibility to reveal the existence of these exotic states in transport experiments. As a major result, we show that the transmission, and correspondingly the conductance at low temperature, shows signatures of the occurrence of BICs. When the system is driven by an AC field the BICs survive and their existence is revealed as dynamic Fano resonances in the transmission probability. Remarkably, it turns out that their energy can be tuned by changing the frequency of the field. Therefore, the conductance at low temperature presents a minimum when the BIC crosses the Fermi level by varying the driving frequency. Furthermore, we find that the LDOS displays presence of sharp peaks at certain energies that we demonstrate to be BICs.

5.2.1 Quantum ring under an AC side-gate voltage

The system under consideration is a 2D gas of noninteracting electrons in a QR, shown schematically in fig. 5.2 a). The ring is connected to two leads (source and drain). A side-gate voltage $V_{\pm}(t)$ breaks the symmetry of the upper and lower arms of the ring and acts as an additional parameter for controlling the electric current, as recently suggested for graphene-based nanorings [227, 228]. We assume that the side-gate voltage can be modulated harmonically in time with frequency ω. We

are not considering capacitance effects as those described in Ref. [229] within the context of QRs threaded by an oscillating AB flux.

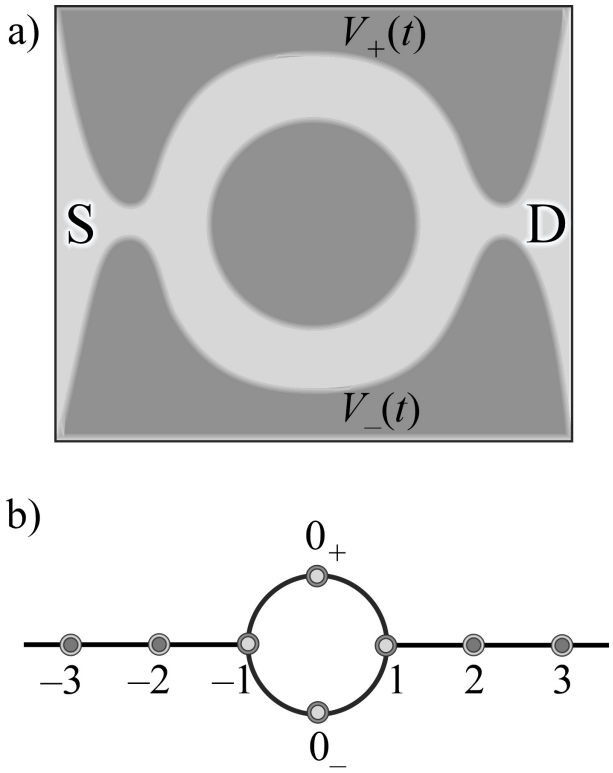

Figure 5.2: a) Schematic diagram of the QR with a side-gate voltage $V_{\pm}(t)$ connected to source (S) and drain (D). b) Equivalent lattice model with two time-dependent site energies $\varepsilon_{\pm}(t)$ at sites labeled $0_{\pm}$ and two other sites with index ± 1 attached to semi-infinite chains.

In order to study electron transport across the QR, we mapped it onto a much simpler yet nontrivial lattice model, depicted in fig. 5.2 b). We replace the actual QR by four sites of a lattice within the tight-binding approximation. This simple tight-binding model has been widely used for studying embedded QDs in closed loop geometries such has AB rings [230, 231]. As pointed out before, it is out of the scope of our study to include the effects of a magnetic flux although the model geometry has some resemblances with those used for that purpose. There are two fundamental reasons for using such a model. On the one hand, it has been able to provide an accurate description of the real physical results despite the simplicity of the geometry. On the other hand, recent advances in nanotechnology open the possibility of building low dimensional systems as the one shown in fig. 5.2. We are confident that our model is versatile enough to meet our objectives in a theoretical study and to present a feasible experimental proposal. Specifically, two sites ($0_{\pm}$) have time-dependent energies $\varepsilon_{\pm}(t)$ and the other two sites, labelled ± 1, are connected to semi-infinite chains. Time-dependent site energies are given by $\varepsilon_{\pm}(t) = \pm 2\Delta \cos \omega t$. To avoid the profusion of free parameters, we assume

a uniform transfer integral and vanishing site energies except at sites $0_{\pm}$, without losing generality. The common value of the transfer integral will be set as the unit of energy and we take $\hbar = 1$ throughout the calculations.

Time-independent side-gate voltage

To gain insight into the possible occurrence of BICs in the system, we consider the time-independent case by setting $\omega = 0$ for the moment. An incoming plane wave $\psi_j^{\rm in}(t) = \exp[i(kj - Et)]$, with energy $E = -2\cos k$ within the bands of the leads, will be partially transmitted in the form $\psi_j^{\rm tr}(t) = t_0 \exp[i(kj - Et)]$. The lattice period is set as the length unit. It is a matter of simple algebra to obtain the transmission amplitude in this case

$$t_0 = \frac{4\sin k}{4\sin k + i\left(E + 4\Delta^2/E\right)} \ . \tag{5.1}$$

The transmission probability $T(E) = |t_0|^2$ presents a dip around the band center and vanishes at $E = 0$.

In the weak coupling limit, namely $\Delta \to 0$, the transmission probability shows a Fano profile [232] close to the band centre, $T(E) = E^2/\left(E^2 + \Delta^4\right)$. The width of the dip scales as $\sim \Delta^2$. Poles of the transmission amplitude have a simple physical interpretation as the natural eigenstates of the scattering potential [186]. The poles occur at a complex energy whose real part gives the energy of the state and the imaginary part is related to its decay rate. There are four poles in the case under study. Two poles correspond to defect modes in the gap and, consequently, they cannot be identified with BICs. However, the other two poles reside at the band centre with an imaginary part equal to $\pm i\Delta^2$ when $\Delta \ll 1$. In the limit $\Delta \to 0$ the poles correspond to truly bound states. Therefore, the Fano resonance of the transmission amplitude eq. (5.1) signals the occurrence of BICs at the band centre. A similar connection between features of the transmission probability and the energies of the electronic states of the closed ring was pointed out by Bütikker *et al.* when the ring is threaded by a static AB flux [233, 234].

To get a better understanding of the nature of the BICs at the band centre we also calculate the LDOS at sites $0_{\pm}$

$$\rho_0(E) = \sum_{\alpha} \frac{1}{2\pi} \int_{-\pi}^{\pi} |\psi^{\alpha}(k)|^2 \delta(E - E_{\alpha}) dk \ , \tag{5.2}$$

where $\alpha = \pm$ labels the sites and $\psi^{\pm}$ is the wave function amplitude at those sites. Close to the band centre, the LDOS is proportional to $|\psi^{+}|^2 + |\psi^{-}|^2$ and is given approximately as

$$\rho_0(E) \sim \frac{E^2}{E^2 + \Delta^4} + \frac{4\Delta^2}{E^2 + \Delta^4} \ . \tag{5.3}$$

The first term is nothing but the transmission probability, vanishing at the band centre. However, the second term approaches $4\pi\delta(E)$ in the limit $\Delta \to 0$, indicating the existence of a truly bound state with energy $E = 0$ located at sites $0_\pm$.

It is important to stress again that the Fano profile in the transmission at the weak coupling limit of eq. (5.1) is the clue that gives us information about the existence of BICs. Fano resonances are the interfering result of a discrete (localised) state with a continuum [232]. This resonant state has a certain width that tends to zero when the state is bound, which has been related to BICs in other studies [235]. However, we have shown that including a small asymmetry in the system through the on-site energies at $0_\pm$ allows us to detect the BICs, which actually exist in the symmetric case (Δ infinitely small) although they are not observable in its corresponding transmission profile. Therefore, the system supports BICs but they are not a consequence of the Fano resonance with an infinite lifetime as could be wrongly interpreted from the presence of a Fano profile. On the contrary, BICs are produced by the hybridisation between localised states coupled to a common continuum. Our result suggests the existence of these BICs and that they could be accessible by varying the value of Δ, leading to a physical fingerprint in the transmission amplitude in the form of a Fano line shape. The symmetry breaking turns the BICs into a sort of resonant quasibound states in the continuum with infinitesimal widths that could be detected. The width of these quasi-BICs can be controlled by tuning the asymmetry of the system.

Time-dependent side-gate voltage

We now turn to our main goal, the occurrence of BICs when the side-gate voltage depends harmonically on time. The time-dependent Schrödinger equation for the amplitudes $\psi_j(t)$ reads

$$i\dot{\psi}_j = \varepsilon_\pm(t)\delta_{j,0_\pm}\psi_j - \sum_{i(j)} \psi_{i(j)} \ , \tag{5.4}$$

where the index $i(j)$ runs over the nearest-neighbour sites of j and the dot indicates the derivative with respect to time. Using the Floquet formalism, the solution can be expressed in the form

$$\psi_j(t) = \sum_{n=-\infty}^{\infty} A_{n,j} e^{-iE_n t} \ , \tag{5.5a}$$

where $E_n = E + n\omega$ and n is the sideband channel index. Since we are interested in electron transmission across the ring, we take the following ansatz for the coefficients $A_{n,j}$ in the expansion eq. (5.5a)

$$A_{n,j} = \begin{cases} \delta_{n0} e^{ik_n j} + r_n e^{-ik_n j} \ , & j \leq -1 \ , \\ f_n^\pm \ , & j = 0_\pm \ , \\ t_n e^{ik_n j} \ , & j \geq 1 \ . \end{cases} \tag{5.5b}$$

Inserting this ansatz in eq. (5.4) leads to the dispersion relation $E_n = -2\cos k_n$ where k_n is real if E_n lies within the band, i.e. $|E + n\omega| \leq 2$. In addition, we obtain $t_n = f_n^+ + f_n^- = r_n + \delta_{n0}$, ensuring current conservation. Finally, one also gets

$$\alpha_n t_n - \frac{\Delta^2}{E_{n-1}}\, t_{n-2} - \frac{\Delta^2}{E_{n+1}}\, t_{n+2} = 4i\delta_{n0} \sin k_0 \ , \tag{5.6a}$$

where for brevity we define

$$\alpha_n = 4i \sin k_n - E_n - \Delta^2 \left(\frac{1}{E_{n+1}} + \frac{1}{E_{n-1}} \right) \ . \tag{5.6b}$$

The continued fraction approach developed in Ref. [189] allows us to obtain numerically the contribution of all channels to the transmission. But if the coupling of the ring to the AC side-gate voltage is weak ($\Delta \ll 1$), only the lowest order sidebands are significant. Then we keep five channels and assume that t_n vanishes if $|n| \geq 3$. Equation (5.6a) implies that $t_{\pm 1} = 0$ in this approximation and

$$t_{\pm 2} = \frac{\Delta^2}{\alpha_{\pm 2} E_{\pm 1}}\, t_0 \ . \tag{5.7a}$$

The transmission amplitude in the elastic channel is

$$t_0 = 4i \sin k_0 \left[\alpha_0 - \Delta^4 \left(\frac{1}{\alpha_2 E_1^2} + \frac{1}{\alpha_{-2} E_{-1}^2} \right) \right]^{-1} \ . \tag{5.7b}$$

Once the transmission amplitudes have been calculated, we can obtain the transmission probability from the general expression

$$T_\omega(E) = \sum_n \frac{\sin k_n}{\sin k_0} \, |t_n|^2 \ , \tag{5.8}$$

where the sum runs over the propagating channels, namely those channels for which $E_n = E + n\omega$ lies within the band of the leads. The factor $\sin k_n / \sin k_0$ comes from the discretization of the system through a tight-binding model. Assuming that the sidebands $n = \pm 2$ are open, i.e. $k_{\pm 2}$ are real, the transmission probability reads

$$T_\omega(E) = |t_0|^2 \left(1 + \frac{\Delta^4}{|\alpha_2|^2 E_1^2} \frac{\sin k_2}{\sin k_0} + \frac{\Delta^4}{|\alpha_{-2}|^2 E_{-1}^2} \frac{\sin k_{-2}}{\sin k_0} \right) \ . \tag{5.9}$$

5.2.2 Results

The five channels approximation discussed above provides a closed analytical expression for the transmission probability eq. (5.9). Admittedly the resulting expression is still involved and must be evaluated numerically for the chosen parameters. We will present simpler expressions latter, valid

in the weak coupling limit, but for the moment we are interested in the closed expression eq. (5.9). We assume that the coupling Δ is smaller or on the order of the frequency ω hereafter. Figure 5.3 shows the results for $\omega = 0.5$ and $\Delta = 0.1$. The pronounced dip observed at the band centre in the static case ($\omega = 0$), commented above and shown in the figure, is absent if $\omega \neq 0$. Similar results can be obtained for other sets of Δ and ω parameters. In fact, transmission at $E = 0$ is unity and the QR becomes transparent at this energy. But the most salient feature of the transmission when the side-gate voltage oscillates is the occurrence of two symmetric and narrow dips, at energies close to $\pm\omega$. Remarkably, the transmission never vanishes in the range of energy plotted in fig. 5.3 and at the dips only drops at about 0.5. Actually, the transmission probability vanishes but only at the band edges, as occurs in the static case too. The inset shows an enlarged view of one of the dips for two different values of the coupling Δ. It is quite apparent that the minimum transmission is slightly smaller than 0.5 and it is reached at an energy close but not exactly equal to ω. In fact, transmission at $E = \omega$ is exactly equal to 0.5 for any value of Δ.

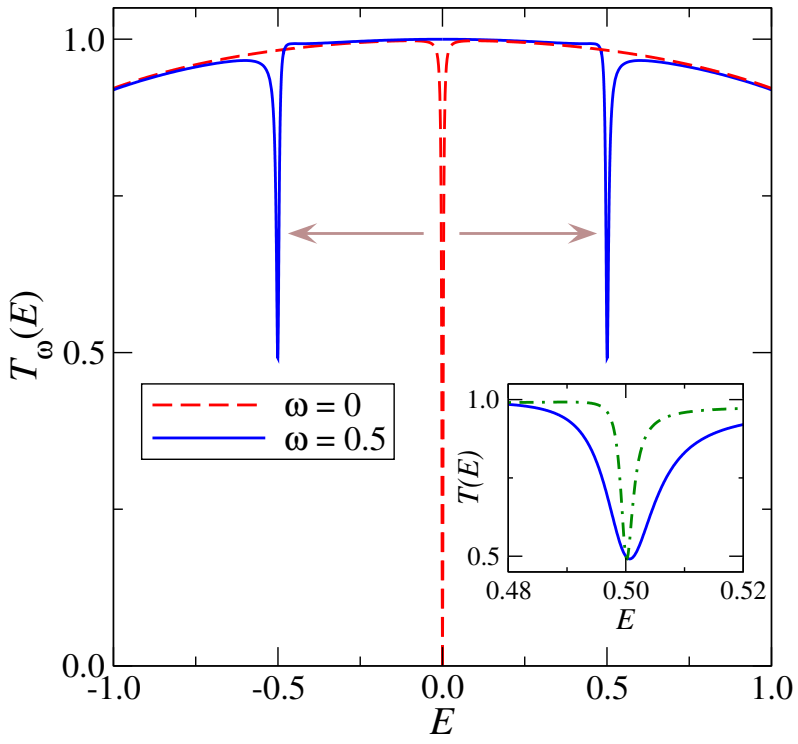

Figure 5.3: Transmission probability as a function of energy at $\omega = 0$ (red dashed line) and $\omega = 0.5$ (blue solid line) for $\Delta = 0.1$. The inset shows an enlarged view of the transmission probability when $E \simeq \omega$ at $\Delta = 0.01$ (green dashed line) and $\Delta = 0.1$ (blue solid line) for $\omega = 0.5$.

It is important to mention that we also solved numerically the general equation (5.6) to obtain the transmission probability from eq. (5.8), increasing the number of the sideband channels. The plots were indistinguishable from those obtained within the five channels approximation, when Δ is

smaller than ω. Thus, we can confidently use this approximation in our analysis.

The transmission probability is an even function of energy. Therefore, for concreteness we now focus in the energy region close $+\omega$, when Δ is small. If ω is not large, we can take $\sin k_{\pm 2} \simeq \sin k_0 \simeq 1$ in eq. (5.9). In addition, the term containing α_2 in eq. (5.7b) and eq. (5.9) is negligible under these assumptions. After lengthy but straightforward algebra, the transmission probability reduces to

$$T_\omega(E) \simeq \frac{8(E-\omega)^2 - \omega(E-\omega)\Delta^2 + \Delta^4}{8(E-\omega)^2 + 2\Delta^4} \ . \tag{5.10a}$$

Since ω and $E-\omega$ are not large, this expression can be further approximated by the following Fano profile

$$T_\omega(E) \simeq \frac{1}{2} + \frac{1}{2}\,\frac{(x-\omega/4)^2}{1+x^2} \ , \quad x = \frac{E-\omega}{\Delta_{\rm eff}^2} \ . \tag{5.10b}$$

To facilitate the comparison with the static case, we have introduced an effective coupling $\Delta_{\rm eff}$ in such a way that $\Delta_{\rm eff}^2 = \Delta^2/2$. From eq. (5.10b) the Fano factor [232] is $q = -\omega/4$ and it becomes independent of the coupling Δ. This parameter represents the ratio to the transition probabilities of the resonant state and to the continuum. When $q \neq 0$ the Fano profile is asymmetric and has a local maximum as is showed in fig. 5.3. Figure 5.4 compares the exact results obtained from eq. (5.9), for two different values of the coupling Δ and $\omega = 0.5$, and the Fano profile eq. (5.10b). In spite of the simplicity of the Fano profile and the assumptions we made, the agreement is remarkable in both cases.

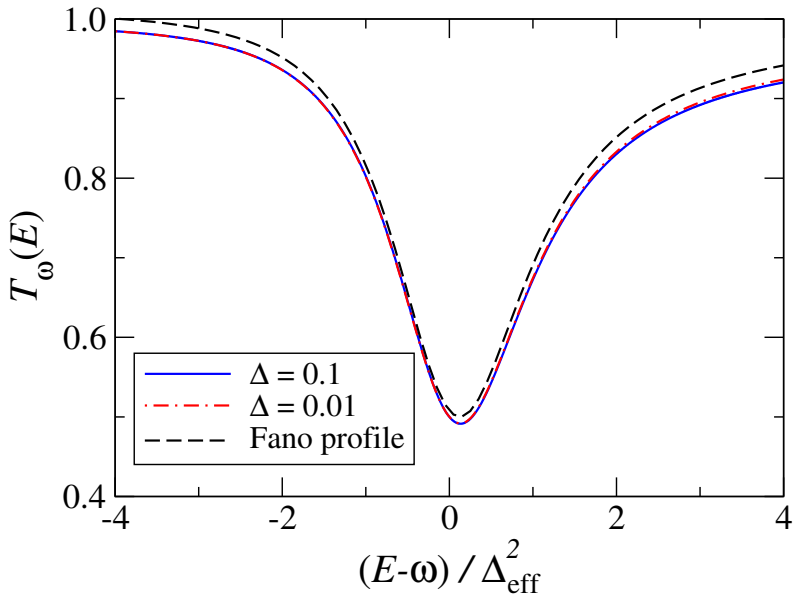

Figure 5.4: Transmission probability as a function of the parameter x defined in eq. (5.10b), for two values of Δ and $\omega = 0.5$. The Fano profile is a good approximation to both curves.

In contrast to the static case, transmission at the dips remains finite when the side-gate voltage is harmonically modulated in time (see fig. 5.3). Therefore, it is not clear at this stage whether the dips are due to the occurrence of BICs in the system. To answer this question we consider again the LDOS at sites $0_{\pm}$. After time-averaging over one time period, one gets

$$\overline{\rho_{0\omega}}(E) \sim \sum_n \left(|f_n^+|^2 + |f_n^-|^2\right) = \frac{1}{2}\sum_n \left(|t_n|^2 + \frac{\Delta^2}{E_n^2}\,|t_{n+1} + t_{n-1}|^2\right) \ . \tag{5.11}$$

Using the five channels approximation, the LDOS close to right dip ($E \sim \omega$) becomes

$$\overline{\rho_{0\omega}}(E) \sim \frac{1}{2}\,T_\omega(E) + \frac{\Delta_{\text{eff}}^2}{(E-\omega)^2 + \Delta_{\text{eff}}^4} \ , \tag{5.12}$$

and a similar expression is obtained for the left dip ($E \sim -\omega$), replacing ω by $-\omega$ in eq. (5.12). Therefore, in the weak coupling limit $\Delta \to 0$, the LDOS reduces to $\overline{\rho_{0\omega}}(E) \sim \delta(E+\omega) + \delta(E-\omega)$. In analogy with the static case, we claim that the two singular peaks in the LDOS at energies $\pm\omega$ are due to a new type of BICs arising by the interaction with the AC field. These peaks correspond with the dips on the transmission. Therefore, BICs play an important role in the transmission properties of the system when an AC field is applied.

We come to the important conclusion that the BICs supported by the QR in the static case survive under harmonic modulation of the side-gate voltage. The two BICs driven by the AC field have energies $\pm\omega$ and they reveal themselves in the transmission, and consequently in the low-temperature conductance, as dynamic Fano resonances. It is worth to mention again that the Fano resonances are the fingerprints of the BICs driven by AC fields. The BICs already exist in the symmetric QR and they are not produced from the resonance of a localised state and the continuum as could be deduced from the appearance of a Fano profile. The symmetry breaking of the system leads BICs to become resonant states with infinitesimal widths that could be detected, in the form of a Fano line shape. Due to the asymmetry side-gate potential, it is possible to observe the appearance of new dips around $\pm\omega$. Furthermore, the position of the BICs inside the spectral band can be continuously tuned by varying the driving frequency and eventually they could be expelled out of the continuum when ω is larger than 2 in units of the transfer integral, i.e. when they approaches the band edge. Therefore, for this phenomenon to be observed, a system like that plotted in fig. 5.2 in combination with a controlling AC field could be built. This is the first proposal of the existence of BICs driven by time-dependent potentials and opens the possibility of detecting them in a solid-state system.

5.3 Scattering of massless Dirac particles by oscillating barriers in one dimension

Shortly after Dirac formulated his celebrated equation for relativistic electrons [38, 236], Klein discovered that Dirac particles undergo anomalous tunnelling at high potential barriers [40]. The classical

example used to discuss the KT is the potential step. When the potential exceeds the rest mass energy, low-energy electrons falling onto the potential step are always transmitted. As a consequence, a strong electrostatic barrier is not able to confine electrons to one side of it. As pointed out by Sauter, this effect is quite independent of the potential profile and eventually depends only on its strength. Sauter studied a potential step with finite slope, representing the effect of an electric field in a certain region of space. He concludes that KT would be observable as long as the potential step is so sharp to occur at distances of the order of the Compton wavelength [237]. This yields extremely large electric fields ($E > 10^{16}\ \mathrm{Vcm}^{-1}$) so KT was regarded as a curiosity in the field of relativistic quantum mechanics. This phenomenon was considered as paradoxical because relativistic fermions can pass through large repulsive potentials in contrast with the intuitive exponential damping expected in non-relativistic quantum tunnelling processes. Some theories tried to explain this effect by means of spontaneous charged particle production when the potential is sufficiently strong [238]. However, it is now known that KT is characteristic of relativistic wave equations and it is not necessarily connected to particle emission [239]. The effect arises from the existence of positive and negative energy solutions of the Dirac equation (electrons and positrons) which are intimately linked and described by different components of the same spinor wave function. This property is known as charge-conjugation symmetry [39, 240].

Due to the required high potentials KT was never experimentally observed. Nevertheless, with the development of experimental methods to isolate graphene [52] came a renewed interest in KT [241–243]. The reason for this interest is that electrons close to the Fermi energy can be described by the Dirac Hamiltonian for massless particles [51] and the electric fields needed for building a well-defined barrier in graphene are around eleven orders of magnitude lower than the fields suggested by Sauter [237]. In this material KT manifests itself as the occurrence of perfect transparency of barriers at normal incidence, as predicted by Katsnelson *et al.* [39, 240] and later observed in experiments [244, 245]. Graphene provides a clearer and deeper understanding of the nature of the Dirac equation. The perfect tunnelling can be explained in terms of the conservation of the pseudospin, defined from the contributions of the two sublattices that build this carbon allotrope. Electrons and holes that belong to the same branch of the energy bands have pseudospin pointing in the same direction, which is parallel to the momentum for electrons and antiparallel for holes. Charged carriers can be scattered only into states of the same branch so the matching of pseudospin directions for quasiparticles inside and outside the barrier leads to perfect tunnelling. However, in this process the quasiparticle flips from electron-like to hole-like behaviour. Besides, at normal incidence there is no backscattering [39, 240].

Continuing our interest in analysing the effects of time-dependent potentials on different quantum systems, in this part of the Chapter we also consider a massless Dirac particle moving in $1+1$

dimensions scattered by a time-dependent potential barrier $V(x,t)$. Using the Floquet theory we find the exact transmission amplitudes when the barrier is an arbitrary sharply-peaked function at the origin $x=0$, approaching the δ-function limit. The δ-function potential is a good approximation to more complex barriers whose width is smaller than any other relevant length scale of the problem. We also study the transmission properties of massless Dirac electrons impinging on time-harmonic barriers of finite width and arbitrary shape, and the exact scattering amplitudes will be compared to those corresponding to a sharply-peaked function. The comparison will allow us to establish the conditions under which a finite-width barrier can be replaced by its δ-function limit. In all cases the scattering amplitudes are found to be independent of the energy of the incoming particle and the transmission coefficient is unity. This is a manifestation of KT in time-harmonic potentials.

Time-periodic potentials have been also studied in the case of 2D graphene, where particles are described by massless 2D Dirac equation [246–249]. Concerning the KT effect, perfect transmission has been predicted at normal incidence upon the time-dependent barrier [247, 249], in complete agreement with our results. The $1+1$ dimensional Dirac equation is a simplified version of the 2D Dirac equation used in those studies assuming normal incidence and then, it provides a much simpler analytical tool for obtaining the transmission amplitudes, as it will be shown below.

5.3.1 Time-harmonic sharply peaked barrier

In this section we study the scattering of massless Dirac particles by a time-dependent potential barrier of the form $V(x,t)=g(t)F(x)$. The spatial part of the potential $F(x)$ is assumed to be sharply peaked at the origin $x=0$, approaching the δ-function limit. This kind of potential barrier has been employed in the study of the transmission properties of non-relativistic particle subjected to a time-dependent potential [186, 189], leading to a better understanding of the meaning of the transmission resonances and poles. However, extra care must be taken when dealing with δ-function potentials in the Dirac equation [250–252]. The resulting equation is ambiguous if one takes the limit $F(x)\to\delta(x)$ from the outset. The origin of the ambiguity is the following. Since the Dirac equation is linear in momentum, the wave function itself must be discontinuous at $x=0$ to account for the singular δ-function potential. However, the product of a discontinuous function and the δ-function is mathematically ill defined. This ambiguity can be overcome by solving the corresponding Dirac equation for any arbitrary sharply peaked function and then taking the δ-function limit with the constraint $\int_{0^-}^{0^+} F(x)\,\mathrm{d}x=1$ [250].

To obtain the proper boundary condition at the origin, we start with the $1+1$ massless Dirac equation

$$i\dot{\boldsymbol{\psi}}(x,t)=\left[-i\sigma_x\frac{\partial}{\partial x}+V(x,t)\right]\boldsymbol{\psi}(x,t)\ , \tag{5.13}$$

where the dot indicates the derivative with respect to time and the Pauli matrix σ_x acts on the two-component wave function $\boldsymbol{\psi}(x,t)$. We take units where the speed of light and $\hbar$ are equal to unity. Following the approach introduced in Ref. [250], the boundary condition at the origin is found to be

$$\boldsymbol{\psi}(0^-,t) = \exp\left[ig(t)\sigma_x\right]\boldsymbol{\psi}(0^+,t)\ . \tag{5.14}$$

In the absence of the potential term ($V(x,t) = 0$), solutions of the massless Dirac equation eq. (5.13) can be written as

$$\boldsymbol{\psi}_\pm(x,t) = \boldsymbol{\phi}_\pm e^{iE(\pm x - t)}\ , \qquad \boldsymbol{\phi}_\pm = \frac{1}{\sqrt{2}}\begin{pmatrix} 1 \\ \pm 1 \end{pmatrix}\ . \tag{5.15}$$

Notice that $\boldsymbol{\phi}_\pm$ are eigenvectors of σ_x since $\sigma_x\boldsymbol{\phi}_\pm = \pm\boldsymbol{\phi}_\pm$. Free solutions are then found to be plane waves travelling to the left or to the right, as deduced from the corresponding current density $j_\pm = \boldsymbol{\psi}_\pm^\dagger\sigma_x\boldsymbol{\psi}_\pm = \pm 1$.

We now turn to our main goal, the study of the effects of the oscillating barrier on the particle tunnelling. The time dependence of the potential will be taken as $g(t) = g_0 + g_1\cos\omega t$. Using the Floquet formalism, the solution can be written as

$$\boldsymbol{\psi}(x,t) = \sum_{n=-\infty}^{\infty}\boldsymbol{A}_n(x)e^{-iE_nt}\ , \quad x \neq 0\ , \tag{5.16a}$$

where $E_n = E + n\omega$, E is the energy of the incoming particle and n is the sideband channel index. Since we are interested in electron transmission across the barrier, we take the following ansatz for the spinors $\boldsymbol{A}_n(x)$ in the expansion eq. (5.16a), in terms of the travelling waves given in eq. (5.15)

$$\boldsymbol{A}_n(x) = i^n \times \begin{cases} \delta_{n0}e^{iE_nx}\boldsymbol{\phi}_+ + r_ne^{-iE_nx}\boldsymbol{\phi}_-\ , & x < 0\ , \\ t_ne^{iE_nx - ig_0}\boldsymbol{\phi}_+\ , & x > 0\ . \end{cases} \tag{5.16b}$$

The first phase factor i^n is introduced for later convenience. Furthermore, the second phase factor $\exp(-ig_0)$ will cancel the term $\exp(i\sigma_xg_0)$ after applying the boundary condition eq. (5.14) since $\exp(i\sigma_xg_0)\boldsymbol{\phi}_+ = \exp(ig_0)\boldsymbol{\phi}_+$.

It is straightforward to calculate the time-averaged current density of the wave function eq. (5.16b)

$$\langle j\rangle = \frac{\omega}{2\pi}\int_0^{2\pi/\omega}\boldsymbol{\psi}(x,t)^\dagger\sigma_x\boldsymbol{\psi}(x,t)\,\mathrm{d}t = \begin{cases} 1-R\ , & x < 0\ , \\ T\ , & x > 0\ . \end{cases} \tag{5.17a}$$

where

$$R = \sum_{n=-\infty}^{\infty}|r_n|^2\ , \qquad T = \sum_{n=-\infty}^{\infty}|t_n|^2\ , \tag{5.17b}$$

are the reflection and transmission probabilities, respectively.

Inserting the ansatz eq. (5.16b) in eq. (5.14), multiplying by $\exp(iE_m t)$, m being an arbitrary integer, and time-averaging over one period we get

$$\delta_{m0}\boldsymbol{\phi}_+ + r_m\boldsymbol{\phi}_- = \sum_{n=-\infty}^{\infty} J_{m-n}(g_1)t_n\boldsymbol{\phi}_+ \ , \qquad m = 0, \pm 1 \cdots \tag{5.18}$$

where $J_\ell(z)$ denotes the Bessel function of the first kind. After multiplying from the left by $\boldsymbol{\phi}_-^{\mathsf{T}}$ we conclude that $r_m = 0$. Consequently, the reflection probability R vanishes. From eq. (5.18) with $r_m = 0$ one gets

$$\delta_{m0} = \sum_{n=-\infty}^{\infty} J_{m-n}(g_1)t_n \ . \tag{5.19a}$$

Recalling the orthonormality condition of Bessel functions, we finally arrive at

$$t_n = J_{-n}(g_1) \ , \qquad n = 0, \pm 1 \cdots \tag{5.19b}$$

which satisfies $T = \sum_{n=-\infty}^{\infty} |t_n|^2 = 1$, as expected from the previous result $R = 0$.

Several important conclusions can be drawn from the above results. First, the transmission probability is always unity, indicating that KT persists even if the barrier is harmonically modulated ($g_1 \neq 0$). Nevertheless, the transmission probability through the elastic channel $T_0 = |t_0|^2 = J_0^2(g_1) < 1$ is reduced as compared to the static barrier, for which $T_0 = 1$. Second, the transmission amplitudes given by eq. (5.19b) are independent of the incoming energy E and the driving frequency ω. We will see in the next section that the latter is a consequence of the peculiarities of having an infinitely narrow barrier.

5.3.2 Time-harmonic square barrier

Having discussed the transmission properties of massless Dirac particles through time-harmonic sharply-peaked barriers, we now consider the scattering from a square barrier of finite width a. In this situation, the potential appearing in the massless Dirac equation eq. (5.13) is

$$V(x,t) = \begin{cases} V_0 + V_1 \cos\omega t \ , & -a/2 < x < a/2 \ , \\ 0 \ , & \text{otherwise} \ . \end{cases} \tag{5.20}$$

Solutions of the Dirac equation (eq. (5.13)) with the time-harmonic of potential eq. (5.20) can be again written down as in eq. (5.16a), now also including the origin of coordinates $x = 0$ since the potential is nonsingular everywhere. Outside the barrier region ($|x| > a/2$) the spinors $\boldsymbol{A}_n(x)$ are expressed as combination of travelling waves

$$\boldsymbol{A}_n(x) = i^n \times \begin{cases} \delta_{n0}e^{i(E_n x + V_0 a/2)}\boldsymbol{\phi}_+ + r_n e^{-i(E_n x + V_0 a/2)}\boldsymbol{\phi}_- \ , & x < -a/2 \ , \\ t_n e^{i(E_n x - V_0 a/2)}\boldsymbol{\phi}_+ \ , & x > a/2 \ . \end{cases} \tag{5.21a}$$

where the phase factors i^n and $\exp(\pm iV_0a/2)$ are introduced for later convenience. Inside the barrier region, solutions are of the form

$$\boldsymbol{A}_n(x) = \sum_{p=-\infty}^{\infty} \left[A_p e^{i(E_p - V_0)x} \boldsymbol{\phi}_+ + B_p e^{-i(E_p - V_0)x} \boldsymbol{\phi}_- \right] J_{n-p}(V_1/\omega) \ , \quad x < |a/2| \ . \tag{5.21b}$$

The Bessel function term $J_\ell(z)$ is obtained from the factorisation of the solution of the Dirac equation in the region where the space-homogeneous time-dependent potential is applied. Nevertheless, is not only a mathematical result but it also has physical relevance. Although it could be derived from the full treatment in terms of Floquet theory of the scattering properties under time-periodic finite-range potentials [187, 188], it could be simply explained from the rather heuristic Tien-Gordon theory [184]. These authors proposed a model for explaining the effect of microwave fields on superconductor-insulator-superconductor tunnelling. Their approach was based on the idea that the time-dependent potential does not change the spatial distribution of the wave function, so it can be safely factorised on position and time contributions. Then, they demonstrated that the wave function under the applied field contains time-dependent components which have energies $E_n = E + n\omega$, meaning that tunnelling can happen from states of incident energy E to these new sidebands. Thus, the effective density of states (DOS) has a probability given by $J_n^2(V_1/\omega)$. Despite its simplicity, this model has been widely used for describing transport in AC-driven nanostructures (for a complete review see [36, 190]) and in the previous cited studies on oscillating barriers on graphene samples [246–248]. The same interpretation could be given in our case because the Tien-Gordon formalism holds for tunnel barriers and uniform gate voltages [253], as the ones used in this Thesis.

Since the potential is nonsingular, the wave function $\boldsymbol{\psi}_\pm(x,t)$ is continuous at $x = \pm a/2$ and we are led to two equations which we do not write down for brevity. Multiplying them by $\exp(iE_mt)$, m being an arbitrary integer, and time-averaging over one period we get

$$\delta_{m0} = \sum_{p=-\infty}^{\infty} A_p e^{i(m-p)\omega a/2} J_{m-p}(V_1/\omega) \ , \tag{5.22a}$$

$$t_m = i^{-m} \sum_{p=-\infty}^{\infty} A_p e^{-i(m-p)\omega a/2} J_{m-p}(V_1/\omega) \ , \tag{5.22b}$$

$$r_m = i^{-m} \sum_{p=-\infty}^{\infty} B_p e^{-i(m-p)\omega a/2} J_{m-p}(V_1/\omega) \ , \tag{5.22c}$$

$$0 = \sum_{p=-\infty}^{\infty} B_p e^{i(m-p)\omega a/2} J_{m-p}(V_1/\omega) \ . \tag{5.22d}$$

Using the orthonormality properties of the Bessel functions it is not difficult to show from eq. (5.22d) that $B_p = 0$. This implies that backscattering at the discontinuity $x = a/2$ is suppressed. From eq. (5.22c) we conclude that $r_m = 0$ and the reflection coefficient vanishes (backscattering at $x = -a/2$ is also suppressed). Taking into account again the orthonormality properties of the Bessel functions, one gets $A_p = \exp(ip\omega a/2)J_{-p}(V_1/\omega)$ from eq. (5.22a). Therefore

$$t_m = i^{-m} \sum_{p=-\infty}^{\infty} e^{-i((m/2)-p)\omega a} J_{m-p}(V_1/\omega) J_{-p}(V_1/\omega) = J_{-m}\Big(2\,\frac{V_1}{\omega}\,\Big|\sin\Big(\frac{\omega a}{2}\Big)\Big|\Big)\,, \tag{5.23}$$

where $m = 0, \pm 1, \ldots$ The sum can be performed by means of the Graf's addition theorem of Bessel functions (see, e.g., Ref. [254]). In accordance with the previous result $R = 0$ for the square barrier, the transmission probability eq. (5.17b) becomes unity in this case ($\sum_\ell J_\ell^2(z) = 1$). Similarly to what we found for the sharply-peaked barrier in eq. (5.19b), the transmission amplitudes are independent of the incoming energy. However, in this case they depend on the driving frequency as well as on the shape of the oscillating barrier, namely its width a and its strength V_1. Another manifestation of KT in the 1+1 Dirac equation with a time-dependent barrier is that, despite the sidebands transmission amplitudes depend on the barrier properties, the full transmission remains unity. This result is in agreement with the independence of the effect of the potential profile as mentioned by Sauter [237]. A quite similar result was obtained for the transmission probability for monolayer graphene subjected to oscillating barriers when the incidence is normal [247]. Nonetheless, our approach is more general because we analytically demonstrate that the transmission including all sidebands is unity, while in [247] only a qualitative statement was given.

The comparison of the result eq. (5.23) with the transmission amplitudes for the sharply-peaked barrier given in eq. (5.19b) allows us to define an *effective* harmonic coupling for the square barrier

$$g_{1,\mathrm{eff}}(\omega a) = 2\,\frac{g_1}{\omega a}\,\Big|\sin\Big(\frac{\omega a}{2}\Big)\Big|\,, \tag{5.24}$$

where now $g_1 = V_1 a$. Therefore, we come the important conclusion that the scattering properties of harmonic-modulated barriers can be successfully described by a sharply-peaked barrier with a *renormalised* coupling constant given by eq. (5.24). The renormalised coupling constant approaches the bare coupling constant g_1 when $\omega a \ll 1$. Figure 5.5 shows the transmission probabilities for the central band, $T_0 = |t_0|^2$, and the first side bands, $T_{\pm 1}$, where $T_n = |t_n|^2 = J_{-n}^2(g_{1,\mathrm{eff}})$, as a function of the bare coupling constant g_1 and different values of ωa. The oscillatory dependence of the transmission amplitudes is due to the Bessel functions. It is quite apparent that the result obtained for the sharply-peaked potential eq. (5.19b), corresponding to $\omega a = 0$ in the plots, is a very good approximation to the square barrier even if ωa is not too small.

All the studies concerning the scattering properties through time-periodic potentials show that they are intimately connected to the Bessel functions $J_\ell(z)$ and the values of its argument z [36,

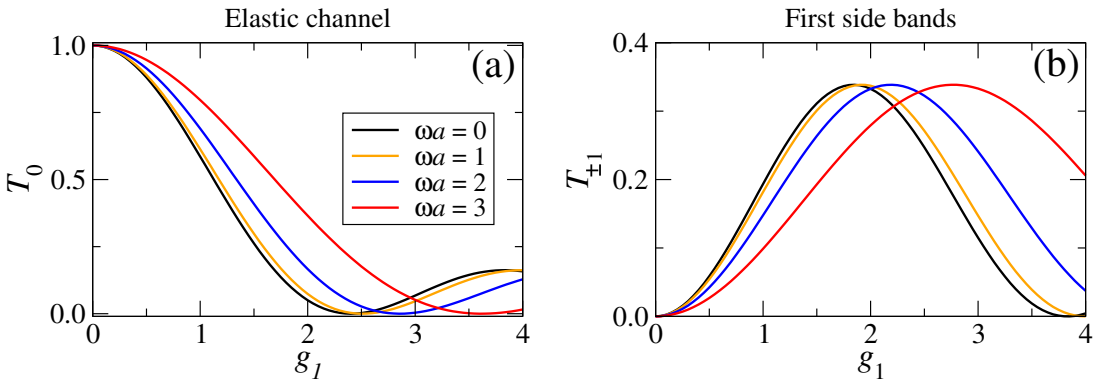

Figure 5.5: Transmission probabilities for (a) the central band, T_0, and (b) the two nearest side bands, $T_{\pm 1}$, as a bare coupling constant $g_1 = V_1 a$ and different values of the parameter ωa.

190, 255]. The former determines the number of coupled modes and then the number of sidebands needed to find accurate results for the transmission coefficient [187, 188]. The exact expression for z depends on the system under study, but in general, for a potential barrier it is $z = V_1/\omega$. On the other hand, for example, the zeros of $J_\ell(z)$ are related to vanishing DOS and thus it could lead to a quenching of the transmission probabilities [256]. Our results are in perfect agreement with the general behaviour also found for non-relativistic particles but show two advantageous differences. The transmission amplitudes can be found analytically for all the sidebands and the argument of the Bessel functions is modulated by $\sin(\omega a/2)$. Therefore, by varying ωa the zeros of the transmission probabilities for the central band and the sidebands can be modified as shown in fig. 5.5. This means that the transmission through a particular sideband could be varied. For instance when $\omega a = 2N\pi$ with $N \in \mathbb{Z}$, only the central band contributes and its amplitude is exactly unity because $J_\ell(0) = \delta_{\ell 0}$.

5.3.3 Barriers of arbitrary shape

The analysis of the scattering solutions for the time-harmonic square barrier pointed out that backscattering is suppressed at the edges $x = \pm a/2$. In addition, the transmission amplitudes eq. (5.23) become independent of the static component of the potential, V_0. All this suggests that the transmission amplitudes for a time-harmonic barrier of arbitrary shape

$$V(x,t) = \begin{cases} V_0(x) + V_1 \cos\omega t \ , & -a/2 < x < a/2 \ , \\ 0 \ , & \text{otherwise} \ , \end{cases} \tag{5.25}$$

should be exactly the same as those obtained in the previous section. The idea behind this conjecture is that any static barrier can be regarded as a superposition of narrow square barriers and heights given by $V_0(x_i)$, x_i being the center of each narrow barrier. But there are not multiple reflections inside the barrier region since backscattering is suppressed, then transmission should be independent of the exact shape of the static component of the potential. To validate this conjecture, we look

for a solution of the form eq. (5.16a). It is a matter of simple algebra to check that the wave function eq. (5.16a) with spinors

$$\boldsymbol{A}_n(x) = \sum_{p=-\infty}^{\infty} A_p e^{i[E_p x - G_0(x)]} J_{n-p}(V_1/\omega)\, \boldsymbol{\phi}_+ \ , \quad x < |a/2| \ , \tag{5.26}$$

satisfies the massless Dirac equation eq. (5.13) for the potential eq. (5.25). Here the function $G_0(x)$ is defined from the relation $V_0(x) = dG_0(x)/dx$. Outside the barrier region the spinors take the form

$$\boldsymbol{A}_n(x) = i^n \times \begin{cases} \delta_{n0} e^{i[E_n x - G_0(-a/2)]}\, \boldsymbol{\phi}_+ \ , & x < -a/2 \ , \\ t_n e^{i[E_n x - G_0(a/2)]}\, \boldsymbol{\phi}_+ \ , & x > a/2 \ . \end{cases} \tag{5.27}$$

Finally, imposing the continuity of the wave function at $x = \pm a/2$ and proceeding as in the previous section we arrive at eq. (5.23). The conclusion from this analysis is that the static part of the potential $V(x,t)$ plays the role of a phase factor in the transmission amplitudes and consequently it does not affect the transmission probabilities $T_n = |t_n|^2$.

5.4 Summary and conclusions

In summary, we have studied the effects of time-dependent potentials in two systems that are intimately connected with the basis of quantum mechanics. Although they are very different, the physical phenomena driven by harmonic potentials can be explained from the fundamental idea behind the scattering properties of time-periodic fields. The oscillating potential leads to a dynamic interaction of the incident energy with the sidebands channels making the transmission amplitudes through these scattering states fundamental for the transport properties of the system. As we have shown, this produces two different effects. Firstly, an existing bound state of the system could be revealed as resonances in the transmission profile as the driving frequency is varied. And secondly, the transmission probability of the sidebands depends on the parameters of the oscillating barrier but this does not affect the perfect transmission of relativistic particles.

Specifically, we have introduced and studied a novel type of BICs in systems whose energy levels are modulated harmonically in time. We have considered a QR subjected to a side-gate voltage oscillating in time with frequency ω and studied its transport properties in a fully coherent regime. We come to the conclusion that the BICs supported by the QR in the static case survive under harmonic modulation of the side-gate voltage. The two BICs driven by the AC field have energies $\pm\omega$ and they reveal themselves in the transmission profile as Fano resonances. The position of the BICs inside the spectral band can be continuously tuned by varying the driving frequency. Similar control of the energy of static BICs have been recently demonstrated by adding weak nonlinearity to semi-infinite systems [217] or by varying the interaction between particles [213]. However, besides

the different origin of the BICs, our proposal seems to be more advantageous for the experimental validation of these exotic states. In this regard, it is still an open question to what extend electron-electron interactions would mask the effect in a real experiment. Žtiko *et al.* have shown that the so-called dark states in parallel double QD systems are robust against interactions within a Hubbard model, at least in the Kondo regime [223]. These states correspond to the BICs shown in the present work when $\omega = 0$, which makes us confident to expect that BICs driven by AC fields are robust even if interactions are taken into account.

Moreover, we have found exactly the scattering solutions of massless Dirac electrons subjected to time-harmonic barriers of arbitrary shape. The Floquet theory allows us to express the corresponding transmission amplitudes in terms of Bessel functions. In all cases the amplitudes are found to be independent of the incoming energy and, in the case of the sharply-peaked barrier, also of the driving frequency. Most important, we proved that the approximation of a finite-width barrier by a sharply-peaked one leads to very accurate results when ωa is not large. We have demonstrated that KT persists in time-harmonic potentials and that our results are in agreement with previous studies of KT on time-modulate barriers on 2D graphene, where carriers could be described in the low energy regime by the Dirac equation [247]. In order to extend properly our model to 2D masless Dirac particles an extra degree of freedom should be included, namely the momentum parallel to the barrier. Then another free parameter is needed, the incident angle for electrons upon the barrier. This is commonly considered in graphene with the result that transmission is not perfect except at normal incidence [39, 247]. It would be a natural extension of the problem presented here.

Chapter 6

Localisation and finite-size effects in graphene flakes

6.1 Introduction

Since the experimental discovery of graphene [52], a large number of researchers have put all their efforts in the study of the physical properties of this material. The numerous articles published, devoted to both experimental and theoretical aspects, have meant tremendous progress in the understanding of graphene only in the last ten years. A complete review of its electronic properties was published just four years ago [54], and the vast graphene literature increase every week. In this Chapter we will focus on the effects of disorder on its electronic properties, namely on the character of its states and how they could contribute to transport. We are interested in the existence of disorder-induced localised states. The source of disorder could be intrinsic or extrinsic. In the first group we can find for example topological defects and surface ripples. But in the second one, disorder can be introduced in the lattice in the form of adatoms or vacancies. We will deal with this latter form of disorder, which is usually short-ranged. On the other hand, in order to have a complete picture of disordered graphene, we study both types of edged graphene samples, namely zigzag (ZZ) and armchair (AC) [54].

In the first part of the Chapter we will review the fundamental concepts of localisation as well as recent studies about a localised-delocalised transition in graphene. Next, the main numerical techniques that we have used will be summarised. And finally, we discuss our most striking results.

6.1.1 Background on Anderson localisation and scaling theory

The standard model used for describing the disorder-induced localised-delocalised transition was introduced by Anderson in 1958 [41] (see for example an article that commemorates the 50th anniversary of its prediction [257]). He studied the electronic diffusion in random potentials. The Anderson model neglects many-body effects and interactions. It is based on a tight-binding approach for an electron in a disordered lattice. At each lattice site the electron feels a random potential and the transfer integrals are non zero only for nearest neighbour sites. It is described by the following Hamiltonian [41]

$$\mathcal{H} = \sum_i \epsilon_i |i\rangle\langle i| + \sum_{i \neq j} t_{ij} |i\rangle\langle j| \ , \tag{6.1}$$

where $|i\rangle$ is the state at lattice i, ϵ_i is the energy level of an electron at site i and t_{ij} is the hopping parameter between site i and j. The disorder is introduced on the onsite energies, which are commonly chosen as a uniform box distribution with width W. Hence $\epsilon_i \in [-W/2, W/2]$. The hopping parameters are assumed to be constant $t_{ij} = t$ because the separation between neighbour sites is almost the same. This is known as diagonal disorder model, since the disorder only appears in the diagonal matrix elements. Two competing effects determine the dynamics of the model. The random potential tends to retain the electron in the energy minima, leading to localising effects. However, the kinetic contribution promotes delocalisation because it allows hopping from site to site of the lattice.

With this model, Anderson showed that in 3D systems there is a critical disorder at which the electron states pass from being extended to exponentially localised. In the absence of disorder, the potential is the same at each site and the states are Bloch states that extend over the crystal. Hence, the electron is free to move and contribute to transport. The conductivity is finite at zero absolute temperature and the system is metallic. Nevertheless, whilst the disorder is increased the character of the wave function changes, becoming eventually localised if the strength of the randomness potential is sufficiently strong. If the Fermi energy lies in a region of localised states, the system is insulating and the conductivity will vanish at absolute zero temperature. This change of behaviour is referred as metal-insulator transition (MIT) or Anderson transition (AT), which involves nowadays a wider range of transitions from extended to localised states besides the electronic one [258, 259].

This effect is more clearly explained through the concept of mobility edge introduced by Mott in 1968 [260]. The mobility edge is a critical energy value E_c that separates the localised states from the extended ones. It is schematically depicted in fig. 6.1 (a). Its fundamental role for understanding AT comes from the DOS. In those energy regions where the DOS is sufficiently small, states could be localised. In the band energy framework these regions are associated with the band tails. In the rest of the band, states are extended. While the disorder is below the critical disorder, localised

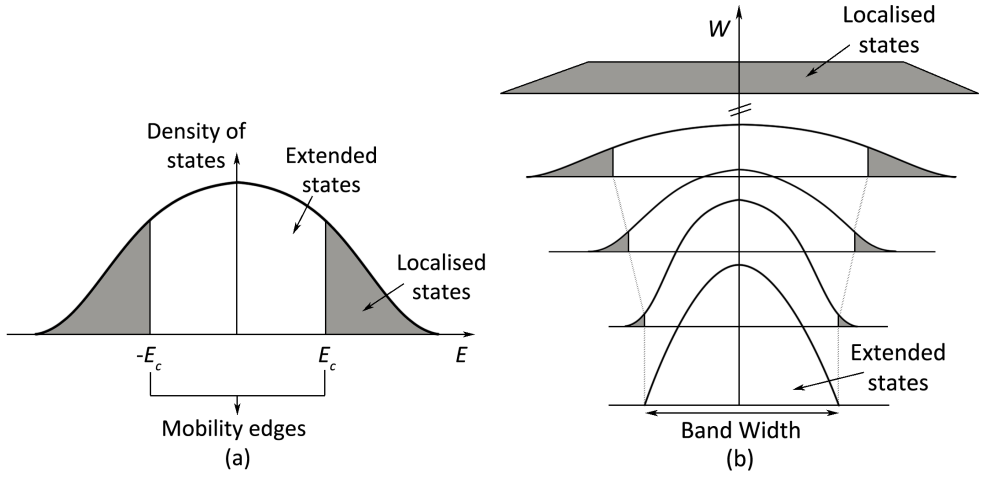

Figure 6.1: (a) Schematic plot of the DOS at a disorder below the critical disorder. Localised states are separated from the extended states by the mobility edges at $\pm E_c$. (b) Evolution of the mobility edges as the disorder is increased, showing the transition from a whole band of extended states to another consistent of localised states. Figures adapted from [1]

and extended states coexist in different regions, as showed on fig. 6.1 (a). The separating lines are referred to as mobility edges. Therefore, there exists a localised-delocalised transition as a function of energy. Depending on the position of the Fermi energy, the system will behave as a metal or as an insulator. But also, the transition could be induced by disorder at a fixed Fermi energy. With increasing disorder, more states become localised, and the mobility edges move inwards into the band centre. At the critical disorder, they coalesce at the centre and all states are localised. So, if the Fermi energy is kept constant but the disorder is increased, the system undergoes a metallic to insulating transition at the critical disorder. An schematic view of this process is given in fig. 6.1 (b).

The mechanism responsible of the localisation is the quantum interference of the electronic wave function. Due to the random potential, the wave function is scattered and may interfere with itself. This coherent quantum mechanical backscattering is the precursor of the exponential localisation. Eventually, the interference is so strong that electrons are restricted to stay in localised states and the electronic transport is forbidden [258]. In order to characterise these localised states different magnitudes have been used. A commonly used one is the localisation length, λ. It is defined from the asymptotic exponential decay of the envelope of the wave function, so $\psi(r) \sim \exp(-r/\lambda)$ [258, 261]. For the case of an extended state, $\lambda \to \infty$ and it is not a well defined quantity for characterisation. The TMM, which will be introduced later, is a convenient method for obtaining λ. Other numerical approaches include the direct diagonalisation of the Hamiltonian and the evaluation of the inverse participation ratio. It measures the sites where the amplitude of the wave function differs markedly from zero [258].

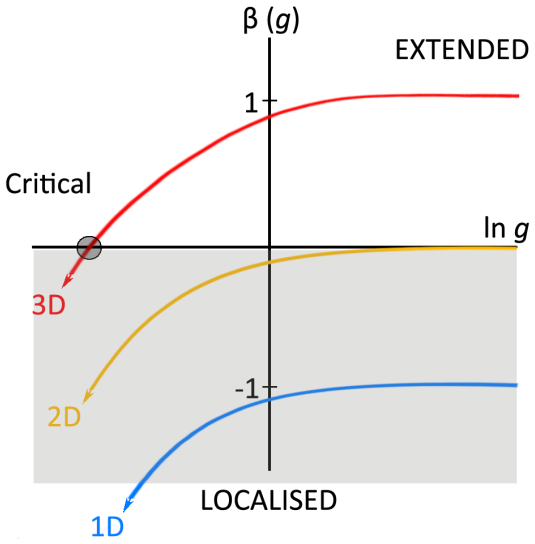

Figure 6.2: Qualitative plot of the scaling function $\beta(g)$ for different dimensions. The regions of extended and localised behaviour are indicated. The point where the MIT happens is indicated by a circle.

After the Anderson model was postulated, the scientific efforts moved towards a description of the phenomena in terms of phase transitions and a proper definition of the localisation criteria. In a series of papers the problem was reformulated in terms of the renormalisation group [262] and in terms of the non-linear σ model [263, 264]. They showed that AT can be described as a second-order phase transition. Other approaches were devoted to relate the conductivity with the boundary conditions of the system [265]. These studies were culminated in 1979 with the development of the one-parameter scaling theory [55].

The essential hypothesis of the scaling theory is that there is only one relevant scaling variable for describing the critical behaviour close to the transition. In [55] the conductance, g, was taken as the scaling variable, which provides an explicit description of the dependence of the conduction on the size of the disordered system and the role of the dimensionality. From the β-function $\beta(g) = d\ln g/d\ln L$ the behaviour of the conductance g in a hypercube of volume L^d with the system size L was described. The main idea behind is that this function only depends on the conductance itself and not on the energy, disorder or L. In fig. 6.2 the qualitative dependence of β on the g is sketched for different dimensions. The curves are obtained by interpolating from the asymptotic behaviour at large and small conductance assuming that $\beta(g)$ is continuous. If $\beta(g) > 0$ the conductance increases with the size of the sample, characteristic of a metallic regime. Therefore, for a normal ohmic conductor $g \sim L^{d-2}$ and thus $\beta(g) = d-2$. For $\beta(g) < 0$ the conductance decreases with increasing the sample size and the system is driven towards the localised regime. Then, the conductance is approximated by $g \sim \exp(-L/\lambda)$, where λ is the localisation length and hence $\beta(g) \sim \ln g$. The fixed point where $\beta(g) = 0$, and the conductance is independent of the system size, defines the disorder induced MIT

as shown in fig. 6.2. The main and fundamental result is that AT is only a critical phenomenon in 3D. In 1D and 2D β is always smaller than zero and g always decreases with L. Therefore, in the thermodynamic limit, all states are localised and there is no MIT for $d \leq 2$. In short, states in a 2D system are marginally localised even for small disorder and $d = 2$ is the lower critical dimension of the AT [258, 261].

Another important result from the one-parameter scaling theory is the expected behaviour of the observables at the transition [258]. Depending on which region where are approaching the MIT, two magnitudes are used for its critical characterisation. The conductivity and the localisation length are self-averaged quantities and then their means are used as the expected values at the thermodynamic limit. In the vicinity of the critical transition they behave as

$$\xi \sim (x - x_c)^{-\nu} \ , \quad \sigma \sim (x_c - x)^s \ , \tag{6.2}$$

where ξ is the correlation length for the infinity system and ν and s are the critical exponents. x is the parameter varied along the transition, which could be either the magnitude of disorder or the energy. The value of the critical parameter x_c is not universal and, for example, depends on the disorder distribution. The critical exponents are related by the relation $s = (d-2)\nu$, so in 3D $s = \nu$ [55, 262]. Their values are determined from numerical techniques, in the case of ν, or by experimental measurements for s. The accurate calculation of the critical parameters has led to an active numerical [266–268] and experimental research [258], but there is no general agreement on their values. There are many experimental systems where MIT have been observed [257]. Most of the studies in solids have been performed on heavily doped semiconductors, where scaling curves have been constructed for the conductivity [269–272]. There are also experimental evidences of light [273], ultrasound waves [274] and atomic matter waves [275, 276] Anderson localisation.

6.1.2 On the possible Anderson transition in 2D

In the mid-90s a series of papers claimed that MIT is possible in 2D system. The first evidence was found in a silicon metal oxide semiconductor field effect transistor (MOSFET), where at low temperatures and zero magnetic field a strong enhancement of the conductivity was observed [277]. Moreover, the resistivity data were scaled, as a function of both the temperature and electric field, to a two-branch curve, which is the fingerprint of a MIT. The critical exponents at the transition were as well found [278, 279]. These results were in clearly contradiction with the one-parameter scaling theory. Nevertheless, the transition was reported in other 2D electronic gases. Systems based on doped Si/Ge quantum wells revealed a similar MIT [280, 281]. 2D hole gases in GaAs systems displayed as well critical phenomena [282–284]. The origin of a 2D MIT opened an active debate in the scientific community. It should be noted that in the aforementioned electronic systems the density

of carriers is low and the Coulomb interaction is strong. However, electron-electron interactions are neglected in the original Anderson model. So, all the efforts focused on the role of this interaction on localisation [285, 286]. The explanation of the apparent 2D MIT is still an open question and arguments supporting different theories are published from time to time [287, 288]. Nonetheless, the most extended idea is that the metallic behaviour is caused by the delocalising effect associated by strong electron-electron interaction which dominates over the quantum localisation [285, 286].

Even without the additional factors introduced by interactions, the 2D situation remains challenging since the extent of the localised states for weak disorder very quickly becomes much larger than the available system sizes and this might lead to results of a feigned extended behaviour. Here is where graphene, as prototypical 2D material [52, 289] enters in the problem. One naturally expects disorder to lead to localisation. However, due to its linear dispersion relation around the Dirac point at energy $E = 0$ and due to the resulting absence of backscattering in clean samples [290], one might expect somewhat unusual behaviour. Some theoretical approaches have directly dealt with the Dirac equation and determined the corresponding scaling β function. It was claimed that disorder weak enough not to lead to inter-valley mixing does not produce localisation [291, 292]. In [291] is shown that the existence of one-parameter scaling holds in graphene and that, for instance, the scaling flow has no fixed point, so in the absence of intervalley scattering the conductivity at Dirac point increases logarithmically with the sample size. However, other contradictory results for long-range disorder, under which the single valley Dirac approximation is valid, have been found. One study [293] claimed that with strong long-range impurities, namely impurities with an exponentially decaying potential with randomly distributed strength, states near the Dirac points are localised for sufficiently strong disorder. They related the localisation to intervalley scattering and characterised the transition from localised to delocalised states as a Kosterlitz-Thouless type [293].

Therefore, the presence of intervalley scattering between two inequivalent Dirac cones deserves a deeper analysis. It becomes possible when the disorder is short-ranged. Consequently, the description of the disordered honeycomb lattice by an Anderson tight-binding Hamiltonian is appropriated. By means of it, the localisation properties of graphene in the vicinity of the Dirac point have been intensively studied, leading to a wide variety of results. It was found early on that strong disorder leads to localisation at $E = 0$ [294, 295]. And that states at the Dirac point are more easily localised than states at other energies [295]. On the other hand, many, mainly numerical, results have indicated the existence of unusually weak localisation at $E = 0$ [296–300] or close to $E = 0$ [301], and results supporting mobility edges [296, 298], critical states [297, 299, 300] and/or a fully developed localisation-delocalisation transition [301] have been put forward. These results led to recent discussions that indicate graphene as an ordinary 2D system which shows Anderson localisation and the absence of mobility edges around the Dirac point [302, 303]. Recently, another study shows

that at strong disorder for $E \gtrsim 0$ [304] complete localisation is found for disorder with inter-valley mixing, in agreement with earlier studies [291, 292, 295]. To complete the varied repertoire of results, it is worth to mention that true MIT has only been observed in hydrogenated graphene [305, 306].

The main reasons of the disagreement among these studies may be found in the wide number of numerical techniques employed and the used criteria for distinguishing between localised and extended states. In detail, some of the methods include the TMM [294, 295], energy-level statistics [297, 300], evaluation of the inverse participation ratios [298, 299] and the analysis of the LDOS [296, 302, 303]. The existence of critical states at weak disorder is characterised by scaling the inverse participation ratio to a line, indicating a power-law decay of the wave functions [299], and by the difficulties to set the energy level-spacing to chaotic or localised distribution [297, 300]. Mobility edges were determined by the zeros of the typical DOS [296], but later argued as numerical deficiencies [302]. Moreover, the localised-delocalised transition is observed at the changing behaviour of the reduced localisation length, λ divided by the system size, with the size [301]. The variety of results and arguments prompts for a more detailed study of the problem taking into account that, explicitly recognised or not in all studies we have referred to, the system size is crucial for properly determine whether the states are localised or not.

On the other hand, some studies have been focused in localisation problems on graphene nanoribbons, which are quasi-1D samples of graphene with finite number of atoms in one direction and infinite in the other. Results indicate that the predominant type of edge along graphene nanoribbons modifies the quantitative strengths of the localisation effects, though Anderson localisation takes place for any disorder strength [307, 308]. However, again the size is an important factor to account for, because the localisation lengths may be greater than the sample size at weak disorder. Thus, metallic behaviour could be expected.

Previous studies still leave the regime of small energies $E \in]0, 1]$, i.e. close to but away from $E = 0$, for weak but inter-valley mixing onsite disorder unresolved, where Ref. [301] found evidences for a transition-like behaviour (see Fig. 2 of this reference). In fig. 6.3 we show this behaviour for 2D ZZ graphene flakes with 700^2 lattice sites. Clearly, around $E \approx 0.25$, increasing the size M^2 of the graphene samples leads to increasing localisation lengths while around $E = 0.9$ the trend seems to have reversed. In this Chapter, we will show that fig. 6.3 does not indicate the existence of the transition to delocalised states. Rather, we find that the finite-size trend reverses towards localised behaviour upon increasing the system size. However, we must go to very large system sizes of the order of 2.25×10^6 to show this. For smaller system sizes, from about $360,000$ to $\approx 10^6$, scaling results indicate roughly a system size independence of $\Lambda_M = \lambda_M / M$. Hence our results explain why there is such a diversity of results for the localisation properties of graphene at and close to $E = 0$,

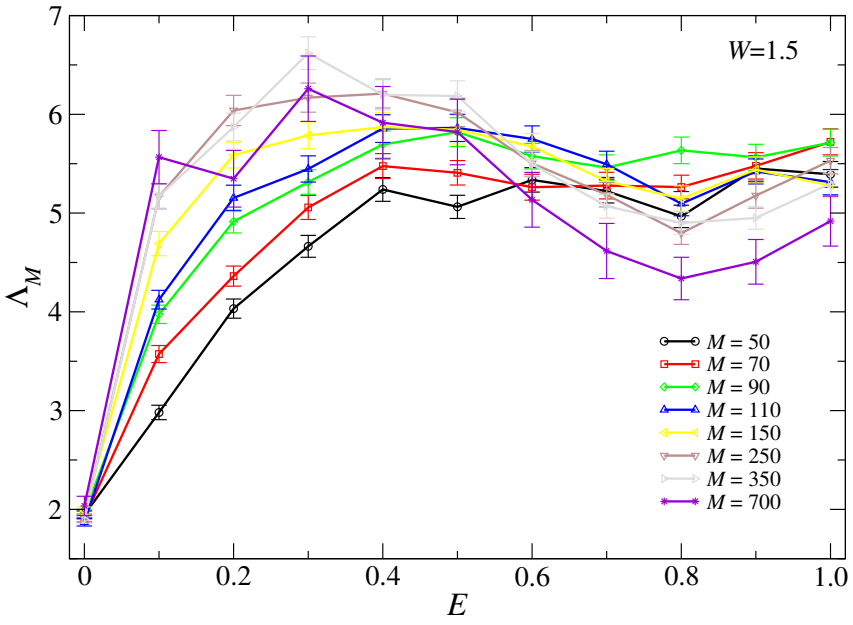

Figure 6.3: Reduced localisation length $\Lambda_M = \lambda_M/M$ as a function of energy E for the ZZ graphene lattice at disorder $W = 1.5$ and sizes ranging from $M \times L = 50 \times 50$ to $M \times L = 700 \times 700$. The error bars indicate the error of the mean from averaging over 500 samples, except for $M \times L = 700 \times 700$ where the average is over 100 samples. The lines are guide to the eye only.

i.e. we find that very large system sizes, larger than 2×10^6 lattice sites, are required to reach the asymptotic regime.

6.2 Numerical method

Our calculation is based on the standard 2D single-particle Hamiltonian

$$\mathcal{H} = \sum_{l=1}^{L} \mathbf{c}_l^\dagger \boldsymbol{\epsilon}_l \mathbf{c}_l - \sum_{l=1}^{L-1} (\mathbf{c}_l^\dagger \mathbf{t}_l \mathbf{c}_{l+1} + \mathbf{c}_{l+1}^\dagger \mathbf{t}_l \mathbf{c}_l) \ , \tag{6.3}$$

on a lattice with $L \times M$ sites. Here, $\boldsymbol{\epsilon}_l$ denotes the $M \times M$ Hamiltonian matrix acting in the (transverse) m direction for each vertical arm at (longitudinal) position l such that

$$\boldsymbol{\epsilon}_l \equiv \begin{pmatrix} \epsilon_{l,1} & \gamma_{l,1} & 0 & \cdots & \cdots & 0 \\ \gamma_{l,1} & \epsilon_{l,2} & \gamma_{l,2} & 0 & & \vdots \\ 0 & \gamma_{l,2} & \epsilon_{l,3} & \gamma_{l,3} & 0 & \vdots \\ \vdots & 0 & \ddots & \ddots & \ddots & 0 \\ \vdots & & 0 & \gamma_{l,M-2} & \epsilon_{l,M-1} & \gamma_{l,M-1} \\ 0 & \cdots & \cdots & 0 & \gamma_{l,M-1} & \epsilon_{l,M} \end{pmatrix} , \tag{6.4}$$

and $\mathbf{c}_l^\dagger \equiv \left(c_{l,1}^\dagger, c_{l,2}^\dagger, \ldots, c_{l,M}^\dagger\right)$, with $c_{l,m}$ ($c_{l,m}^\dagger$) the usual annihilation (creation) operators of a tight-binding orbital at the site $\{l, m\}$. The diagonal elements for each $\boldsymbol{\epsilon}_l$ correspond to random onsite

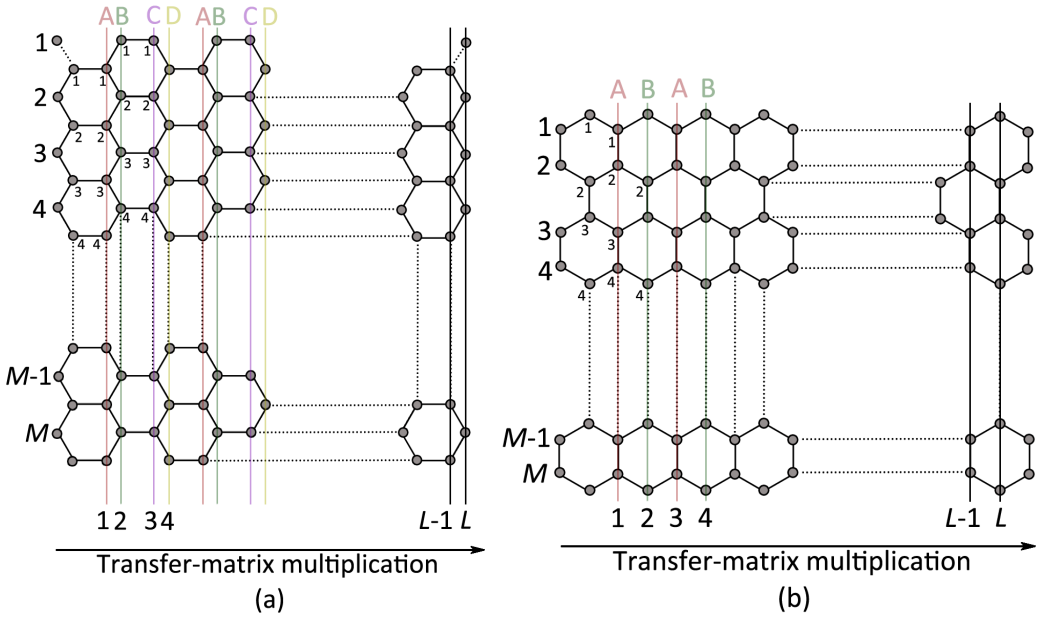

Figure 6.4: Graphene lattice for (a) AC and (b) ZZ graphene. The first four M lines are shown with numbers for guidance, as an example of the implementation of the TMM used. The layers that build a unit cell are labelled as A, B, C and D for (a) AC and A and B for (b) ZZ graphene. The direction of the transfer-matrix multiplication is indicated as well.

potentials $\epsilon_{l,m} \in [-W/2, W/2]$, $m = 1, \ldots, M$, and are uniformly distributed. Depending on the selected lattice connectivity in the m direction, the hopping term $\gamma_{l,m}$ between sites (l, m) and $(l, m+1)$ can be either t or 0. Also, $\mathbf{t}_l \equiv t\,\boldsymbol{C}_l$ is the hopping along the l direction with $\boldsymbol{C}_l$ denoting the connectivity matrix between layers l and $l+1$ [294, 304, 309]. All energies are measured in units of the hopping energy, t ($t = 2.7$ eV in graphene).

A pictorial representation of the lattice is shown in fig. 6.4 for the cases of graphene with AC and ZZ edges, detailing the chosen indexing scheme. We note that it can of course be used for the case of a square lattice, in which case $\gamma_{l,m} \equiv t$ and $\mathbf{t}_l \equiv t\mathbf{1}_M$ with $\mathbf{1}_M$ the $M \times M$ unit matrix. We emphasise that the choice of layers l in fig. 6.4 (b) leads to equal spacing for ZZ graphene with inter-layer distance $\cos(\pi/6) \times 0.142\,\mathrm{nm} = 0.123\,\mathrm{nm}$, while for AC graphene the inter-layer spacing alternates between $0.142\,\mathrm{nm}$ (from B to C and D to A in fig. 6.4 (a)) and $\sin(\pi/6) \times 0.142\,\mathrm{nm} = 0.071\,\mathrm{nm}$ (from A to B and C to D in fig. 6.4 (a)). Similar considerations apply in the m (transverse) direction. We will not attempt to rescale these length scales here.

6.2.1 A modified transfer-matrix approach

One of the preferred methods for computing localisation lengths in quantum disordered systems is the TMM [268, 310–312]. It is based on a recursive formulation of the Schrödinger equation $\mathcal{H}\psi = E\psi$ for the Hamiltonian (6.3). Assuming that the wave function describing the electron state can be

expanded in a lattice site basis for each layer, the Schrödinger equation is reformulated into a matrix equation as

$$\begin{pmatrix} \psi_{l+1} \\ \psi_l \end{pmatrix} = \boldsymbol{T}_l \begin{pmatrix} \psi_l \\ \psi_{l-1} \end{pmatrix} \ , \tag{6.5}$$

with the symplectic transfer matrix

$$\boldsymbol{T}_l = \begin{pmatrix} \boldsymbol{C}_l^{-1}(\boldsymbol{\epsilon}_l - E\mathbf{1}) & -\boldsymbol{C}_l^{-1}\boldsymbol{C}_{l-1} \\ \mathbf{1} & \mathbf{0} \end{pmatrix} \ , \tag{6.6}$$

where $\psi_l = (\psi_{l,1}, \ldots, \psi_{l,M})^T$ denotes the wave function at all sites of the lth slice. $\boldsymbol{\epsilon}_l$ is the Hamiltonian matrix acting in the (transverse) m direction and $\boldsymbol{T}_l$ is referred to as transfer matrix of the lth slice, because it connects the amplitudes ψ_l, ψ_{l-1} and ψ_{l+1}, ψ_l. $\mathbf{1}$ and $\mathbf{0}$ denote the unit and zero matrices. $\boldsymbol{C}_l$ and $\boldsymbol{C}_{l-1}$ are the connectivity matrices describing the connections of the lth slice to slices $l+1$ and $l-1$ on this non-square lattice [294, 309]. Element c_{jk} of the connectivity matrix equals 1 if the site j in one layer is connected to the site k in the other, and $c_{jk} = 0$ otherwise. The evolution of the wave function is determined by iterating eq. (6.5) for a given E and initial conditions for the wave functions ψ_0, ψ_1. Assuming that we have a system with cross-section M and length $N \gg M$, the amplitudes ψ_{N+1}, ψ_N are given by

$$\begin{pmatrix} \psi_{N+1} \\ \psi_N \end{pmatrix} = \boldsymbol{T}_N \boldsymbol{T}_{N-1} \cdots \boldsymbol{T}_1 \begin{pmatrix} \psi_1 \\ \psi_0 \end{pmatrix} = \tau_N \begin{pmatrix} \psi_1 \\ \psi_0 \end{pmatrix} \ . \tag{6.7}$$

τ_N is a product of random matrices that satisfies the Oseledec's theorem [313]. It states that the limiting matrix $\Gamma = \lim_{N\to\infty}(\tau_N^\dagger \tau_N)^{1/2N}$ exists and its eigenvalues have the form $\exp(\pm\gamma_i)$. γ_i denotes the Lyapunov exponents of τ_N, which determine the exponential increase or decrease of the wave function at long distances. The smallest of these, $\gamma_{\min} > 0$, eventually determines the localisation length $\lambda = 1/\gamma_{\min}$. From the Oseledec's theorem, the Lyapunov exponents are given by $\gamma_i = \lim_{N\to\infty}(1/N)\ln||(\tau_N u_i)||$, where u_i are the eigenvectors of Γ. Nevertheless, the numerical procedure that we use for obtaining the Lyapunov exponents does not actually need to diagonalise Γ. It is a complex but well-known technique, which could be found in detail in [117, 314, 315]. However, we summarise below the main steps. We start the iteration with a set of orthonormal vectors for u_i. After several multiplications, the vectors loose their orthogonality and they are reorthonormalised by the Gram-Schmidt method. The idea is that the obtained u_i vectors will converge to the eigenvectors which correspond to the complete set of Lyapunov exponents. Reorthonormalisation is a fundamental step because it prevents numerical overflow due to the exponential increase of vectors size. After each of these reorthonormalisation steps an approximated value for γ_i is calculated from the norm of the vectors. A relative error between two subsequent values of γ_i is as well evaluated. The relative error of λ is equal to the relative error of $\gamma_{\min}$. It gives us information about the convergence of the procedure and sets the accuracy of our calculations. In general, in order to achieve a reasonable accuracy ($< 1\%$) for λ, N is typically of the order of few millions.

For the aim of our research, however, we want to study a 2D system with area $M \times M$. Iterating eq. (6.5) only $M \ll N$ times will not usually lead to convergence. Therefore, we define the usual forward calculation with the global transfer matrix $\mathcal{T}_M = \boldsymbol{T}_M \boldsymbol{T}_{M-1} \cdots \boldsymbol{T}_2 \boldsymbol{T}_1$, after which we add a backward calculation with transfer matrix $\mathcal{T}_M^\dagger$, with † meaning transpose matrix. This forward-backward-multiplication procedure is repeated K times. The effective number of TMM multiplications is $2KM$ and the global transfer-matrix is

$$\tau_M = (\boldsymbol{T}_1^\dagger \cdots \boldsymbol{T}_l^\dagger \cdots \boldsymbol{T}_M^\dagger \boldsymbol{T}_M \cdots \boldsymbol{T}_l \cdots \boldsymbol{T}_1)^K = (\mathcal{T}_M^\dagger \mathcal{T}_M)^K \ . \tag{6.8}$$

As usual, we construct the matrix

$$\Gamma_M = \lim_{K\to\infty} (\tau_M^\dagger \tau_M)^{1/4KM} \to \mathrm{diag}(e^{\pm\gamma_i}) \ , \tag{6.9}$$

and as before, the localisation length is defined as the inverse of the smallest Lyapunov exponent, $\lambda_M = 1/\gamma_{\min}$. For a reliable convergence check, only the accumulated changes of λ_M after each complete forward-backward loop need to be taken into account. This is quite different from the aforementioned standard TMM convergence check using self-averaging arguments [258]. Here, the disorder in each $M \times M$ system is fixed during the forward-backward TMM and convergence is straightforwardly achieved when the value of λ_M changes less than 10^{-5} after a complete forward-backward loop. Usually, we find that convergence can be achieved after just a few K multiplications. Then, the method yields the localisation length, but only for a single $M \times M$ graphene sample. Afterwards, the localisation length should be sample-averaged for many different such $M \times M$ disorder realisations with same M, E and W parameters. With at least 100 samples for each parameter set, we typically find a relative error of 5% or less for the energies, disorders and system sizes studied in this Chapter. This procedure has been applied previously for studying the pair localisation length of two interaction electrons in 1D disordered systems [316] and the 3D Anderson MIT in the presence of scale-free disorder [317].

It should be noted that in a *square* $M \times M$ sample as the ones shown in fig. 6.4 for, e.g. ZZ graphene physically corresponds to a rectangle of size $(3M/2 - 1) \times \sqrt{3}M/2a_0$, being $a_0 = 0.142$ nm the carbon-carbon distance, i.e. a length to width ratio of $\sqrt{3}M/(3M-2) \sim 0.58$ for the system sizes used in our study. For AC graphene, the ratio is $(3M-2)/\sqrt{3}M$.

6.2.2 Incorporating the lattice structure

In order to apply the above procedure, the honeycomb lattice topology should be properly incorporated, because it determines the connectivity matrices. We explain in detail the way we have faced the problem. In the ZZ graphene shown in fig. 6.4 (b) the width M of our sample is given by the number of ZZ lines, and the length L by the number of layers in the horizontal direction. As an

example the first four ZZ lines along the transfer matrix direction are indicated with numbers. Each site within the ZZ line has only one connection to the preceding and succeeding layer. Hence all matrices $\boldsymbol{C}_l$ are simply unit matrices and the transfer matrix T_l for ZZ graphene of "square" size $M = L$ reduces to the standard TMM form,

$$\boldsymbol{T}_l = \begin{pmatrix} \boldsymbol{\epsilon}_l - E\mathbf{1} & -\mathbf{1} \\ \mathbf{1} & \mathbf{0} \end{pmatrix} , \tag{6.10}$$

where $\boldsymbol{T}_l$ is a $2M \times 2M$ matrix. $\mathbf{1}$ and $\mathbf{0}$ denote the unit and zero matrices of size $M \times M$. However, the exact form of $\boldsymbol{\epsilon}_l$ and the $\gamma_{l,m}$ will depend on whether the layer index l is even or odd since the position of connected and unconnected sites in each layer alternates as shown in fig. 6.4 (b). Let us classify the layers as A or B according to these connections. In each A (odd) layer, every odd site [counting from the top as indicated in fig. 6.4 (b)] is connected to its following even site, but even sites are *not* connected to following odd sites. Conversely, in each B (even) layer, even sites are connected to the following odd sites, but these odd sites are not connected to their following even sites. For just the first four lines that appear in fig. 6.4 (b), the Hamiltonian matrices are, e.g.

$$\boldsymbol{\epsilon}_1^{\mathrm{A}} = \begin{pmatrix} \epsilon_1 & 1 & 0 & 0 \\ 1 & \epsilon_2 & 0 & 0 \\ 0 & 0 & \epsilon_3 & 1 \\ 0 & 0 & 1 & \epsilon_4 \end{pmatrix}, \quad \boldsymbol{\epsilon}_2^{\mathrm{B}} = \begin{pmatrix} \epsilon_1 & 0 & 0 & \mathit{0} \\ 0 & \epsilon_2 & 1 & 0 \\ 0 & 1 & \epsilon_3 & 0 \\ \mathit{0} & 0 & 0 & \epsilon_4 \end{pmatrix} . \tag{6.11}$$

Hence, in order to compute the transfer matrix for a complete unit cell in ZZ graphene, we shall use $\boldsymbol{T}_{l+1}^{\mathrm{B}} \boldsymbol{T}_l^{\mathrm{A}}$. In $\boldsymbol{\epsilon}_1^{\mathrm{B}}$ we highlight two corner zero's to indicate where the boundary conditions for ZZ graphene are important. The present choice reflects hard wall boundaries. For periodic boundary conditions, M_{ZZ} will have to be chosen an even number. There is no such restriction for hard wall boundaries.

For transfer multiplication along a direction with AC boundaries, we have the additional complication that a simple application of standard TMM [294] will not work due to missing horizontal connections from every second site. The problem can be overcome by using four different transfer matrices as shown in fig. 6.4 (a). Therefore, for computing the transfer matrix for a complete unit cell in AC graphene, we shall use $\boldsymbol{T}_{l+3}^{\mathrm{D}} \boldsymbol{T}_{l+2}^{\mathrm{C}} \boldsymbol{T}_{l+1}^{\mathrm{B}} \boldsymbol{T}_l^{\mathrm{A}}$, defined by the general form of eq. (6.6). For all the matrices, $\boldsymbol{\epsilon}_l$ is just a diagonal matrix, its elements being the onsite energies of the M lattice sites within each layer. However, the connectivity matrices $\boldsymbol{C}_l$ are more complicated than before, but still invertible for each transverse width M within hard wall boundaries in the transverse direction. Under periodic boundary conditions, odd values of M should be taken. As an example, the connectivity matrices for AC graphene for the four lines showed in fig. 6.4 (a) are given here. Recall that $\boldsymbol{C}_l$ and $\boldsymbol{C}_{l-1}$ are the connectivity matrices describing the connections of the lth slice to slices $l+1$ and $l-1$ on this non-square lattice. Element c_{jk} of the connectivity matrix equals 1 if the site j in one layer is connected to the site k in the other, otherwise $c_{jk} = 0$. The boundary terms are indicated in italics

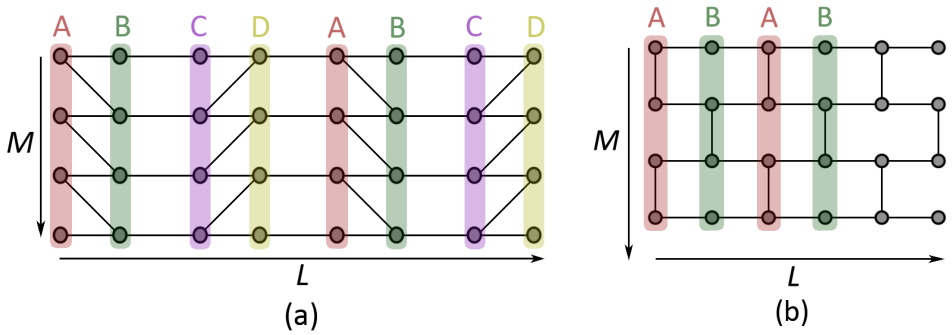

Figure 6.5: Brick-type lattice adaptation of the graphene lattice for (a) AC and (b) ZZ edges. The layers that build a unit cell are labelled as A, B, C and D for (a) AC and A and B for (b) ZZ graphene.

(0 for hard wall and 1 for periodic boundary conditions). For A-layer we get $\boldsymbol{C}_l = \mathcal{C}$ and $\boldsymbol{C}_{l-1} = \mathbf{1}$, for B-layer $\boldsymbol{C}_l = \mathbf{1}$ and $\boldsymbol{C}_{l-1} = \mathcal{C}^\dagger$, for C-layer $\boldsymbol{C}_l = \mathcal{C}^\dagger$ and $\boldsymbol{C}_{l-1} = \mathbf{1}$ and finally for D-layer $\boldsymbol{C}_l = \mathbf{1}$ and $\boldsymbol{C}_{l-1} = \mathcal{C}$ with

$$\mathcal{C} = \begin{pmatrix} 1 & 1 & 0 & 0 \\ 0 & 1 & 1 & 0 \\ 0 & 1 & 1 & 0 \\ 0 & 0 & 1 & 1 \end{pmatrix} . \tag{6.12}$$

It is easily demonstrated that the matrix $\mathcal{C}$ is invertible for all the possible sizes $M \times M$ when hard wall boundary conditions are considered. The disorder is introduced via the onsite energies, so these connectivity matrices are constant and their inverse need to be calculated just once.

The honeycomb lattice can be represented in a brick-type lattice without losing its topology. In fig. 6.5 these equivalent lattices for both AC and ZZ graphene are plotted. They have been a fundamental tool for adapting the code to this particular lattice. Moreover, from fig. 6.5 could be seen that in order to have the same number of atoms ($M \times L$) for both ZZ and AC edges, the width of the AC sample should be chosen as $M_{\mathrm{AC}} = L_{\mathrm{ZZ}}/2$ and the length as $L_{\mathrm{AC}} = 2M_{\mathrm{ZZ}}$. In this way we ensure that we are studying the same sample but in both directions of transfer matrix multiplication.

6.2.3 Finite-size scaling

As mentioned before, the one-parameter scaling theory predicts that a certain scaling variable exists and it could be used for explaining the critical behaviour close to the transition. For applying it to our computed λ_M we need to extrapolate its values with respect to M, because the required quantity is the correlation length for the infinite system [see eq. (6.2)]. However, only finite M values are numerically accessible. Nevertheless, the problem could be addressed from the scaling hypothesis for finite-sized systems, which implies the following scaling law

$$\Lambda_M(E,W) \equiv \frac{\lambda_M(E,W)}{M} = f(\xi(E,W)/M) \ , \tag{6.13}$$

for a suitably chosen scaling parameter $\xi(E, W)$ [261, 311]. The scaling parameter is the localisation length for infinitely large systems [311]. This finite-size scaling (FSS) is equivalent to the scaling theory of localisation because it involves collapsing the data to a single scaling function f. The λ_M data can be rescaled numerically by a least-squares fitting procedure to produce f [258, 311]. For strong disorders, $\lambda_M \propto \xi$. In the case of the 2D Anderson model on a square lattice, this function has a single FSS branch with decreasing Λ_M for increasing M — indicating the localised regime. For the 3D Anderson model, the same procedure leads to two branches, the first one denoting the localised regime and the second one indicating the extended regime with increasing Λ_M values as M increases. This two-branch behaviour is the signature of the transition from localised to extended states [258]. The critical parameters are obtained from fitting the values of ξ to the expressions (6.2). In most of the studies this FSS procedure has been successfully obtained within the accuracy of the data.

Alternatively, we can assume an analytical form for f and test whether this form fits the data with the required accuracy [318, 319]. Assuming e.g. the power-law behaviour $f \propto |1 - E/E_c|L^{1/v}$ of the 3D Anderson transition, the approach allows us not only to find f, but also it gives values of the critical exponent ν and the energy E_c (or disorder W_c) at which the transition occurs [318, 320]. In detail, this method [318] includes two kinds of corrections to scaling: an irrelevant scaling variable and nonlinearities of the disorder dependence of the scaling variables. Then, a family of fit functions is constructed taking into account these contributions to the scaling. The data are fitted by means of a nonlinear fit based on built-in functions of *Mathematica*. Readers are referred to references [117, 267, 318] for further details of the theoretical model and the implementation. For the purpose of our research this FSS approach will serve as a double check of the absence of a localised-delocalised transition in graphene. This procedure assumes the critical behaviour of ξ, which holds in 3D but not in 2D system. In the next section, we will see the differences of both FSS approaches.

6.3 Calculations and results

6.3.1 Localisation lengths as a function of energy

In fig. 6.6 we show the variation of the disorder-averaged localisation lengths $\lambda_M(E)$ for different disorders W[1]. The lattices correspond to square lattices, AC and ZZ graphene. The system sizes where chosen such that $M \times L = 10^4$ lattice sites in each case, corresponding to $M = 100$ and $L = 100$ for the square lattice and the ZZ graphene, but $M = 50$ and $L = 200$ for the AC graphene lattice. The λ_M values have a relative error smaller than 2.5%, obtained by averaging over at least

[1]The results presented in this Chapter have been computed thank to the resources of the Red Española de Supercomputación - Barcelona Supercomputing Center, the Centre for Scientific Computing, University of Warwick and the high capacity cluster for physics of the Campus of International Excellence of Moncloa.

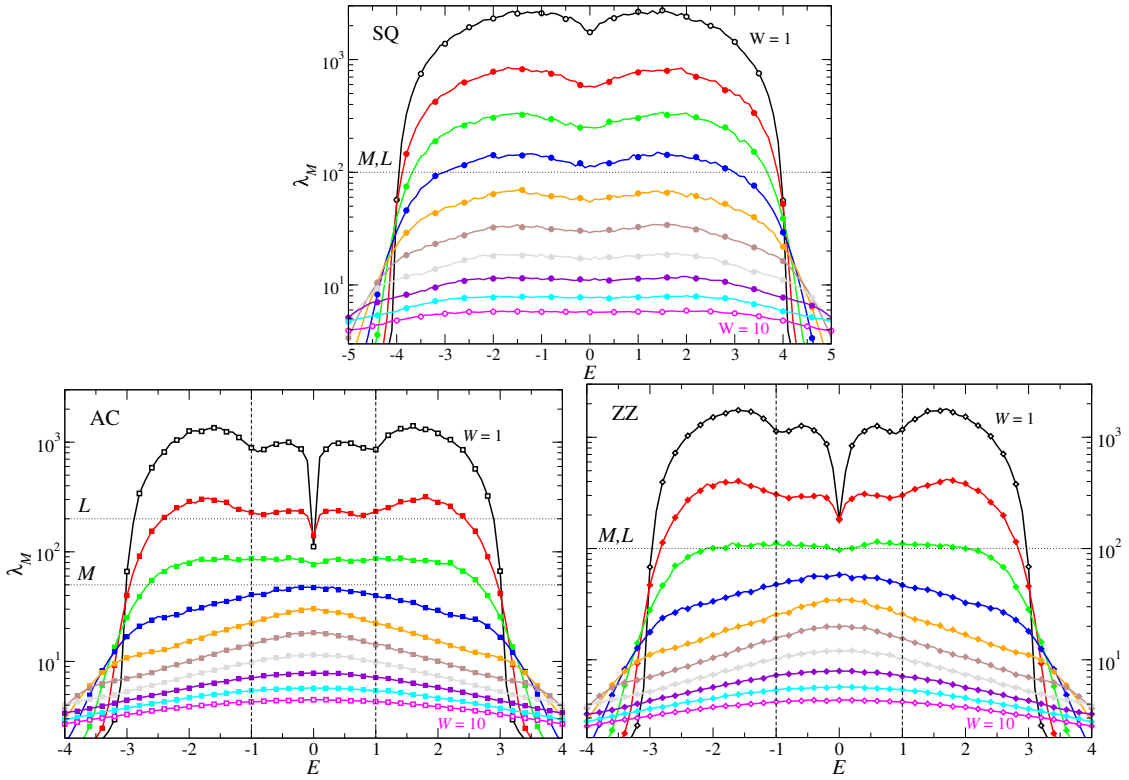

Figure 6.6: Average localisation length λ_M as a function of energy E for a square lattice (top panel), AC (left bottom panel) and ZZ (right bottom panel) graphene lattices for systems with 10^4 lattices sites and different disorders $W = 1, 2, \ldots, 10$. Lines connecting the data values are guides to the eyes only. For clarity, we only indicate the labels for $W = 1$ and $W = 10$ (open symbols). The error bars are within the symbol sizes. The M and L values are indicated by horizontal dashed lines. The vertical lines at $E = \pm 1$ for AC and ZZ graphene mark the position of the van-Hove singularities in the DOS of clean graphene.

500 disorder configurations. We first note that at weak disorder ($W \sim 1$) the energy band width reflects the number of nearest neighbours and hence tends to 4 for the square lattice and to 3 for AC and ZZ graphene [321]. Furthermore, there is the usual approximate symmetry between positive and negative energies. When the strength of the disorder is increased, the λ_M values decrease for all lattices as the wave functions become more localised. For very strong disorder, the localisation lengths are much smaller than the system sizes M and L and the states are exponentially localised with λ_M representing the decay length. On the other hand, for weaker disorders, the localisation lengths are comparable or larger than the system sizes, and we can no longer assume that the exponential decay implicit in the use of λ_M is still justified. Then λ_M is simply a convenient measure of the spatial extent of the wave functions, but not necessarily linearly related to a localisation length. Still, a larger spatial extend will imply larger λ_M values. With this in mind, we see in fig. 6.6 that, for $W \lesssim 4$, the localisation lengths increase rapidly as we decrease W for the square lattice. However,

for the case of AC and ZZ graphene lattices, we observe that in the vicinity of $E = 0$, the λ_M values again decrease, leading to values of $\lambda_M(E \approx 0)$ which seem very similar for $W = 1$ and 2. Clearly, the drop in λ_M in the graphene lattices at $E = 0$ is a signature of the Dirac point with reduced DOS [51, 322].

6.3.2 Localisation lengths at and near the Dirac point

In standard quasi-1D TMM, an increasing value of Λ_M for weak disorders as $M \to \infty$ signals the beginning of the extended regime. Even with $\Lambda_M > 1$, λ_M can still be interpreted as a localisation length since we have $L \gg M$ and localisation in the l direction is well-defined. As discussed before, the situation might be different for our modified TMM. Nevertheless, we see already from fig. 6.6 that for energies $|E| \gtrsim 1$, the λ_M values for square lattice and AC/ZZ graphene behave fairly similar. If any new, graphene-specific, finite-size behaviour can be expected, it should be around $E \approx 0$. We have therefore studied in fig. 6.3 the finite size behaviour of Λ_M in ZZ graphene for energies $0 \leq E \leq 1$ at weak disorder $W = 1.5$ when $\Lambda_M \geq 1$. As one can see from the figure, for energies larger than $E = 0.9$, increasing M (and L) leads to a decrease of Λ_M, the traditional signature of localisation. However, for energies $E \lesssim 0.6$, increasing M gives *increasing* Λ_M values. Such a behaviour for $M \to \infty$ would indicate extended states. Quite similar findings have been reported previously in the same energy range for smaller systems up to $M = 252$ [301].

Clearly, the existence of extended states in the vicinity of the Dirac point in weakly disordered (but inter-valley mixing) graphene would be surprising. However, let us note several suspicious observations, namely, (i) there is no clear crossing point, rather a series of not well-defined crossing points in the region $E \in [0.7, 0.9]$. Furthermore, (ii) increasing the system size does not lead to a clearer crossing, and we can also not identify a simple, monotonic in M (irrelevant) shift of such a crossing point. Let us also emphasise that system widths of $M = 700$ as used in fig. 6.3 are already reasonably large for TMM [318]. If there truly was a MIT in the indicated energy range, then we would expect to see good quality FSS. On the other hand, if the behaviour of fig. 6.3 was simply due to not large enough system sizes, then we should of course see if the increase in Λ_M vanishes for large enough M. Since the increase seems largest at energy $E = 0.25$, we shall study this energy in detail for square as well as AC/ZZ graphene. This energy value has been also debated in Refs. [302, 303]. In addition, we will use the Dirac point energy $E = 0$ as a further test case.

6.3.3 FSS results

In fig. 6.7, fig. 6.8 and fig. 6.9 we show computed Λ_M and FSS results in square lattices and ZZ/AC graphene at $E = 0$ and $E = 0.25$, respectively. We choose M and L values such that the number of sites $M \times L$ ranges from 100^2 to 700^2. In the case of AC graphene recall that we

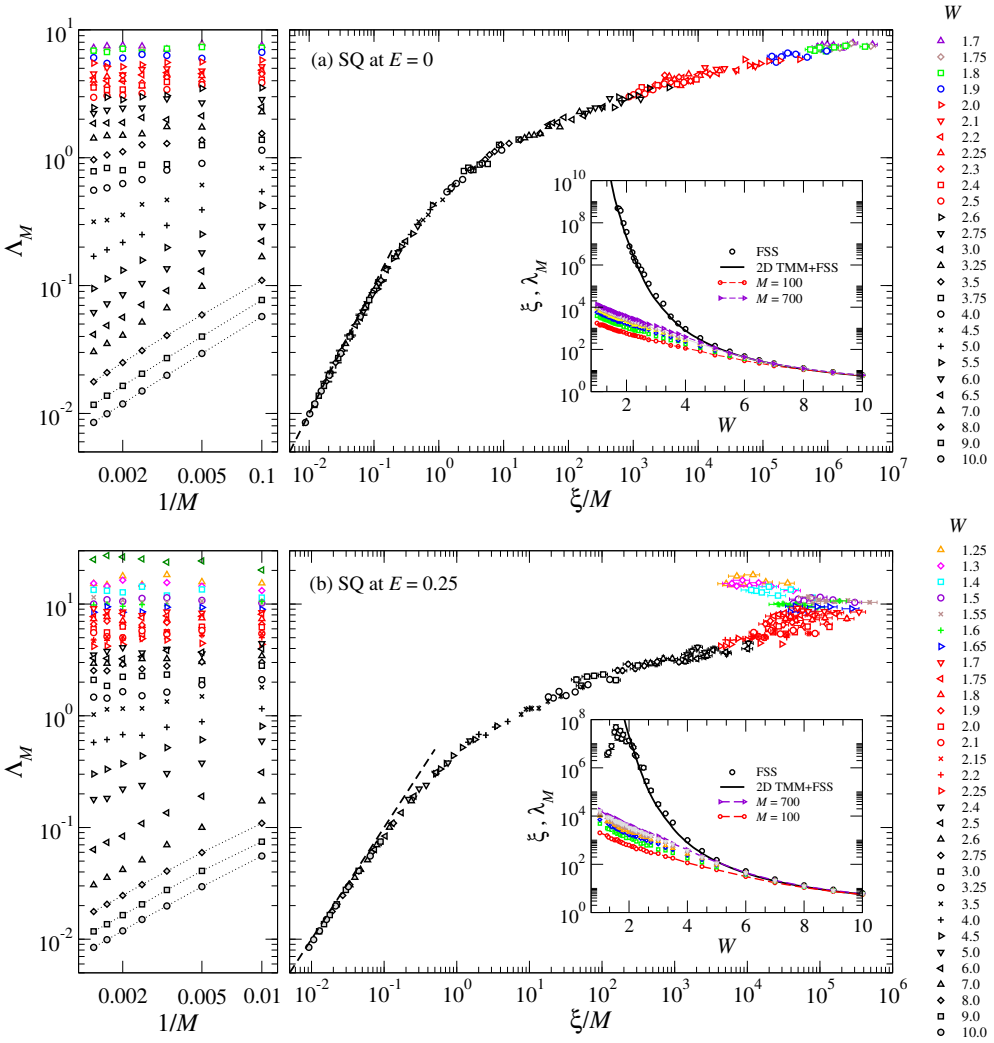

Figure 6.7: Reduced localisation length Λ_M for a square lattice at energies (a) $E = 0$ and (b) $E = 0.25$. The left panels show Λ_M as a function of $1/M$ and. They correspond to the raw data with 1% accuracy computed for at most 500 random configurations of the same M, E and W. The error bars are within the symbols size. The disorder values used are $W \in [1, 10]$ as indicated in the legends. The dotted lines are guides to the eye. In the right panels Λ_M is scaled by ξ. This means that the data on the left is relocated in the horizontal direction such a way that the deviations of the data from the common scaling curve become minimal [311]. The dashed line in each plot indicates the expected relation $\lambda_M(W) \propto \xi(W)$ for large W. The error bars are only shown when larger than symbol sizes and have been generated by resampling the FSS according to the accuracy of each Λ_M value. The insets show $\xi(W)$ scaled to coincide with λ_M values for large W. The solid line in the inset corresponds to $\xi(W)$ obtained after FSS of standard TMM localisation lengths in quasi-1D square lattices [323]. Other lines in the insets are guides to the eye only.

choose $M_{\mathsf{AC}} = L_{\mathsf{ZZ}}/2$ and $L_{\mathsf{AC}} = 2M_{\mathsf{ZZ}}$. The λ_M values are obtained from the modified TMM method outlined in section 6.2.1. The chosen disorders for each lattice and energy are indicated in

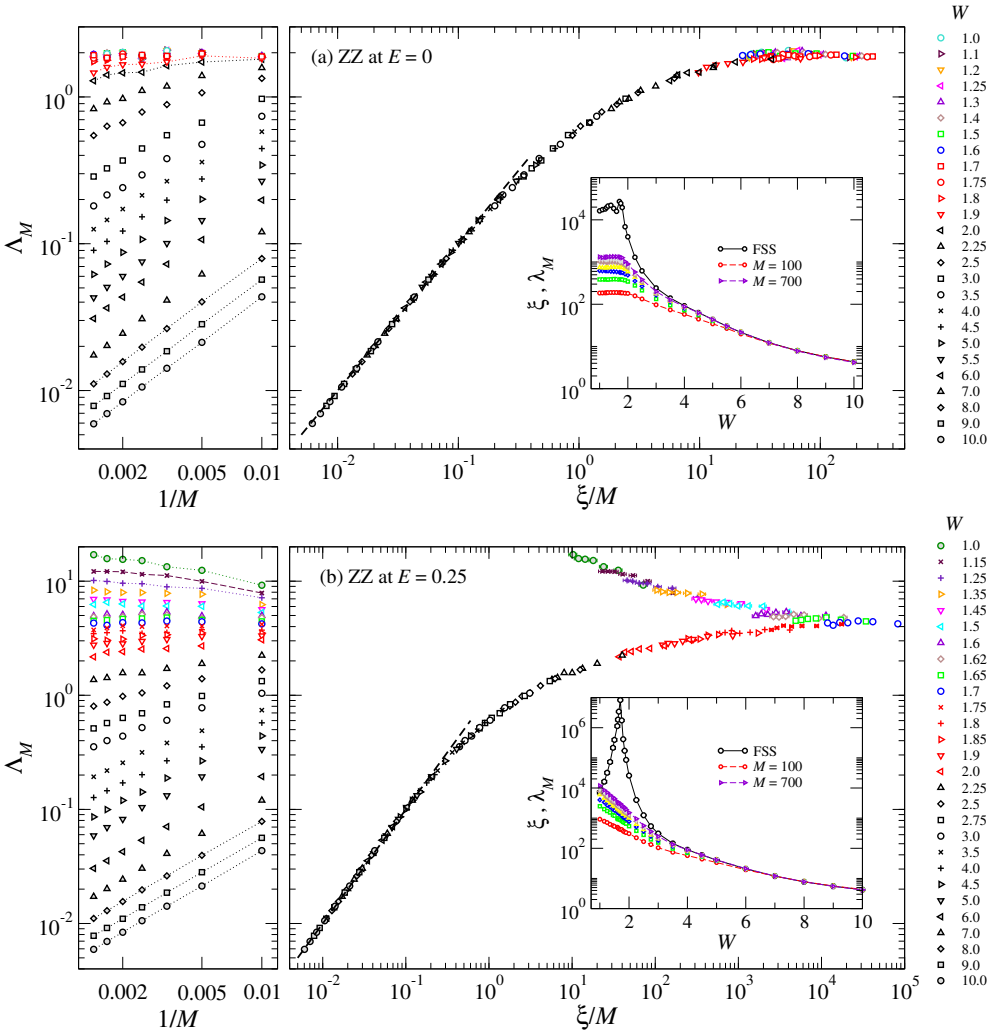

Figure 6.8: Same results as in fig. 6.7 but for ZZ graphene.

the legends of the figures. The relative error of the λ_M values is $\sim 1\%$ and is computed from the error of the mean after averaging over at most 500 different disorder configurations for each M and E. In the case of AC graphene some results are obtained for 200 configurations, but the relative error remains in the same order of magnitude. In the left panels of the figures the reduced localisation length, Λ_M, is plotted as a function of $1/M$. While the disorder is strong Λ_M increases with $1/M$ as expected from a localised behaviour. At the strongest disorders, three dotted lines are included in the figures for showing explicitly this size dependence. However, when the disorder is decreased, Λ_M starts to become independent of M and almost horizontal lines are observed. This effect is indicated by using red symbols. Eventually, at weaker disorders Λ_M seems to decrease with $1/M$, which could be interpreted as a fingerprint of the presence of extended states. This behaviour is more prominent for $E = 0.25$, has we have pointed out from fig. 6.3.

In order to find a scaling curve of our data, we have used the first of the FSS procedures described

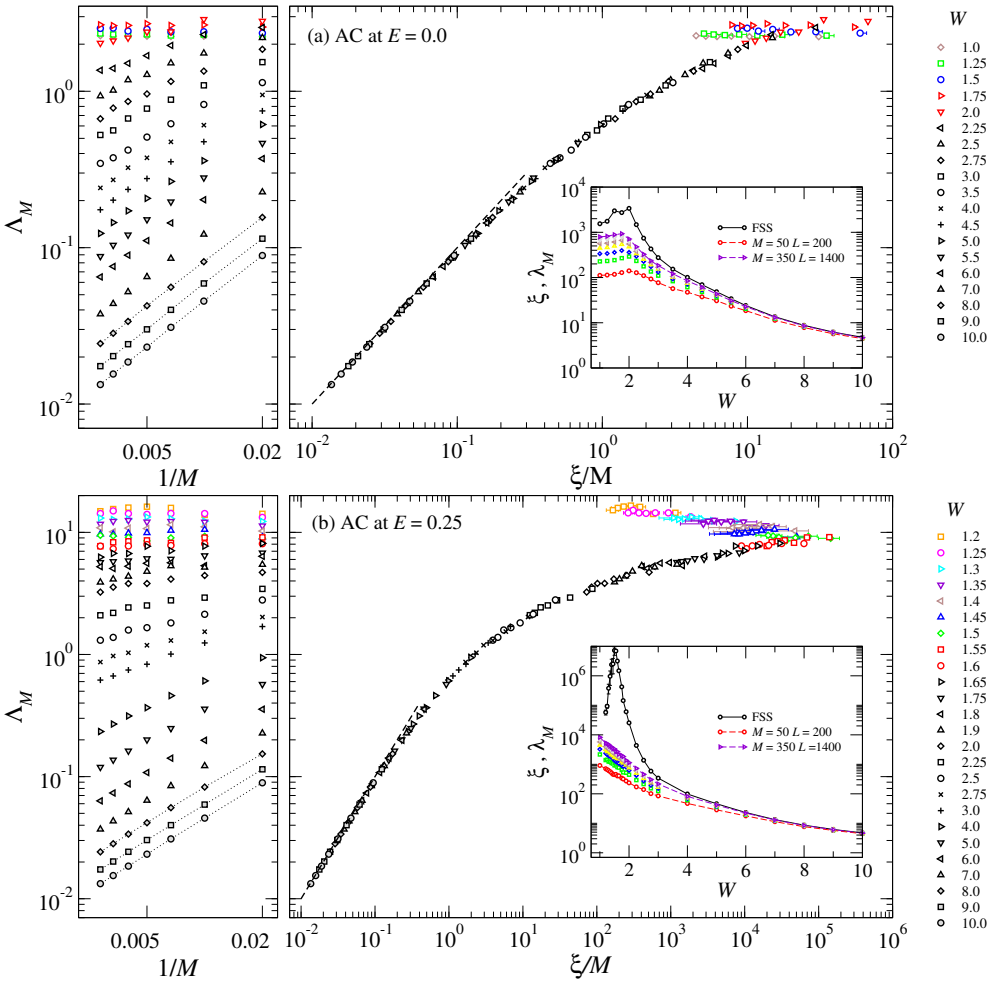

Figure 6.9: Same results as in fig. 6.7 but for AC graphene.

in section 6.2.3 and introduced in [311]. This FSS approach does not make any assumptions in the form of the scaling function. It is based on a least-squares fitting procedure. The underlying idea is to scale all the data by minimising the deviations of the data from a common scaling curve. It means that we take the raw data from the left panels and we collapse them by a horizontal relocation achieved from displacing the data with the scaling parameter $\xi(W)$, which depends only of the disorder. From this procedure the values of $\xi(W)$ are obtained. We calculate an error estimation of $\xi(W)$ taking into account the accuracy of our original data. Namely, we repeat the FSS several hundred times changing randomly the values of Λ_M within its 1% accuracy. The values are chosen from a Gaussian distribution. Afterwards, we calculate the standard deviation of the obtained values of the scaling parameter.

For strong disorders, we have $\Lambda_M \propto 1/M$ as expected since states are highly localised and λ_M is constant for $M \gg \lambda_M$ as indicated. Decreasing the disorder — or, equivalently, decreasing M — leads to deviations from the simple $1/M$ behaviour and indicates that $\xi(W)$ starts to increase.

In the standard quasi-1D square lattice TMM, this leads to an evermore flat behaviour for $\Lambda_M(W)$ as $W \to 0$. We indeed observe this behaviour for $E = 0$ in both square lattices, ZZ and AC graphene [see panels (a) of fig. 6.7, fig. 6.8 and fig. 6.9]. For smaller disorders, $W \lesssim 2$, we find the reconstruction of a well-defined FSS curve becomes numerically difficult. This is the reason why we could not scale the data for the square lattice up to $W = 1$. Nevertheless, the estimated scaling parameter $\xi(W)$ agrees very well with a previous high-precision FSS from a quasi-1D TMM [323]. Furthermore, the scaled data for squares and ZZ/AC graphene shows a single branch only, consistent with complete localisation. A special mention of the results for AC should be made. Previous studies have demonstrated that the finite width of AC flakes determines its metallic or insulating behaviour at $E = 0$ besides the disorder [324]. In the case that $2M_{\mathsf{AC}} = 3n - 1$ with $n \in \mathbb{Z}$, the system is metallic. At weak disorders, we observe this effect in our calculation through a large increase of λ_M for such M_{AC} that satisfies the above condition. Although the width of our systems are supposed large enough for not observing these size effects, the existence of a finite length promotes this phenomenon. In order to overcome the different behaviour of the AC lattice with M, we chose system sizes such as AC is in the insulating regime ($2M_{\mathsf{AC}} \neq 3n - 1$). Despite this assumption, at weak disorders traces of supposed metallic states, or at least states where Λ_M does not depend on $1/M$, are found as seen in the construction of the scaling at $W \lesssim 2$ in fig. 6.9 (a). Nonetheless, note that the scaling curves for the different lattices are qualitatively the same up to disorder $W = 4$, so it would be possible to overlap all in a single curve. This shows the universality of the scaling hypothesis. However, when the disorder becomes weaker, the topology of the lattice dominates, and the quantitative form of the curves changes. Data should be rescaled taking into account the different spacing between to neighbour sites on the square and ZZ/AC lattice.

The situation is rather different for $E = 0.25$ as shown in panel (b) of fig. 6.7, fig. 6.8 and fig. 6.9. We see that FSS gives rise to localised branches as well as the beginnings of what look like extended branches. Here it is intriguing to see that even for a square lattice, for the range of available system sizes and disorders — determined by the longest TMM runs available to us — we find an apparent transition-like behaviour. Obviously, this would be in disagreement with the scaling theory and of course also to the body of numerical results based, among others, on quasi-1D TMM [258, 259]. Similarly, we observe transition-like behaviour also for ZZ graphene at $E = 0.25$ with a better defined extended branch [see fig. 6.8 (b)]. As in the square lattice case, the onset of this branch is around $W \lesssim 2$. We have found similar results also for AC graphene as shown in fig. 6.9. However, the formation of the extended branch needs further inspection, and cannot be assumed directly as a MIT in graphene. In the next section we relate the existence of this two branch scaling curve with a finite-size effect.

On the other hand, the insets of the figures show that at strong disorders $\xi(W)$ coincide with the values of $\lambda_M(W)$, reinforcing our conclusion that all states are well localised. Therefore, as long as disorder is strong, with system sizes of around 700^2, we are able to obtain convergence of the thermodynamic limit. The discrepancies start around $W \sim 4$ for square lattice and $W \sim 3$ for ZZ/AC graphene. These values coincide with the point where $\Lambda_M(W) \sim 1$, namely when the localisation length becomes of the order of the system size. As pointed out before, under that circumstances λ_M should be seen as the spatial extent of the wave function and in the finite system and not linearly related to the localisation length.

We have also tried to apply FSS assuming the expansions of the power-law behaviour [318, 320]. However, we never found an acceptable fit to the data, although we vary not only the expansion coefficients, but also the initial values used in the non-linear fits for W_c, ν, etc. Upon closer inspection, we find that most of such attempts to fit the data lead to $W_c \sim 0$ and large values of $\nu > 5$. But even with these large ν values, the Λ_M values rise much faster for small disorders. This suggests that the true behaviour is not power-law but rather exponential as in the well-known square lattice [325]. Therefore, although the analysis of the results of fig. 6.8 (b) could be interpreted as some kind of MIT in graphene, the FSS with a well-contrasted method for determining the critical exponents fails. Thus, the least-squares fitting procedure works satisfactorily to collapse the data to a single curve, but its two branch form should be not taken as the unique evidence of AT in graphene. In the next section we study with more detail the extended branch.

6.3.4 The behaviour for very large system sizes

The FSS results of fig. 6.7, fig. 6.8 and fig. 6.9 for $E = 0.25$ and $W \lesssim 2$ do not show a very clear formation of extended branches, particularly for the square case. In order to test the stability of these branches in FSS, we would need even larger system sizes for all disorders $W \lesssim 2$. This is, however, numerically prohibitive. The calculation of a single $M \times L = 700 \times 700$ sample for ZZ graphene can take more than 6 hours at small $W \lesssim 2$ one a single processor core. This increases to about a week for some 1500×1500 samples. We have therefore restricted ourselves to two disorders, $W = 1$ and 1.25 for $E = 0.25$. Even with this restriction, a considerable number of runs for $M > 900$ do not finish within our chosen maximum time limit of ≈ 1 week. Such λ_M values have therefore a relative error ϵ_n, with n denoting the sample, larger than the target of $\epsilon_0 = 5 \times 10^{-5}$. Hence we weigh such results less when computing an average. With (i) $w_n = 1/\epsilon_n^2$ or (ii) $w_n = \mathrm{max}(1, \epsilon_0/\epsilon_n)$, we define averaged Lyapunov exponents as $\overline{\gamma}_M = \sum_n w_n \gamma_n / \sum_n w_n$ with weighted standard-deviations $\sqrt{\sum_n w_n (\gamma_n - \overline{\gamma}_M)^2 / \sum_n w_n}$. In case (ii), we weigh those samples less that have converged better than the target in order to test the robustness of our results.

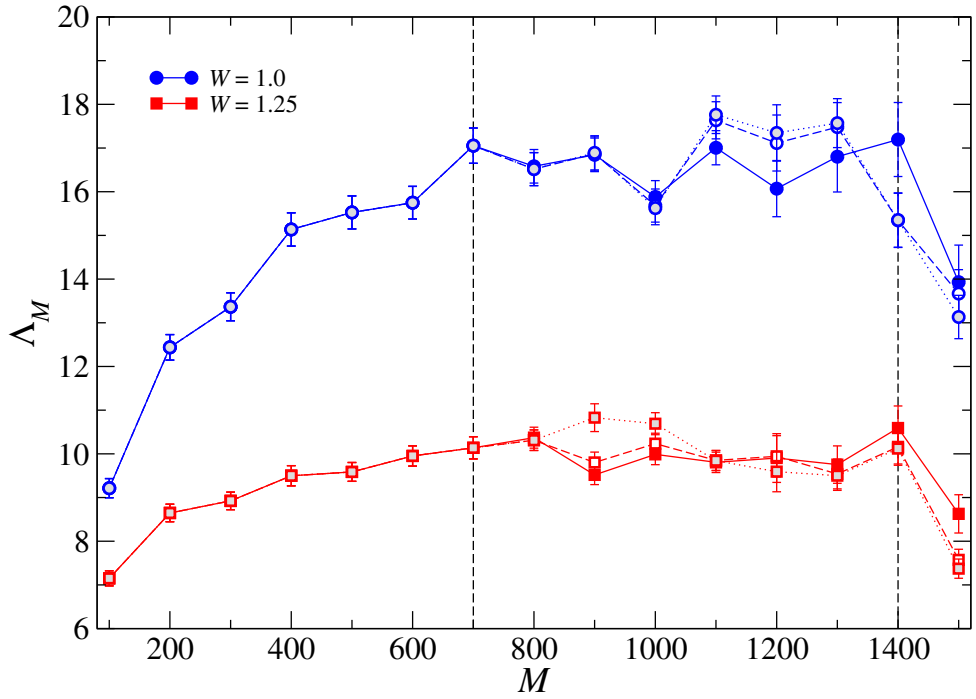

Figure 6.10: Reduced localization length Λ_M as a function of M for ZZ grapheme at $E = 0.25$ with $W = 1.0$ and 1.25. The error bars indicate the error of mean. The mean itself has been computed using the standard arithmetic average $\sum_{\text{samples}} \lambda_M^{-1}$ (solid symbols) as well as two weighted means (open/greyed symbols) as explained in the text. The data lines are guides to the eye only. The vertical lines indicate regions of different size dependence for Λ_M.

We show the resulting system size dependence of Λ_M values up to $M = 1500$ in fig. 6.10. We see that up to $M = 700$, the Λ_M values increase with increasing M, as for extended states. From $M = 800$ onwards, there is a regime in which we see little or no dependence on M within the fluctuations of the data. Such behaviour, if it were to continue for $M \to \infty$, would be indicative of critical states. Finally, at $M = 1500$, we find a drop in Λ_M. The drop is present both in the unweighted mean as well as, and even stronger, in the weighted means. This indicates that the observed increase in Λ_M with increasing M up to $M = 1400$ is simply a finite-size effect. Going to larger system sizes recovers the expected behaviour for localised states with decreasing Λ_M for increasing M. The "extended" FSS curves in fig. 6.7, fig. 6.8 and fig. 6.9 should simply be interpreted as an intermediate regime in which localisation lengths become very large. Indeed, with $\Lambda_M \approx 10$, this is much beyond what has been observed in most previous TMM studies.

6.3.5 Wave functions

Once the modified TMM has reached convergence, the wave functions (ψ_l, ψ_{l-1}) are true eigenfunctions of the global $2M \times 2M$ forward-backward transfer matrix $\mathcal{T}_L^\dagger \mathcal{T}_L$ for a given sample. Hence

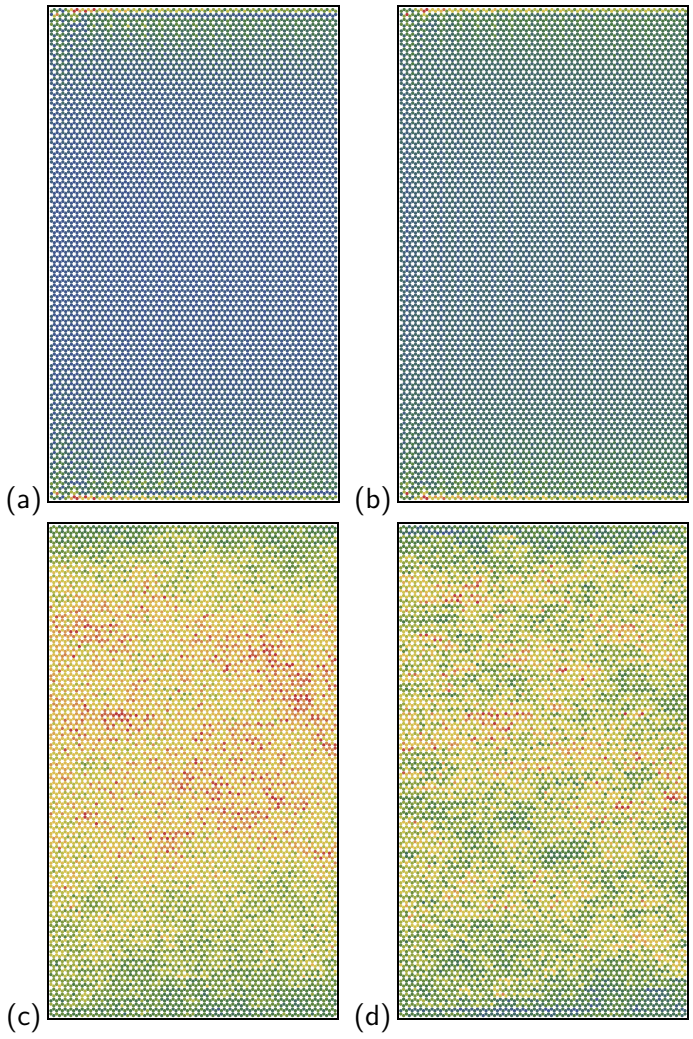

Figure 6.11: Disorder-averaged $|\psi_{l,m}|^2$ values for 500 ZZ graphene samples with 10^4 lattice sites at $E = 0$ and (a) $W = 0.5$, (b) $W = 1$, (c) $W = 5$ and (d) $W = 10$. Each wave function has been normalised prior to averaging. The colours go from $|\psi|^2 \in [0.9, 1]$ (red) to $|\psi|^2 \in [0, 0.1]$ (blue).

$\psi_{l,m}$ for $l, m = 1, \ldots, M$, is the eigenfunction of $\mathcal{H}$. In fig. 6.11 we show results for ZZ graphene at four different disorder values at $E = 0$. For weak disorders $W = 0.5$ and 1, one can clearly see the enduring presence of edge states previously predicted for clean ZZ samples [324, 326]. For stronger disorder values, the spatial disorder distribution itself becomes dominant. At $E = 0.25$ there is no evidence of edge states, as expected. Results for AC graphene are similarly consistent with the literature, i.e. we find an absence of edge states for the chosen number of AC graphene lattice sizes [324, 326]. For square lattices, we do of course not observe those strong edge states. In fig. 6.12 are plotted two examples of these results for a square and AC lattice at $W = 0.5$.

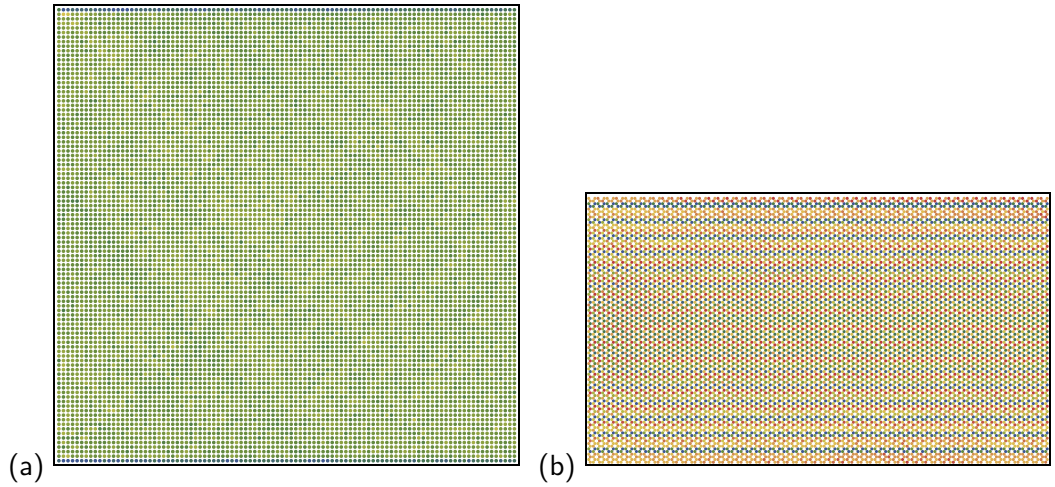

Figure 6.12: Disorder-averaged $|\psi_{l,m}|^2$ values for 500 samples with 10^4 lattice sites at $E = 0$ and $W = 0.5$ for (a) square lattice and (b) AC graphene. Each wave function has been normalised prior to averaging. The colours go from $|\psi|^2 \in [0.9, 1]$ (red) to $|\psi|^2 \in [0, 0.1]$ (blue).

6.4 Summary and conclusions

In this Chapter we have studied the Anderson localisation effects in graphene. Our approach is based on a modified TMM which allows studying "square" flakes of graphene. We have applied the method to both AC and ZZ edged graphene as well as square lattice. This TMM can convincingly reproduce the infinite-size estimates of localisation lengths obtained from standard TMM and we expect the method to be useful in other contexts as well. We have performed a FSS analysis of the calculated data in order to see the formation of a single scaling curve and derive the value of the scaling parameter, which is the localisation length for infinitely large systems. A complete analysis of the FSS results have been explained with special attention to the origin of the apparent extended states observed.

Our results show that up to lengths scales of 1500 times the carbon-carbon distance in graphene, i.e. up to 213 nm, diagonal disordered graphene, even with inter-valley scattering, exhibits surprisingly delocalised states in the vicinity of the Dirac point. This explains consistently the trend towards similar such delocalisation-like behaviour found previously [296–301], while also reaffirming that the true infinite system limit obeys the localisation predictions [291, 292, 295, 307, 308, 327]. In fact, the tendency for large localisation lengths is so strong that even FSS can be misled to construct seemingly extended branches, although a very large system size analysis shows that only the localised behaviour corresponds to the true thermodynamic behaviour [291, 292]. We emphasise that our results also explain graphene's robustness against defects in similarly experimentally fabricated sized ribbons [328, 329], billiards [330] and QDs [331].

Chapter 7

Overall conclusions and future perspectives

This Thesis is focused on three relevant aspects related to the physical properties of low-dimensional systems. Interactions, external fields and disorder are basic phenomena that govern the behaviour of quantum systems. Commonly, they appear simultaneously, but we deal with them independently. However, in some cases an explicit reference to how they could be modified by the presence of the others is added. Our proposals are based on a double effort. First, we develop an analytical framework broad enough to include different systems. And secondly, we aim that the numerical solution is as simple as possible. However, the use of high performance computing systems has been needed in several problems. In this Chapter the main conclusions of this Thesis are put together and summarised. A critical analysis is made, exploring the limitations of our approaches. Finally, some possible prospects are commented as well .

7.1 Modelling of interaction between particles

In Chapter 2 and 3 we explain and adapt the NLSP method to examining electronic states of excitons in QWs, hydrogenic impurities in QDs and energy levels of cold atoms in harmonic traps. The technique is based on the replacement of a local potential by a separable non-local potential [9]. This approach has demonstrated to be a useful tool for the study of the physical properties of low-dimensional systems. There are no theoretical limitations to the application of this approach, because it can be made exact once that the eigenstates are known. However, when putting it into practice, a certain shape function has to be chosen. We have proved that accurate results are obtained with Gaussian, Yamaguchi and δ-shell functions. The criteria for using one or another depend on the symmetry of the system and the actual local potential that we are modelling. With the examples

addressed in this Thesis, we have settled a complete theoretical framework, so we expect that the NLSP method could be used in the other scenarios. For instance, low-dimensional systems with harmonic potentials are good candidates for this method because the eigenstates are well known. Most of the confinement potentials can be approximated by a parabolic shape at low energies, so this reinforces our main conclusion that this approach may be interesting for the scientific community. The analytical procedure does not require very complicate mathematical tasks and the final calculation is based on little computational efforts, so the NLSP method could be implemented straightforward.

Regarding the physical systems that we have studied, the following main results have been achieved. The binding energy of excitons in QWs increases with the reduction of the lateral size of the QWs. Our results are in good agreement with perturbative calculations as long as the confinement is weak. In the strong confinement regime the use of the NLSP method seems to be more accurate. We choose as a working example a QW based on $In_{0.06}Ga_{0.94}N$, but results could be easily generalised to other materials provided the effective masses and the relative dielectric constant are known. Other theoretical approaches led to a similar quantum confinement effects for excitons in QWs [12, 71, 75, 76]. For the case of two atoms in a harmonic trap, we firstly examine the problem without trapping, in order to obtain the main scattering parameters, and later we confine the atoms in a trap to see how the energy levels are modified. We use two possible NLSP and our results are in agreement with those obtained from the standard Fermi pseudopotential when the size of the trap is not very small [19]. The inclusion of a new parameter, which determines the range of the interaction respect to the size of the trap, shows that the energy level shifts are even more dramatic at smaller trap sizes. Our model is a good alternative to other self-consistent methods [92, 98].

The NLSP method is also a useful mathematical approach when external fields are applied to the system. Their actual effects on the physical properties will be summarised later in this Chapter. Nevertheless, the application in other problems supports our main reasoning about the versatility of the NLSP method. It is not only suitable for modelling two-particle interaction but also for analysing more complex problems in low-dimensional systems. In Chapter 3 we show that the exciton energy in QWs and the hydrogenic impurity states in QDs could be tuned by an intense laser field. Its dressing effect is incorporated in the NLSP as two displaced centres of interaction. Consequently the method is more complicated than before. But the analytical and computational efforts remain manageable. Thus the method could be extended to systems where two simultaneous local interactions have to be taken into account. However, it would require a better refinement of the resolvent of the Hamiltonian because many-body effects will be present. On the other hand, we demonstrate that the NLSP technique is, indeed, appropriated for analysing hydrogenic energy states when the impurity is continuously displaced from the centre of the QD. We are able to study the full range of impurity positions, which is an advantage compared with other theoretical methods.

Despite the good results presented in this Thesis, some presumed approximations pose limitations to the applicability of the method if a direct comparison with experimental results is required. At least in the way it is presented now. We assume semiconductor-based nanostructures, so the effective-mass approximation holds. A single exciton or hydrogenic impurity is also presupposed. This is not a realistic situation in experiments under intense excitation conditions, because many exciton could be created and the concentration of dilute impurities is finite. Moreover, this approach does not capture at the moment electron-electron correlations. Despite these drawbacks, we are confident that the NLSP method is a fantastic starting point for the study of low-dimensional systems.

7.2 Effects of external fields

From Chapter 3 to 5 we studied the effects of three possible external fields. They are one of the principal tools for controlling the performance of optoelectronic devices. We are not focused on the design of new devices, but in the physical properties that could arise when an external potential is applied to the system. The first phenomenon that attracts our attention is the light-matter interaction. It is a quite broad area, so we focus on the modification of the energy states when a high intense laser field is applied. The effect of the laser is introduced by a dressing of the interaction potentials, developed from a nonperturbative theory previously used for describing atomic states [106–110]. We obtain a closed analytical expression for the magnitudes of interest. In detail, we examine the electronic structure of hydrogenic impurities in parabolic QDs. Two regimes are distinguished when the confinement is strong, namely when the QD size is in the order of the effective Bohr radius. At low irradiation conditions, the binding energy decrease as the impurity moves apart from the QD centre. On the other hand, under strong interaction the opposite behaviour is found. This defines a crossing point that scales with the size of the QD. In addition, the effect of the laser polarisation is taken into account, leading to a shift of the crossing point as a function of the polarisation angle. With a simplified 1D model we are able to explain qualitatively the observed behaviours and to give some reasons to this change of tendency as the impurity is moved. An InSb/GaAs QD could be used as a test for our predictions because its effective Bohr radius is quite large. Compared to previous works [28, 29], we study the strong confinement situation, where this new phenomenon is observed. An exciton in a parabolic QW under intense laser radiation is also examined. We show that the exciton energy could be varied by the laser parameters and that this could be detected in the linear absorption coefficient. Therefore, our theoretical approach suggests new quantum confinement effects that could be of interest in some electronic applications.

Obviously, our approach has several limitations. We have focused our attention on the case of an intense laser field, which reduces the complexity of the problem. But, as well, it leads to some approximations that may be or may be not fulfilled in experiments. On the other hand, we only regard

the laser effects on the electronic properties, but it could as well influence the thermal properties of the low-dimensional system. Then, other excited states could be formed. However, only single excitons or hydrogenic impurities are considered.

The AB effect is one of the most striking phenomena predicted on the second half of the 20th century [30]. It provides a beautiful demonstration that the magnetic vector potential has actually physical relevance and it is not only a mathematical construction. The effect can only be examined from quantum mechanics and is produced from the phase factor introduced by the vector potential. The theoretical implications of this discovery are deeply related to the concept of locality and thus are a fundamental knowledge for understanding the world around us. The experimental evidences of its existence paved the way for more elaborate theories of quantum interference under other kinds of interaction. In Chapter 4 we study the XAB in a 2D QR. Our work mixes three fundamental ingredients present nowadays in theoretical calculations, a thin magnetic flux, an excited bound particle and a low-dimensional system. We analyse all in a simple 2D model with a short-range interaction for the electron-hole pair. The method developed allows us to extract the exciton state from a matrix eigenequation. Although the system is 2D we observe XAB oscillations even if the radius-to-width ratio is quite small. We demonstrate that the main condition for observing the XAB effect in finite-width rings is to have a truly non-simply connectedness geometry. This only requirement contrasts with other studies that suggest that the XAB oscillations could not be observed or, at least only for polarised excitons. Recent experimental results indicate that the used confinement potential is not far from QRs already fabricated [151, 178].

The theoretical model for the XAB is based on previous studies of this effect on 1D rings [32, 155]. Therefore, our approach has some drawbacks. Although our extension to 2D is quite satisfactory, the short-range interaction may be too naive under some circumstances. Extra terms that represent the competitive effects of the exciton size and the finite width of the ring could be included. Most studies in this field use a displaced parabola for modelling the confinement potential. Therefore, it would be interesting to extend our model to that situation in order to determine the range of validity of both confinements.

Another way of tuning the physical properties of quantum systems is the application of a time-dependent field. We explore this way in Chapter 5. We assume harmonic time-dependent potentials, in one case for modelling an AC-side gate voltage and in another an oscillating barrier. From the Floquet theory the time dependence is translated in the appearance of sidebands at $\pm n\hbar\omega$ that determine the number of open channels for transport. The transmission is used as the reference magnitude for observing new phenomena. Our main results in this topic are the formation of BICs [37] in QRs subjected to an AC voltage and the complete description of the scattering amplitudes for a 1D Dirac equation under a time-dependent potential. Further inspect in each of them shows that

time-varying fields are not only a useful tool for controlling electroptical devices but also a very versatile theoretical framework for testing fundamental physical laws. BICs are strange mathematical constructs that reveal themselves as a very powerful test of the quantum behaviour of systems. We propose for the first time a configuration where BICs could be detected by varying the driven frequency of the field. They are displayed as Fano resonances in the transmission profile. The symmetry breaking produced by the two AC side-gate voltages in the upper and lower arms of the ring is the possible mechanism responsible of the BICs manifestation. Compared with other theoretical approaches, ours seems advantageous because it has a better experimental feasibility. On the other hand, a deeper understanding of the KT [40] for masless Dirac particles could be achieved by means of an oscillating barrier. This relativistic quantum effect persists despite the time dependence of the barrier. The analytical scattering amplitudes obtained show that, if only certain sidebands are considered, the KT can be modulated by the strength of the oscillating field. However, from the whole transport picture this is difficult to observe and perfect transmission is dominant. Our results could be of interest giving the huge boost that graphene has experimented in recent years [54]. At low energies its Hamiltonian is described by a Dirac-type equation and KT for normal incidence could not be avoided [39, 240].

As in the previous cases, our approach suffers from limitations. The approximation of a QR by a ring with four sites is usually employed, but is quite crude. A full discretisation of the QR is needed to accurately describe real QRs. In this regard, a finite width of the ring would be more realistic. Nevertheless, despite its simplicity, the model captures the essence of a connected geometry where BICs could be seen. Although we use only few sidebands, the transmission profile agrees well with a Fano line shape. In the case of the 1D masless Dirac equation, only normal incidence is studied. Different angles of incidence are relevant to experiments, so our model should be modified in the future to account this extra degree of freedom.

7.3 Presence of imperfections

Geometrical imperfections, dilute impurities and disorder are some of the fundamental modifications of the crystalline lattice that could enhance or reduce certain physical properties of low-dimensional systems. The case of a hydrogenic impurity has been already mentioned. On the other hand, Anderson-type disorder is the seminal model for examining disorder-induced localisation effects [41]. The theoretical framework that supports this model and the ones derived from it, such as the one-scaling parameter theory [55], conclude that states in 2D should be localised and no MIT should be observed. Graphene is the best material for checking this assertion due to its 2D nature, but very shocking results have been obtained in the last years. Some studies have claimed that graphene undergoes a MIT and some critical values have been estimated. However, in Chapter 6 we study how

finite-size effects could wrongly lead to the conclusion that weakly disordered graphene has extended states. We implement the TMM in AC and ZZ graphene flakes of finite sizes in both spatial directions. In addition, we perform two types of FSS analysis with our data. The computational part have been challenging and high performance computers have been used. Finally, after a huge number of calculations we have been able to demonstrate that all states are localised and graphene does not undergo an AT. At certain energies two branch scaling curves are obtained, but we relate it to finite-size effects. A proper FSS does not work for our results and a decrease of the reduced localisation length with the system size is observed at large system sizes, as expected. Our results are part of the series of theoretical papers that debate about a possible AT in 2D, which left it up to the advances in graphene. However, the controversy is quite old and still today is an open question. We are confident that our study sheds some light on the subject and settle clear ideas of the necessary system sizes to see complete localisation.

It is clear that our approach has some limitations. The system sizes are constrained to resources and computation time available. We have done a big effort to adapt our method to finite sizes and to the computational limitations. In this regard, when dealing with large system sizes some calculations have not reached the desired convergence. However, we include these results in our final calculations with a proper weighting. Ideally, larger system sizes and the full spectrum of disorders and energies should be examined. Moreover, with the Anderson model short-range disorder is introduced in the system, so in order to widen the localisation study in graphene, other models of disorders should be considered and studied.

7.4 Future perspectives

During the work of this Thesis a number of questions remained open and they could be the main subject of future research. In this section we present some of the envisioned projects.

As an extension of the NLSP method developed on Chapters 2 and 3, non-linear optical effects due to excitonic transitions in QDs could be studied [332]. In most of the optical activate systems several excitonic states could be formed, and a full description of their influence on the absorption spectrum is needed. To this end, the entire range of exciton states is required. In our current approach we obtain the ground state, but the following states could be straightforwardly obtained. This could be achieved including extra potential term in the definition of the NLSP, representing excited states.

The confinement potential for the QR studied in Chapter 4 was chosen because its geometry prevents the ring to be connected through the centre. In real QR more complicated potentials are present [135]. Therefore, it would be interesting to apply our model to other confinements. And, for instance, analyse how the oscillations are affected by the continuous transition from a non-connected

to a connected geometry. Other studies have included also the effect of an external field, which produces an inversion of the oscillation pattern [158]. A proper inclusion of the electric field in our 2D model is also another challenging area of research.

A widely studied phenomenon in driven transport is the ratchet effect. It consists in the conversion of fluctuation forces without any net bias into directed motion (see [190] for a review). An AC potential in combination with an asymmetric and periodic potential is the standard working example of a ratchet. However, the effect could be also observed in spatial symmetric systems subjected to a driving field that includes higher harmonics. The suggested geometry in Chapter 5 for the detection of BICs could be extended to the study of ratchet phenomena. For example, another QR could be added to the system and time-harmonic potentials with certain phase shift could be applied to the rings (in a similar way as the system of [333]). The transmission through the device will show the possible ratchet effect. On the other hand, electron-electron and electron-phonon interactions could be added to our original problem and studied by means of the Keldysh formalism [334].

Lastly, the TMM method developed for studying Anderson disorder in graphene flakes could be extended to other kinds of imperfections. In the experimental fabrication of graphene, adatoms or localised impurities could emerge. Our method could account for this effect with a proper choice of the onsite energies in the honeycomb lattice. In this area, hydrogenated graphene is running as a candidate for exploring new phenomena [335]. On the other hand, if the randomness of the disorder is introduced in the hopping terms we could model the roughness of monolayer graphene, which is experimentally observed in the form of ripples. This is an area of growing interest [336].

Brief summary of the Thesis

Introduction and objectives

Condensed matter physics is one of the most prolific branches of contemporary physics. In the latest 50 years over 20 Nobel Prizes have been awarded to research in the context of condensed matter physics. In 1956, the discovery of the transistor was awarded [21], which is the traditional example of a solid state device with a decisive influence on the progress of our everyday world and of course, our professional career. Since then, every few years either the development of essential scientific instruments for the study of matter or the discovery of new phases of matter or the proposal of new theories that explain observed physical phenomena are recognised. Thus, a new scientific paradigm is put forward, the field of condensed matter physics, including a large number of current physics research [1]. It is constantly expanding and increasing its links with other scientific disciplines such as biology and chemistry. An area related to condensed matter physics with growing interest is nanoscience [4]. Due mainly to both technological advances and theory developments for controlling and predicting physical phenomena in reduced dimensions. Most studies examine low-dimensional systems in which the charge carriers are confined to 0D, 1D or 2D dimensions. Quantum mechanics, a great scientific revolution in the 20th century [3], is the fundamental ingredient of the condensed matter theoretical models. Therefore, new theories and models that capture the diversity of phenomena observed in low-dimensional systems are needed.

This Thesis is focused on the study of the behaviour of the fundamental constituents of matter in low-dimensional systems. This depends on three fundamental aspects: interaction with other particles, the effects of external fields and contributions of disorder in their wave functions. Specifically, the study was centred in four systems such as QDs, QWs, QRs and graphene. The interaction between particles has been explored in excitons in QWs and QRs, hydrogenic impurities in QDs and atoms confined in harmonic traps. Three possible external fields are considered: an intense laser beam acting on the nanostructures, a magnetic field in a QR and time-varying fields in QRs and 1D relativistic systems. The effects of the disorder on the localisation of the electronic wave function in graphene have been as well analysed. Our main objective has been to develop theoretical models and numerical procedures to be applied to the aforementioned systems, with the goal of proposing

new physical properties. We have made use of well-established theories in the scientific community and computational resources available in the workplace where this Thesis has been developed. With this work we have understood and introduced the arising of phenomena such as the AB effect [30] for excitons in 2D QRs, BICs [37] in time-dependent systems, KT [40] in time-varying barriers and Anderson localisation [41] in graphene.

Main contributions of the Thesis

The main results of this Thesis are presented in more detail below. The three main areas of work, presented above, are simultaneously examined throughout the manuscript. For the purpose of presenting in a orderly way the fundamental contributions of this work, this section has been divided into subsections corresponding to each Chapter of the Thesis.

Two interacting particles confined in harmonic potentials

In order to develop an efficient and effective method for analysing the energy states in low-dimensional systems with a two-particle interaction we have implemented the NLSP method [9, 59]. The specific details of this procedure can be found in sections 2.1 and 2.2 of the Thesis. However, we stress a couple of characteristics that make this technique relevant to the scientific community. First, the NLSP method is based on replacing a local potential such as the Coulomb interaction between the electron and hole, by a projective operator. This substitution is exact and therefore, there is no theoretical limitation to the accuracy with which results are obtained. However, it is necessary to know the wave functions of the original problem, which are unknown in advance. This drawback can be overcome, in practice, with the choice of a number of free parameters, the shape function and the coupling constant. Taking into account the dimensionality of the system and the confinement potential, it has been shown that some shape functions such as Gaussian or Yamaguchi-type are suitable for the study of QDs [73, 74]. Finally, we obtain a closed expression for the energy levels, which can be solved with reduced computational effort. This is the second advantage in using this technique in comparison with other numerical methods. Therefore, we state that the NLSP method allow us to study in a systematic and simple way the effect that interparticle interaction has on the physical properties of low-dimensional systems.

Regarding the physical systems we have studied, the following results can be highlighted, which are deeply explained in **Chapter 2**. We have obtained the exciton binding energy in a QW, demonstrating that it increases with the reduction of the lateral size of the wire. Our results are in agreement with those obtained by perturbative methods, and can be adapted to different semiconductor materials provided that the dielectric constant and the effective mass of the charge carriers are known. In the case of two atoms confined in a harmonic trap, we calculated the scattering properties in the

absence of confinement and studied the effects of the trapping in the energy levels. We tested two possible NLSP, getting very similar results to those that have been achieved by the regularised Fermi pseudopotential in wide traps [19]. Nonetheless, our method allows us to include an additional parameter to control the trap size respect to the interaction strength. Thus, we can analyse the strong confinement regime, thereby we provide an alternative to other self-consistent methods [92, 98].

Effects of intense laser radiation on low-dimensional systems

In this Thesis we have extended the use of the NLSP method to the presence of external fields such as an intense laser beam. We have demonstrated that the above explained technique is not only valid for the study of the interaction between particles but also for situations in which an external field can modify the physical properties. The intense laser irradiation is introduced through a dressing of the interaction potentials. This approach is based on a perturbation theory previously used in the study of atomic states [106–110]. In our method this results in two Coulomb centres shifted in an amount related to the laser intensity. To cope with this new scenario we have adapted the NLSP method as described in section 3.1.2. At first glance, this seems more complex, but closed expressions are obtained for the magnitudes of interest and computational requirements remain minimal. Consequently, the NLSP technique is suitable for studying the effects of external fields.

The reader is referred to **Chapter 3** for a comprehensive explanation of the specific results in this theme. In summary, we distinguished two regimes for the energy states of hydrogenic impurities in QDs under the action of an intense laser beam. On the one hand, when the intensity is low, the binding energy decreases as the impurity moves from the centre to the edge of the QD. However, when the laser intensity is high, the opposite behaviour is observed for the binding energy. Thus, we find a crossing point in the energy that scales with the size of the QD. Additionally, we analysed the effect of the polarisation of the laser, resulting into a shift of this crossing point. We propose a 1D model that captures the underlying physics of this effect and helps to better understand the results. To complete the study we suggest a semiconductor material in which this phenomenon could be observed. Our model complements a number of previous studies where similar behaviours were detected [27, 29, 103]. Moreover, we have also studied the optical absorption in parabolic QWs under laser irradiation. We have seen that the ground state energy of the exciton reaches a saturation regime as the laser intensity increases, being the saturation value higher for QWs with smaller size. This effect can be detected in the optical spectrum due to a shift to higher energies of the absorption peak.

Excitonic Aharanov-Bohm effect in a two-dimensional quantum ring

The AB effect [30] is one of the most amazing phenomena proposed in the second half of the 20th century in the context of condensed matter physics. It is a purely quantum phenomenon that has not analogue in classical physics. The AB effect explains why charged particles are affected by an electromagnetic field even when the field is not acting directly on them. This is due to the fundamental role of the vector potential. Although initially it has be considered as a mathematical artifact, actually it has physical relevance because it introduces a phase factor due to the path followed by an electron beam. In the circular geometry proposed for observing the AB effect this leads to a phase difference between the two possible paths that can traverse the electron beam. This phase difference can be detected in the physical properties of the system as oscillations with the magnetic flux enclosed within the ring. A detailed description of the effect and its experimental observation can be found in section 4.1. Low-dimensional systems are one of the main scenarios where this phenomenon has been studied. QRs are the best candidates due to their geometry. In these systems the Coulomb interaction plays a very important role because electrons and holes are restricted to move in lower dimensions. Previous studies have shown that excitons are also sensitive to the vector potential, and thus the AB effect is also observed. This is known as the excitonic AB effect (XAB) [31, 32].

In **Chapter 4** we study the existence of the XAB effect in 2D QRs. Other studies have claimed that this effect will be difficult to observe in 2D and certain conditions on the type of confinement must be met in order to be measurable [159, 160, 162–165]. However, we have shown that the effect is robust in 2D and oscillations in the exciton binding energy and in the oscillator strength may be detected. The XAB effect will be observable even in QRs with radius-to-width ratio larger than one. We have proposed the use of a confinement potential with a repulsive barrier at the centre, so a non-simply connected geometry is ensured. This is the essential ingredient for the effect to persist in 2D. Recent experimental studies show that our confinement potential describes properly fabricated QRs [178]. We assumed that the electron-hole interaction is short-ranged, allowing us to obtain the energy of the exciton from a matrix equation. Then, the numerical requirements are not very demanding. We expect the model to be suitable for the study of more realistic geometries of QRs and to allow a better understanding of recent results of XAB effect in QRs.

Quantum systems driven by time-dependent fields

In order to control the energy states of low-dimensional systems time-dependent external fields can be used [36]. Moreover, the scattering properties of a system are usually studied under time-varying potential barriers [187, 188]. The transmission coefficient provides information of the bound states of the system and about the open channels for electronic conduction. In this Thesis we have studied

two low-dimensional systems where different physical phenomena can be controlled and characterised by an oscillating potential. We employed the Floquet theorem to obtain relevant quantities for our study. Other methods that have been commonly used are the non-equilibrium Green's functions and the formalism of the scattering matrix [36].

The main results obtained in this study are detailed in **Chapter 5**. Firstly, we saw the formation of BICs in QRs subjected to a time-varying gate voltage. A BIC is a state whose energy lies in the continuum spectra but is normalisable. They were originally proposed by von Neumann and Wigner [37], but for a long time were seen as a mathematical strangeness rather than an experimentally realisable physical state. However, the advances in nanotechnology led to similar states in low-dimensional systems such as superlattices [200, 201]. In section 5.2 more details of the nature of these states can be found. In this Thesis we propose a physical system where the energy of the BICs can be controlled by the driving frequency of an external field. We observe the appearance of two BICs by the application of asymmetrical gate potentials in the two arms of the QR. The BICs are shown in the transmission profile as Fano resonances [232]. Varying the frequency of the AC gate voltage we can tune the energy of these exotic states. We have developed all the necessary theoretical formalism to obtain an analytical expression of the transmission coefficient, which is an important advantage to understand the formation of BICs. Secondly, we studied the KT [40] in the presence of a time-dependent potential. This phenomenon is a property of the relativistic Dirac equation [38], and it is named tunnelling because relativistic electrons impinging normally onto a barrier are fully transmitted. In this Thesis, we obtained the transmission amplitudes for 1D relativistic electrons when the barrier varies with time. In particular we have analysed the cases of δ-like, square and finite width barrier. We found that the KT holds for barriers modulated in time. Our results are of particular interest to recent studies on KT in graphene [39, 240], because graphene charge carriers can be described by a relativistic Dirac equation close to the Fermi energy.

Localisation and finite-size effects in graphene flakes

Graphene is a material that has received huge attention in recent years due to its extraordinary physical properties [54]. It is a purely 2D system, making itself an outstanding candidate for the study of those physical phenomena that manifest only at that scale. The localisation of the wave functions of the charge carriers due to the presence of disorder is well known since Anderson proposed a model for the study of electronic diffusion in random potentials [41]. From this model and the one-parameter scaling theory [55], developed a few years later, it has been explained that in 3D a disorder-induced MIT arises. However, in 1D and 2D systems all states are localised despite the disorder. In section 6.1.1 reader can find a full explanation of the Anderson model and the one-parameter scaling theory. Graphene has recently been employed as a probe to test the hypothesis

of the scaling theory [291, 292, 295–300, 304]. The research has yielded quite different results, and an exciting debate has been opened in the scientific community about the peculiarities of graphene in terms of the localisation of states. A wide number of numerical techniques have been employed, including the TMM, energy-levels statics and the analysis of the LDOS. Some studies have noted the presence of mobility edges [296, 298], critical states [297, 299, 300] and a localised-delocalised transition [301]. Nevertheless, others have found that all states are localised and thus graphene behaves like a prototypical 2D material [294, 295].

In this Thesis we studied the localisation and finite size effects in graphene. This analysis is deeply explained in **Chapter 6**. First, we have proposed a modification of the TMM for computing localisation lengths of finite sized systems in both spatial directions. This has allowed us to study of "square" graphene samples. The numerical calculation has involved the use of high performance computers because the results have been averaged over a large number of configurations to achieve the desired accuracy. Subsequently, we have conducted a FSS study in order to determine the behaviour of the localisation length in the thermodynamic limit. We found that at certain energies the system apparently undergoes a localised-delocalised transition as function of disorder. However, when looking for the characteristics of the possible transition no satisfactory results are obtained. This indicates that the system is not really driven through a MIT. Moreover, we have studied larger system sizes and the localisation length reverts its behaviour compared with smaller sizes. This indicates that the apparent delocalised states are due to the finite sizes we are using. If we had been able to deal with larger systems, we would see that graphene shows the expected 2D behaviour. This work allows us to understand the diversity of results obtained by other researchers and we are confident that the employed method can be suitable for studying other disordered systems.

Conclusions

This Thesis successfully developed various theoretical models that have been implemented for the study of the physical properties of low-dimensional systems. In view of the contributions raised throughout the work, it is expected that the results of this Thesis will be of relevance to the scientific community, as shown by the achieved publications listed at the end of the manuscript. In addition, once that the objectives of this Thesis have been accomplished, we expect that the elaborated theoretical models and numerical techniques can be applied to other problems in condensed matter physics. Specifically, we could study non-linear effects in the optical properties of QDs [332], other confinement potentials for QRs and their effects on the observation of the XAB effect, study the ratchet phenomenon related to QRs [190] and other types of disorder in graphene [335, 336].

Breve resumen en español

Introducción y objetivos

La física de la materia condensada es uno de los campos más prolíficos de la física contemporánea. En los últimos 50 años más de 20 Premios Nobel han sido concedidos a investigaciones que se pueden enmarcar dentro de la física de la materia condensada. En 1956 se galardonó el descubrimiento del transistor [21], ejemplo tradicional de un dispositivo de estado sólido con una influencia decisiva para el avance de nuestro mundo cotidiano y por supuesto, de nuestra carrera profesional. Desde entonces hasta ahora, cada ciertos años se reconoce bien el desarrollo de instrumental científico fundamental para el estudio de la materia o el descubrimiento de nuevas fases de la materia o la propuesta de nuevas teorías que permitan entender los fenómenos físicos observados. Se ha establecido un nuevo paradigma científico, el campo de la física de la materia condensada, que incluye un amplio número de las investigaciones actuales en física [1]. Este campo está en constante expansión y sus conexiones con otras disciplinas científicas, tales como la biología y la química, son cada vez mayores. Un área relacionada con la materia condesada con creciente interés es el de la nanociencia [4]. Esto se debe tanto a los avances tecnológicos a escala nanométrica como a la formulación de teorías que permiten controlar y predecir los fenómenos físicos en dimensiones reducidas. Habitulamente se estudian sistemas de baja dimensionalidad en los que los portadores de carga están confinados en cero (0D), una (1D) o dos (2D) dimensiones. La mecánica cuántica, gran revolución científica del siglo XX [3], es el ingrediente fundamental de los modelos teóricos de la física de la materia condensada. Por tanto, se hace necesario plantear nuevas teorías y modelos que capturen la diversidad de fenómenos observados en sistemas de baja dimensionalidad.

Esta Tesis está centrada en el estudio del comportamiento de los constituyentes fundamentales de la materia en sistemas de baja dimensionalidad. Éste depende de tres aspectos fundamentales: la interacción con otras particulas, los efectos de campos externos y las contribuciones del desorden en sus funciones de onda. En concreto, el estudio se ha enfocado a cuatro sistemas tales como puntos (QDs), hilos (QWs), anillos (QRs) cuánticos y grafeno. La interacción entre particulas se ha explorado en excitones en QWs y QRs, impurezas hidrogenoides en QDs y átomos confinados en trampas armónicas. Se han considerado tres posibles campos externos: un haz láser intenso incidiendo

sobre las nanoestructuras, un campo magnético en un QR y campos oscilantes en el tiempo en QRs y sistemas 1D relativistas. Los efectos del desorden y su consecuencias sobre la localización de la función de onda electrónica se han analizado en grafeno. El objetivo fundamental ha sido desarrollar modelos teóricos y procedimientos numéricos para aplicarlos a los sistemas anteriormente mencionados, y así comprender y proponer nuevas propiedades físicas de los mismos. Para ello hemos hecho uso tanto de teorías bien establecidas entre la comunidad científica como de los recursos computacionales disponibles en los centro de trabajo donde esta Tesis se ha desarrollado. Con este trabajo hemos entendido la aparición de fenómenos tales como el efecto Aharonov-Bohm (AB) [30] de excitones en QRs bidimensionales, estados ligados al continuo (BIC) [37] en sistemas dependientes del tiempo, el túnel de Klein (KT) [40] en barreras variables con el tiempo y la localización de Anderson [41] en grafeno.

Contribuciones fundamentales de la Tesis

A continuación describimos con más detalle los resultados obtenidos en los diversos estudios que componen esta Tesis. Los tres principales ejes del trabajo, presentados anteriormente, aparecen simultáneamente a lo largo de todo el manuscrito. Para presentar de forma más ordenada las contribuciones fundamentales derivadas de este trabajo, se ha estructurado este apartado en epígrafes correspondientes a cada uno de los capítulos de la Tesis.

Modelización de la interacción entre partículas confinadas en potenciales armónicos

Con el fin de desarrollar un método eficiente y eficaz para analizar los estados energéticos en sistemas de baja dimensionalidad cuando existe una interacción entre dos partículas hemos empleado el método del potencial no local separable (NLSP) [9, 59]. Los detalles concretos de este procedimiento pueden encontrarse en las secciones 2.1 y 2.2 de la Tesis. Sin embargo, pueden destacarse un par de características que hacen esta técnica relevante para la comunidad científica. En primer lugar, el método NLSP se basa en reemplazar el potencial local, como puede ser la interacción de Coulomb entre electrón y hueco, por un operador proyectivo. Esta sustitución es exacta y no hay, por tanto, limitaciones teóricas a la precisión con la que se pueden obtener los resultados. No obstante, para ello es necesario conocer las funciones de onda del problema original, que son desconocidas. Este inconveniente puede salvarse en la práctica con la elección de una serie de parámetros libres, la función de forma y la constante de acoplamiento. Teniendo en cuenta la dimensionalidad del sistema y el potencial de confinamiento se ha demostrado que algunas funciones de forma, tales como funciones Gaussianas o de tipo Yamaguchi, son muy convenientes para el estudio de QDs [73, 74]. Finalmente se obtiene una expresión cerrada para los niveles energéticos, que puede resolverse con un esfuerzo computacional reducido. Esta es la segunda ventaja en el uso de esta técnica en comparación con

otros métodos numéricos. Por todo ello consideramos que el uso del método NLSP permite estudiar de una forma sistemática y sencilla los efectos de la interacción entre partículas en las propiedades físicas de sistemas de baja dimensionalidad.

Respecto a los sistemas físicos que hemos estudiado, pueden destacarse los siguientes resultados, que están explicados en profundiad en el **Capítulo 2**. Hemos obtenido la energía de ligadura de excitones en un QW, comprobando que ésta se incrementa con la reducción del tamaño lateral del hilo. Nuestros resultados están en consonancia con los obtenidos por métodos perturbativos, y pueden extenderse a diferentes materiales semiconductores siempre que la constante dieléctrica y las masas efectivas de los portadores de carga sean conocidos. En el caso de dos átomos confinados en una trampa armónica, hemos obtenido tanto las propiedades de dispersión en ausencia de confinamiento como los efectos de la trampa en los niveles energéticos. Probamos dos posibles NLSP, obteniendo resultados muy similares a los que se han obtenido por medio del pseudopotencial de Fermi en trampas anchas [19]. Sin embargo, nuestro método permite incluir un parámetro extra para el control del tamaño de la trampa con respecto al rango de la interacción. De esta forma, podemos analizar régimenes de alto confinamiento, proporcionando así una alternativa a otros métodos autoconsistentes [92, 98].

Efectos de un láser intenso en sistemas de baja dimensionalidad

En esta Tesis hemos ampliado el uso del método NLSP cuando el sistema se encuentra bajo radiación láser intensa. Con ello hemos demostrado que la técnica anteriormente descrita no es sólo válida para el estudio de la interacción entre partículas sino, también, para aquellas situaciones en las que un campo externo pueda modificar las propiedades físicas. El haz láser intenso aparece en las ecuaciones como un revestimiento de los potenciales de interacción. Esta técnica está basada en una teoría perturbativa empleada previamente en el estudio de estados atómicos [106-110]. En nuestro caso se traduce en dos centros de interacción Coulombiana desplazados en una cantidad relacionada con la intensidad del láser. Para poder hacer frente a este nuevo escenario hemos adaptado el método NLSP, tal y como se describe en la sección 3.1.2. Aunque en primera instancia parece más complejo, se obtienen expresiones compactas para las magnitudes de interés y los requisitos computacionales siguen siendo mínimos. Por todo ello la técnica del NLSP es muy adecuada para el estudio de los efectos de campos externos.

El lector puede acudir al **Capítulo 3** para una amplia explicación de los resultados. En resumen, hemos visto que en un QD con impurezas hidrogenoides y bajo la acción de un haz láser intenso dos regímenes para los estados energéticos pueden distinguirse. Por una parte, cuando la intensidad es baja, la energía de ligadura disminuye conforme la impureza es desplazada desde el centro hasta el borde del QD. Por otra parte, cuando la intensidad láser es alta, se observa el comportamiento opuesto

para la energía de ligadura. Así encontramos un punto de cruce en la energía que hemos demostrado que escala con el tamaño del QD. Además, hemos analizado el efecto de la polarización del láser, que implica un desplazamiento de este punto de cruce. Para entender mejor estos resultados proponemos un modelo 1D, que captura la física subyacente en este efecto. Para completar el estudio sugerimos un material semiconductor en el que este fenómeno podría ser observado. Nuestro modelo complementa una serie de estudios previos donde se habían detectado comportamientos similares [27, 29, 103]. Por otra parte, también hemos estudiado la absorción óptica en QW parabólicos bajo irradiación láser. Hemos visto que la energía del estado fundamental del excitón alcanza un régimen de saturación a medida que la intensidad láser aumenta, siendo el valor de saturación mayor para QWs con menor tamaño lateral. Este efecto puede detectarse en el espectro óptico debido al desplazamiento hacia mayores energías del pico de absorción.

Efecto Aharonov-Bohm en excitones confinados en un anillo cuántico bidimensional

El efecto AB [30] es uno de los fenómenos más sorprendentes propuestos en la segunda mitad del siglo XX en el contexto de la física de la materia condensada. Es un fenómeno puramente cuántico que no tiene análogo en la física clásica. El efecto AB explica por que las partículas cargadas se ven afectadas por un campo electromagéntico incluso cuando éste no actúa directamente sobre ellas. Esto se debe al papel fundamental del potencial vector. Aunque inicialmente se consideró simplemente como un artefacto matemático, en realidad tiene relevancia física puesto que introduce una fase en la función de onda de los electrones. En la geometría circular propuesta para la observación del efecto AB esto conduce a una diferencia de fase entre los dos posibles caminos que puede recorrer el haz de electrones. Esta diferencia de fase puede detectarse en las propiedades físicas del sistema como oscilaciones con el flujo magnético encerrado en el anillo. Una descripción detallada del efecto y de su observación experimental se puede encontrar en la sección 4.1. Este fenómeno se ha estudiado ampliamente en los sistemas de baja dimensionalidad. Los QRs son los mejores candidatos dada su geometría anular. En estos sistemas la interacción Coulombiana tiene un papel muy relevante dado que los electrones y huecos están restringidos a moverse en menores dimensiones espaciales. Estudios previos han demostrado que los excitones también son sensibles al potencial vector y que, por tanto, pueden observarse oscilaciones AB. Esto se conoce como el efecto AB para excitones (XAB) [31, 32].

En el **Capítulo 4** estudiamos la existencia del efecto XAB en QRs bidimensionales. Otros estudios han afirmado que el efecto XAB es dificil de observar en 2D y determinadas condiciones sobre el tipo de confinamiento deben cumplirse para que sea posible [159, 160, 162-165]. Sin embargo, nosotros hemos mostrado que el efecto es robusto en 2D y que pueden detectarse oscilaciones en la energía de ligadura de los excitones y en la fuerza de oscilador en función del flujo magnético. El efecto sería

observable incluso para anillos en los que su anchura sea similar a su radio. Hemos propuesto el uso de un potencial de confinamiento con una barrera repulsiva en el origen, de forma que contamos con una geometría no simplemente conexa. Este es el ingrediente fundamental para que el efecto persista en 2D. Estudios experimentales recientes muestran que este potencial de confinamiento describe adecuadamente los QRs fabricados [178]. En este trabajo consideramos que la interacción electrón-hueco es de corto alcance, lo que nos permite obtener la energía del excitón a partir de una ecuación matricial. Por tanto, los requisitos computacionales no son muy altos. Esperamos que el modelo que proponemos sea adecuado para el estudio de geometrías más realistas de QRs y permita entender los resultados recientes del efecto XAB en QRs.

Sistemas cuánticos en presencia de campos dependientes del tiempo

Para controlar los estados energéticos de los sistemas de baja dimensionalidad puede aplicarse un campo externo dependiente del tiempo [36]. Además, para el estudio de las propiedades de dispersión de un sistema se emplea habitualmente un potencial variable en el tiempo [187, 188]. El coeficiente de transmisión proporciona información sobre los estados ligados presentes en el sistema y sobre los canales abiertos a la conducción electrónica. En esta Tesis se han estudiado dos sistemas de baja dimensionalidad donde diversos fenómenos físicos pueden ser controlados y caracterizados por medio de un potencial oscilante en el tiempo. Hemos empleado el teorema de Floquet para obtener las magnitudes relevantes para nuestro estudio. Otros métodos que se han empleado habitualmente son las funciones de Green fuera del equilibrio o el formalismo de la matriz de dispersión [36].

Los principales resultados obtenidos en este estudio se encuentran explicados en detalle en el **Capítulo 5**. En primer lugar hemos visto la formación de BICs en QRs sometidos a un voltaje de puerta variable en el tiempo. Un BIC es un estado cuya energía se encuentra en el continuo pero que es normalizable. Fueron originalmente propuestos por von Neumman y Wigner [37], pero durante largo tiempo se consideraron una extrañeza matemática más que un estado físico realizable experimentalmente. Sin embargo, con los avances de la nanotecnología se vio que se podían obtener estados similares en sistemas de baja dimensionalidad tales como superredes [200, 201]. En la sección 5.2 se presentan más detalles sobre las características de estos estados y los diversos estudios que se han realizado sobre ellos. En esta Tesis proponemos un sistema físico donde la energía de los BICs puede controlarse por la frecuencia del campo externo aplicado. Gracias a dos potenciales de puerta asimétricos aplicados en los dos brazos del QR observamos la aparición de dos BICs. Estos se muestran en el perfil de transmisión como resonancias Fano [232]. Variando la frecuencia de la puerta AC podemos controlar la energía de estos exóticos estados. Hemos desarrollado todo el formalismo teórico necesario para obtener una expresión analítica del coeficiente de transmisión, lo cual es una importante ventaja para poder entender la formación de los BICs. En segundo lugar hemos estudiado

el KT [40] en presencia de un potencial oscilante en tiempo. Este fenómeno es una propiedad de la ecuación relativista de Dirac [38], y se conoce como túnel porque los electrones relativistas que inciden normalmente contra una barrera son totalmente transmitidos. En esta Tesis hemos obtenido las amplitudes de transmisión para electrones relativistas en 1D cuando la barrera varía con el tiempo. Se han analizado, en concreto, los casos de una barrera tipo δ, cuadrada y de anchura finita. Hemos comprobado que el KT se mantiene para barreras moduladas en el tiempo. Nuestros resultados son de especial interés para los recientes estudios realizados sobre el KT en grafeno [39, 240], ya que en este material y a baja energía los portadores de carga pueden describirse por la ecuación relativistica de Dirac.

Localización y efectos de tamaño finito en grafeno

El grafeno es un material que ha recibido un amplio interés en los últimos años dadas sus extraordinarias propiedades físicas [54]. Es un sistema puramente 2D por lo que es un candidato excepcional para el estudio de aquellos fenómenos físicos que sólo se manifiesten en sistemas bidimensionales. La localización de las funciones de onda debido a la presencia de desorden es bien conocido desde que Anderson propuso un modelo para el estudio de la difusión electrónica en potenciales aleatorios [41]. El grado de localización está relacionado con el carácter metálico o aislante del material. A partir del modelo de Anderson y de la teoría de escala [55], desarrollada unos años después, se ha podido explicar que en tres dimensiones (3D) se puede producir una transición metal-aislante (MIT) inducida por el desorden. En cambio, en sistemas 1D y 2D todos los estados están localizados en presencia de desorden, y el material sería aislante. En la sección 6.1.1 se puede encontrar un amplia explicación del modelo de Anderson y de la teoría de escala. El grafeno ha sido empleado recientemente como marco para comprobar las hipótesis de la teoría de escala [291, 292, 295-300, 304]. Las investigaciones han arrojado resultados muy diversos, y se ha abierto un apasionante debate en la comunidad científica acerca de las pecularidades del grafeno en cuanto a la localización de estados y una posible MIT. Las técnicas numéricas empleadas han sido muy variadas, incluyendo el método de la matriz de transferencia (TMM), estadísitica de los niveles energéticos y el análisis de la densidad de estados local. Algunos estudios han observado la presencia de bordes de movilidad [296, 298], estados críticos [297, 299, 300] y una transición entre estados localizados y extendidos [301]. Sin embargo, otros han encontrado que todos los estados están localizados y que el grafeno se comporta como un material 2D prototípico [294, 295].

En esta Tesis hemos realizado un estudio profundo sobre el fenómeno de localización en grafeno. Este análisis puede encontrarse en el **Capítulo 6**. En primer lugar, hemos propuesto una modificación del TMM para obtener las longitudes de localización en sistemas de tamaño finito en ambas direcciones espaciales. Esto ha permitido el estudio de muestras de grafeno cuadradas. El cálculo numérico

ha implicado el uso de ordenadores de alta capacidad dado que los resultados debían promediarse a un gran número de configuraciones para alcanzar la precisión deseada. Posteriormente se ha realizado un estudio de escala de tamaños finitos (FSS) con el fin de determinar el comportamiento de la longitud de localización en el límite termodinámico. A ciertas energías el sistema parece sufrir, aparentemente, una transición de estados localizados a extendidos en función del desorden. Sin embargo, cuando se evalúan las posibles caracerísiticas de la transición no se obtienen resultados satisfactorios. Esto nos indica que el sistema no experimenta realmente un MIT. Es más, se han realizado estudios en tamaños mayores y se ha encontrado que el comportamiento observado para la longitud de localización se revierte comparado con tamaños menores. Los fenómenos de localización observados son causados por los tamaños finitos que empleamos. Si acudiésemos a sistemas mayores veríamos que el grafeno muestra los resultados esperados para un sistema 2D. Nuestro trabajo permite entender la diversidad de resultados obtenidos por otros investigadores. Esperamos que el método empleado sea adecuado para el estudio de la localización por desorden en sitemas físicos similares.

Conclusiones

En esta Tesis se han desarrollado satisfactoriamente diversos modelos teóricos que se han implementado para el estudio de las propiedades físicas de sistemas de baja dimensionalidad. A la vista de las contribuciones obtenidas a lo largo del trabajo, se espera que los resultados de esta Tesis sean de relevancia para la comunidad científica, tal y como muestran las publicaciones que se enumeran al final del manuscrito. Además, una vez que se han alcanzado adecuadamente los objetivos de esta Tesis, esperamos que las teorías y técnicas numéricas elaboradas pueden ser aplicadas en otros problemas de la física de la materia condensada. En concreto, se podrían estudiar efectos no lineales en las propiedades ópticas de QDs [332], otros potenciales de confinamiento en QRs para ver sus efectos en la observación del efecto XAB, el fénomeno trinquete en QRs [190] y otros tipos de desorden en grafeno [335, 336].

List of abbreviations

1D	One-dimensional
2D	Two-dimensional
3D	Three-dimensional
AB	Aharonov-Bohm
AC	Armchair
AT	Anderson transition
BIC	Bound states in the continuum
DOS	Density of states
KT	Klein tunnelling
LDOS	Local density of states
MIT	Metal-insulator transition
NLSP	Non Local Separable Potential
QD	Quantum dot
QR	Quantum ring
QW	Quantum wire
TMM	Transfer-matrix method
XAB	Excitonic Aharonov-Bohm
ZZ	Zigzag

List of publications

Articles and Letters

1. **Modeling of Coulomb interaction in parabolic quantum wires**

   C. González-Santander and F. Domínguez-Adame

   Physica E **41**, 1645 (2009)

2. **Exciton states and optical absorption in quantum wires under laser radiation**

   C. González-Santander and F. Domínguez-Adame

   Physics Letters A **374**, 2259 (2010)

3. **Non-local separable solutions of two interacting particles in a harmonic trap**

   C. González-Santander and F. Domínguez-Adame

   Physics Letters A **375**, 314 (2011)

4. **Excitonic Aharonov-Bohm effect in a two-dimensional quantum ring**

   C. González-Santander, F. Domínguez-Adame and R. A. Roemer

   Physical Review B **84**, 235103 (2011)

5. **Bound states in the continuum driven by AC fields**

   C. González-Santander, P. A. Orellana and F. Domínguez-Adame

   EPL (Europhysics Letters) **102**, 17012 (2013)

6. **Binding energy of hydrogenic impurities in quantum dots under intense laser radiation**

   C. González-Santander, T. Apostolova and F. Domínguez-Adame

   Submitted (2013)

7. **Scattering of masless Dirac particles by oscillating barriers in one dimension**

   C. González-Santander, C. Hernández, E. Diez and F. Domínguez-Adame

   Submitted (2013)

8. **Localization and finite-size effects in graphene flakes**

   C. González-Santander, F. Domínguez-Adame and R. A. Roemer

   In preparation (2013)

Other publications

1. **Donor-bound electrons in quantum rings under magnetic fields**

   M. Amado, R. P. Lima, C. González-Santander and F. Domínguez- Adame.

   Physical Review B **76**, 071332 (2007)

2. **Electronic states in quantum rings based on narrow-gap III-V semiconductors**

   C. González-Santander and F. Domínguez-Adame

   Semiconductor Science and Technology **23**, 125008 (2008)

Conference contributions

1. **A solvable model of exciton states in a quantum wire**

   C. González-Santander and F. Domínguez- Adame

   Poster at *OECS11 - Optics of excitons in confine systems*, Madrid (Spain) 7-11 September 2009

2. **Modelización de la interacción coulombiana en nanoestructureas**

   C. González-Santander and F. Domínguez- Adame

   Oral contribution at *III Escuela de Nanostructuras*, Valparaíso (Chile) 12-15 January 2010

3. **Non-local potential approach of two interacting atoms in a harmonic trap**

   C. González-Santander and F. Domínguez- Adame

   Poster at *ECAMP10 - 10th European Conference on Atoms, Molecules and Photons*, Salamanca (Spain) 4-9 July 2010

4. **A solvable model of excitons states and optical absorption in a quantum wire**

   C. González-Santander and F. Domínguez- Adame

   Oral contribution at *CMD23 - 23rd General Conference on the Condensed Matter Division of the European Physical Society*, Warsaw (Poland) 30 August - 3 September 2010

5. **Excitonic Aharonov-Bohm effect in a two-dimensional quantum ring**

   C. González-Santander, F. Domínguez- Adame and R. A. Römer

   Poster at *OECS12 - Optics of excitons in confined systems*, Paris (France) 12-16 September 2011

6. **Efecto Aharonov-Bohm en excitons confinados en anillos cuánticos bidimensionales**

   C. González-Santander, F. Domínguez- Adame and R. A. Römer

   Poster at *XXXIII Reunión bienal de la Real Sociedad Española de Física*, Santander (Spain) 19-23 September 2011

7. **Localization of states in graphene-type lattices**

   C. González-Santander, F. Domínguez- Adame and R. A. Römer

   Poster at *8th International Workshop on Disordered Systems*, Benasque (Spain) 26 August - 1 September 2012

   Poster awarded by EPL (Europhysics Letters)

8. **Localization of states in graphene-type lattices**

   C. González-Santander, F. Domínguez- Adame and R. A. Römer

   Poster at *TNT 2012 Trends in Nanotechnology*, Madrid (Spain) 10-14 September 2012

   Poster awarded by Keren Prize to the best theoretical work in condensed matter physics

Bibliography

[1] D. Feng and G. Jin *Introduction to Condensed Matter Physics: Volume 1*. World Scientific Publishing Company (2005).

[2] N. Hall (Ed.) *Physics for future technology: Condensed matter*. IOP and EPSRC (2007).

[3] G. Gamov *Thirty Years that Shook Physics: The Story of Quantum Theory*. Dover Publications (1966).

[4] J. A. Martín Gago (Ed.) *Unidad diáctica Nanociencia y Nanotecnología. Entre la ciencia ficción del presente y la tecnlogía del futuro*. Fundación Española para la Ciencia y la Tecnología (2009) [in Spanish].

[5] J. Hubbard "Electron Correlations in Narrow Energy Bands", *Proceedings of the Royal Society of London A* **276**, 238–257 (1963).

[6] P. W. Anderson "Localized Magnetic States in Metals", *Physical Review* **124**, 41–53 (1961).

[7] N. F. Mott "The Basis of the Electron Theory of Metals, with Special Reference to the Transition Metals", *Proceedings of the Physical Society. Section A* **62**, 416 (1949).

[8] J. Kondo "Resistance Minimum in Dilute Magnetic Alloys", *Progress of Theoretical Physics* **32**, 37–49 (1964).

[9] B. W. Knight and G. A. Peterson "Solvable Three-Dimensional Lattice Models", *Physical Review* **132**, 1085–1092 (1963).

[10] H. Fock "Energy band calculations for a perfect crystal and a crystal with impurities using a nonlocal potential model", *physica status solidi (b)* **47**, 573–580 (1971).

[11] J. Reyes et al. "WannierMott excitons formed by electrons in a quantum wire and holes in a perpendicular quantum layer", *Physica E: Low-dimensional Systems and Nanostructures* **15**, 124 –130 (2002).

[12] M. Combescot and T. Guillet "Excitons in quantum wires", *European Physical Journal B* **34**, 9–24 (2003).

[13] E. W. S. Caetano et al. "Exciton confinement in InGaN/GaN cylindrical quantum wires", *Brazilian Journal of Physics* **34**, 702 –704 (2004).

[14] H. Hassanabadi et al. "Spectrum of Exciton in a Quantum Wire", *Few-Body Systems* **45**, 71–76 (2009).

[15] W. Huang and F. Jain "Reduced threshold current density due to excitonic optical gain in the presence of dislocations and surface states in tensile strained ZnCdSe quantum wire lasers", *Journal of Applied Physics* **81**, 6781 (1997).

[16] W. Huang and F. Jain "Enhanced optical gain in InGaNAlGaN quantum wire and quantum dot lasers due to excitonic transitions", *Journal of Applied Physics* **87**, 7354 (2000).

[17] J. Weiner et al. "Experiments and theory in cold and ultracold collisions", *Reviews of Modern Physics* **71**, 1–85 (1999).

[18] C. H. Greene "Universal insights from few-body land", *Physics Today* **63**, 40–45 (2010).

[19] T. Busch et al. "Two Cold Atoms in a Harmonic Trap", *Foundations of Physics* **28**, 549–559 (1998).

[20] J. H. Davies *The Physics of Low-dimensional Semiconductors: An Introduction*. Cambridge University Press (1998).

[21] W. B. Shockley *Nobel Lecture: Transistor Technology Evokes New Physics*. Nobelprize.org (1956).

[22] C. Waschke et al. "Coherent submillimeter-wave emission from Bloch oscillations in a semiconductor superlattice", *Physical Review Letters* **70**, 3319–3322 (1993).

[23] M. Ben Dahan et al. "Bloch Oscillations of Atoms in an Optical Potential", *Physical Review Letters* **76**, 4508–4511 (1996).

[24] K. von Klitzing *Nobel Lecture: The Quantized Hall Effect*. Nobelprize.org (1985).

[25] M. Combescot "Semiconductors in strong laser fields: from polariton to exciton optical Stark effect", *Physics Reports* **221**, 167 –249 (1992).

[26] H. S. Brandi, A. Latgé, and L. E. Oliveira "Dressed-band approach to laser-field effects in semiconductors and quantum-confined heterostructures", *Physical Review B* **64**, 035323 (2001).

[27] H. S. Brandi, A. Latgé, and L. E. Oliveira "Laser effects on donor states in low-dimensional semiconductor heterostructures", *Physical Review B* **70**, 153303 (2004).

[28] Q. Fanyao, A. L. A. Fonseca, and O. A. C. Nunes "Hydrogenic impurities in a quantum well wire in intense, high-frequency laser fields", *Physical Review B* **54**, 16405–16408 (1996).

[29] Q. Fanyao, A. L. A. Fonseca, and O. A. C. Nunes "Intense field effects on hydrogen impurities in quantum dots", *Journal of Applied Physics* **82**, 1236–1241 (1997).

[30] Y. Aharonov and D. Bohm "Significance of Electromagnetic Potentials in the Quantum Theory", *Physical Review* **115**, 485–491 (1959).

[31] A. Chaplik "Magnetoexcitons in quantum rings and antidots", *Pis'ma Zhurnal Éksperimental'noi i Teoreticheskoi Fiziki* **62**, 885–889 (1995) [JETP Letters **62**, 900–904 (1995)].

[32] R. A. Römer and M. E. Raikh "Aharonov-Bohm effect for an exciton", *Physical Review B* **62**, 7045–7049 (2000).

[33] B. J. Keay et al. "Dynamic Localization, Absolute Negative Conductance, and Stimulated, Multiphoton Emission in Sequential Resonant Tunneling Semiconductor Superlattices", *Physical Review Letters* **75**, 4102–4105 (1995).

[34] E. Haller et al. "Inducing Transport in a Dissipation-Free Lattice with Super Bloch Oscillations", *Physical Review Letters* **104**, 200403 (2010).

[35] E. Prada, P. San-Jose, and H. Schomerus "Quantum pumping in graphene", *Physical Review B* **80**, 245414 (2009).

[36] G. Platero and R. Aguado "Photon-assisted transport in semiconductor nanostructures", *Physics Reports* **395**, 1 –157 (2004).

[37] J. von Neumann and E. Wigner "Über merkwürdige diskrete Eigenwerte", *Physikalische Zeitschrift* **30**, 465 (1929) [in German].

[38] P. A. M. Dirac "The Quantum Theory of the Electron", *Proceedings of the Royal Society of London A* **117**, 610 (1928).

[39] M. Katsnelson, K. Novoselov, and A. Geim "Chiral tunnelling and the Klein paradox in graphene", *Nature Physics* **2**, 620–625 (2006).

[40] O. Klein "Die Reflexion von Elektronen an einem Potentialsprung nach der relativistischen Dynamik von Dirac", *Zeitschrift fr Physik* **53**, 157 (1929) [in German].

[41] P. W. Anderson "Absence of Diffusion in Certain Random Lattices", *Physical Review* **109**, 1492–1505 (1958).

[42] J.-L. Zhu et al. "D^- centers in spherical quantum dots", *Physical Review B* **46**, 7546–7550 (1992).

[43] N. Porras-Montenegro and S. T. Pérez-Merchancano "Hydrogenic impurities in GaAs-(Ga,Al)As quantum dots", *Physical Review B* **46**, 9780–9783 (1992).

[44] N. Porras-Montenegro, S. T. Perez-Merchancano, and A. Latge "Binding energies and density of impurity states in spherical GaAs-(Ga,Al)As quantum dots", *Journal of Applied Physics* **74**, 7624–7626 (1993).

[45] F. J. Ribeiro and A. Latgé "Impurities in a quantum dot: A comparative study", *Physical Review B* **50**, 4913–4916 (1994).

[46] J.-L. Zhu, J.-H. Zhao, and J.-J. Xiong "Neutral and negative donors in quantum dots", *Journal of Physics: Condensed Matter* **6**, 5097 (1994).

[47] C. Bose "Binding energy of impurity states in spherical quantum dots with parabolic confinement", *Journal of Applied Physics* **83**, 3089–3091 (1998).

[48] C.-Y. Hsieh, D.-S. Chuu, and C.-Y. Hsieh "Donor states in a multi-layered quantum dot", *Journal of Physics: Condensed Matter* **12**, 8641 (2000).

[49] J. Z. García, P. Pietiläinen, and P. Hyvönen "Donor centers and absorption spectra in quantum dots", *Physical Review B* **66**, 195324 (2002).

[50] J. H. M. Luis F. García and I. D. Mikhailov "Negatively Charged Donors in Flat Quantum Dots", *Brazilian Journal of Physics* **36**, 878 (2006).

[51] P. R. Wallace "The Band Theory of Graphite", *Physical Review* **71**, 622–634 (1947).

[52] K. S. Novoselov et al. "Electric Field Effect in Atomically Thin Carbon Films", *Science* **306**, 666–669 (2004).

[53] A. Geim *Nobel Lecture: Random Walk to Graphene*. Nobelprize.org (2010).

[54] A. H. Castro Neto et al. "The electronic properties of graphene", *Reviews of Modern Physics* **81**, 109–162 (2009).

[55] E. Abrahams et al. "Scaling Theory of Localization: Absence of Quantum Diffusion in Two Dimensions", *Physical Review Letters* **42**, 673–676 (1979).

[56] C. Bertulani *Nuclear Physics in a Nutshell*. Princeton University Press (2007).

[57] Y. Yamaguchi "Two-Nucleon Problem When the Potential Is Nonlocal but Separable. I", *Physical Review* **95**, 1628–1634 (1954).

[58] F. Perey and B. Buck "A non-local potential model for the scattering of neutrons by nuclei", *Nuclear Physics* **32**, 353 –380 (1962).

[59] M. Glasser "A class of interface state models. I", *Surface Science* **64**, 141 –156 (1977).

[60] F. Domínguez-Adame et al. "Non-local separable potential approach to multicentre interactions", *Molecular Physics* **74**, 1065–1069 (1991).

[61] Y. Yamaguchi and Y. Yamaguchi "Two-Nucleon Problem When the Potential Is Nonlocal but Separable. II", *Physical Review* **95**, 1635–1643 (1954).

[62] E. Maciá and F. Domnguez-Adame "Three-dimensional effects on the electronic structure of quasiperiodic systems", *Physica B: Condensed Matter* **216**, 53 –62 (1995).

[63] F. Domínguez-Adame, E. Diez, and A. Sánchez "Three-dimensional effects on extended states in disordered models of polymers", *Physical Review B* **51**, 8115–8124 (1995).

[64] F. Domínguez-Adame and M. González "A generalized Dirac-Kronig-Penney model with nonlocal separable potentials", *Physica B: Condensed Matter* **176**, 180 –188 (1992).

[65] S. Laux, D. Frank, and F. Stern "Quasi-one-dimensional electron states in a split-gate GaAs/AlGaAs heterostructure", *Surface Science* **196**, 101 –106 (1988).

[66] C. Sikorski and U. Merkt "Spectroscopy of electronic states in InSb quantum dots", *Physical Review Letters* **62**, 2164–2167 (1989).

[67] F. M. Peeters "Magneto-optics in parabolic quantum dots", *Physical Review B* **42**, 1486–1487 (1990).

[68] W. Que "Excitons in quantum dots with parabolic confinement", *Physical Review B* **45**, 11036–11041 (1992).

[69] T. Demel et al. "Far-infrared response of one-dimensional electronic systems in single- and two-layered quantum wires", *Physical Review B* **38**, 12732–12735 (1988).

[70] G. Y. Hu and R. F. O'Connell "Electron-electron interactions in quasi-one-dimensional electron systems", *Physical Review B* **42**, 1290–1295 (1990).

[71] S. Glutsch and F. Bechstedt "Effects of the Coulomb interaction on the optical spectra of quantum wires", *Physical Review B* **47**, 4315–4326 (1993).

[72] T. Stöferle et al. "Molecules of Fermionic Atoms in an Optical Lattice", *Physical Review Letters* **96**, 030401 (2006).

[73] S López and F Domínguez-Adame "Non-local potential approach to the ground state of confined excitons in quantum dots", *Semiconductor Science and Technology* **17**, 227 (2002).

[74] R. P. A. Lima, M Amado, and F Domínguez-Adame "A solvable model of hydrogenic impurities in quantum dots", *Nanotechnology* **19**, 135402 (2008).

[75] S. Glutsch and F. Bechstedt "Interplay of Coulomb attraction and spatial confinement in the optical susceptibility of quantum wires", *Physical Review B* **47**, 6385–6389 (1993).

[76] F. Rossi et al. "Theory of excitonic confinement in semiconductor quantum wires", *Journal of Physics: Condensed Matter* **11**, 5969 (1999).

[77] F. Rossi, G. Goldoni, and E. Molinari "Shape-Independent Scaling of Excitonic Confinement in Realistic Quantum Wires", *Physical Review Letters* **78**, 3527–3530 (1997).

[78] M. H. Degani and O. Hipólito "Exciton binding energy in quantum-well wires", *Physical Review B* **35**, 9345–9348 (1987).

[79] R. Rinaldi et al. "Exciton Binding Energy in GaAs V-Shaped Quantum Wires", *Physical Review Letters* **73**, 2899–2902 (1994).

[80] Y. Sidor, B. Partoens, and F. M. Peeters "Exciton in a quantum wire in the presence of parallel and perpendicular magnetic fields", *Physical Review B* **71**, 165323 (2005).

[81] S. Benner and H. Haug "Influence of external electric and magnetic fields on the excitonic absorption spectra of quantum-well wires", *Physical Review B* **47**, 15750–15754 (1993).

[82] S. Bednarek et al. "Effective interaction for charge carriers confined in quasi-one-dimensional nanostructures", *Physical Review B* **68**, 045328 (2003).

[83] G. Bastard "Hydrogenic impurity states in a quantum well: A simple model", *Physical Review B* **24**, 4714–4722 (1981).

[84] G. Bastard "Hydrogenic impurity states in a quantum well", *Surface Science* **113**, 165 –169 (1982).

[85] G. Bastard et al. "Variational calculations on a quantum well in an electric field", *Physical Review B* **28**, 3241–3245 (1983).

[86] M. Abramowitz and I. Stegun *Handbook of Mathematical Functions with Formulas, Graphs, and Mathematical Tables*. Courier Dover Publications (1972).

[87] D. Chruściński "Quantum damped oscillator II: Batemans Hamiltonian vs. 2D parabolic potential barrier", *Annals of Physics* **321**, 840 –853 (2006).

[88] M. Greiner et al. "Quantum phase transition from a superfluid to a Mott insulator in a gas of ultracold atoms", *Nature* **415**, 39–44 (2002).

[89] C. Chin et al. "Feshbach resonances in ultracold gases", *Review of Modern Physics.* **82**, 1225–1286 (2010).

[90] M. Köhl et al. "Strongly interacting atoms and molecules in a 3D optical lattice", *Journal of Physics B: Atomic, Molecular and Optical Physics* **39**, S47 (2006).

[91] E. Tiesinga et al. "Interacting atoms under strong quantum confinement", *Physical Review A* **61**, 063416 (2000).

[92] D. Blume and C. H. Greene "Fermi pseudopotential approximation: Two particles under external confinement", *Physical Review A* **65**, 043613 (2002).

[93] I. Demkov and V. Ostrovskiĭ *Zero-range potentials and their applications in atomic physics*. Plenum Press (1988).

[94] W. Ketterle "Nobel lecture: When atoms behave as waves: Bose-Einstein condensation and the atom laser", *Reviews of Modern Physics* **74**, 1131–1151 (2002).

[95] O. Morsch and M. Oberthaler "Dynamics of Bose-Einstein condensates in optical lattices", *Reviews of Modern Physics* **78**, 179–215 (2006).

[96] I. Bloch "Ultracold quantum gases in optical lattices", *Nature Physics* **1**, 23–30 (2005).

[97] E. C. de Oliveira "Green's functions of the Schrödinger equation for the simplest systems", *Revista Brasileira de Física* **3**, 697 (1979).

[98] E. L. Bolda, E. Tiesinga, and P. S. Julienne "Effective-scattering-length model of ultracold atomic collisions and Feshbach resonances in tight harmonic traps", *Physical Review A* **66**, 013403 (2002).

[99] T. Gherghetta and Y. Nambu "Nonlocal separable solutions of the inverse scattering problem", *International Journal of Modern Physics A* **8**, 3163 (1993).

[100] V. Bakhrakh and S. Vetchinkin "Green's functions of the Schrödinger equation for the simplest systems", *Theoretical and Mathematical Physics* **6**, 283–290 (1971).

[101] R. Lima and M. Amado "Electronic states of on- and off-center donors in quantum rings of finite width", *Journal of Luminescence* **128**, 858 –861 (2008) [Proceedings of the 16th International Conference on Dynamical Processes in Excited States of Solids].

[102] G. Morgan et al. "Optical characterization of GaAs quantum wire microcrystals", *Solid State Communications* **80**, 235 –238 (1991).

[103] U. Yesilgul et al. "Hydrogenic impurities in quantum dots under intense high-frequency laser field", *Physica B: Condensed Matter* **406**, 1441 –1444 (2011).

[104] H. Sari et al. "Optical transitions in quantum well wires under intense laser radiation", *Physics Letters A* **319**, 211 –216 (2003).

[105] E. Kasapoglu et al. "Exciton absorption in quantum-well wires under the electric field", *Physica E: Low-dimensional Systems and Nanostructures* **16**, 237 –243 (2003).

[106] H. Kramers *Collected Scientific Papers*. North-Holland Pub. Co. (1956).

[107] W. C. Henneberger "Perturbation Method for Atoms in Intense Light Beams", *Physical Review Letters* **21**, 838–841 (1968).

[108] M. Gavrila and J. Z. Kamiński "Free-Free Transitions in Intense High-Frequency Laser Fields", *Physical Review Letters* **52**, 613–616 (1984).

[109] M. Pont et al. "Dichotomy of the Hydrogen Atom in Superintense, High-Frequency Laser Fields", *Physical Review Letters* **61**, 939–942 (1988).

[110] F Ehlotzky "Positronium decay in intense high frequency laser fields", *Physics Letters A* **126**, 524 –527 (1988).

[111] V. Kraĭnov et al. *Radiative processes in atomic physics*. Wiley (1997).

[112] C. A. S. Lima and L. C. M. Miranda "Atoms in superintense laser fields", *Physical Review A* **23**, 3335–3337 (1981).

[113] A. N. Forshaw and D. M. Whittaker "Optical absorption of wide quantum wires", *Physical Review B* **54**, 8794–8798 (1996).

[114] G. Bastard *Wave mechanics applied to semiconductor heterostructures*. Les Éditions de Physique (1988).

[115] F. Vas'ko and A. Kuznecov *Electronic States and Optical Transitions in Semiconductor Heterostructures*. Springer-Verlag GmbH (1999).

[116] D. Lindley "*Landmarks:* Ghostly Influence of Distant Magnetic Field", *Physical Review Focus* **28**, 4 (2011).

[117] A. M. Fischer. "Disorder and interaction in graphene and other quantum systems". PhD thesis. University of Warwick, 2011.

[118] W Ehrenberg and R. E. Siday "The Refractive Index in Electron Optics and the Principles of Dynamics", *Proceedings of the Royal Society of London B* **62**, 8 (1949).

[119] Y. Aharonov and D. Bohm "Further Considerations on Electromagnetic Potentials in the Quantum Theory", *Physical Review* **123**, 1511–1524 (1961).

[120] R. G. Chambers "Shift of an Electron Interference Pattern by Enclosed Magnetic Flux", *Physical Review Letters* **5**, 3–5 (1960).

[121] G. Möllenstedt and W. Bayh "Messung der kontinuierlichen Phasenschiebung von Elektronenwellen im kraftfeldfreien Raum durch das magnetische Vektorpotential einer Luftspule", *Die Naturwissenschaften* **49**, 81 (1962) [in German].

[122] A. Tonomura et al. "Observation of Aharonov-Bohm Effect by Electron Holography", *Physical Review Letters* **48**, 1443–1446 (1982).

[123] A. Tonomura et al. "Evidence for Aharonov-Bohm effect with magnetic field completely shielded from electron wave", *Physical Review Letters* **56**, 792–795 (1986).

[124] N. Osakabe et al. "Experimental confirmation of Aharonov-Bohm effect using a toroidal magnetic field confined by a superconductor", *Physical Review A* **34**, 815–822 (1986).

[125] N. Byers and C. N. Yang "Theoretical Considerations Concerning Quantized Magnetic Flux in Superconducting Cylinders", *Physical Review Letters* **7**, 46–49 (1961).

[126] F. Bloch "Simple Interpretation of the Josephson Effect", *Physical Review Letters* **21**, 1241–1243 (1968).

[127] M. Büttiker et al. "Generalized many-channel conductance formula with application to small rings", *Physical Review B* **31**, 6207–6215 (1985).

[128] Y. Gefen, Y. Imry, and M. Y. Azbel "Quantum Oscillations and the Aharonov-Bohm Effect for Parallel Resistors", *Physical Review Letters* **52**, 129–132 ().

[129] R. A. Webb et al. "Observation of h/e Aharonov-Bohm Oscillations in Normal-Metal Rings", *Physical Review Letters* **54**, 2696–2699 (1985).

[130] H.-F. Cheung et al. "Persistent currents in small one-dimensional metal rings", *Physical Review B* **37**, 6050–6062 (1988).

[131] B. S. Deaver and W. M. Fairbank "Experimental Evidence for Quantized Flux in Superconducting Cylinders", *Physical Review Letters* **7**, 43–46 (1961).

[132] W. A. Little and R. D. Parks "Observation of Quantum Periodicity in the Transition Temperature of a Superconducting Cylinder", *Physical Review Letters* **9**, 9–12 (1962).

[133] R. D. Parks and W. A. Little "Fluxoid Quantization in a Multiply-Connected Superconductor", *Physical Review* **133**, A97–A103 (1964).

[134] A. Lorke et al. "Electronic Structure of nanometer-Size Quantum Dots and Quantum Rings", *Microelectronic Engineering* **47**, 95– (1999).

[135] A. Lorke et al. "Spectroscopy of Nanoscopic Semiconductor Rings", *Physical Review Letters* **84**, 2223–2226 (2000).

[136] P. Pietilinen and T. Chakraborty "Interacting-electron states and the persistent current in a quantum ring", *Solid State Communications* **87**, 809 –812 (1993).

[137] A. Bruno-Alfonso and A. Latgé "Semiconductor quantum rings: Shallow-donor levels", *Physical Review B* **61**, 15887–15894 (2000).

[138] Z. Barticevic, M. Pacheco, and A. Latgé "Quantum rings under magnetic fields: Electronic and optical properties", *Physical Review B* **62**, 6963–6966 (2000).

[139] A. Puente and L. Serra "Ground state and far-infrared absorption of two-electron rings in a magnetic field", *Physical Review B* **63**, 125334 (2001).

[140] J. Planelles, W. Jaskólski, and J. I. Aliaga "Energy structure of quantum rings in a magnetic field", *Physical Review B* **65**, 033306 (2001).

[141] J. I. Climente, J. Planelles, and W. Jaskólski "Magneto-optical transitions in nanoscopic rings", *Physical Review B* **68**, 075307 (2003).

[142] O. Voskoboynikov et al. "Energy states and magnetization in nanoscale quantum rings", *Physical Review B* **66**, 155306 (2002).

[143] Z. Barticevic, G. Fuster, and M. Pacheco "Effect of an electric field on the Bohm-Aharonov oscillations in the electronic spectrum of a quantum ring", *Physical Review B* **65**, 193307 (2002).

[144] A. Bruno-Alfonso and A. Latgé "Aharonov-Bohm oscillations in a quantum ring: Eccentricity and electric-field effects", *Physical Review B* **71**, 125312 (2005).

[145] H. Hu, J.-L. Zhu, and J.-J. Xiong "Energy levels and far-infrared spectroscopy for two electrons in a nanoscopic semiconductor ring", *Physical Review B* **62**, 16777–16783 (2000).

[146] J.-L. Zhu, Z. Dai, and X. Hu "Two electrons in one-dimensional nanorings: Exact solutions and interaction energies", *Physical Review B* **68**, 045324 (2003).

[147] R. Warburton et al. "Optical emission from a charge-tunable quantum ring", *Nature* **405**, 926–929 (2000).

[148] D. Haft et al. "Magneto-optical properties of ring-shaped self-assembled InGaAs quantum dots", *Physica E: Low-dimensional Systems and Nanostructures* **13**, 165 –169 (2002).

[149] E. Ribeiro et al. "Aharonov-Bohm Signature for Neutral Polarized Excitons in Type-II Quantum Dot Ensembles", *Physical Review Letters* **92**, 126402 (2004).

[150] I. R. Sellers et al. "Aharonov-Bohm Excitons at Elevated Temperatures in Type-II $\mathrm{ZnTe/ZnSe}$ Quantum Dots", *Physical Review Letters* **100**, 136405 (2008).

[151] M. D. Teodoro et al. "Aharonov-Bohm Interference in Neutral Excitons: Effects of Built-In Electric Fields", *Physical Review Letters* **104**, 086401 (2010).

[152] M. Bayer et al. "Hidden symmetries in the energy levels of excitonic 'artificial atoms'", *Nature* **405**, 923–926 (2000).

[153] M. Bayer et al. "Optical Detection of the Aharonov-Bohm Effect on a Charged Particle in a Nanoscale Quantum Ring", *Physical Review Letters* **90**, 186801 (2003).

[154] F. Ding et al. "Gate controlled Aharonov-Bohm-type oscillations from single neutral excitons in quantum rings", *Physical Review B* **82**, 075309 (2010).

[155] R. A. Römer and M. E. Raikh "Aharonov-Bohm Oscillations in the Exciton Luminescence from a Semiconductor Nanoring", *physica status solidi (b)* **221**, 535–539 (2000).

[156] K. Maschke et al. "Coherent Dynamics of magnetoexcitons in semiconductor nanorings", *European Physical Journal B* **19**, 599 (2001).

[157] T. V. Shahbazyan, I. E. Perakis, and M. E. Raikh "Spin Correlations in Nonlinear Optical Response: Light-Induced Kondo Effect", *Physical Review Letters* **84**, 5896–5899 (2000).

[158] A. M. Fischer et al. "Exciton Storage in a Nanoscale Aharonov-Bohm Ring with Electric Field Tuning", *Physical Review Letters* **102**, 096405 (2009).

[159] H. Hu et al. "Size effects on excitons in nano-rings", *Journal of Physics: Condensed Matter* **12**, 9145 (2000).

[160] H. Hu et al. "Aharonov-Bohm effect of excitons in nanorings", *Physical Review B* **63**, 195307 (2001).

[161] F. Palmero et al. "Aharonov-Bohm effect for an exciton in a finite-width nanoring", *Physical Review B* **72**, 075343 (2005).

[162] J. Song and S. E. Ulloa "Magnetic field effects on quantum ring excitons", *Physical Review B* **63**, 125302 (2001).

[163] I. Galbraith, F. Braid, and R. Warburton "Magneto-Excitons in Semiconductor Quantum Rings", *physica status solidi (a)* **190**, 781–785 (2002).

[164] M. Grochol, F. Grosse, and R. Zimmermann "Optical exciton Aharonov-Bohm effect, persistent current, and magnetization in semiconductor nanorings of type I and II", *Physical Review B* **74**, 115416 (2006).

[165] M. Grochol and R. Zimmermann "Noncircular semiconductor nanorings of types I and II: Emission kinetics in the excitonic Aharonov-Bohm effect", *Physical Review B* **76**, 195326 (2007).

[166] A. V. Maslov and D. S. Citrin "Enhancement of the Aharonov-Bohm effect of neutral excitons in semiconductor nanorings with an electric field", *Physical Review B* **67**, 121304 (2003).

[167] B. Li and F. M. Peeters "Tunable optical Aharonov-Bohm effect in a semiconductor quantum ring", *Physical Review B* **83**, 115448 (2011).

[168] A. O. Govorov et al. "Polarized excitons in nanorings and the optical Aharonov-Bohm effect", *Physical Review B* **66**, 081309 (2002).

[169] L. G. G. V. Dias da Silva, S. E. Ulloa, and A. O. Govorov "Impurity effects on the Aharonov-Bohm optical signatures of neutral quantum-ring magnetoexcitons", *Physical Review B* **70**, 155318 (2004).

[170] L. G. G. V. Dias da Silva, S. E. Ulloa, and T. V. Shahbazyan "Polarization and Aharonov-Bohm oscillations in quantum-ring magnetoexcitons", *Physical Review B* **72**, 125327 (2005).

[171] Z. Barticevic et al. "Coulomb-interaction effects on the electronic structure of radially polarized excitons in nanorings", *Physical Review B* **73**, 165311 (2006).

[172] P. Hui and Z. Jia-Lin "Impurity effects on energy levels and far-infrared spectra of nanorings", *Journal of Physics: Condensed Matter* **15**, 7287 (2003).

[173] P. T. T. Meier and S. W. Koch "Linear and nonlinear optical properties of semiconductor nanorings with magnetic field and disorder -Influence on excitons and biexcitons", *European Physical Journal B* **22**, 249 (2001).

[174] W.-C. Tan and J. C. Inkson "Electron states in a two-dimensional ring - an exactly soluble model", *Semiconductor Science and Technology* **11**, 1635 (1996).

[175] V. M. Kovalev and A. V. Chaplik "AharonovBohm Effect for Plasmons in a Finite Width Quantum Ring", *Pis'ma Zhurnal Éksperimental'noi i Teoreticheskoi Fiziki* **90**, 753–755 (2009) [JETP Letters, **90** 679–682 (2009)].

[176] A. Emperador et al. "Far-infrared spectroscopy of nanoscopic InAs rings", *Physical Review B* **62**, 4573–4577 (2000).

[177] J. Simonin et al. "Single-particle electronic spectra of quantum rings: A comparative study", *Physical Review B* **70**, 205305 (2004).

[178] M. D. Teodoro et al. "In-plane mapping of buried InGaAs quantum rings and hybridization effects on the electronic structure", *Journal of Applied Physics* **112**, 014319 (2012).

[179] B Szafran, J Adamowski, and S Bednarek "Effect of the repulsive core on the exciton spectrum in a quantum ring", *Journal of Physics: Condensed Matter* **14**, 73 (2002).

[180] A. Govorov et al. "Excitons in quantum-ring structures in a magnetic field: optical properties and persistent currents", *Physica E: Low-dimensional Systems and Nanostructures* **13**, 297 –300 (2002).

[181] E. H. Lieb and W. Liniger "Exact Analysis of an Interacting Bose Gas. I. The General Solution and the Ground State", *Physical Review* **130**, 1605–1616 (1963).

[182] Z. Dai and J.-L. Zhu "Dimensional effects on exciton states in nanorings", *Journal of Physics: Condensed Matter* **19**, 346202 (2007).

[183] C. González-Santander, F. Domínguez-Adame, and R. A. Römer "Excitonic Aharonov-Bohm effect in a two-dimensional quantum ring", *Physical Review B* **84**, 235103 (2011).

[184] P. K. Tien and J. P. Gordon "Multiphoton Process Observed in the Interaction of Microwave Fields with the Tunneling between Superconductor Films", *Physical Review* **129**, 647–651 (1963).

[185] M. Wagner "Photon-assisted transmission through an oscillating quantum well: A transfer-matrix approach to coherent destruction of tunneling", *Physical Review A* **51**, 798–808 (1995).

[186] P. F. Bagwell and R. K. Lake "Resonances in transmission through an oscillating barrier", *Physical Review B* **46**, 15329–15336 (1992).

[187] G. Burmeister and K. Maschke "Scattering by time-periodic potentials in one dimension and its influence on electronic transport", *Physical Review B* **57**, 13050–13060 (1998).

[188] W. Li and L. E. Reichl "Floquet scattering through a time-periodic potential", *Physical Review B* **60**, 15732–15741 (1999).

[189] D. F. Martinez and L. E. Reichl "Transmission properties of the oscillating δ-function potential", *Physical Review B* **64**, 245315 (2001).

[190] S. Kohler, J. Lehmann, and P. Hnggi "Driven quantum transport on the nanoscale", *Physics Reports* **406**, 379 –443 (2005).

[191] C. E. Creffield "Quantum Control and Entanglement using Periodic Driving Fields", *Phys. Rev. Lett.* **99**, 110501 (2007).

[192] J. H. Shirley "Solution of the Schrödinger Equation with a Hamiltonian Periodic in Time", *Phys. Rev.* **138**, B979–B987 (1965).

[193] A.-P. Jauho, N. S. Wingreen, and Y. Meir "Time-dependent transport in interacting and noninteracting resonant-tunneling systems", *Phys. Rev. B* **50**, 5528–5544 (1994).

[194] G. Burmeister and K. Maschke "Bound states revealed by time-periodic perturbing scattering potentials", *Physical Review B* **59**, 4612–4614 (1999).

[195] T. A. Weber and D. L. Pursey "Continuum bound states", *Physical Review A* **50**, 4478–4487 (1994).

[196] F. H. Stillinger and D. R. Herrick "Bound states in the continuum", *Physical Review A* **11**, 446–454 (1975).

[197] A. K. Jain and C. S. Shastry "Bound states in the continuum for separable nonlocal potentials", *Physical Review A* **12**, 2237–2238 (1975).

[198] H. Friedrich and D. Wintgen "Physical realization of bound states in the continuum", *Physical Review A* **31**, 3964–3966 (1985).

[199] H. Friedrich and D. Wintgen "Interfering resonances and bound states in the continuum", *Physical Review A* **32**, 3231–3242 (1985).

[200] D. R. Herrick "Construction of bound states in the continuum for epitaxial heterostructure superlattices", *Physica B+C* **85**, 44 –50 (1976).

[201] F. Stillinger "Potentials supporting positive-energy eigenstates and their application to semiconductor heterostructures", *Physica B+C* **85**, 270 –276 (1976).

[202] F. Capasso et al. "Observation of an electronic bound state above a potential well", *Nature* **358**, 565–567 (1992).

[203] Y. Plotnik et al. "Experimental Observation of Optical Bound States in the Continuum", *Physical Review Lett.* **107**, 183901 (2011).

[204] A. Albo, D. Fekete, and G. Bahir "Electronic bound states in the continuum above (Ga,In)(As,N)/(Al,Ga)As quantum wells", *Physical Review B* **85**, 115307 (2012).

[205] D. C. Marinica, A. G. Borisov, and S. V. Shabanov "Bound States in the Continuum in Photonics", *Physical Review Lett.* **100**, 183902 (2008).

[206] E. N. Bulgakov and A. F. Sadreev "Bound states in the continuum in photonic waveguides inspired by defects", *Physical Review B* **78**, 075105 (2008).

[207] E. N. Bulgakov and A. F. Sadreev "Resonance induced by a bound state in the continuum in a two-level nonlinear Fano-Anderson model", *Physical Review B* **80**, 115308 (2009).

[208] N. Moiseyev "Suppression of Feshbach Resonance Widths in Two-Dimensional Waveguides and Quantum Dots: A Lower Bound for the Number of Bound States in the Continuum", *Physical Review Lett.* **102**, 167404 (2009).

[209] N Prodanović, V Milanović, and J Radovanović "Photonic crystals with bound states in continuum and their realization by an advanced digital grading method", *Journal of Physics A: Mathematical and Theoretical* **42**, 415304 (2009).

[210] E. N. Bulgakov and A. F. Sadreev "Bound states in photonic Fabry-Perot resonator with nonlinear off-channel defects", *Physical Review B* **81**, 115128 (2010).

[211] S. Longhi "Bound states in the continuum in a single-level Fano-Anderson model", *European Physical Journal B* **57**, 45–51 (2007).

[212] H. Nakamura et al. "Quasibound States in the Continuum in a Two Channel Quantum Wire with an Adatom", *Physical Review Lett.* **99**, 210404 (2007).

[213] J. M. Zhang, D. Braak, and M. Kollar "Bound States in the Continuum Realized in the One-Dimensional Two-Particle Hubbard Model with an Impurity", *Physical Review Lett.* **109**, 116405 (2012).

[214] M Robnik "A simple separable Hamiltonian having bound states in the continuum", *Journal of Physics A: Mathematical and General* **19**, 3845 (1986).

[215] A. F. Sadreev, E. N. Bulgakov, and I. Rotter "Bound states in the continuum in open quantum billiards with a variable shape", *Physical Review B* **73**, 235342 (2006).

[216] D. W. L. Sprung et al. "Continuum bound states as surface states of a finite periodic system", *Physical Review B* **67**, 085318 (2003).

[217] M. I. Molina, A. E. Miroshnichenko, and Y. S. Kivshar "Surface Bound States in the Continuum", *Physical Review Lett.* **108**, 070401 (2012).

[218] J. U. Nöckel "Resonances in quantum-dot transport", *Physical Review B* **46**, 15348–15356 (1992).

[219] G. Ordonez, K. Na, and S. Kim "Bound states in the continuum in quantum-dot pairs", *Physical Review A* **73**, 022113 (2006).

[220] A. Sadreev and T. Babushkina "Two-electron bound states in a continuum in quantum dots", *JETP Letters* **88**, 312–317 (2008).

[221] G. Cattapan and P. Lotti "Bound states in the continuum in two-dimensional serial structures", *European Physical Journal B* **66**, 517–523 (2008).

[222] G. Rajput, P. K. Ahluwalia, and K. C. Sharma "Partial swapping of Fano resonance and bound states in continuum in a correlated double-quantum-dot system", *EPL (Europhysics Letters)* **94**, 17003 (2011).

[223] R. Žitko, J. Mravlje, and K. Haule "Ground State of the Parallel Double Quantum Dot System", *Physical Review Lett.* **108**, 066602 (2012).

[224] E. Bulgakov and A. Sadreev "Formation of bound states in the continuum for a quantum dot with variable width", *Physical Review B* **83**, 235321 (2011).

[225] J. W. González et al. "Bound states in the continuum in graphene quantum dot structures", *EPL (Europhysics Letters)* **91**, 66001 (2010).

[226] D. Dutta and P. Roy "Bound states in continuum in effective-mass models", *EPL (Europhysics Letters)* **89**, 20007 (2010).

[227] J Munárriz, F Domínguez-Adame, and A. V. Malyshev "Toward graphene-based quantum interference devices", *Nanotechnology* **22**, 365201 (2011).

[228] J Munárriz et al. "Graphene nanoring as a tunable source of polarized electrons", *Nanotechnology* **23**, 205202 (2012).

[229] M Buttiker "Characteristic Potentials For Mesoscopic Rings Threaded By An Aharonov-Bohm Flux", *Physica Scripta* **54**, 104–110 (1994) [16th Nordic Semiconductor Meeting, Laugarvatn, Iceland, Jun 12-15, 1994].

[230] Z. Y. Zeng, F. Claro, and A. Pérez "Fano resonances and Aharonov-Bohm effects in transport through a square quantum dot molecule", *Physical Review B* **65**, 085308 (2002).

[231] B. Kubala and J. König "Flux-dependent level attraction in double-dot Aharonov-Bohm interferometers", *Physical Review B* **65**, 245301 (2002).

[232] U. Fano "Effects of Configuration Interaction on Intensities and Phase Shifts", *Physical Review* **124**, 1866–1878 (1961).

[233] M. Büttiker, Y. Imry, and M. Y. Azbel "Quantum oscillations in one-dimensional normal-metal rings", *Physical Review A* **30**, 1982–1989 (1984).

[234] T. Taniguchi and M. Büttiker "Friedel phases and phases of transmission amplitudes in quantum scattering systems", *Physical Review B* **60**, 13814–13823 (1999).

[235] A. E. Miroshnichenko, S. Flach, and Y. S. Kivshar "Fano resonances in nanoscale structures", *Reviews of Modern Physics* **82**, 2257–2298 (2010).

[236] B. Thaller *The Dirac Equation*. Springer-Verlag (1992).

[237] F. Sauter "Über das Verhalten eines Elektrons im homogenen elektrischen Feld nach der relativistischen Theorie Diracs", *Zeitschrift für Physik* **69**, 742 (1931) [in German].

[238] F. Hund "Materieerzeugung im anschaulichen und im gequantelten Wellenbild der Materie", *Zeitschrift für Physik* **117**, 1 (1941) [in German].

[239] A. Calogeracos and N. Dombey "History and physics of the Klein paradox", *Contemporary Physics* **40**, 313–321 (1999).

[240] M. I. Katsnelson *Graphene. Carbon in two dimensions*. Cambridge University Press (2012).

[241] C. W. J. Beenakker "*Colloquium* : Andreev reflection and Klein tunneling in graphene", *Reviews of Modern Physics* **80**, 1337–1354 (2008).

[242] P. Allain and J. Fuchs "Klein tunneling in graphene: optics with massless electrons", *European Physical Journal B* **83**, 301–317 (2011).

[243] J. M. Cerveró and E. Díez "The Massless Dirac Equation in the Refrigerator", *International Journal of Theoretical Physics* **50**, 2134–2143 (2011).

[244] N. Stander, B. Huard, and D. Goldhaber-Gordon "Evidence for Klein Tunneling in Graphene p-n Junctions", *Physical Review Letters* **102**, 026807 (2009).

[245] A. F. Young and P. Kim "Quantum interference and Klein tunnelling in graphene heterojunctions", *Nature Physics* **5**, 222–226 (2009).

[246] B. Trauzettel, Y. M. Blanter, and A. F. Morpurgo "Photon-assisted electron transport in graphene: Scattering theory analysis", *Physical Review B* **75**, 035305 (2007).

[247] M. A. Zeb, K. Sabeeh, and M. Tahir "Chiral tunneling through a time-periodic potential in monolayer graphene", *Physical Review B* **78**, 165420 (2008).

[248] W.-T. Lu et al. "Fano-type resonance through a time-periodic potential in graphene", *Journal of Applied Physics* **111**, 103717 (2012).

[249] S. E. Savel'ev, W. Häusler, and P. Hänggi "Current Resonances in Graphene with Time-Dependent Potential Barriers", *Physical Review Letters* **109**, 226602 (2012).

[250] B. H. J. McKellar and G. J. Stephenson "Klein paradox and the Dirac-Kronig-Penney model", *Physical Review A* **36**, 2566–2569 (1987).

[251] M. G. Calkin, D. Kiang, and Y. Nogami "Nonlocal separable potential in the one-dimensional Dirac equation", *Physical Review C* **38**, 1076–1077 (1988).

[252] F. Domínguez-Adame "Exact solutions of the Dirac equation with surface delta interactions", *Journal of Physics A: Mathematical and Theoretical* **23**, 1993 (1990).

[253] S. Camalet, S. Kohler, and P. Hänggi "Shot-noise control in ac-driven nanoscale conductors", *Physical Review B* **70**, 155326 (2004).

[254] B. Korenev *Bessel functions and their applications*. Taylor & Francis (2002).

[255] C. Creffield "Location of crossings in the Floquet spectrum of a driven two-level system", *Phys. Rev. B* **67**, 165301 (2003).

[256] M. Wagner "Quenching of resonant transmission through an oscillating quantum well", *Physical Review B* **49**, 16544–16547 (1994).

[257] A. Lagendijk, B. van Tiggelen, and D. S. Wiersma "Fifty years of Anderson localization", *Physics Today* **62**, 24–29 (2009).

[258] B Kramer and A MacKinnon "Localization: theory and experiment", *Reports on Progress in Physics* **56**, 1469 (1993).

[259] F. Evers and A. D. Mirlin "Anderson transitions", *Reviews of Modern Physics* **80**, 1355–1417 (2008).

[260] N. Mott "Conduction in glasses containing transition metal ions", *Journal of Non-Crystalline Solids* **1**, 1 –17 (1968).

[261] P. A. Lee and T. V. Ramakrishnan "Disordered electronic systems", *Reviews of Modern Physics* **57**, 287–337 (1985).

[262] F. Wegner "Electrons in disordered systems. Scaling near the mobility edge", *Zeitschrift für Physik B Condensed Matter* **25**, 327–337 (1976).

[263] S. Hikami "Anderson localization in a nonlinear-sigma-model representation", *Physical Review B* **24**, 2671–2679 (1981).

[264] D. Belitz and T. R. Kirkpatrick "The Anderson-Mott transition", *Reviews of Modern Physics* **66**, 261–380 (1994).

[265] J. T. Edwards and D. J. Thouless "Numerical studies of localization in disordered systems", *Journal of Physics C: Solid State Physics* **5**, 807 (1972).

[266] A MacKinnon "Critical exponents for the metal-insulator transition", *Journal of Physics: Condensed Matter* **6**, 2511 (1994).

[267] T. Ohtsuki, K. Slevin, and T. Kawarabayashi "Review of recent progress on numerical studies of the Anderson transition", *Annalen der Physik* **8**, 655–664 (1999).

[268] R. Rmer and M. Schreiber. "Numerical Investigations of Scaling at the Anderson Transition". In: *Anderson Localization and Its Ramifications*. Ed. by T. Brandes and S. Kettemann. Vol. 630. Lecture Notes in Physics. Springer Berlin Heidelberg, 2004, 3–19.

[269] H. Stupp et al. "Possible solution of the conductivity exponent puzzle for the metal-insulator transition in heavily doped uncompensated semiconductors", *Physical Review Letters* **71**, 2634–2637 (1993).

[270] T. F. Rosenbaum, G. A. Thomas, and M. A. Paalanen "Critical behavior of Si:P at the metal-insulator transition", *Physical Review Letters* **72**, 2121–2121 (1994).

[271] H. Stupp et al. "Stupp *et al* . reply", *Physical Review Letters* **72**, 2122–2122 (1994).

[272] S. Waffenschmidt, C. Pfleiderer, and H. v. Löhneysen "Critical Behavior of the Conductivity of Si:P at the Metal-Insulator Transition under Uniaxial Stress", *Physical Review Letters* **83**, 3005–3008 (1999).

[273] D. S. Wiersma et al. "Localization of light in a disordered medium", *Nature* **390**, 671–673 (1997).

[274] H. Hu et al. "Localization of ultrasound in a three-dimensional elastic network", *Nature Physics* **4**, 945–948 (2008).

[275] J. Chabé et al. "Experimental Observation of the Anderson Metal-Insulator Transition with Atomic Matter Waves", *Physical Review Letters* **101**, 255702 (2008).

[276] G. Lemarié et al. "Observation of the Anderson metal-insulator transition with atomic matter waves: Theory and experiment", *Physical Review A* **80**, 043626 (2009).

[277] S. V. Kravchenko et al. "Possible metal-insulator transition at B =0 in two dimensions", *Physical Review B* **50**, 8039–8042 (1994).

[278] S. V. Kravchenko et al. "Scaling of an anomalous metal-insulator transition in a two-dimensional system in silicon at B =0", *Physical Review B* **51**, 7038–7045 (1995).

[279] S. V. Kravchenko et al. "Electric Field Scaling at a $B = 0$ Metal-Insulator Transition in Two Dimensions", *Physical Review Letters* **77**, 4938–4941 (1996).

[280] J. Lam et al. "Scaling and the metal-insulator transition in Si/SiGe quantum wells", *Physical Review B* **56**, R12741–R12743 (1997).

[281] P. T. Coleridge et al. "Metal-insulator transition at $B = 0$ in p-type SiGe", *Physical Review B* **56**, R12764–R12767 (1997).

[282] M. Y. Simmons et al. "Metal-Insulator Transition at $B = 0$ in a Dilute Two Dimensional GaAs-AlGaAs Hole Gas", *Physical Review Letters* **80**, 1292–1295 (1998).

[283] Y. Hanein et al. "Properties of the apparent metal-insulator transition in two-dimensional systems", *Physical Review B* **58**, R7520–R7523 (1998).

[284] J. Yoon et al. "Wigner Crystallization and Metal-Insulator Transition of Two-Dimensional Holes in GaAs at $B = 0$", *Physical Review Letters* **82**, 1744–1747 (1999).

[285] E. Abrahams, S. V. Kravchenko, and M. P. Sarachik "Metallic behavior and related phenomena in two dimensions", *Reviews of Modern Physics* **73**, 251–266 (2001).

[286] S. V. Kravchenko and M. P. Sarachik "Metalinsulator transition in two-dimensional electron systems", *Reports on Progress in Physics* **67**, 1 (2004).

[287] M. Y. Simmons et al. "Weak Localization, Hole-Hole Interactions, and the "Metal"-Insulator Transition in Two Dimensions", *Physical Review Letters* **84**, 2489–2492 (2000).

[288] A. Punnoose and A. M. Finkel'stein "Metal-insulator transition in disordered two-dimensional electron systems.", *Science* **310**, 289–91 (2005).

[289] A. K. Geim "Graphene: Status and Prospects", *Science* **324**, 1530–1534 (2009).

[290] T. Ando, T. Nakanishi, and R. Saito "Berry's Phase and Absence of Back Scattering in Carbon Nanotubes", *Journal of the Physical Society of Japan* **67**, 2857–2862 (1998).

[291] J. H. Bardarson et al. "One-Parameter Scaling at the Dirac Point in Graphene", *Physical Review Letters* **99**, 106801 (2007).

[292] K. Nomura, M. Koshino, and S. Ryu "Topological Delocalization of Two-Dimensional Massless Dirac Fermions", *Physical Review Letters* **99**, 146806 (2007).

[293] Y.-Y. Zhang et al. "Localization and the Kosterlitz-Thouless Transition in Disordered Graphene", *Physical Review Letters* **102**, 106401 (2009).

[294] M Schreiber and M Ottomeier "Localization of electronic states in 2D disordered systems", *Journal of Physics: Condensed Matter* **4**, 1959 (1992).

[295] S.-J. Xiong and Y. Xiong "Anderson localization of electron states in graphene in different types of disorder", *Physical Review B* **76**, 214204 (2007).

[296] M. Amini, S. A. Jafari, and F. Shahbazi "Anderson transition in disordered graphene", *EPL (Europhysics Letters)* **87**, 37002 (2009).

[297] I. Amanatidis and S. N. Evangelou "Quantum chaos in weakly disordered graphene", *Physical Review B* **79**, 205420 (2009).

[298] Y. Song, H. Song, and S. Feng "The effects of disorder and interactions on the Anderson transition in doped graphene", *Journal of Physics: Condensed Matter* **23**, 205501 (2011).

[299] J. E. Barrios-Vargas and G. G. Naumis "Critical wavefunctions in disordered graphene", *Journal of Physics: Condensed Matter* **24**, 255305 (2012).

[300] H. Amanatidis et al. "Critical level-statistics for weakly disordered graphene", *ArXiv e-prints: 1302.2470* (, 2013).

[301] M. Hilke "Metallic-to-insulating transition in disordered graphene monolayers", *ArXiv e-prints: 0912.0769* (, 2009).

[302] J. Schleede, G. Schubert, and H. Fehske "Comment on "Anderson transition in disordered graphene" by Amini M. et al.", *EPL (Europhysics Letters)* **90**, 17002 (2010).

[303] M. Amini, S. A. Jafari, and F. Shahbazi "Reply to the Comment by J. Schleede et al.", *EPL (Europhysics Letters)* **90**, 17003 (2010).

[304] K. L. Lee et al. "Analytical and numerical study of uncorrelated disorder on a honeycomb lattice", *Physical Review B* **87**, 144202 (2013).

[305] J. Bang and K. J. Chang "Localization and one-parameter scaling in hydrogenated graphene", *Physical Review B* **81**, 193412 (2010).

[306] G. Schubert and H. Fehske "Metal-to-Insulator Transition and Electron-Hole Puddle Formation in Disordered Graphene Nanoribbons", *Physical Review Letters* **108**, 066402 (2012).

[307] A. Lherbier et al. "Transport Length Scales in Disordered Graphene-Based Materials: Strong Localization Regimes and Dimensionality Effects", *Physical Review Letters* **100**, 036803 (2008).

[308] G. Schubert, J. Schleede, and H. Fehske "Anderson disorder in graphene nanoribbons: A local distribution approach", *Physical Review B* **79**, 235116 (2009).

[309] A. Eilmes, A. M. Fischer, and R. A. Römer "Critical parameters for the disorder-induced metal-insulator transition in FCC and BCC lattices", *Physical Review B* **77**, 245117 (2008).

[310] J. L. Pichard and G Sarma "Finite size scaling approach to Anderson localisation", *Journal of Physics C: Solid State Physics* **14**, L127 (1981).

[311] A. MacKinnon and B. Kramer "One-parameter scaling of localization length and conductance in disordered systems", *Physical Review Letters* **47**, 1546–1549 (1981).

[312] B. Kramer and M. Schreiber. "Transfer-Matrix Methods and Finite-Size Scaling for Disordered Systems". In: *Computational Physics*. Ed. by K. Hoffmann and M. Schreiber. Springer Berlin Heidelberg, 1996, 166–188.

[313] V. I. Oseledec "A multiplicative ergodic theorem. Ljapunov characteristic numbers for dynamical systems", *Transactions of the Moscow Mathematical Society* **19**, 197–231 (1968).

[314] F. Milde. "Disorder-induced metal-insulator transition in anisotropic systems". PhD thesis. TU Chemnitz, 2000.

[315] T. Edwards. "Parallelising the Transfer-Matrix Method using Graphics Processors". MA thesis. University of Warwick, 2012.

[316] K. Frahm et al. "Scaling in Interaction-Assisted Coherent Transport", *EPL (Europhysics Letters)* **31**, 169 (1995).

[317] M. L. Ndawana, R. A. Römer, and M. Schreiber "The Anderson metal-insulator transition in the presence of scale-free disorder", *EPL (Europhysics Letters)* **68**, 678–684 (2004).

[318] K. Slevin and T. Ohtsuki "Corrections to Scaling at the Anderson Transition", *Physical Review Letters* **82**, 382–385 (1999) ArXiv: cond-mat/9812065.

[319] A. Rodriguez et al. "Multifractal finite-size scaling and universality at the Anderson transition", *Physical Review B* **84**, 134209 (2011).

[320] A. Rodriguez et al. "Critical Parameters from a Generalized Multifractal Analysis at the Anderson Transition", *Physical Review Letters* **105**, 046403 (2010).

[321] S. Gershgorin "Über die Abgrenzung der Eigenwerte einer Matrix", *Izv. Akad. SSSR, Otd. Mat. Estest. Nauk* **VII**, 749–754 (1931).

[322] U. Grimm, R. A. Römer, and G. Schliecker "Electronic states in topologically disordered systems", *Annals of Physics (Leipzig)* **7**, 389–393 (1998).

[323] M. Leadbeater, R. A. Römer, and M. Schreiber "Interaction-dependent enhancement of the localisation length for two interacting particles in a one-dimensional random potential", *European Physical Journal B* **8**, 643–652 (1999).

[324] K. Nakada et al. "Edge state in graphene ribbons: Nanometer size effect and edge shape dependence", *Physical Review B* **54**, 17954–17961 (1996).

[325] A. MacKinnon and B. Kramer "The scaling theory of electrons in disordered solids: additional numerical results", *Zeitschrift für Physik B* **53**, 1–13 (1983).

[326] L. Brey and H. A. Fertig "Electronic states of graphene nanoribbons studied with the Dirac equation", *Physical Review B* **73**, 235411 (2006).

[327] D. Gunlycke and C. T. White "Scaling of the localization length in armchair-edge graphene nanoribbons", *Physical Review B* **81**, 075434 (2010).

[328] X. Wang et al. "Graphene nanoribbons with smooth edges behave as quantum wires", *Nature* **6**, 563–567 (2011).

[329] X. Li et al. "Chemically Derived, Ultrasmooth Graphene Nanoribbon Semiconductors", *Science* **319**, 1229–1231 (2008).

[330] F. Miao et al. "Phase-Coherent Transport in Graphene Quantum Billiards", *Science* **317**, 1530–1533 (2007).

[331] L. A. Ponomarenko et al. "Chaotic Dirac Billiard in Graphene Quantum Dots", *Science* **320**, 356–358 (2008).

[332] I. Karabulut, H Safak, and M Tomak "Excitonic effects on the nonlinear optical properties of small quantum dots", *Journal of Physics D: Applied Physics* **41**, 155104 (2008).

[333] D. Shin and J. Hong "Electron transport in the Aharonov-Bohm pump", *Physical Review B* **70**, 073301 (2004).

[334] D. Ryndyk et al. "Green Function Techniques in the Treatment of Quantum Transport at the Molecular Scale". In: *Energy Transfer Dynamics in Biomaterial Systems*. Ed. by I. Burghardt et al. Vol. 93. Springer Series in Chemical Physics. Springer Berlin Heidelberg, 2009, 213–335.

[335] D. H. Choe, J. Bang, and K. J. Chang "Electronic structure and transport properties of hydrogenated graphene and graphene nanoribbons", *New Journal of Physics* **12**, 125005 (2010).

[336] A. Fasolino, J. Los, and M. Katsnelson "Intrinsic ripples in graphene", *Nature Materials* **6**, 858–861 (2007).